

ABSTRACT

PEARSON, JAMES DEON. Microstructural Modeling and Design Optimization of Adaptive Thin-Film Nanocomposite Coatings For Durability and Wear. (Under the direction of Mohammed A. Zikry).

Adaptive thin-film nanocomposite coatings comprised of crystalline ductile phases of gold and molybdenum disulfide, and brittle phases of diamond like carbon (DLC) and yttria stabilized zirconia (YSZ) have been investigated by specialized microstructurally-based finite-element techniques. A new microstructural computational technique for efficiently creating models of nanocomposite coatings with control over composition, grain size, spacing and morphologies has been developed to account for length scales that range from nanometers to millimeters for efficient computations. The continuum mechanics model at the nanometer scale was verified with molecular dynamic models for nanocrystalline diamond. Using this new method, the interrelated effects of microstructural characteristics such as grain shapes and sizes, matrix thicknesses, local material behavior due to interfacial stresses and strains, varying amorphous and crystalline compositions, and transfer film adhesion and thickness on coating behavior have been investigated. A mechanistic model to account for experimentally observed transfer film adhesion modes and changes in thickness was also developed. One of the major objectives of this work is to determine optimal crystalline and amorphous compositions and behavior related to wear and durability over a wide range of thermo-mechanical conditions.

The computational predictions, consistent with experimental observations, indicate specific interfacial regions between DLC and ductile metal inclusions are critical regions of stress and strain accumulation that can be precursors to material failure and wear. The predicted results underscore a competition between the effects of superior tribological properties associated with MoS₂ and maintaining manageable stress levels that would not exceed the coating strength. Varying the composition results in tradeoffs between lubrication, toughness, and strength, and the effects of critical stresses and strains can be controlled for desired behavior. The analysis also indicates that coating strength increases at a higher rate than the internal coating stresses with decreasing grain size. For transfer films, the present study underscores the beneficial material effects of increasing transfer film thickness and reducing transfer film extrusion due to increased thickness.

© Copyright 2009 by James Deon Pearson

All Rights Reserved

Microstructural Modeling and Design Optimization of Adaptive Thin-Film Nanocomposite
Coatings For Durability and Wear

by
James Deon Pearson

A dissertation submitted to the Graduate Faculty of
North Carolina State University
in partial fulfillment of the
requirements for the degree of
Doctor of Philosophy

Mechanical Engineering

Raleigh, North Carolina

2009

APPROVED BY:

Dr. Jeffrey Eischen

Dr. Kara Peters

Dr. Yong Zhu

Dr. Mohammed Zikry
Chair of Advisory Committee

DEDICATION

This work is dedicated to a dedicated God, country, family and considerable number of caring, supporting, and entertaining(!), cast. Without your constant support this project could not have succeeded. Cheers!!!

BIOGRAPHY

James Pearson was born in Greensboro, NC April 13th 1981 to Benjamin (Jim) and Debbie Pearson three and ½ years after his sister Jennifer. After moving to Newport News Virginia, he settled in Winston-Salem NC and attended middle and high school at Northwest Middle and North Forsyth High respectively.

James was selected as a D.A.R.E essay contest winner in the fifth grade. He later joined Cub scouts and finally Boy Scouts before being awarded the rank of Eagle Scout at the age of 17. James was a founding member of his Church youth band, playing bass guitar for 2 years before leaving for college. At high school graduation, James was awarded the Montague Award for the highest GPA among the senior class during the senior year.

Upon high school graduation, he attended North Carolina State University in pursuit of a Bachelors of Science in Mechanical Engineering. James was awarded the Edgar B. Nichols scholarship the same year he was elected to Phi Kappa Phi in 2002. He was later nominated for Golden Key and Tau Beta Phi Honors Societies. He was also nominated for the 2003 College of Engineering Senior Award for Scholarly Achievement. An internship was performed his sophomore year at the Duke Power Catawba Nuclear Station in Rock Hill SC. James performed undergraduate research in the field of ballistic impact on composites for two summers after his sophomore year. At graduation, James was valedictorian of the 2003 class of mechanical engineering at North Carolina State University with a 4.0 GPA and had achieved Dean's List all semesters at N.C. State University.

Upon graduation after four years, he pursued a Masters of Science in Mechanical Engineering at North Carolina State University under the oversight of Professor Mohammed A. Zikry in the experimental field of instrumented low velocity impact upon composites in conjunction with highly local strain measurements from optical strain gauge sensors with funding from the National Science Foundation through grant # CMS 0219690. Fourteen publications, comprising ten proceedings, three journal articles and his Masters Thesis, were produced and presented from the work.

After graduation, he pursued a Doctor of Philosophy degree in Mechanical Engineering at North Carolina State University under the oversight of Professor Mohammed A. Zikry in the field of finite element modeling of nano-tribological wear and friction of nanocomposite metal alloy surface coatings with support from the United States Air Force through MURI Award #FA9550-04-1-0381. Seven publications, comprising two proceedings, four journal articles and his Ph.D. dissertation, were produced and presented from the work. James was awarded a United States Department of Education GAANN Computational Science Fellowship in 2007. He also won the Department of Mechanical and Aerospace Engineering Graduate Student Poster Competition in both 2006 and 2008 and the ECE Fall 2007 Seminar Event Poster Competition. James served as President of the Mechanical and Aerospace Graduate Student Association in 2007 and helped to secure the first ever block grant, hold the first ever new student seminars, participate for the first time in the ECE Fall Seminar (where the department won over half the prizes) and helped to place a fellow Mechanical and Aerospace graduate student onto the UGSA Executive Board. During

this time he played the piano for four weddings, three departmental graduations, two funerals, two Valentine's day banquets and one church band. He became Treasurer of Trailside Commons Home Owners Association in 2008. After graduation, James accepted a position with Applied Research Associates, Southeast Division, in Raleigh, NC.

The following publications were produced during his tenure at North Carolina State University:

Journal Articles

- 1) Pearson J.D., Zikry M.A., Prabhugoud M., Peters K.J. (2007) "Measurement of Low Velocity and Quasi-Static Failure Modes in PMMA" *Journal of Polymer Composites*, Vol. 28, No. 3, pp. 381-391
- 2) Prabhugoud M., Peters K.J., Pearson J.D., Zikry M.A. (2007) "Independent Measurement of Strain and Sensor Failure Features in Bragg Grating Sensors through Multiple Mode Coupling" *Journal of Sensors and Actuators A*, Vol. 135, pp. 433-442
- 3) Pearson J.D., Zikry M.A., Prabhugoud M., Peters K.J. (2007) "Global-Local Assessment of Low-Velocity Impact Damage in Woven Composites" *Journal of Composite Materials*, Vol. 41, No. 23, pp. 2759-2783

- 4) Pearson J.D., Zikry M.A., Wahl K.J. (2009) “Microstructural Modeling of Adaptive Nanocomposite Coatings For Durability and Wear” *Journal of Wear, In Press, Manuscript ID: IH-4966*
- 5) Pearson J.D., Zikry M.A. (2009) “Computational Design of Thin-Film Nanocomposite Coatings For Optimized Stress and Velocity Accommodation Response” *Journal of Wear, In Press, Manuscript ID: 0121R2*
- 6) Dawson B., Barefoot K., Baker C., Pan L., Pearson J.D., Zikry M.A., Voevodin A.A., Krim J. (2008) “Nanoscale Design of Adaptive Tribological Coatings and Gold-Yttrium Stabilized Zirconia Based Nanocomposites” *Submitted to Journal of Vacuum and Science Technology B*
- 7) Pearson J.D., Harrison J., Guangtu G., Zikry M.A. (2008) “Nanoindentation of Nanocrystalline Amorphous Diamond Composites: A Hierarchical Molecular Dynamics and Finite-Element Approach” *Submitted to Journal of Computational Materials Science, Manuscript ID: COMMAT-D-08-00476*

Refereed Proceedings

- 8) Pan L., Dawson B., Barefoot K., Krim J., Pearson J.D., Zikry M.A., Baker C., Voevodin A.A. (2008) “Nanoscale Design of Adaptive Tribological Coatings” *Proceedings of the STLE/ASME International Joint Tribology Conference, Miami, Florida, Paper #71196, October 20-22*

- 9) Pearson J.D., Zikry M.A., Peters K.J. (2008) “Local and Global Measurements of Dynamic Damage Evolution in Woven Composite Systems” *Proceedings of the 2nd International Joint Conference on Knowledge Management for Composite Materials (KMCM08)*, Vancouver, B.C., Canada, Paper #87, July 8-11
- 10) Pearson J.D., Zikry M.A., Peters K.J., Prabhugoud M. (2007) “Local and Global Measurements of Dynamic Damage Evolution in Woven Composite Systems” *16th International Conference on Composite Materials*, Japan, Paper #904, July
- 11) Garrett R.C., Pearson J.D., Peters K.J., Zikry M.A. (2007) “Optimization of Fiber Bragg Grating Sensor Configurations for In-Situ Failure Identification in Woven Composites Throughout Impact” *SPIE Proceedings, Sensors and Smart Structures Technologies*, Vol. 6529, Paper #6529-24, May
- 12) Pearson J.D., Zikry M.A., Rezvanian O. (2006) “Computational Modeling and Design of Adaptive Thin-Film Composite Coatings” *MRS Symposium Proceeding*, Vol. 977, Paper # 0977-FF08-10, November
- 13) Pearson J., Zikry M., Peters K., Prabhugoud M. (2006) “Local and Global Measurements of Dynamic Damage Evolution in Woven Composite Systems” *8th International Conference on Textile Composites (TEXCOMP-8)*, Editor: A. Long, Nottingham, UK, pp. T41-T47, October 16-18
- 14) Pearson J., Prabhugoud M., Zikry M., Peters K. (2006) “In Situ Failure Identification in Woven Composites Throughout Impact Using Fiber Bragg Grating Sensors” *SPIE*

- Proceedings, Smart Structures and Materials*, Vol. 6174, Paper #6174-2V, pp. 908-918, March
- 15) Prabhugoud M., Pearson J., Peters K., Zikry M. (2005) “Radiation and Cladding Modes as Independent Measurements of Bragg Grating Sensor Integrity” *SPIE Proceedings, 12th Annual International Symposium, Smart Structures and Materials / NDE*, Vol. 5758, pp. 440-450, May
 - 16) Pearson J., Prabhugoud M., Zikry M., Peters K., Sitar M., Davis L. (2005) “Failure and Damage Initiation in Woven Composites with Fiber Bragg Gratings Sensors” *SPIE Proceedings, 12th Annual International Symposium, Smart Structures and Materials / NDE*, San Diego, CA, Vol. 5765, pp. 540-551
 - 17) Pearson J., Prabhugoud M., Zikry M., Peters K. (2005) “Damage Progression and Identification in Woven Composites with Fiber Bragg Grating Sensors” *ASME International Mechanical Engineering Congress and Exposition, Proceedings of the IMECE2005*, Orlando, FL, Paper # 80487
 - 18) Pearson J., Prabhugoud M., Zikry M., Peters K. (2004) “Failure Identification Methodology for Woven Composites Incorporating Sensor Degradation” *ASME International Mechanical Engineering Congress and Exposition, Proceedings of the IMECE2004*, Anaheim, CA, Paper # 61802
 - 19) Prabhugoud M., Pearson J., Peters K., Zikry M. (2004) “Demonstration of Failure Identification Methodology Incorporating Sensor Degradation” *SPIE Proceedings*,

Sensors and Smart Structures Technology for Civil, Mechanical, and Aerospace Systems, San Diego, CA, Vol. 5391, pp. 107-116

ACKNOWLEDGMENTS

James would like to thank God, country, and family; Jim Pearson, Debbie Pearson, and Jennifer Pearson, first and foremost for their dedicated and unquestioned support over the past 27 years. A special acknowledgement is provided for the support from Dr. Mohammed A. Zikry in the pursuit of this degree, without whose patience and guidance this work would not have been possible. Thank you sincerely.

James would like to acknowledge the financial support of the United States Air Force through MURI Award #FA9550-04-1-0381 and the United States Department of Education through the GAANN Computational Science Fellowship. The support of the Office of Naval Research (ONR), the Naval Research Laboratory (NRL) and the Air Force Research Laboratory (AFRL) are also gratefully acknowledged.

James would like to thank Andrey Voevodin, Kathryn Wahl, Rich Chromik, and Colin Baker for the design, fabrication and characterization of the nanocomposite coatings studied in this work. Ben Dawson of North Carolina State University is also acknowledged for the TEM images of the nanocomposite coating microstructure. Judith Harrison and Guangtu Gao of the United States Naval Academy are also acknowledged for performing the molecular dynamics simulations. Tarek Hatem, Khalil ElKhodary, Jibin Shi, Pratheek Shanthraj, William Lee, Siqi Xu, Omid Rezvanian, Fadi Abdel Jawad, Brian Bouterse, Paul Whatley, Giovanna Ombretta Scifo and Waeil Ashmawi are also acknowledged for many helpful lab discussions and providing new perspective.

There are numerous colleagues and cast too numerous to list here who also deserve recognition for their advice and assistance throughout the years. In lieu of a formal listing, Thank you so much!

TABLE OF CONTENTS

LIST OF TABLES	xv
LIST OF FIGURES	xvi
LIST OF SYMBOLS	xxi
1. INTRODUCTION	1
2. COMPUTATIONAL METHOD	7
2.1 Nanocomposite Finite Element Model	8
2.1.1 Composite Mechanics RVE and ROM.....	13
2.1.2 Transfer Film.....	15
2.1.3 Coating RVE.....	16
2.2 Material Models.....	19
2.3 Method of Radial Return For Ductile Materials.....	22
2.4 Microstructural Modeling Optimization and Grain Morphology Representation	28
2.5 Continuum Verification Model	32
2.5.1 Molecular Dynamics Approach	33
2.5.2 Finite Element Model	36
2.6 Tables and Figures (Chapter 2)	39

3.	CONTINUUM MODEL VERIFICATION	62
	3.1 Conclusions	68
	3.2 Figures (Chapter 3).....	70
4.	NANOCOMPOSITE COATING BEHAVIOR	78
	4.1 Composition Variations and Indentation Response.....	79
	4.1.1 Indentation to 20% Nominal Strain.....	81
	4.1.2 Indentation to 56% Nominal Strain.....	87
	4.2 Sliding Models.....	89
	4.3 Microstructural Optimization.....	94
	4.4 Conclusions	99
	4.5 Tables and Figures (Chapter 4)	102
5.	TRANSFER FILM MODELS	131
	5.1 Conclusions	137
	5.2 Figures (Chapter 5).....	139
6.	WEAR MODELS	146
	6.1 Element Failure.....	149

6.2	Material Transfer Techniques: Change of Material Constituents.....	152
6.3	Conclusions	155
6.4	Figures (Chapter 6).....	156
7.	FUTURE RESEARCH RECOMMENDATIONS	187
8.	REFERENCES	189
9.	APPENDIX	197
	9.1 Appendix A	198

LIST OF TABLES

Table 2.1	Mechanical Properties for Each Constituent and Typical Friction Coefficients.....	40
Table 2.2	Set of 20 Unique Seed Points Whose Voronoi Tessellation Produces Even Sided Cells Over a Unit Domain.....	41
Table 4.1	Coating Composition and Predicted Homogenized Coating Modulus Using the Composite Mechanics Approach and the Composite Mechanics Rule of Mixtures.....	103
Table 4.2	Locations and Magnitudes of Maximum Effective Stress in Each Nanocomposite Coating With the Refined Mesh and 300-600 nm Grain Size Under 20% Nominal Strain	105
Table 4.3	Nominal Strain at the Start of Plastic Deformation in the Steel Substrate With and Without Thin Film Coatings With 300-600 nm Grain Size and Refined Mesh.....	106
Table 4.4	Fracture Toughness, K_{IC} , of DLC Matrix Material and Surface Energy, γ^* , of Coating Constituents.....	107

LIST OF FIGURES

Figure 2.1	Dimensions and Materials Involved in the Nanocomposite Coating Finite Element Models.....	42
Figure 2.2	The Center of the ‘Active Zone’	43
Figure 2.3	The Transition Between the ‘Active Zone’ and the Homogenized Coating	44
Figure 2.4	The ‘Active Zone’ Underneath the Indenter With a Transfer Film of 200 nm Thickness	45
Figure 2.5	Composite Mechanics RVE of Coating Samples.....	46
Figure 2.6	Transfer Film With Varying Thickness.....	47
Figure 2.7	Multi-Linear Model for Gold and MoS ₂	48
Figure 2.8	Method of Radial Return	49
Figure 2.9	TEM Image of a Nanocomposite Coating	50
Figure 2.10	Possible Quadrilateral Element Meshes for Even Sided, Convex, Polygonal Grains	51
Figure 2.11	Method of Producing Even Sided Voronoi Tessellations Over a Variable Sized Domain.....	52
Figure 2.12	Relationship Between Grain Size and Number of Elements in the Optimized Mesh Coating Finite Element Models	53
Figure 2.13	‘Active zone’ Mesh Underneath the Indenter at the Center of the Contact for the Grain Sizes Investigated Using the Optimized Mesh Technique	54
Figure 2.14	MD Starting Configurations for the MDN Systems.....	55

Figure 2.15	The Finite Element Model of MDN System (Film 1) Used in the MD Simulations.....	58
Figure 3.1	Example of Diamond Nano-Crystal in MDN System With No Surface Morphology and a Deeper Substrate.....	71
Figure 3.2	Average Normal Contact Pressure, P_{Avg} , Versus Radius From Equation (23) for MD and FE Simulations	72
Figure 3.3	Average Normal Contact Pressure, P_{Avg} , Distribution for MD and FE Simulations Versus Loading.....	75
Figure 3.4	MDN Grain Surface Contact Status for Indicated FE Simulations and Maximum FE Contact Pressure, $P_{Contact}$, and von Mises Stress for Selected Simulations Versus Indenter Displacement.....	76
Figure 3.5	Representative Contour of the von Mises Stress Through a Cross-Section of a Diamond Crystal (and the Indenter) Middle.....	77
Figure 4.1	SEM Images of Nanocomposite Coating Cross-Sections Taken During FIB Cutting of a TEM Sample.....	108
Figure 4.2	Locations and Magnitudes of Greatest Effective Stress for a Typical 25% Equal Composition Coating, a 50% Gold Composition Coating, and a 50% MoS ₂ Composition Coating With 300-600 nm Grain Size and a Refined Mesh	111
Figure 4.3	Coating Maximum Normal Stress, σ_{yy} , in Each Material and Effective von Mises Plastic Strain Developed in the MoS ₂ , Gold, and Steel Phases for the 25% Equal Composition Nanocomposite and for a Pure DLC Coating and Titanium Interlayer.....	112
Figure 4.4	Total Energy Dissipated (J) Through Plastic Work in the Ductile Coating Phases (Au and MoS ₂) Versus Total Slid Distance of the Indenter for Coatings With Equal Composition and 300-600 nm Grain Size With Refined Mesh and Ratio of Total Energy Dissipated Via Plastic Work to the Energy Input During Sliding.....	115

Figure 4.5	Shear Stress Developed Under the Slider Within the Same Region of Coating in the Leading Edge of the Contact and the Trailing Edge of the Contact as the Slider Passes for the First Trip	116
Figure 4.6	Maximum Effective Stress (MPa) in the DLC Matrix Material When Between MoS ₂ and Gold Inclusions.....	117
Figure 4.7	In Plane Tensile Stresses (MPa) Developed 21 μm Behind Indenter, In Plane Tensile Stresses Developed +60 μm Behind Indenter and Typical Semi-Elliptical Surface-Flaw Dimensions.....	118
Figure 4.8	Coating Maximum Effective von Mises Stress in Each Material and Effective von Mises Plastic Strain Developed in the MoS ₂ , Gold, Titanium and Steel Phases for the 25% Equal Composition Nanocomposite Coating Using the Optimized Mesh Versus Nominal Strain for Grain Sizes 270 nm, 135 nm and 54 nm.....	119
Figure 4.9	Normalized Effective Stress in the Equal Composition Nanocomposite Coating Using the Optimized Mesh from Simulations at 50% Nominal Strain and Normalized Strength Increase Based on Equation (33) from the Hall-Petch Effect as Grain Size Decreases.....	123
Figure 4.10	Variation in Horizontal and Vertical DLC Matrix Width for a 91 nm Grain Size Nanocomposite Coating Using the Optimized Mesh	124
Figure 4.11	Coating Maximum Effective von Mises Stress in Each Material and Effective von Mises Plastic Strain Developed in the MoS ₂ , Gold, Titanium and Steel Phases for the 25% Equal Composition Nanocomposite Using the Optimized Mesh Versus Coating Nominal Strain With Grain Size 91 nm and Expanded DLC Matrix in Horizontal and Vertical directions.....	125

Figure 4.12	Hardness to Elastic Modulus ($H/E/d^{1/2}$) for Experimental Characterization of Nanocomposite Coatings Based on Composition and Computational Simulations of Nanocomposite Coatings Based on Grain Size Using the Optimized Coating Mesh	128
Figure 5.1	Coating and 200 nm Thick Transfer Film Maximum Effective Stress in Each Material for the 25% Equal Composition Nanocomposite With Refined Mesh and Transfer Film Effective Stress in the Central Most Loaded Region Under 1.4% Nominal Coating Strain for Stable and Unstable Models	140
Figure 5.2	Maximum Effective Stress and Maximum Effective Plastic Strain Developed in the Unstable Transfer Film Under Indentation With Change in Thickness When Indented Against the Nanocomposite Coatings With 300-600 nm Grain Size and Optimized Mesh	143
Figure 6.1	Progression of Coating Failure Under Sliding Loads Using Element Failure and Criterion of 0.55% Plastic Strain for Ductile Elements and 0.25% Ratio of Maximum von Mises Stress to Elastic Modulus for Brittle Materials	157
Figure 6.2	Progression of Coating Failure Under Sliding Loads Using Element Failure and Criterion of 1.0% Plastic Strain for Ductile Elements and 0.2% Ratio of Maximum von Mises Stress to Elastic Modulus for Brittle Materials	165
Figure 6.3	Progression of Coating Failure Under Sliding Loads Using Element Failure and Criterion of 1.0% Plastic Strain for Ductile Elements and 0.2% Ratio of Maximum von Mises Stress to Elastic Modulus for Brittle Materials and a Reduction of the Failed Elements Moduli to 25% and 75% of the Original Elastic Modulus	166
Figure 6.4	Coating Conversion into Transfer Film Material Within Two Sliding Trips Using Failure Criteria of 0.1% Plastic Strain for Ductile Elements and 0.05% Ratio of Maximum von Mises Stress to Elastic modulus for Brittle Materials	169

Figure 6.5	Coating Conversion of Ductile Elements Into Transfer Film Material Using Failure Criteria of 0.1% Plastic Strain for Ductile Elements and 0.6% Ratio of Maximum von Mises Stress to Elastic Modulus for Brittle Materials.....	172
Figure 6.6	Coating Conversion of Elements Into Transfer Film Material Over Ten Sliding Trips Using Failure Criteria of 2% Plastic Strain for Ductile Elements and 0.4% Ratio of Maximum von Mises Stress to Elastic Modulus for Brittle Materials.....	176

LIST OF SYMBOLS

a	Maximum crack depth.
\bar{a}	Radius of contact area.
c	Crack half-width.
d	Indicates the variable immediately following is an increment.
d	Grain diameter.
e	Deviatoric strain tensor.
E	Linear elastic Young's modulus.
E_e	Effective elastic modulus.
E_t	Tangent, or current modulus.
\bar{E}	Homogenized modulus.
E^*	Energy.
f	Volume fraction.
$f(t)$	Coefficient of friction as a function of time.
F	J ₂ plasticity formulation yield criterion.
F_z	Contact force in the z direction.
H	Hardness.
H_p	Plastic modulus.
k	Iteration number.
K_I	Mode I stress intensity factor.
K_{IC}	Fracture toughness.
\hat{n}	Unit vector normal to the yield surface.
p_o	Maximum pressure.
P	Applied load.
P_{Avg}	Average normal contact pressure.
P_{Avg}^{MB}	Maximum bound on average normal contact pressure.
$P_{Contact}$	True contact pressure.
P_Y	Allowable load before plastic deformation.
Q	Plastic potential.
Q^*	Stress intensity factor parameter.
R	Radius of body under indentation.
R_e	Effective radius.
s	Deviatoric stress tensor.
$t_{Coating}$	Thickness of the coating.
t_f	Final time.
u	Nodal displacement.
ν	Poisson's ratio.

V	Sliding velocity.
W_p	Total plastic work, scalar.
$\{d\alpha\}$	Change in translation of the yield surface.
$\{\alpha\}$	Translation of the yield surface, or, back-stress and center of the yield surface.
α	Euler angle.
β	Euler angle.
$\{C\}$	Elastic moduli tensor.
∂	Indicates the variable immediately following is a differential.
$\delta_{Y \text{ Max Coating}}$	Maximum vertical displacement of the free surface of the coating.
$\{d\epsilon\}$	Total increment of strain tensor.
$\{d\epsilon^e\}$	Increment of elastic (recoverable) strain tensor.
$\{d\epsilon^p\}$	Increment of plastic (nonrecoverable) strain tensor.
$\{\epsilon\}$	Strain tensor.
$\{\bar{\epsilon}\}$	Second invariant of the strain tensor.
$\{\epsilon^p\}$	Plastic strain tensor.
ϵ_{Break}	Ultimate elongation before rupture.
$\epsilon_{Nominal}$	Nominal strain.
$\tilde{\epsilon}$	Axial strain.
γ	Euler angle.
γ^*	Surface energy.
$\{I\}$	Identity matrix.
$d\lambda$	Plastic multiplier.
$\{d\sigma\}$	Total increment of stress tensor.
$\{\sigma\}$	Stress tensor.
$\{\bar{\sigma}\}$	Second invariant of the stress tensor.
σ_{Ult}	Ultimate stress at rupture.
σ_Y	Yield stress.
σ_{YY}	Maximum normal stress.
σ_{vm}	von Mises, or effective, stress.
σ^*	Mode I tensile stress field.
τ_{Max}	Maximum shear stress.
μ	Lamé's second parameter, or, shear modulus.
$\{\xi\}$	Deviatoric stresses offset to the center of the deviatoric stress space.

1. INTRODUCTION

Thin-film coatings for lubrication are commonly used in applications related to severe changes in loading conditions and environments. Lubrication, wear mitigation and a stable coefficient of friction under sliding conditions in extreme environments are challenging requirements, which cannot be met by a single material alone or liquid lubricants (Baker *et al.* 2007; Singer *et al.* 2003; Chromik *et al.* 2006; Wahl *et al.* 1997). Extreme environments are typically described as high strain rate, high and low temperature (+500° to -100° C) and variable atmospheric and vacuum conditions.

Recent experiments (Chromik *et al.* 2006) and processing have identified thin-film nanocomposite coatings with different combinations of crystalline and amorphous constituents exhibiting intrinsic low-friction that is adaptive in real time to changes in the environment as well as possessing good wear resistance and durability. These multicomponent coating systems provide good tribological performance over a greater operational range than a single phase coating can provide. From a design standpoint, these coatings combine the mechanical advantage of nanostructured hard phases such as nitrides and carbides with friction modifying phases. In general, these tribological coatings are one micron thick thin-film nanocomposite (1 μm) coatings comprised of brittle diamond-like carbon (DLC) and yttria stabilized zirconia ($\text{ZrO}_2\text{-Y}_2\text{O}_3$, YSZ) phases along with ductile molybdenum disulfide (MoS_2) and gold (Au) phases.

These coatings are created through novel hybrid pulsed laser deposition (PLD) and ion beam assisted magnetron sputtering processes to possess adaptive lubrication, as well as strengthening and toughening mechanisms, which satisfy the desired operational requirements (Pearson *et al.* 2009; Pearson *et al.* 2006; Voevodin and Zabinski 2000; Voevodin *et al.* 2001; Voevodin and Zabinski 1998). These systems are referred to as adaptive coatings in that low wear, environmental stability, and low friction coefficient can be attained in dry, humid, and high temperature (500° C) operating conditions (Voevodin *et al.* 2002). This coating performance is highly promising for a myriad of thermo-mechanical and wear applications. This thin film coating can potentially be optimized with an integrated experimental and modeling framework in terms of microstructure (grain size, morphology and spacing) and material constituents and distributions to provide tailored low wear, stable friction, and multi-environment operational capabilities with a single material system.

Computational modeling of thin-film coating wear has traditionally been based on the homogenization of coating properties to compute wear rates (Podra and Andersson 1999a; Molinari *et al.* 2001; Liu *et al.* 2004; Gonzalez *et al.* 2005; Ding *et al.* 2007). In contrast, nanocomposite thin-film (1 μm) coatings may comprise different material constituents, with each one being used for a desired behavior, such as lubrication, toughening, and strengthening (Voevodin and Zabinski 2003). For these advanced materials there is a need to understand how composition and microstructure (Baker *et al.* 2007; Seitzman *et al.* 1995; Tilbook *et al.* 2007; Patscheider *et al.* 2001), as well as velocity accommodation modes (VAMs) (Singer *et al.* 2003; Dvorak *et al.* 2007) affect the wear response and endurance.

Models based on traditional Hertzian contact are limited to homogenous bodies and frictionless surfaces (Wu and Wang 1995) and thus cannot be used to optimize these coatings in terms of composition, microstructure and velocity accommodation modes. Hence, there is a need to (i) develop mechanical models to evaluate how coating microstructure and composition impact tribological properties as well as (ii) provide predictive capabilities to tailor multi-constituent thin-film response at the coating design stage.

Sliding wear modelling of thin-film (1 μm) solid lubricant coatings using the finite element method has generally been limited to implementations of empirical equations, notably Archard's wear law, or single pass cutting and scratch tests (Hegadekotte *et al.* 2006; Hegadekotte *et al.* 2005; Ko *et al.* 2002; Kang *et al.* 1998; Gonzalez *et al.* 2005; Cantizano *et al.* 2002; Podra and Andersson 1999a; Podra and Andersson 1999b; Liu *et al.* 2004; Ding *et al.* 2007; Molinari *et al.* 2001; Blanchet *et al.* 2001; Bellemare *et al.* 2008). Mechanics based failure criteria have also been examined for modelling wear including energy (Mary and Fouvry 2007; Dragon-Louiset 2001), ultimate strain (Hu *et al.* 2007; Pramanik *et al.* 2007; Elalem and Li 1999; Yan *et al.* 2002), ultimate stress (Xia *et al.* 2007), and fracture mechanics (Ko *et al.* 2001) approaches. However, for advanced multi-component coatings containing both lubricant and strengthening phases specifically designed for adaptive use in changing environments (e.g. temperature and atmosphere) (Baker *et al.* 2007; Chromik *et al.* 2007; Baker *et al.* 2006; Voevodin *et al.* 2002; Voevodin and Zabinski 2000), these empirical models do not elucidate the roles of individual coating constituents, owing to the necessary

homogenization of the coating, and hence make computational optimization of the coating difficult (Hsu *et al.* 1997).

If the mechanisms that result in improved wear and thermo-mechanical response can be accurately identified, then the constituent components and coating properties can be further optimized. Hardness improvements in nanocrystalline materials are understood to be controlled by resistance to dislocation formation and movement (Patschieder 2003). Toughness improvements can be achieved with the addition of ductile materials. Determining optimum configurations for multicomponent mixtures with lubricating phases is challenging as optimizing hardness is not the only concern. What is not known or easily determined are what specific combinations of crystalline, amorphous, brittle, and ductile materials would be optimal, and what the dominant microstructural characteristics are that affect and control this adaptive behavior.

What is desired is a computational tool which includes the individual materials, microstructure (grain shape, size, and distribution), wear effects (i.e. debris and transfer films) and wear modes and mechanisms for parametric predictive studies of these parameters on either coating superior or inferior performance. With this tool, experimental results (Baker *et al.* 2007; Chromik *et al.* 2006) can be used to validate the computational models and predictions of the coating, and the computational models could then be used to efficiently explore the material and microstructure design space to highlight areas of desirable mechanical and tribological performance.

To computationally model this nanocomposite system, a specialized finite element technique has been created (Pearson and Zikry 2009; Pearson *et al.* 2009; Pearson *et al.* 2006) to accurately represent material behavior and microstructure. This model is capable of representing the different length scales pertaining to the constituent grain sizes (10^0 - 10^1 nm), coating thickness (10^3 nm) and experimental wear test sliders and indenters (10^6 nm). Importantly, this technique maintains a manageable computational processing load and time that would be associated with the needed highly detailed, intensive simulations. This computational methodology accounts for the interrelated effects of different material distributions, microstructural effects such as grain shapes and spacing of material constituents, stress and strain evolution, and thermal effects.

Hence, the major objective of the present study is to use microstructurally-based finite element techniques to examine how deformation and failure modes evolve in a simulated sliding contact of a multicomponent, nanostructured composite coating. In this study, detailed finite element simulations of a linear reciprocating ball-on-flat configuration are used to examine local strain and stress evolution as a function of composition and scale. Single component coatings of each constituent (Au, YSZ, MoS₂, DLC) were modeled and used as a limiting case to determine the effects of grain morphology, interfacial regions between the constituents, and mechanical properties for coatings with different compositions. Sliding simulations were undertaken to demonstrate the influence of tangential forces on plastic deformation, fracture, and transfer film formation. Molecular dynamics simulations were used to validate the applicability of the continuum simulations at the nano level.

Transfer film (T.F.) models were also developed, and the T.F.s were represented as both a free (unstable) or bonded (stable) third body in the contact. Based on this, third body velocity accommodation modes (VAMs) relating to experimentally observed wear and interfacial sliding were identified. The effect of transfer film thickness was compared to experimental measurements. Sliding simulations were undertaken to demonstrate the influence of tangential forces on plastic deformations. In the wake of the sliding body, the stress state is analyzed for potential Mode I fracture of the brittle DLC matrix material. Composite mechanics approaches were used to characterize the coating in terms of voids and density. Coating grain size and matrix dimensions were varied computationally to highlight rates of coating strength and stress increase. Hardness measurements were calculated from the finite element results and compared to experimental measurements. The effects of coating composition changes were studied and critical locations where failure would begin were modeled.

This dissertation is organized as follows: the finite element and molecular dynamics modeling techniques are briefly outlined in Section 2. The continuum verification model using the molecular dynamics simulations is presented in Section 3. The results of the finite element simulations of the nanocomposite coatings are presented in Section 4. Models of transfer films for adaptive multicomponent coatings are presented in Sections 5. The results of computational simulations of the coatings failure and evolution are presented in Section 6. In closure, future recommendations for research using computational modeling of the nanocomposite coatings are presented in Section 7.

2. COMPUTATIONAL METHOD

To computationally model the nanocomposite coating system, a combination of composite mechanics and a specialized finite element technique were used. The finite element technique has been created (Pearson and Zikry 2009; Pearson *et al.* 2009; Pearson *et al.* 2006) to accurately represent material behavior and microstructure. This model is capable of representing the different length scales pertaining to the constituent grain sizes (10^0 - 10^1 nm), coating thickness (10^3 nm) and experimental wear test sliders and indenters (10^6 nm). Importantly, this technique maintains a manageable computational processing load and time that would be associated with the needed highly detailed, intensive simulations. This computational methodology accounts for the interrelated effects of different material distributions, microstructural effects such as grain shapes and spacing of material constituents, stress and strain evolution, and thermal effects.

2.1 NANOCOMPOSITE FINITE ELEMENT MODEL

A two-dimensional finite element plane-strain quasi-static model was used in the indentation and sliding simulations. Based on a convergence analysis, 125,000 quadrilateral elements were used for the 300 nm grain size simulations with refined mesh. The coating was represented as two regions: 1) a far-field region with elements of homogenized properties and no microstructural morphologies, and 2) an active zone centered beneath the slider (Figure 2.1) with relevant microstructural morphologies, constituents, and sizes. This active zone is essentially a representative volume element (RVE) that accounts for physically realistic crystalline and amorphous microstructures. This level of morphological detail cannot be represented over the entire coating, since it would be computationally prohibitive due to the mesh size requirements associated with grain and inclusion sizes and shapes. More critically, by using this two-field approach, material behavior can be investigated at appropriate physical scales within the active zone.

It should also be noted that the model system has significantly different physical scales (Chromik *et al.* 2006): coating thicknesses on the order of microns and grain sizes on an order of nanometers, and an indenter or slider on the order of millimeters. By using this two-field approach, interrelated material and system behavior at different physical scales can be accounted for. To treat the differences in length scale within the model (from millimeter sized substrate and contact, to micron thick coating, to nanometer sized grains), non-dimensionalization of the length scales was used to rescale a unit nanometer to a unit length

in the finite element model. All other relevant parameters and material properties with units of length, such as elastic modulus and yield stress, were also scaled appropriately.

The coatings were modeled based on the nanocomposite coating specimens prepared by Baker *et al.* 2007 and the test geometry described by Chromik *et al.* 2006. The model is a representation of 1 micron thick nanocomposite coatings on a 14 x 0.5 mm 440C steel coupon with a 0.3 micron thick uniform interlayer of pure titanium (for coating adhesion) between the steel substrate and the coating (Figure 2.1 and Figure 2.2). Far-field regions away from the center of the steel substrate were assigned homogenized material properties based on reported experimental measurements in Baker *et al.* 2007 and Chromik *et al.* 2006 and as detailed in Section 2.2.

The active microstructural zone, Figure 2.1 and Figure 2.2, is a 100 micron wide region at the center of contact. This region directly underneath the indenter is a physical representation of the coating constituents Au, YSZ, and MoS₂ as randomly distributed and randomly sized and shaped inclusions separated by a DLC regions. The model microstructure corresponds to partially crystalline phases of Au, YSZ, and MoS₂, and amorphous DLC that forms as a dispersed matrix phase. Previous studies for nanocomposite films indicated that the DLC matrix phase exhibited sp² bonding at the inclusion interfaces and sp³ bonding away from inclusions of other constituents (Voevodin *et al.* 2002).

A specialized Voronoi tessellation algorithm was developed for these simulations to generate the random inclusion sizes and distributions in the active zone. Inclusion sizes varied from 300 to 600 nm in average diameter in the models with refined mesh of the

coating. Matrix phase interfacial material had an average thickness of approximately 0.1 μm (Figure 2.1, Figure 2.2 and Figure 2.3) around each inclusion and was added into the model between each cell/grain in a post processing step. Coating regions, which surround the inclusions and their interfaces, were modeled as DLC regions extending towards the free surface and downwards to the titanium interlayer for a thickness of 1 micron. Matlab was used to code the tessellation algorithm and produce the coating geometry which was meshed with a commercial FEA package. With this algorithm, the coating composition, grain size, matrix dimensions and thickness can be controlled explicitly. Models meshed using the commercial FEA package are referred to as the “fine mesh of the coating” models or refined mesh. A different, optimized, mesh is presented in Section 2.4.

To determine the relative volume fraction of each coating constituent, the surrounding DLC areas were not used. Rather, the total volume of the coating was taken to be the volume of the inclusions and borders. The percentages of Au, MoS₂, and YSZ phases were obtained by summing up the volumes of each separate material and dividing by the total volume of the coating. The DLC percentage was obtained by summing the volume of DLC in the interfacial regions and dividing by the total volume of the coating.

The refined coating mesh for 300-600 nm diameter grain size models is shown in Figure 2.1, Figure 2.2 and Figure 2.3. Material distributions within this mesh were varied to create different coating compositions. Specifically, the 100 micron wide coating model was set to have an approximately equal composition (25%) of all materials in the active zone, and this will be referred to as the equal composition nanocomposite. Two other nanocomposite

coatings were simulated, one with 50% MoS₂, and another with 50% Au. The remaining constituent compositions were 25% DLC, 12.5% YSZ, and 12.5% Au or MoS₂. For benchmark purposes, one micron thick coatings of: 1) pure gold, 2) pure DLC, 3) pure MoS₂, and 4) pure homogenized far-field properties were also simulated. Additionally, the substrate was modeled without a coating or interlayer to delineate the mechanical response of an uncoated substrate. The material properties for these models are presented in Section 2.2.

To simulate the experiments, the indenter in Figure 2.1, Figure 2.2, Figure 2.3 and Figure 2.4 was modeled as a 6.35 mm diameter deformable hemisphere with the properties of synthetic sapphire. Contact elements were meshed along the hemispherical surface of the indenter and along the entire free surface of both the active zone and far-field regions. A constant friction coefficient of 0.05 was used for the sapphire hemisphere (Chromik *et al.* 2006). The thick steel substrate was fixed along the bottom edge against translation and the remaining three exterior edges of the model were free to deform and translate. The sapphire indenter was displacement controlled through applying displacement boundary conditions on the top free surface nodes. The amount of displacement was controlled to provide the desired amount of indentation and sliding nominal strain.

Sliding simulations were conducted at a velocity of 1 $\mu\text{m/s}$. For the sliding simulations, the indentation begins at the origin in the center of the active zone, then sliding occurs in the $-x$ direction for 40 μm , then reverses toward the $+x$ direction for 80 μm , and finally toward the $-x$ direction 40 μm to end again at the initial location. This represents one sliding cycle, and each sliding simulation was run for two cycles total.

For all coatings and models, the results are reported as a function of the percent nominal strain applied to the coating. The nominal strain, $\epsilon_{Nominal}$, is the ratio of the maximum displacement of the top surface of the coating, $\delta_{Y Max Coating}$, to the original thickness of the coating, $t_{Coating}$ (1 μm), and is given by:

$$\epsilon_{Nominal} (\%) = \frac{\delta_{Y Max Coating}}{t_{Coating}} \times 100 \quad (1)$$

Experiments using the sapphire indenter previously described were typically conducted with loads ranging from 1 to 6.4 N (Chromik *et al.* 2006; Baker *et al.* 2007), corresponding to nominal strains of 7% to 22% as computed from a Hertzian analysis. At these strains, the contact width varies from 50 to 95 μm , and is thus completely within the active zone of the finite element model. The nominal strain induces deformations and stresses within each phase of the coating. The stresses are reported as the effective, or von Mises σ_{vm} , stress defined by:

$$\sigma_{vm} = \sqrt{\frac{(\sigma_1 - \sigma_2)^2 + (\sigma_2 - \sigma_3)^2 + (\sigma_3 - \sigma_1)^2}{2}} \quad (2)$$

In this equation, σ_1 , σ_2 and σ_3 are the principal stresses from the finite element simulations.

2.1.1 COMPOSITE MECHANICS RVE AND ROM

A square representative volume element (RVE) based solely on the coating composition was created to predict an overall elastic modulus of the coating. This quadrilateral mesh, two-dimensional, quasi-static finite element model excluded the effects of grain size and shape and treated each constituent of the coating as equal sized, randomly distributed elements in the RVE. This model is shown in Figure 2.5 (a)-(e) for different coating compositions. In each composition, the element size was kept identical. The compositions were varied in steps of 5% and 10% where each constituent had a maximum concentration of 55% by volume. The material properties for these simulations are presented in Section 2.2.

The composite mechanics RVE was not modeled as plane-strain as the other models were, but as a uniaxial two-dimensional model. One side of the model was fixed in place by forcing all nodes along the edge to have zero displacements. The two adjacent sides had periodic boundary conditions applied. The periodic boundary conditions consisted of tying the displacement of one node (i) to its counterpart node (j) on the opposite side such that they displaced in the same direction with the same magnitude. This relationship is expressed as:

$$\begin{aligned} \mathbf{u}_x^i - \mathbf{u}_x^j &= 0 \\ \mathbf{u}_y^i - \mathbf{u}_y^j &= 0 \end{aligned} \quad (3)$$

In this equation, \mathbf{u} , is the nodal displacement of a node. The remaining free surface of the composite mechanics RVE (opposite the side fixed in place) had a uniform 5 KPa pressure applied. The homogenized modulus for the system and coating from this model was

taken by measuring the maximum deflection of the loaded surface, ΔL , and computing the axial strain, $\tilde{\epsilon}$, in the model using the original length of the RVE, L . Then the pressure was used to compute a homogenized modulus, \tilde{E} , using Hooke's Law as:

$$\tilde{\epsilon} = \frac{\Delta L}{L_{orig}} \quad (4)$$

$$\tilde{E} = \frac{\sigma}{\tilde{\epsilon}} = \frac{Pressure}{\tilde{\epsilon}} = \frac{Pressure * L_{orig}}{\Delta L}$$

This modulus was used to compare to homogenized experimental measurements of the coating modulus measured by nano-indentation.

Along with the composite mechanics RVE, a rule of mixtures (ROM) approach was also used to predict a homogenized coating modulus. This value was compared to the composite mechanics RVE approach and the experimental measurements. The modulus in this case is calculated using the elastic moduli and volume fraction, f , of each constituent as:

$$\begin{aligned} \tilde{E} &= f_{Gold} E_{Gold} + f_{MoS_2} E_{MoS_2} + f_{YSZ} E_{YSZ} + f_{DLC} E_{DLC} \\ 1 &= f_{Gold} + f_{MoS_2} + f_{YSZ} + f_{DLC} \end{aligned} \quad (5)$$

2.1.2 TRANSFER FILM

Transfer films (T.F.s), which play a dominant role in the coating response and failure (Chromik *et al.* 2006; Lince 2004; Godet 1990; Fayeulle 1990), were represented by including a free third body in the contact. The friction coefficient of this material was set at 0.05 for both the interface with the coating, and the interface with the indenter. This value was assumed from both the properties of the coating and the observation that the transfer film is composed almost entirely of the friction reducing constituents of the coating. The lower and upper surfaces of the transfer film were assumed to be smooth (Figure 2.1 and Figure 2.4). Contact elements were placed along the upper and lower surfaces. The upper surface of the transfer film had the same curvature of the indenter, while the lower surface was flat. Therefore, the transfer film increased in thickness with increased distance from the center of contact. The thickness underneath the center of contact is approximately 200 nm, and the width of the transfer films was 1.5 mm for models with 300-600 nm diameter grain size and refined mesh of the coating (Figure 2.4). The thickness was varied from 50 to 1000 nm for models described in Section 2.4 using the optimized mesh with 300-600 nm grain size (Figure 2.6). This results in an aspect ratio greater than unity and an increasing thickness away from the center of contact consistent with that typically observed experimentally (Suh 1977). Based on a convergence analysis, transfer films in all cases were meshed with 10,000 quadrilateral elements.

2.1.3 COATING RVE

In order to reduce the computational time needed to solve the sliding simulations of the nanocomposite coating models, an RVE approach was used in some simulations of the optimized mesh models presented in Section 2.4. Essentially, a 30 micron wide slice was taken out of the center of the nanocomposite model's active zone. This slice extended from the coating to the bottom of the substrate. The bottom free edge of the substrate was fixed in place similar to the previous models. The two adjacent sides had periodic boundary conditions applied. The periodic boundary conditions consisted of tying the displacement of one node (i) to its counterpart node (j) on the opposite side such that they displaced in the same direction with the same magnitude. This is seen in equation (3). In general, the slice taken out had jagged edges in the region of the coating because the grains do not line up well with the vertical edge of the slice taken. This was accounted for by ensuring that the jagged edge of the slice mated with the opposite side of the model perfectly. In effect, the jaggedness of one side was inversely mirrored in the other side to ensure a perfect fit similar to a cup and cone.

In these models, the surrounding DLC areas which created the top and bottom of the coating supplying a final thickness of 1 micron were removed. In their place, the top surface was left jagged with surface roughness to simulate the true coating. In the region below the coating, the gap was filled with titanium thus making the titanium interlayer thicker than 0.3 microns in some places. Furthermore, this better simulated the actual coating, which is

deposited onto a titanium interlayer that is not necessarily smooth and without surface roughness as modeled in Section 2.1.

In these models, the contact elements and explicit sapphire indenter were also not modeled, but instead a pressure load and shear traction were applied to the top free surface of the coating to simulate the contact and friction loads from the indenter. The pressure load was applied based on the pressure load as seen in Hertzian contact with a quadratic or parabolic distribution of force. The force peaked in the center of the load parabola and fell off in a parabolic fashion to the edges of the model and terminated at 40% of the peak load. Thus, the entire model was under compressive load at all times. The peak force was adjusted to provide the desired nominal strain applied to the coating.

The shear traction was applied as a horizontal force on every node that the pressure load was applied to. The friction coefficient determined the magnitude of the shear force based on the classic Amonton's Law for friction, and the original friction coefficient of 0.05 was used.

To replicate sliding, the pressure load and shear traction were moved laterally, in succession, in 3 micron steps. The shear force was applied in the direction of motion of the pressure traction, which, in general, was always in the positive x direction. These simulations modeled unidirectional sliding tests typical of a pin-on-disk tribometer. In these tests, the material being tested only sees one sliding direction. In the pin-on-linear reciprocating flat wear tests carried out experimentally on the nanocomposite coatings, the

coating experiences sliding in both directions alternately. This form of sliding was modeled explicitly in Section 2.1.

In order to enforce the periodic boundary conditions, as the load moves off one side of the model, it reappears at equal magnitude on the opposite side of the model. This is similar to the periodic conditions enforced in molecular dynamics simulations of atom ensembles. When the peak of the loading curve had translated back to the starting location, one trip is complete. By removing the contact elements and over half the model (by using the RVE approach) significant computational time was saved, and in general these simulations were carried out for 10 or more sliding trips as compared to only 2 trips for the model with refined mesh of the coating presented in Section 2.1.

2.2 MATERIAL MODELS

In the simulations described in Section 2.1, the material model used for the brittle constituents of the finite element model is an isotropic elastic model. This model is used for the synthetic sapphire indenter, DLC matrix and YSZ. This model is appropriate because these phases do not experience significant plastic deformations before failure. Decohesion and fracture occur after the ultimate stress is surpassed. In the loads applied in the finite element simulations, which replicate the experimental loads, this ultimate stress is generally not reached for these materials except for the DLC matrix. Experimental measurements of the decohesion stress required to separate the individual coating inclusions of gold, MoS₂ and YSZ from the DLC matrix and the titanium interlayer are not readily available.

The material model used for the ductile constituents is an elastic, isotropic formulation with a rate-independent, kinematic hardening plasticity model using an associative flow rule based on von Mises J_2 plasticity. The J_2 formulation is a phenomenological plasticity model appropriate for metals, which is based on relating local stresses to plastic flow (Cook *et al.* 2002). In all models except for the coating RVE models, all ductile materials use a bi-linear plasticity formulation with tangent modulus equal to 25% of the original elastic modulus. As can be seen in Figure 2.7, this is an acceptable approximation for the magnitude of plastic strain developed in these models. In the 30 micron wide coating RVE models, coating constituents gold and MoS₂ are multi-linear models and the remaining ductile materials, transfer film, 440C steel substrate, titanium interlayer and far-field homogenized coating, use the original bi-linear model.

The multi-linear model used for the gold and MoS₂ is adapted from experimental measurements reported by Chasiotis *et al.* 2007 for 2800 nm thick gold films loaded at a strain rate of 10⁻³. Multi-linear models for gold and MoS₂ are shown in Figure 2.7. The multi-linear model for MoS₂ is adapted from that of gold by offsetting the curve for gold by an amount slightly less than the difference in yield stress between gold and MoS₂ (Table 2.1, Figure 2.7). Currently, there are no reliable measurements of the true stress true strain curve for MoS₂ due to the inability to obtain large single crystals for testing (Feldman 1976). Data reported for compacts of MoS₂ is highly dependent on the nature of compact forming, i.e. explosive or pressure forming (Tyler and Ku 1967).

The material properties for all materials are shown in Table 2.1, along with friction coefficients for the four individual coating constituents (Bhushan 1999; Chromik *et al.* 2006; Lovell and Khonsari 1993; Seitzman *et al.* 1995; Singer *et al.* 1996; Voevodin and Zabinski 1998; Voevodin and Zabinski 2000; Voevodin *et al.* 2001; Voevodin *et al.* 2005). Friction coefficients of the four individual coating constituents given in Table 2.1 are representative of experimental values recorded for each individual material that was tested (Kester *et al.* 1999; Lince 2004; Voevodin *et al.* 2001). The elastic modulus of DLC was chosen to provide an average between the properties of sp² and sp³ bonded carbon. The evolving strength of the coating constituents was not assumed to change with inclusion and grain size.

The transfer film was assumed to have uniform homogenized material properties based on an equal weighted average using properties of Au, MoS₂ and DLC which were identified by microscopy to be the primary constituents of the transfer film (Chromik *et al.*

2006). The transfer film is assumed not to contain oxidation products as the components of the transfer film, with the exception of MoS₂, do not readily form oxides.

2.3 METHOD OF RADIAL RETURN FOR DUCTILE MATERIALS

In order to obtain solutions from the finite element model when using a J_2 plasticity formulation with kinematic hardening, a radial return method was used as shown in Figure 2.8. This method is necessary because the yield surface location changes with and within each increment of plastic strain. An iterative approach is used, to first predict the new plastic strain, second determine the new location of the yield surface with this new plastic strain and then third solve for the correct plastic strain taking into account the new location of the yield surface.

This algorithm, for an increment of loading in which the strains are plastic, appears as follows. The solution proceeds in increments to the final load. The strain increments, indicated by d , in this case are composed of elastic and plastic components as:

$$\{d\boldsymbol{\varepsilon}\} = \{d\boldsymbol{\varepsilon}^e\} + \{d\boldsymbol{\varepsilon}^p\} \quad (6)$$

where $\{d\boldsymbol{\varepsilon}\}$ is the total increment of strain, $\{d\boldsymbol{\varepsilon}^e\}$ is the total increment of elastic strain and $\{d\boldsymbol{\varepsilon}^p\}$ is the total increment of plastic strain.

The yield criterion, F , for a J_2 plasticity formulation is a function based on the state of stress, $\{\boldsymbol{\sigma}\}$, the translation of the yield surface, $\{\boldsymbol{\alpha}\}$, and the plastic work, \mathbf{W}_p , as:

$$F = F(\{\boldsymbol{\sigma}\}, \{\boldsymbol{\alpha}\}, \mathbf{W}_p) = \{\bar{\boldsymbol{\sigma}}\} - \sigma_Y(\{\bar{\boldsymbol{\varepsilon}}\}) \quad (7)$$

where the second invariant of the stress, $\{\bar{\boldsymbol{\sigma}}\}$, the second invariant of the strain, $\{\bar{\boldsymbol{\varepsilon}}\}$ and the yield stress, σ_Y , are functions of the plastic strain. When F is less than zero, the strains are elastic. When F is zero, yielding is occurring and the state of stress is on the current yield

surface. When yielding is occurring, the state of stress is always on the yield surface and thus dF is always zero. The incremental plastic strains in this case appear as:

$$\{d\boldsymbol{\varepsilon}^p\} = \left\{ \frac{\partial Q}{\partial \boldsymbol{\sigma}} \right\} d\lambda \quad (8)$$

where Q is the plastic potential which in general is equal to F for associative plasticity and determines the direction of plastic straining. The plastic multiplier, $d\lambda$, determines the amount of plastic straining. This is the flow rule which relates the state of stress to the plastic strain when yielding occurs. The incremental stress is found from the strains and the elastic moduli tensor of the material, $\{C\}$, as:

$$\{d\boldsymbol{\sigma}\} = \{C\} : (\{d\boldsymbol{\varepsilon}\} - \{d\boldsymbol{\varepsilon}^p\}) \quad (9)$$

where the colon indicates the dot product for tensors, or a tensor contraction. Since the location of the yield surface depends on the plastic strain, and vice versa, the change in translation of the yield surface, $\{d\boldsymbol{\alpha}\}$, is found from:

$$\begin{aligned} \{d\boldsymbol{\alpha}\} &= [C] \{d\boldsymbol{\varepsilon}^p\} \\ &= \frac{2}{3} \mathbf{H}_p \begin{bmatrix} 1 & 1 & 1 & \frac{1}{2} & \frac{1}{2} & \frac{1}{2} \end{bmatrix}^{diagonal} \\ &= \frac{2}{3} \frac{\mathbf{E}_t}{1 - (\mathbf{E}_t/\mathbf{E})} \begin{bmatrix} 1 & 1 & 1 & \frac{1}{2} & \frac{1}{2} & \frac{1}{2} \end{bmatrix}^{diagonal} \end{aligned} \quad (10)$$

where \mathbf{E} is the original linear elastic modulus, \mathbf{E}_t is the tangent, or current modulus and \mathbf{H}_p is the plastic modulus. Note that $[C]$ is a diagonal matrix. The translation, or current location of the yield surface, $\{\boldsymbol{\alpha}\}$, is found by integrating equation (10) over the entire increment.

The plastic multiplier is found by enforcing the condition that dF is zero during plastic straining, thus:

$$dF = 0$$

$$\left\{ \frac{\partial F}{\partial \sigma} \right\}^T \{d\sigma\} + \left\{ \frac{\partial F}{\partial \alpha} \right\}^T \{d\alpha\} + \frac{\partial F}{\partial W_p} dW_p = 0 \quad (11)$$

Substituting the flow rule in equation (8) into the increment of stress in equation (9) and the translation of the yield surface in equation (10) yields:

$$\{d\sigma\} = \{C\} : \left(\{d\epsilon\} - \left\{ \frac{\partial Q}{\partial \sigma} \right\} d\lambda \right)$$

$$dW_p = \{\sigma\}^T \left\{ \frac{\partial Q}{\partial \sigma} \right\} d\lambda \quad (12)$$

$$\{d\alpha\} = [C] \left\{ \frac{\partial Q}{\partial \alpha} \right\} d\lambda$$

The plastic multiplier can be found by substituting equation (12) into equation (11) and rearranging as:

$$d\lambda = [P_\lambda] \{d\epsilon\}$$

$$d\lambda = \frac{\left\{ \frac{\partial F}{\partial \sigma} \right\}^T : \{C\} : \{d\epsilon\}}{\left\{ \frac{\partial F}{\partial \sigma} \right\}^T : \{C\} : \left\{ \frac{\partial Q}{\partial \sigma} \right\} - \left\{ \frac{\partial F}{\partial \alpha} \right\}^T [C] \left\{ \frac{\partial Q}{\partial \alpha} \right\} - \frac{\partial F}{\partial W_p} \{\sigma\}^T \left\{ \frac{\partial Q}{\partial \sigma} \right\}} \quad (13)$$

With these quantities, the radial return algorithm, which is known as an Euler backward integration scheme, is performed as explained in Simo and Taylor 1985, Belytschko *et al.* 2000 and as earlier verified by Kreig and Kreig 1977. The algorithm begins

at time n and proceeds to time $(n + 1)$ by proposing an initial or trial strain, $\{\boldsymbol{\varepsilon}_{n+1}\}$, via a strain increment $\{\Delta\boldsymbol{\varepsilon}\}$. This appears as:

$$\{\boldsymbol{\varepsilon}_{n+1}\} = \{\boldsymbol{\varepsilon}_n\} + \{\Delta\boldsymbol{\varepsilon}\} \quad (14)$$

An elastic predictor, or initial stress, $\{\boldsymbol{\sigma}_{n+1}^{(0)}\}$, is then computed using the elastic moduli tensor of the material, $\{\mathbf{C}\}$, and the initial plastic strains in the material at time n as:

$$\begin{aligned} \{\boldsymbol{\sigma}_{n+1}^{(0)}\} &= \{\mathbf{C}\} : \left(\{\boldsymbol{\varepsilon}_{n+1}\} - \{\boldsymbol{\varepsilon}_{n+1}^{p(0)}\} \right) \\ \{\boldsymbol{\varepsilon}_{n+1}^{p(0)}\} &= \{\boldsymbol{\varepsilon}_n^{p(0)}\} \end{aligned} \quad (15)$$

The initial iteration number, k , and the plastic strain multiplier, $\Delta\lambda_{n+1}^{(0)}$, are set equal to zero. The initial second invariant of the strain tensor at time $(n + 1)$, $\{\bar{\boldsymbol{\varepsilon}}_{n+1}^{(0)}\}$, is set equal to the second invariant of the strain tensor at time n , $\{\bar{\boldsymbol{\varepsilon}}_n\}$. The deviatoric stresses, \mathbf{s} , and strains, \mathbf{e} , are computed at the time n as:

$$\begin{aligned} \{\mathbf{s}_n\} &= \{\boldsymbol{\sigma}_n\} - \frac{1}{3} \{\text{trace } \boldsymbol{\sigma}_n\} \{\mathbf{I}\} \\ \{\mathbf{e}_n\} &= \{\boldsymbol{\varepsilon}_n\} - \frac{1}{3} \{\text{trace } \boldsymbol{\varepsilon}_n\} \{\mathbf{I}\} \end{aligned} \quad (16)$$

where $\{\mathbf{I}\}$ is the identity matrix. In kinematic hardening the center of the yield surface is shifted when $\{\boldsymbol{\alpha}\}$ is not zero. For this reason, a measure of the deviatoric stress which takes into account this shift and is based on the origin of the deviatoric stress space is computed as:

$$\{\boldsymbol{\xi}_n\} = \{\mathbf{s}_n\} - \{\boldsymbol{\alpha}_n\} \quad (17)$$

During yielding, the stress state starts on the yield surface as shown in Figure 2.8. Thus the unit normal vector to the new yield surface is defined as:

$$\hat{\mathbf{n}} = \frac{\{\boldsymbol{\xi}_n\}}{\|\{\boldsymbol{\xi}_n\}\|} \quad (18)$$

The shear modulus, also known as Lamé's second parameter, $\boldsymbol{\mu}$, is computed. This can be expressed in terms of either the modulus of elasticity, \mathbf{E} , and the Poisson's ratio, ν , or the elastic moduli tensor of the material, $\{\mathbf{C}\}$, and the unit normal vector to the yield surface, $\hat{\mathbf{n}}$, as:

$$\boldsymbol{\mu} = \frac{\mathbf{E}}{2 + 2\nu} = \frac{1}{3} \left(\left(\sqrt{\frac{3}{2}} \hat{\mathbf{n}} \right) : \{\mathbf{C}\} : \left(\sqrt{\frac{3}{2}} \hat{\mathbf{n}} \right) \right) \quad (19)$$

The flow rule and yield criterion in equation (7) are evaluated first at $k = 0$ as:

$$F_{n+1}^{(k)} = \{\bar{\boldsymbol{\sigma}}_{n+1}^{(k)}\} - \sigma_Y \left(\{\bar{\boldsymbol{\epsilon}}_{n+1}^{(k)}\} \right) = \left(\{\bar{\boldsymbol{\sigma}}_{n+1}^{(0)}\} - 3\boldsymbol{\mu}\Delta\boldsymbol{\lambda}_{n+1}^{(k)} \right) - \sigma_Y \left(\{\bar{\boldsymbol{\epsilon}}_{n+1}^{(k)}\} \right) \quad (20)$$

Where the term $3\boldsymbol{\mu}\Delta\boldsymbol{\lambda}_{n+1}^{(k)}$ is the plastic corrector. If the flow rule in equation (20) is greater than the specified tolerance (which is necessarily greater than zero) then the plastic multiplier is recomputed to correct the plastic strains in this step. The incremental change in the plastic multiplier is given as:

$$d\boldsymbol{\lambda}^{(k)} = \frac{\left(\{\bar{\boldsymbol{\sigma}}_{n+1}^{(0)}\} - 3\boldsymbol{\mu}\Delta\boldsymbol{\lambda}_{n+1}^{(k)} \right) - \sigma_Y \left(\{\bar{\boldsymbol{\epsilon}}_{n+1}^{(k)}\} \right)}{3\boldsymbol{\mu} + \mathbf{H}_p^{(k)}} = \frac{F_{n+1}^{(k)}}{3\boldsymbol{\mu} + \mathbf{H}_p^{(k)}} \quad (21)$$

In this equation the plastic tangent modulus and the yield stress are both taken directly from the materials stress strain curve for the level of strain the model is under at time $n + 1$. With this the plastic strain, deviatoric strain, stress (and thus deviatoric stress), plastic multiplier and the iteration number k are updated as:

$$\begin{aligned}
\{\Delta \boldsymbol{\varepsilon}_{n+1}^{p(k)}\} &= -d\boldsymbol{\lambda}^{(k)} \sqrt{\frac{3}{2}} \hat{\boldsymbol{n}} \\
\{\boldsymbol{\varepsilon}_{n+1}^{p(k+1)}\} &= \{\boldsymbol{\varepsilon}_{n+1}^{p(k)}\} + \{\Delta \boldsymbol{\varepsilon}_{n+1}^{p(k)}\} = \{\boldsymbol{\varepsilon}_{n+1}^{p(k)}\} - d\boldsymbol{\lambda}^{(k)} \sqrt{\frac{3}{2}} \hat{\boldsymbol{n}} \\
\{\Delta \bar{\boldsymbol{\varepsilon}}_{n+1}^{(k)}\} &= d\boldsymbol{\lambda}^{(k)} \\
\{\bar{\boldsymbol{\varepsilon}}_{n+1}^{(k+1)}\} &= \{\bar{\boldsymbol{\varepsilon}}_{n+1}^{(k)}\} + \{\Delta \bar{\boldsymbol{\varepsilon}}_{n+1}^{(k)}\} = \{\bar{\boldsymbol{\varepsilon}}_{n+1}^{(k)}\} + d\boldsymbol{\lambda}^{(k)} \\
\{\boldsymbol{\sigma}_{n+1}^{(k+1)}\} &= \{\mathbf{C}\} : \left(\{\boldsymbol{\varepsilon}_{n+1}\} - \{\boldsymbol{\varepsilon}_{n+1}^{p(k+1)}\} \right) \\
\Delta \boldsymbol{\lambda}^{(k+1)} &= \Delta \boldsymbol{\lambda}^{(k)} + d\boldsymbol{\lambda}^{(k)} \\
\mathbf{k} &= \mathbf{k} + 1
\end{aligned} \tag{22}$$

The flow rule in equation (20) is recalculated using the updated values and if the residual is greater than the specified tolerance then the process is repeated again in equations (21) and (22) until the desired tolerance is met. In the present study, the tolerance is set at 0.5% or a magnitude of 0.005. After convergence, the plastic strains, elastic strains, work hardening and translation of the yield surface are updated with the final values. This process is shown graphically in Figure 2.8.

2.4 MICROSTRUCTURAL MODELING OPTIMIZATION AND GRAIN MORPHOLOGY REPRESENTATION

The refined mesh coating models in Section 2.1 were meshed with a commercial FEA package and modeled grain sizes from 300-600 nm. On average, the experimental grain size of the nanocomposite coatings has been measured from TEM images to be under 50 nm (Pan *et al.* 2008). With smaller grains, the Voronoi tessellation of the coatings microstructure has a much greater correlation to the form as seen from TEM images shown in Figure 2.9.

In order to reduce the grain size and maintain a manageable number of elements, a code was written using Matlab to create the microstructure and then mesh the resulting model using far fewer quadrilateral elements than was obtainable from a commercial FEA package. In essence, the random grain shapes and sizes were represented through Voronoi tessellations again, and the presence of a matrix was added in between each cell/grain during a post processing step of the tessellation. Through dimensional scaling, the tessellations could be made to represent any desired grain size.

For an optimal minimized mesh size, the Voronoi tessellations were restricted to tessellations of even sided cells, which can be shown to be meshed with a minimum of quadrilateral elements without splitting a side of the grain with a mid-side node. Thus, a four-sided grain is meshed with one element, a six sided grain with two elements, an eight sided grain with 3 elements and so on. Even sided cells/grains can be meshed having one element edge along each side of the grain as seen by the examples in Figure 2.10. Odd sided cells/grains require more than one element edge/division for at least one side of the grain.

This necessarily causes a neighboring grains mesh to possess more than one element edge/division on one side of the grain. This undesirable trend propagates through the mesh and prevents obtaining a minimal mesh unless every cell/grain is even sided. The possible minimal, optimal meshes for even sided grains with more than four sides are shown in Figure 2.10, and the mesh chosen was based on the mesh producing all internal element angles greater than 20° and less than 160° . When more than one possible mesh scheme satisfied this requirement for an individual grain, then the mesh producing a cumulative determinant of the Jacobian, $\det(J)$, matrix which had the greatest value above zero was chosen. The Jacobian was evaluated and summed at each node of each element in isoparametric form constituting the grain, and the cumulative Jacobian was taken by summing over all elements in the grain. Additionally, the maximum efficiency quadrilateral transition mesh from high element density in the 'active zone' to lower element densities in the far-field regions was coded in Matlab and used in the finite element models. The Matlab code written to produce the optimized mesh coatings is given in Appendix A.

Voronoi tessellations of only even sided grains were produced by using a special subset of seed points (Table 2.2) over a unit cell domain. These points have the unique capability of representing a Voronoi tessellation of even sided cells over the unit domain. Further, these points produce tessellations of completely even sided cells over a larger n by n domain, where n is an integer of unit cells from one to infinity. This is achieved by copying and offsetting the subset of points by integer values in the x and/or y directions filling the entire $x y$ plane of the larger domain uniformly. This technique is essentially a self-

tessellating tessellation of even sided cells. It is worth noting that the set of points in Table 2.2 is the only set of 20 points with this unique characteristic that could be obtained after multiple extensive randomized searches. This process is illustrated in Figure 2.11. The number of significant digits in the seed points is required for accuracy due to the small unit domain which demands a high tolerance to prevent overlapping and the development of small odd sided tessellations. It should be noted that additional sets of points are likely to be able to be found if the number of seed points is varied above or below 20.

The criteria for identifying whether a trial set of points will self tessellate properly to produce only even sided cells over any size domain depends on the number of seed points. For 20 seed points, if the set will self tessellate with even sided cells over any and all domains which vary from both one to seven unit cells in one dimension and one to seven unit cells in the perpendicular dimension, then this set of cells will properly tessellate over any size larger domain. The criteria of seven domains is a consequence of the number of seed points (20). The basis for this essentially lies in the number of cells produced in the 1 x 1 domain which necessarily dictates the shortest distance between a cell and the edge of the domain.

Using this technique, the number of elements required to produce 300-600 nm grain size models (as in Section 2.1) was reduced from 125,000 to 15,000. The relationship between the number of elements using this technique and the original mesh produced by a commercial FEA package versus grain size is shown in Figure 2.12. As can be seen from the graph, the reduced mesh has grain sizes of 54 nm possible without exceeding 500,000

elements, as compared to the original mesh which would have required a higher number of elements for 130 nm diameter grain size models. This is referred to as the optimized mesh. The impact on accuracy of the results using the reduced, optimized mesh is discussed in Section 4.3.

The results of recreating the models in Section 2.1 using this reduced mesh can be seen in Figure 2.13. As can be seen, grain sizes from 270 nm to ~54 nm have been modeled. As the grain size decreases, the matrix dimension of the DLC decreases proportional to the grain size. The maximum efficiency transition mesh can be seen in Figure 2.13 for the 270 nm grain size beginning in the steel substrate and propagating toward the edges of the model.

2.5 CONTINUUM VERIFICATION MODEL

Complementary molecular dynamics (MD) and finite element (FE) simulations of a model diamond nanocomposite (MDN) system subjected to nanoindentation by a curved indenter were undertaken to validate the use of finite element continuum mechanics, and phenomenological materials models, for systems with critical length dimensions on the nano scale. The structure of the model diamond nanocomposite system used here is loosely based on the structure of nanocrystalline diamond (NCD). NCD is being used in a wide range of applications, such as machine tools and microelectromechanical systems (MEMS) because it has robust mechanical and desirable tribological properties.

The molecular dynamics simulations were performed by Judith Harrison and Guangtu Gao of the United States Naval Academy.

2.5.1 MOLECULAR DYNAMICS APPROACH

The MDN systems for the MD simulations were created by embedding 16 hydrogen-terminated diamond nano-grains, or crystals, in an amorphous carbon matrix that is supported by six layers of diamond (111). While the predominate facets in experimentally grown NCD films are a function of deposition conditions (Erdemir *et al.* 2001), it is possible to create films where the (111) and (110) grains predominate (Chromik *et al.* 2008). The model diamond nanocomposites created here are generally based on the NCD films described by Chromik *et al.* 2008 which contain diamond grains separated by an amorphous carbon matrix. It should be noted, however, that the width of the amorphous carbon region in the model diamond nanocomposites used here is larger than the amorphous regions obtained experimentally. In the MDN, eleven of the diamond grains embedded in the carbon matrix had the (111) orientation and the remaining five had the (110) orientation (Figure 2.14 (a) and (b)). The predominance of the (111) orientation of the grains is observed experimentally (Chromik *et al.* 2008). The exposed face of the hydrogen-terminated (111) grain in the MDN was 1.13 nm by 1.24 nm and its thickness was 0.61 nm. The exposed surface of the hydrogen-terminated (110) crystal was 0.88 nm by 0.98 nm and its thickness was 0.73 nm. The entire simulation system containing the diamond grains had surface dimensions of 6.43 nm by 6.48 nm and a total thickness of 2.02 nm.

The roughness of NCD films is also a function of the growth conditions (Erdemir *et al.* 2001). NCD films can have roughness in the range of 26 to 78 nm (Chromik *et al.* 2008). In this work, two MDN films with different roughness were created for use in the MD

simulations. Roughness was introduced into the MDN by placing the diamond grains within the amorphous carbon matrix after adjusting their Euler angles (α , β , γ). The range of selected angles fixes the surface roughness. In particular, the centers of the diamond grains were located on a 4 by 4 lattice. The angle α was randomly selected from the range 0 ° to 180 °. The angles β and γ were set equal to each other and randomly chosen from the range 0 to 10° for film 1 (MDN1) (Figure 2.14 (a)) and 0 to 20° for film 2 (MDN2) (Figure 2.14 (b)). Thus, MDN2 is rougher.

Empty spaces between the diamond grains were filled with carbon atoms to create an amorphous carbon matrix. Film 1 and film 2 contained 13,640 and 13,348 atoms, respectively. The amorphous carbon atoms were then heated to a high temperature (approximately 8000 K), while holding the diamond substrate and the diamond grains rigid. The heating phase was approximately 2 ps. After the heating, the system temperature was lowered rapidly to 100 K in another 2 ps interval. The resulting MDN films (Figure 2.14) contained the diamond grains embedded in an amorphous carbon matrix which was attached to the diamond (111) substrate.

In the MD simulations, a curved hydrogen-terminated diamond tip was brought into contact with three positions (Figure 2.14) on two MDN samples. The tip was constructed from a diamond (111) crystal by removing atoms to make it roughly hemispherical (radius = 15 Å). Hydrogen atoms were added to saturate all bonds on the tip surface. This tip contains 1352 sp^3 -bonded carbon atoms and 520 hydrogen atoms. Additional details regarding the tip can be found in Gao *et al.* 2007. The forces acting on all atoms were derived from the

second-generation reactive empirical bond-order (REBO) potential, which contains short-range covalent interactions needed to model chemical reactions but does not contain long-range, intermolecular interactions (Brenner *et al.* 2002). This potential reproduces the zero-Kelvin elastic constants of diamond and graphite accurately and reproduces the correct qualitative behavior of the elastic properties with temperature (Gao *et al.* 2006; Van Workum *et al.* 2006).

Periodic boundary conditions were applied in the plane containing the diamond grains. The bottom two layers of the diamond substrate and the curved tip were held rigid, the remaining four layers of diamond were maintained at a constant temperature (300 K) using the Langevin thermostat (Aldeman and Doll 1976). All remaining atoms were free to move according to Newton's equations without additional constraints. The equations of motion for all non-rigid atoms were integrated using the fifth-order Gear predictor-corrector algorithm with a constant step size of 0.25 fs. An additional equation of motion was used to maintain a constant load on the tip (Gao *et al.* 2007; Lupkowski and van Swol 1990). As a result, the tip oscillated slightly around an average height relative to the MDN, which results in an average load on the MDN equal to the constant load on the tip. The contact area was calculated by dividing the surface of the films (in the xy -plane) into 28 by 28 small pieces, with areas of about 5.477 \AA^2 . If the normal force in this small surface segment was greater than zero, the area was added to the total contact area.

2.5.2 FINITE ELEMENT MODEL

To maximize overlap between the systems studied using both methods, the MDN labeled film 1 used in the MD simulation was used as a template for the FE mesh. The profile and orientation of the diamond grains embedded in the amorphous film were represented in the FE models as oriented cubes of identical dimensions with all exterior edges rounded to a radius equal to the interatomic spacing of diamond (1.54 Å) (Figure 2.15 (a)-(e)). The terminal surface carbon atoms of the individual diamond grains were represented in the FE simulations as a set of spheres, whose radius was equal to the atomic radius of carbon. These spheres protruded from the model diamond grains topmost surface by one atomic radius and they were positioned to model either a (111) or (110) diamond grain (Figure 2.15 (a)-(e)). Hydrogen atoms, which terminate the surface of the MDN in the MD simulations, were not included in the FE simulations.

The hemispherical indenter in the FE simulations was geometrically smooth (i.e., lacking the discrete atomic-scale morphology) and was modeled as both rigid and deformable with the mechanical properties of (111) diamond (Figure 2.15 (d)-(e)). Under normal indentation, the crystal expands laterally and must slip as the load is increased on the indenter. A constant friction coefficient of 0.05 was used in all FE simulations. This friction value has been used previously to represent the diamond like carbon (DLC) component of adaptive composite coatings (Voevodin and Zabinski 1998). The indenter was centered over a (110) diamond grain within the MDN in all the FE simulations and one of the MD simulations to facilitate comparison of results obtained with each method. All FE models

were meshed with approximately 100,000 to 150,000 tetrahedral elements (Figure 2.15 (b)-(e)), and in all cases the bottom surface of the FE model was fixed against displacement and displacement control used for the indenter.

Material properties for the diamond grains within the MDN in the FE simulations were calculated from the experimentally determined elastic constants of diamond at room temperature and are given in Gao *et al.* 2007 and Gao *et al.* 2006. A linear elastic isotropic modulus of 300 GPa and a Poisson ratio of 0.3, typical of amorphous carbon, were used for the 20nm square amorphous film substrate. In separate FE simulations, the substrate supporting the diamond grains was modeled as a shallow, 1.3 nm thick amorphous carbon matrix with a 0.7 nm thick (111) diamond layer below it, to correspond with the MD simulations, or as a deep, 20 nm thick amorphous matrix without the diamond lower layer. Such a thick substrate would be prohibitive to model in MD due to the number of atoms required to create the system dimensions. In contrast, this type of extension to the system is ideally suited for FE simulations.

In both the FE and MD simulations, the average normal contact pressure, P_{Avg} , was defined as:

$$P_{Avg} = \frac{\sum_{r=0}^{r=r_{final}} F_z(r)}{\pi r_{final}^2} \quad (23)$$

In this equation, r is the indenter radius measured from its center ($r = 0$) and F_z is the contact force in the z direction within a radius r_{final} . It should be noted that this pressure is

not typically calculated in FE simulations. The contact pressure, $\mathbf{P}_{Contact}$, which is typically used in FE simulations and elasticity theory, is given by:

$$\mathbf{P}_{Contact} = \frac{1}{3} \sigma_{ii} = \frac{\sigma_{xx} + \sigma_{yy} + \sigma_{zz}}{3} \quad (24)$$

To facilitate comparison between the MD and FE simulations, the quantity \mathbf{P}_{Avg} (equation (23)) was used. With the diamond grains in the MDN randomly oriented, all three stress components were significant at the surface. For the FE simulations, the von Mises stress, σ_{vm} , in equation (2) was used to take into account all six stress components developed in the crystal under contact.

2.6 TABLES AND FIGURES
(CHAPTER 2)

Table 2.1: Mechanical properties (bulk) for each constituent and typical friction coefficients for sliding at room temperature in ambient atmosphere. Data for multi-linear materials presented in Figure 2.7. T.F. indicates transfer film.

Material property	440C Steel	Gold	YSZ	DLC	MoS ₂	Titanium	Sapphire (Synthetic)	Far Field Coating	T.F.
Modulus (GPa)	200	78	210	250	170	116	400	100	166
Yield/Ultimate Strength (MPa)	400	125	600	7300	190	500	2100	125	158
Poisson Ratio	0.25	0.42	0.31	0.12	0.13	0.32	0.31	0.25	0.22
Tangent Modulus (Gpa)	50	19.5	--	--	47.5	29	--	25	41.5
Friction Coefficient	--	0.1 – 0.4	0.1 – 0.2	<0.1	<0.1	--	0.05	0.05	0.05
Density (kg/m ³)	7500	19300	5600	2100	4500	4510	3980	7875	8633

Table 2.2: Set of 20 unique seed points whose Voronoi tessellation produces even sided cells over a unit domain, and a self-tessellating tessellation of even sided cells over larger domains.

Coordinates of self-tessellating seed points over 1 by 1 unit cell domain (x , y)	
1. (0.721700564087 , 0.399704581576)	11. (0.299571179292 , 0.178333105942)
2. (0.376574022531 , 0.956666362604)	12. (0.737013506837 , 0.11778181047)
3. (0.120395313149 , 0.436438347669)	13. (0.000260434546734 , 0.00198872501756)
4. (0.663705934121 , 0.892841407256)	14. (0.044583452224 , 0.248090153068)
5. (0.476545691555 , 0.22027833225)	15. (0.585792648601 , 0.56091984404)
6. (0.262073399719 , 0.545352657032)	16. (0.534508851848 , 0.617884165694)
7. (0.667761696105 , 0.36399853118)	17. (0.853341104651 , 0.337335395232)
8. (0.567862433873 , 0.78663638759)	18. (0.886236263137 , 0.416964446331)
9. (0.696008616421 , 0.499563576994)	19. (0.00596873856865 , 0.367091214774)
10. (0.962965189732 , 0.754092853004)	20. (0.496090523945 , 0.872820254269)

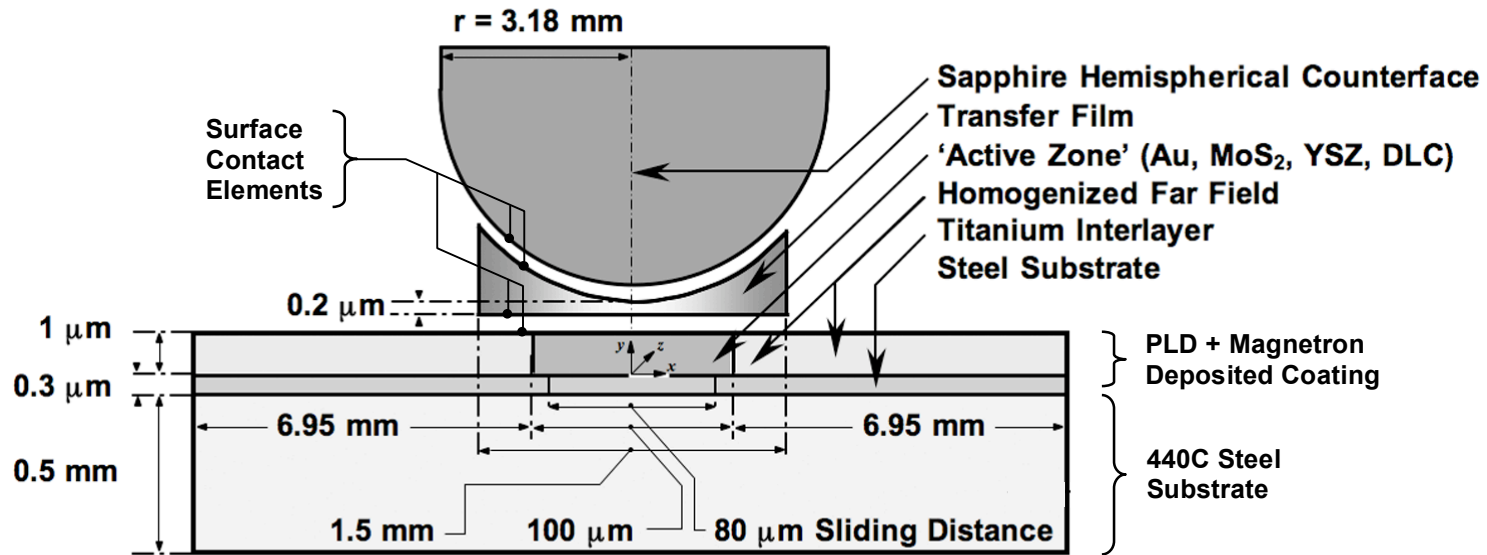


Figure 2.1: Dimensions and materials involved in the nanocomposite coating finite element models with 300-600 nm diameter grain size and refined mesh of the coating.

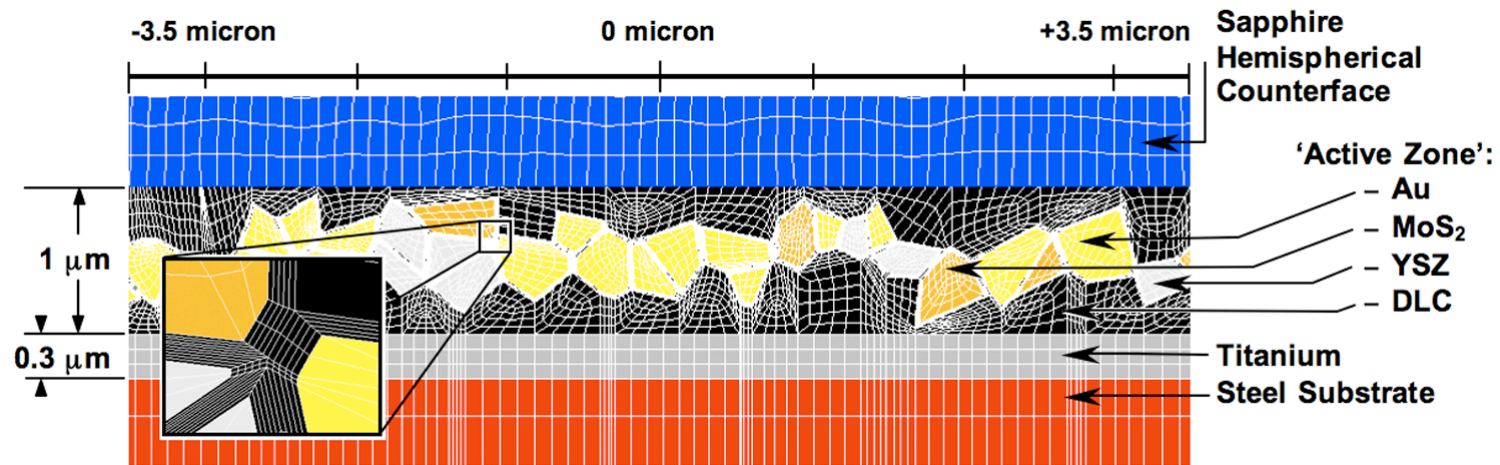


Figure 2.2: The center of the ‘active zone’ underneath the slider. The zoom shows the level of detail in meshing of the DLC borders around each inclusion. Models with 300-600 nm diameter grain size and refined mesh of the coating.

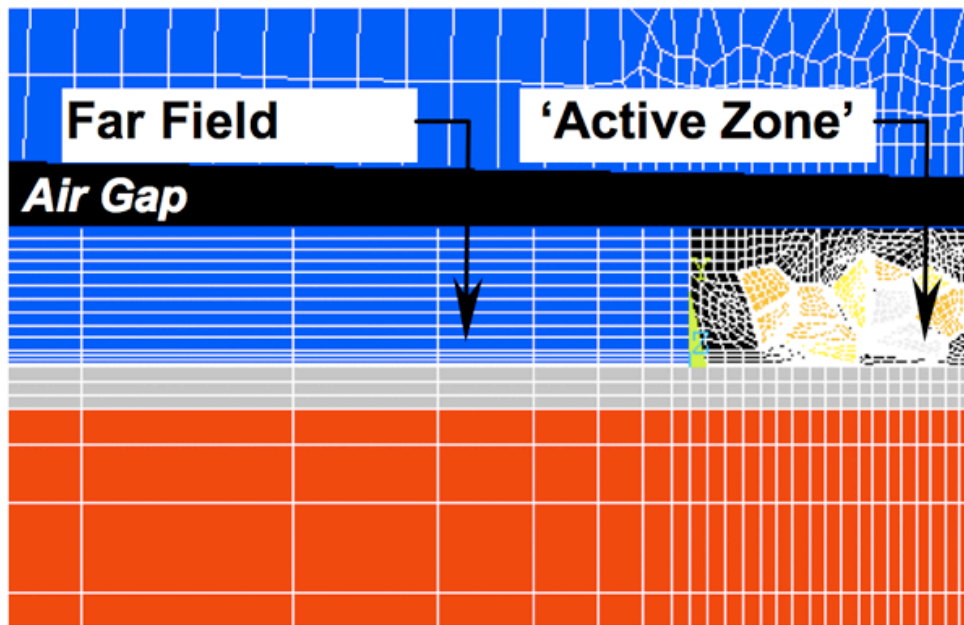


Figure 2.3: The transition between the ‘active zone’ and the homogenized coating region for models with 300-600 nm diameter grain size and refined mesh of the coating.

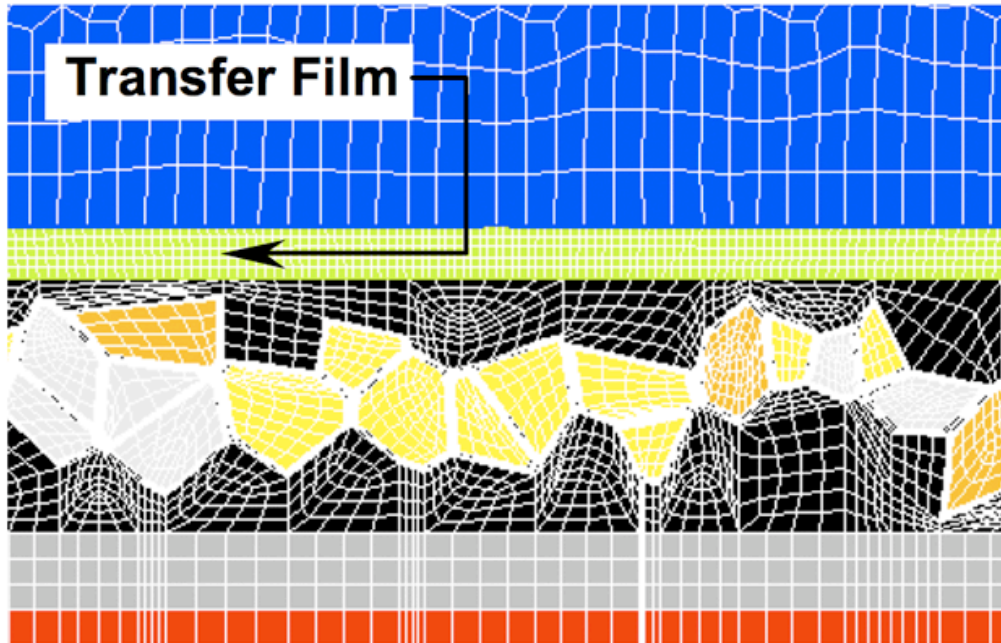


Figure 2.4: The ‘active zone’ underneath the indenter with a transfer film of 200 nm thickness for models with 300-600 nm diameter grain size and refined mesh of the coating.

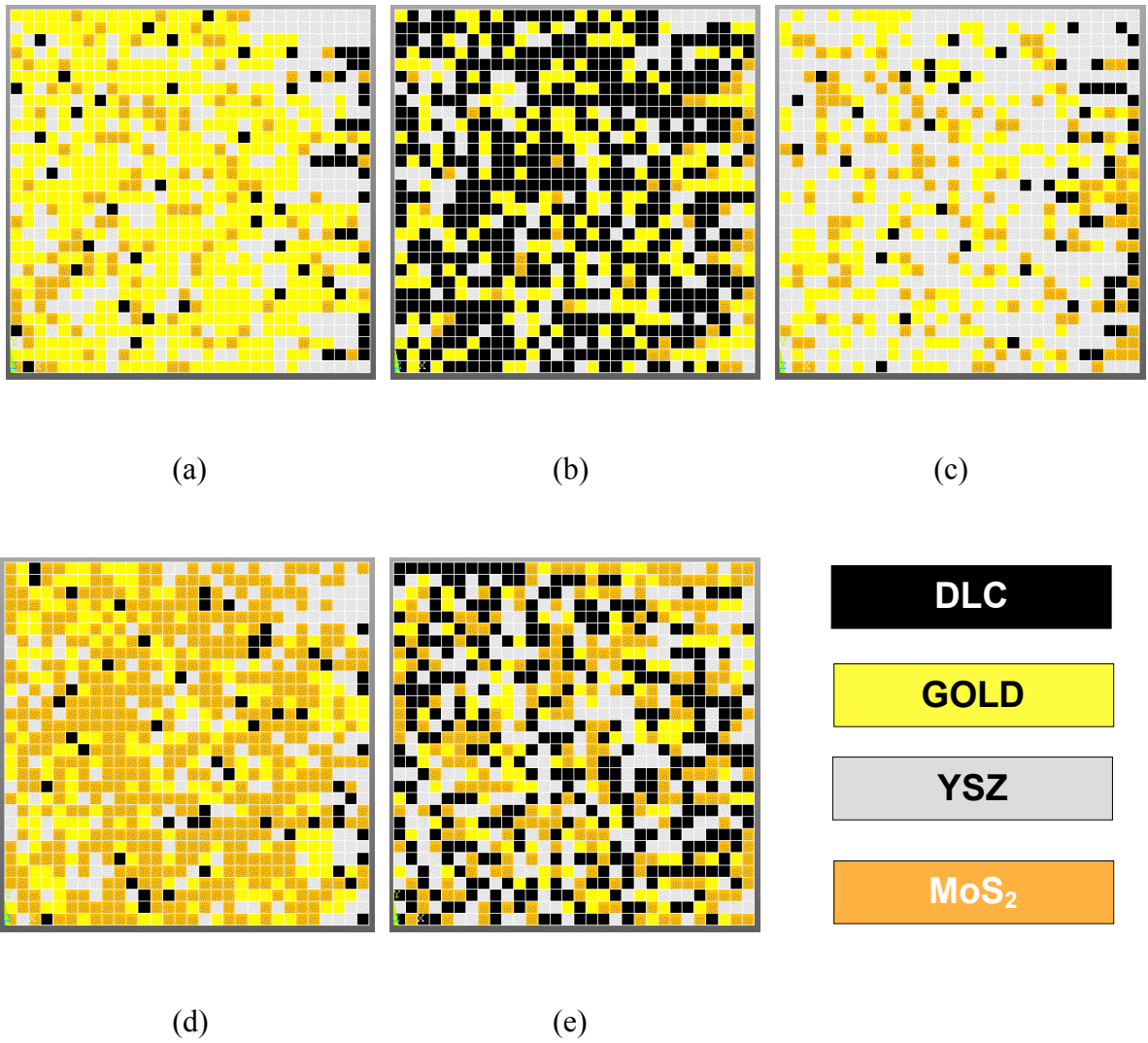


Figure 2.5: Composite mechanics RVE of coating samples with compositions (a) $(\text{YSZ})_{0.25}\text{Au}_{0.55}(\text{MoS}_2)_{0.15}\text{C}_{0.05}$; (b) $(\text{YSZ})_{0.15}\text{Au}_{0.25}(\text{MoS}_2)_{0.05}\text{C}_{0.55}$ 55%; (c) $(\text{YSZ})_{0.55}\text{Au}_{0.25}(\text{MoS}_2)_{0.15}\text{C}_{0.05}$; (d) $(\text{YSZ})_{0.15}\text{Au}_{0.25}(\text{MoS}_2)_{0.55}\text{C}_{0.05}$ 55%; (e) $(\text{YSZ})_{0.25}\text{Au}_{0.15}(\text{MoS}_2)_{0.25}\text{C}_{0.35}$. Color of element indicates constituent material.

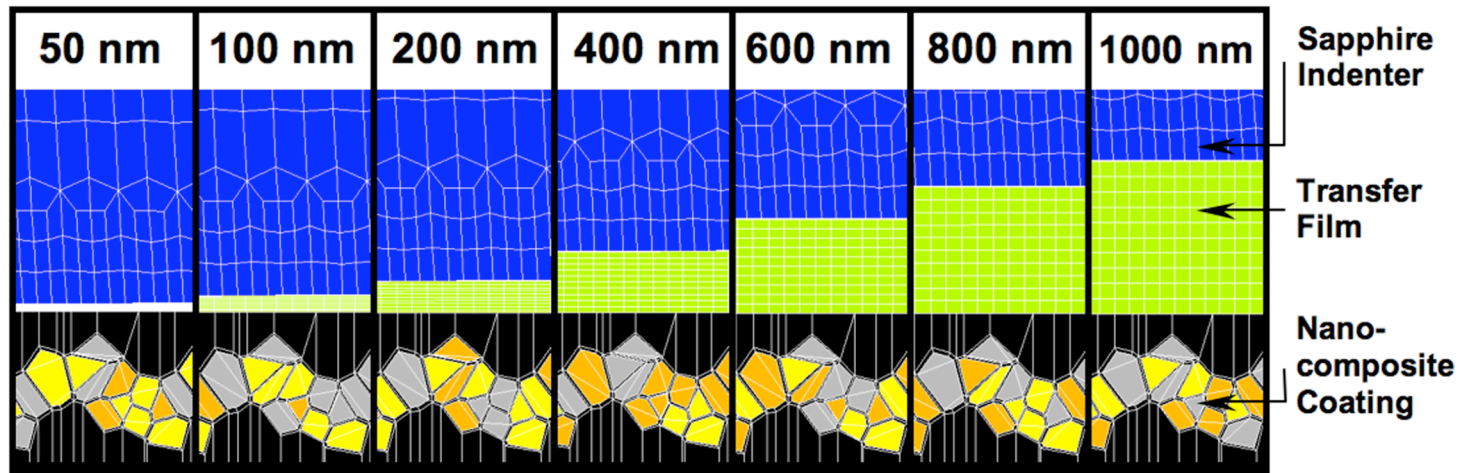


Figure 2.6: Transfer film with varying thickness between the indenter and the coating for models with 300-600 nm grains using the optimized mesh. Bold text indicates transfer film thickness.

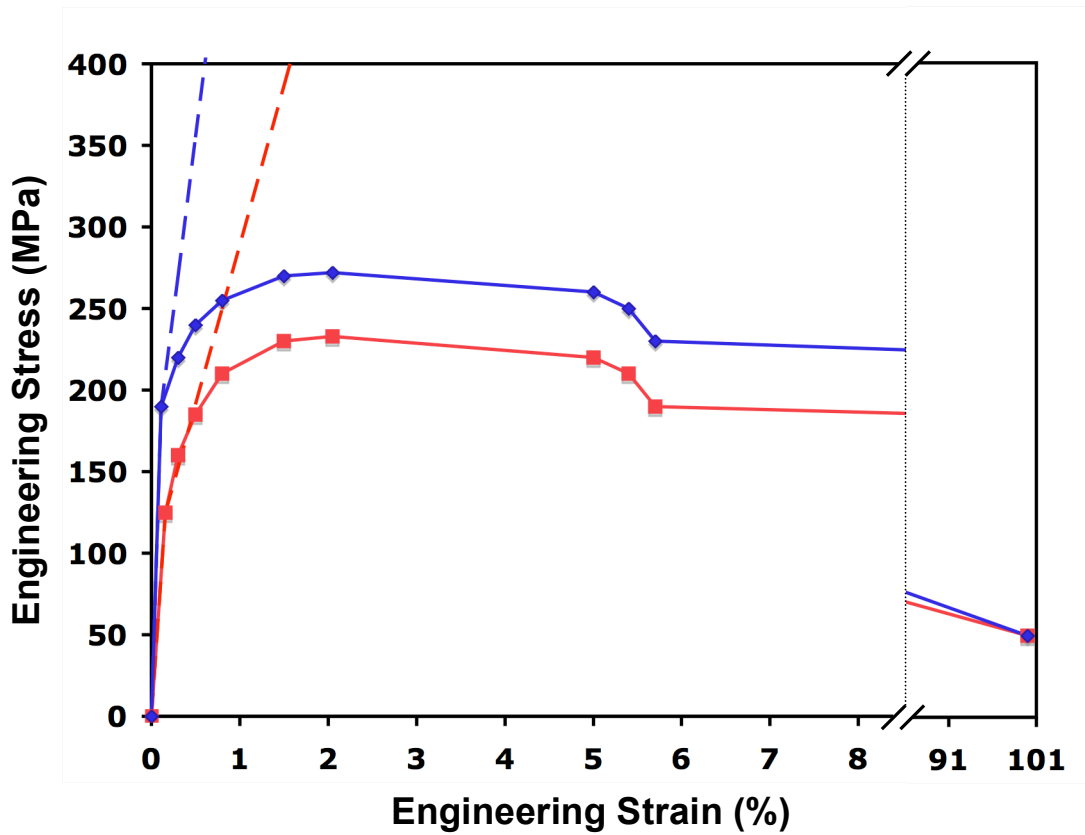


Figure 2.7: Multi-linear model used for gold (solid, red) and MoS₂ (solid, blue). Bi-linear tangent modulus for gold in dashed red and MoS₂ in dashed blue. Multi-linear data points for gold are (Stress (Mpa) , Strain (%)) (0,0; 125,0.16; 160,0.3; 185,0.5; 210,0.8; 230,1.5; 233,2.05; 220,5; 210,5.4; 190,5.7; 50,100). Multi-linear data points for MoS₂ are (Stress (Mpa) , Strain (%)) (0,0; 190,0.11; 220,0.3; 240,0.5; 255,0.8; 270,1.5; 272,2.05; 260,5; 250,5.4; 230,5.7; 50,100).

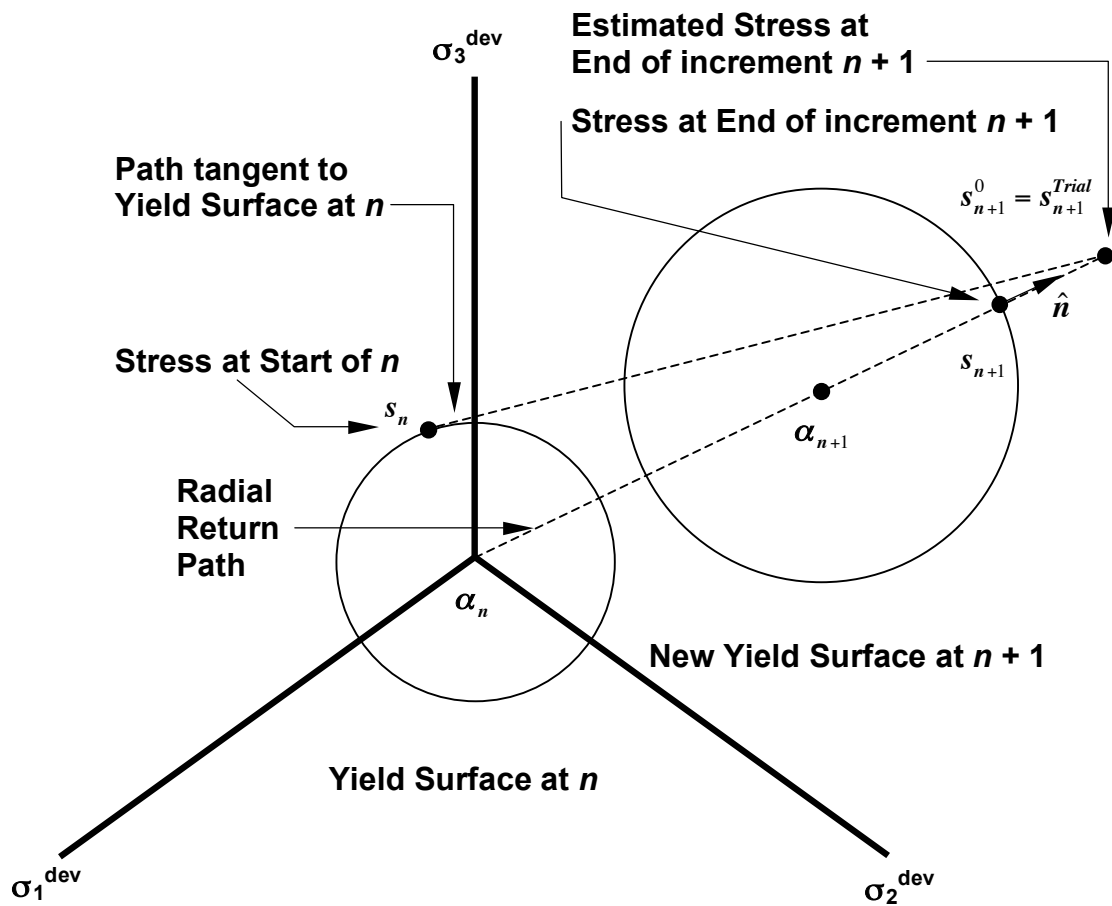


Figure 2.8: Method of radial return for nonlinear kinematic hardening. Deviatoric stress space shown.

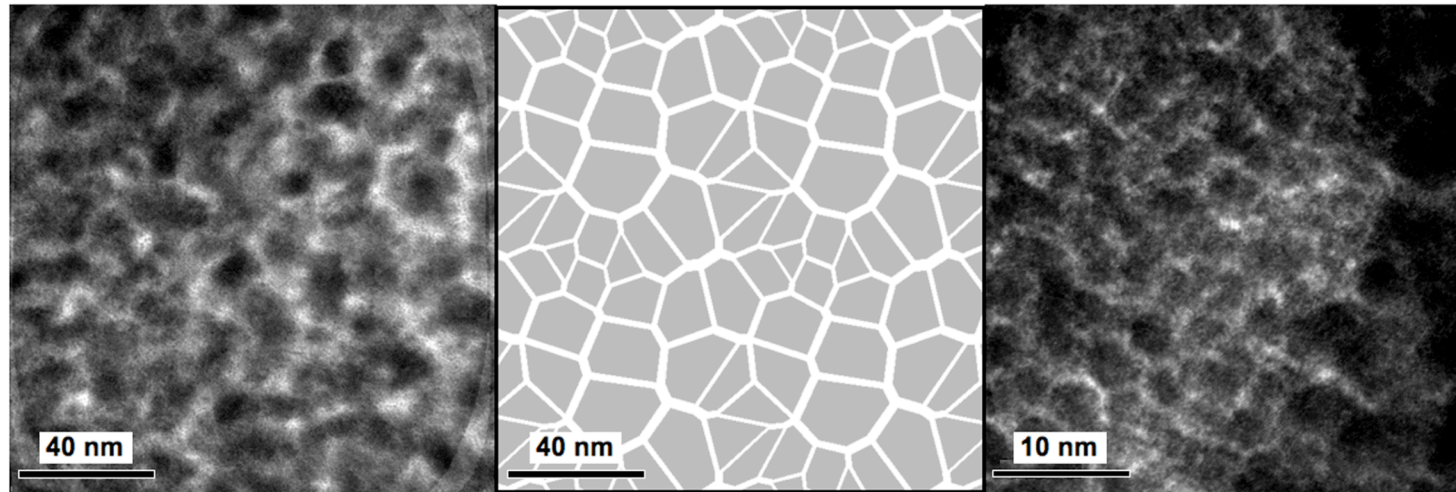


Figure 2.9: TEM image of a nanocomposite coating with composition $(YSZ)_{0.42}Au_{0.31}(MoS_2)_{0.16}C_{0.11}$ on the left and $(YSZ)_{0.33}Au_{0.14}(MoS_2)_{0.15}C_{0.36}$ by volume fraction on the right. Grains (dark regions), grain size and presence of DLC matrix (in white) separating inclusions are visible, along with a comparison of the FEM generated microstructure (without mesh) in the middle.

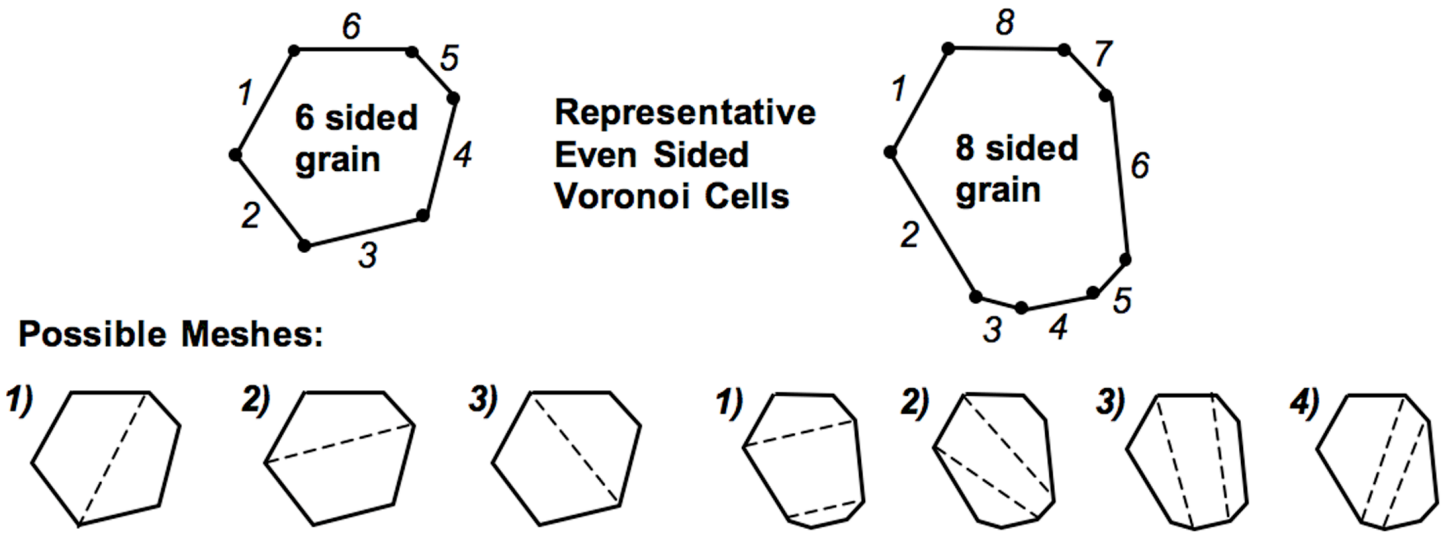
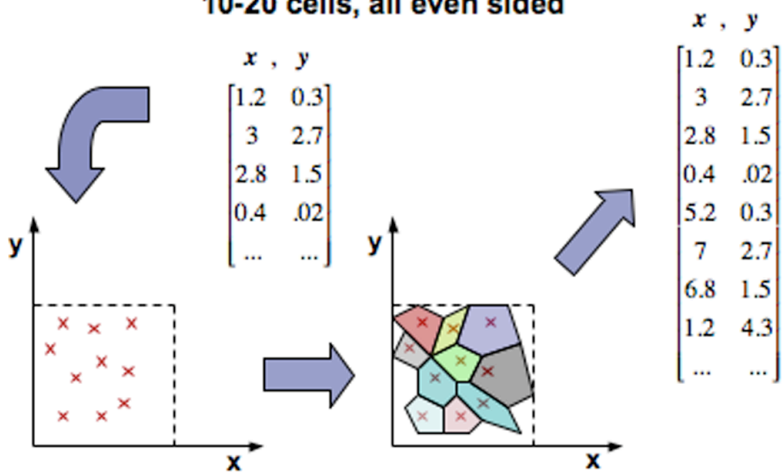


Figure 2.10: Possible quadrilateral element meshes for even sided, convex, polygonal grains with more than 4 sides created from Voronoi tessellations. Grains with a higher number of sides similar.

Step 1) Find a subset of 20-40 *Bounded* coplanar points whose tessellation produces only 10-20 cells, all even sided



Step 2)

Form a master set of points from the subset, expand Bounds by 7 times, check if self tessellation produces only even sided cells, if so, problem solved.

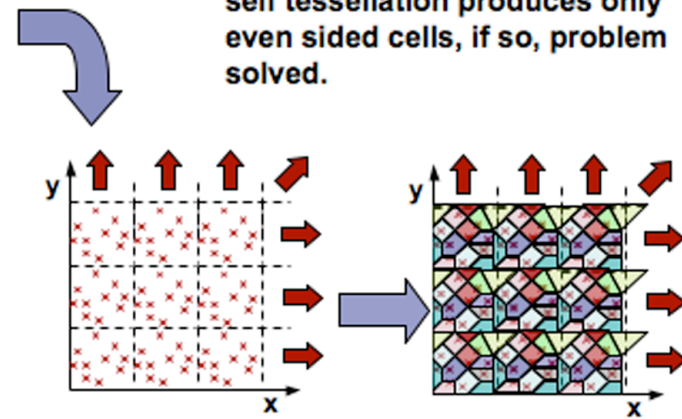


Figure 2.11: Method of producing even sided Voronoi tessellations over a variable sized domain using a self tessellating set of seed points over a unit domain.

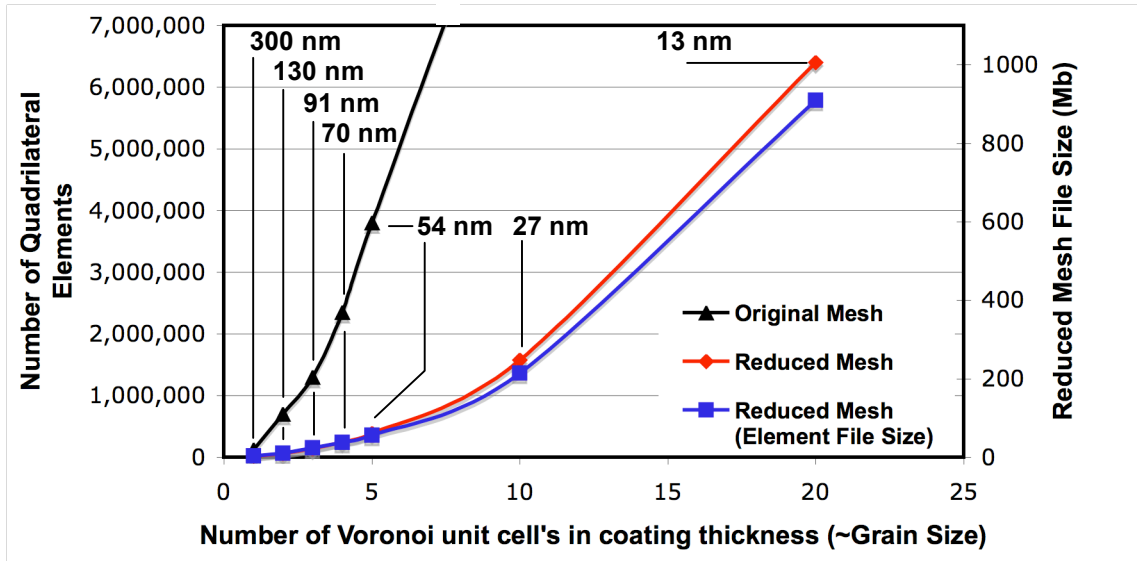


Figure 2.12: Relationship between grain size and number of elements in the optimized mesh coating finite element models versus the refined mesh technique obtained with a commercial FEA package. Grain size of each data point noted with bold text in graph. Element file size for the reduced mesh is measured against the right-most ordinate.

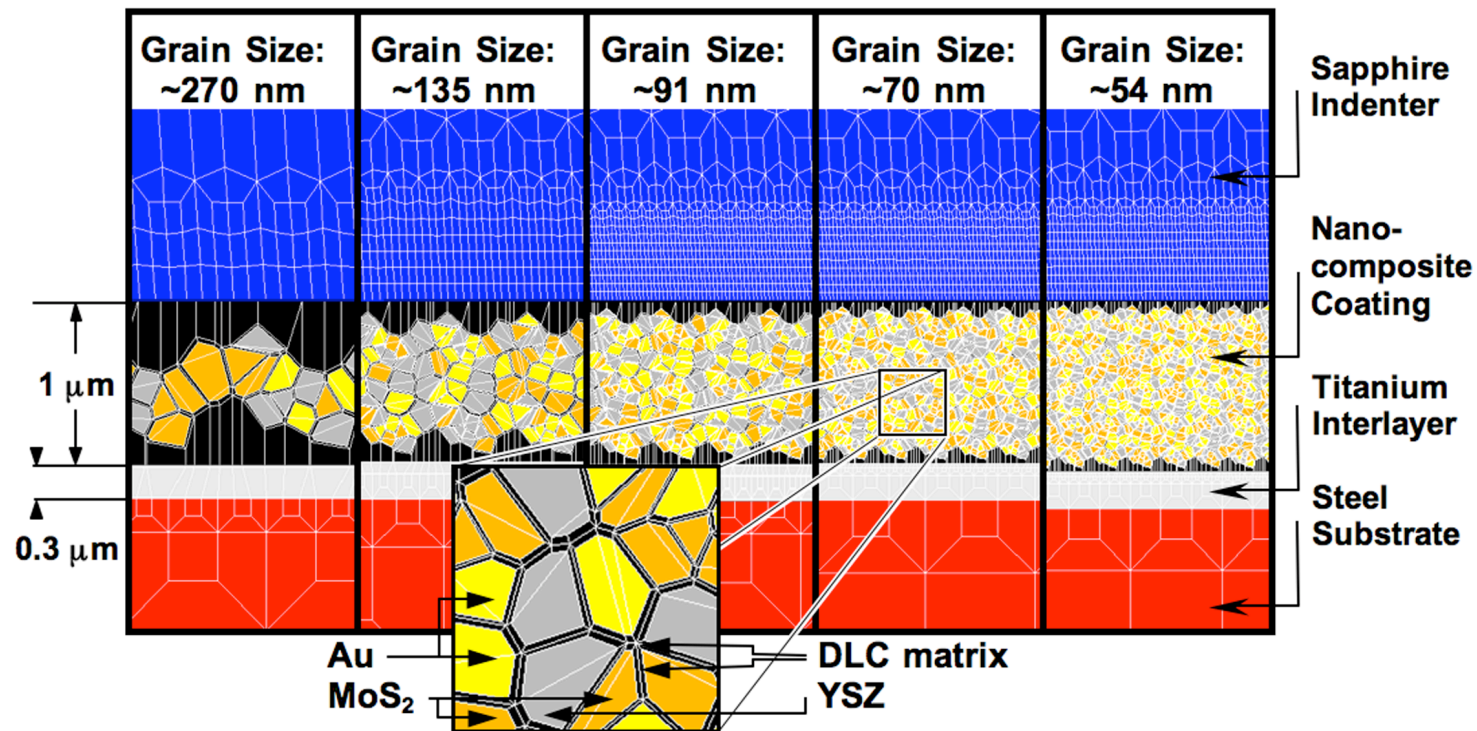
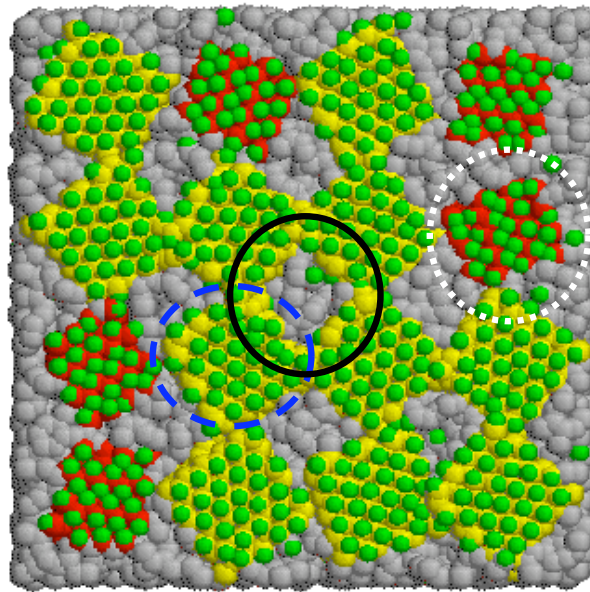
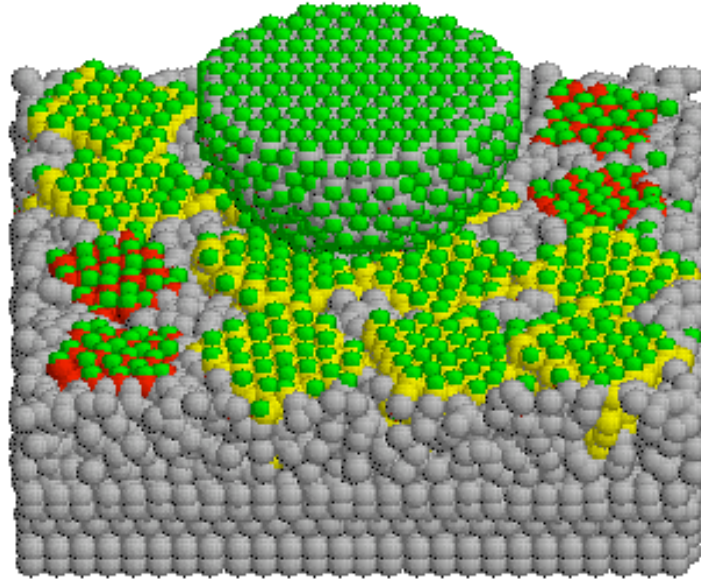
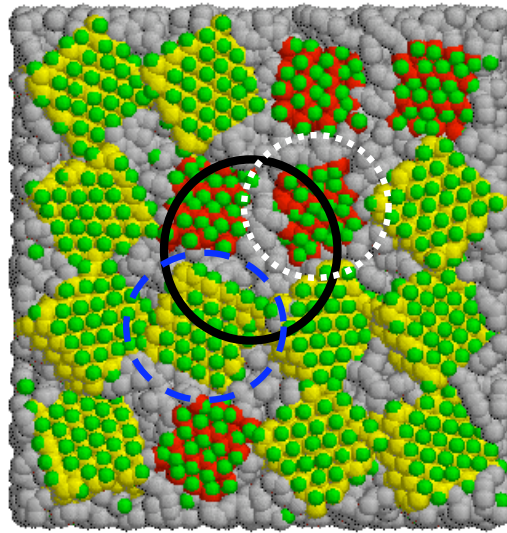
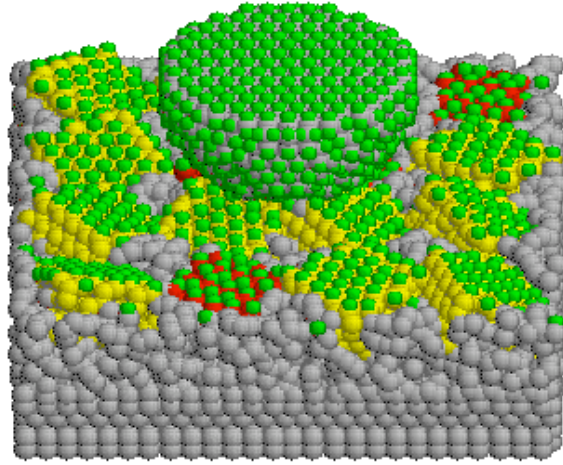


Figure 2.13: ‘Active zone’ mesh underneath the indenter at the center of the contact for the grain sizes investigated using the optimized mesh technique. The magnified inset shows the mesh of the DLC matrix around each grain.

Figure 2.14: MD starting configurations for the MDN systems shown from side (left) and top views (right). Panels (a) and (b) correspond to MDN films 1 and 2, respectively. Yellow and green squares represent (111) grains while red and green squares represent (110) grains. Large and small spheres represent carbon and hydrogen atoms, respectively. Black-solid, blue-dashed, and white-dotted circles in right panels are approximately centered over indentation locations 1, 2, and 3, respectively.

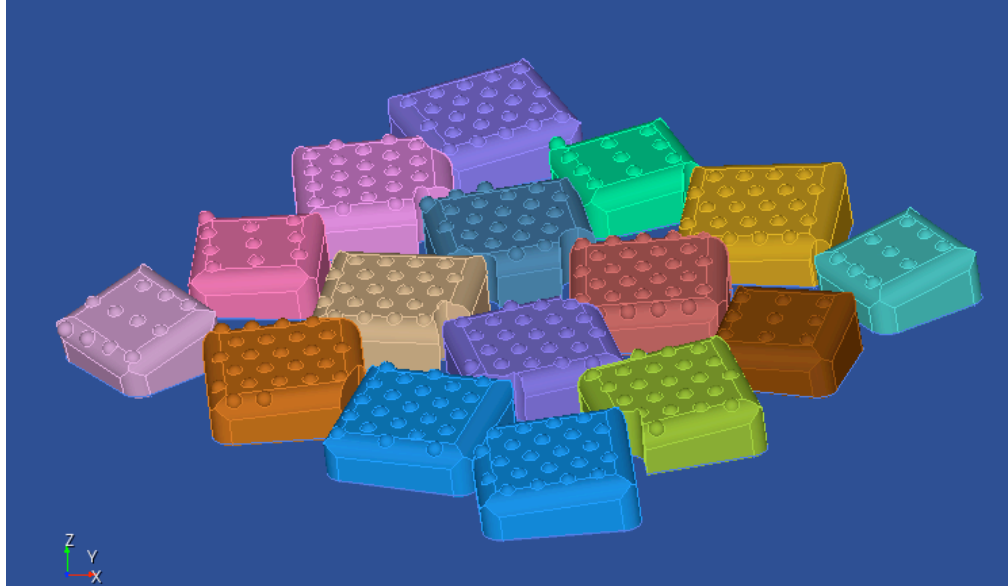


(a)

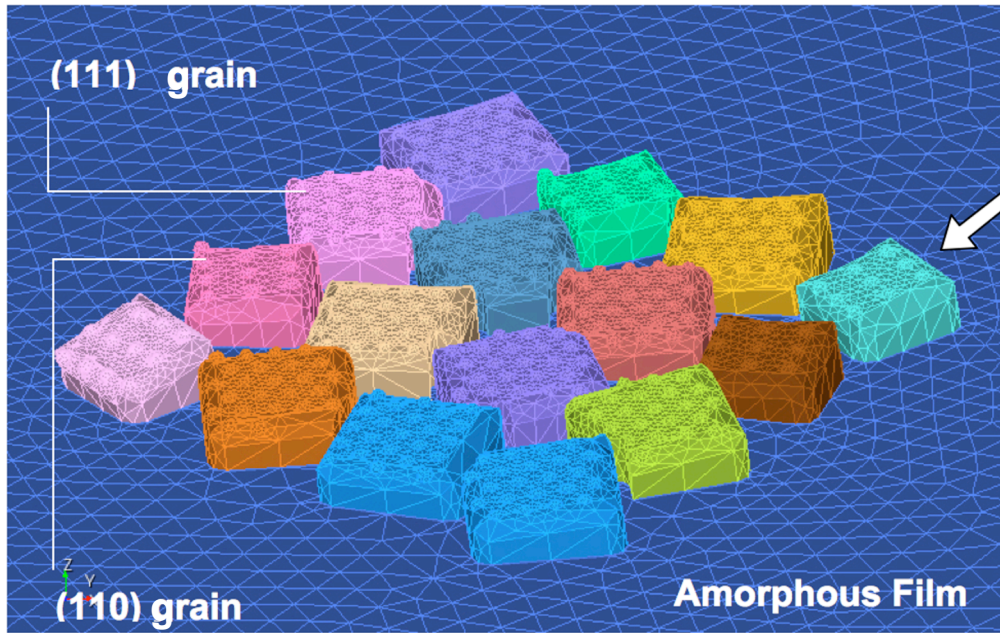


(b)

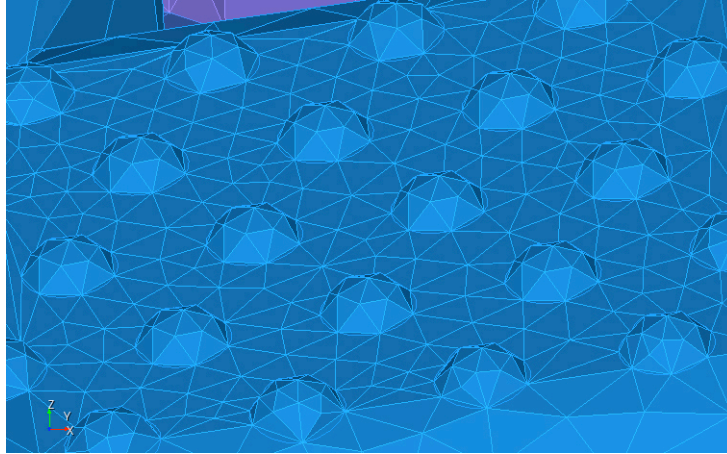
Figure 2.15: The finite element model of MDN system (film 1) used in the MD simulations. The geometry of the MDN system is shown in (a). The mesh of the geometry in (a) is shown in (b). A zoom of the surface of a diamond crystal in the amorphous carbon substrate is shown in (c). The indenter centered over a diamond crystal removed from the substrate shown in (d). Zoom of the crystal surface showing the atomic surface morphology shown in (e).



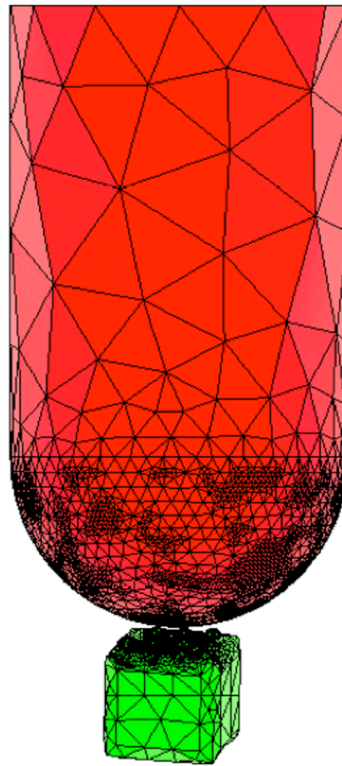
(a)



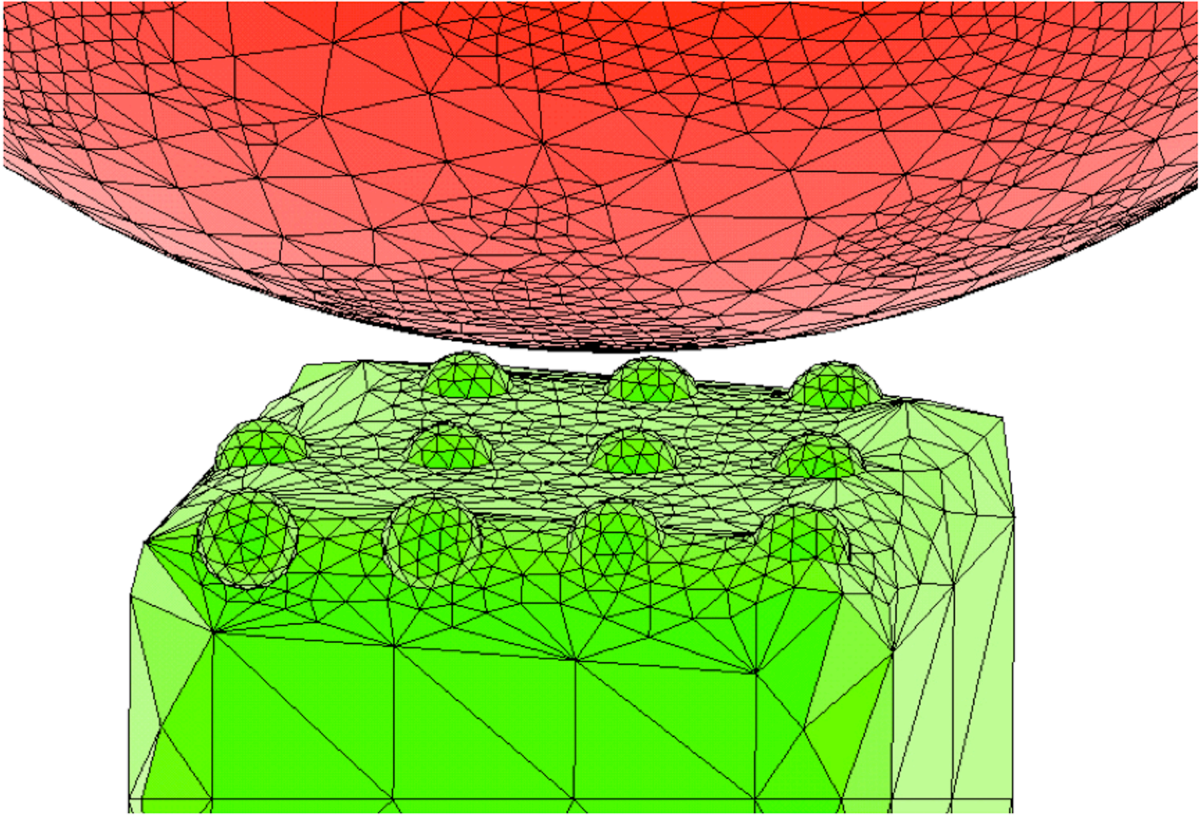
(b)



(c)



(d)



(e)

3. CONTINUUM MODEL VERIFICATION

In order to compare and validate the FE simulations with the MD simulations of nano-indentation of the MDN system with a spherical indenter, multiple sets of FE simulations were conducted with and without surface morphology that represents atomic-scale structure, with a shallow and deep diamond substrate attached to the films, and using both rigid and deformable indenters (Figure 3.1).

Recently, Luan and Robbins 2005 examined the applicability of continuum mechanics to nanoscale contacts by comparing analytic continuum solutions to MD simulations. Those studies showed that the roughness that arises from the presence of discrete atoms can lead to dramatic deviations from analytical continuum solutions during indentation and sliding. Contact areas and stresses can be changed by a factor of two, whereas friction and lateral contact stiffness change by an order of magnitude compared to the continuum solutions. These findings underscore the importance of utilizing methods that encompass atomic-scale information in conjunction with continuum methods. Through comparing the FE and MD results for indentation of the MDN system it is shown that continuum scale modeling can provide excellent qualitative and satisfactory quantitative predictive capabilities when atomic-scale surface morphology is treated as surface roughness at the continuum level and similar elastic properties, as determined from MD simulations, are used as input.

The average normal contact pressure P_{Avg} for all FE simulations with shallow substrate is shown as a function of distance from the center of the indenter in Figure 3.2 (a) and (b). The data for the shallow and deep substrates are shown in Figure 3.2 (c) and (d) and Figure 3.2 (e) and (f) respectively. The peaks and valleys in the MD simulation results can be explained by observing the location of the peaks is in the same vicinity of the hydrogen atoms which terminate the surface carbon atoms. While the hydrogen atoms were not represented in the FE simulations (because these atoms have bonds with more flexibility than the carbon atoms which are rigidly locked in place in a lattice, and thus the means of incorporating these dynamic, fluid-like entities in a quasi-static, solid continuum model is not immediately clear) the surface carbon atoms are included and these are both in the same location and also much larger and thus have a dominating effect on the apparent surface area of, and contact pressure experienced by, the crystal. Several interesting trends are apparent from an analysis of the data in Figure 3.2.

At values of the radius larger than approximately 4.5 Å, the FE results are nearly identical at both loads examined. In other words, far from the center of the contact in the long-range, the indenter hardness, the thickness of the substrate, and the atomic-scale surface morphology have no influence on the average normal contact pressure but do control the location of the edge of the contact. The maximum bound on the average contact pressure P_{Avg}^{MB} is also shown as the dotted line in Figure 3.2 (a)-(e). This is calculated in the same way as P_{Avg} in equation (23) except that the force is a constant 25 or 100 nN. The point where

P_{Avg}^{MB} deviates from the FE solutions is known as the short- to long-range transition point. It is below this point where the conditions imposed on the FE simulations, i.e. shallow substrate, begin to cause the FE solutions to diverge. Close to the center of the contact the best quantitative agreement between the MD and the FE solutions is obtained at high load and with the shallow substrate (Figure 3.2 (d)). At low load (25 nN), the FE simulations have peak values for P_{Avg} of 110% to 210% of the MD predicted values depending on the model parameters (Figure 3.2 (c)). At the higher load (100 nN), the FE results are 80% to 160% of the MD predictions (Figure 3.2 (d)). Far from the center of the contact, the MD and the FE simulations at both loads are nearly identical. The larger the load, the farther from the center of the contact this point occurs (Figure 3.2 (c)-(d)).

The best qualitative agreement between the MD and FE predictions was obtained when the FE simulations utilized atomic-scale surface morphology, a shallow substrate, and a deformable indenter (Figure 3.2 (c)). This FE simulation most closely resembled the MD system modeled. Thus, FE simulations when prepared properly can be used to model nano systems with reasonable results.

In all the FE simulations, the trend in pressure distribution is affected less by loading and more by model parameters, such as atomic-scale surface morphology (Figure 3.2 (c)-(d)) and substrate depth (Figure 3.2 (e)-(f)). At low loads (Figure 3.2 (c)), the presence of the atomic-scale surface morphology causes the pressure distributions from FE and MD simulations to have similar shapes. In contrast, the qualitative agreement between the FE and MD simulations in the presence of atomic-scale surface morphology is lost at high loads

(Figure 3.2 (d)). At low loads, the atomic-scale surface morphology is the dominant effect on the distribution of the contact pressure (Figure 3.2 (c)) and contact area. At high loads, the substrate is more active in the load support and the random orientation of the crystals has a larger influence on the pressure distribution and contact area rather than the presence of surface morphology (Figure 3.2 (e)-(f)).

The magnitude and distribution of P_{Avg} is insensitive to the rigid or deformable nature of the indenter when the load is low and the substrate is shallow (Figure 3.2 (c)) or deep (Figure 3.2 (d)). In contrast, at the higher load the deformable indenter has a lower peak pressure (Figure 3.2 (f)). In general, the magnitude of the peak in P_{Avg} appears to arise from the local contact behavior associated with each surface morphology.

The continuous distribution of P_{Avg} over all loadings from 0 to 120 nN is shown for two FE simulations in Figure 3.3. For both simulations, the pressure does not decrease monotonically from the center of the contact outward but rather contains a secondary peak. This is due to the presence, and random tilting, of the embedded diamond grains. As expected, both the MD and the FE simulations have increasing peak contact pressures with increasing load.

The contact pressure $P_{Contact}$ normally computed in continuum mechanics contact simulations (equation (24)) is approximately an order of magnitude larger than the average normal contact pressure P_{Avg} . The evolution of peak contact pressure, $P_{Contact}$, and von Mises stress (equation (2)) for selected FE simulations, with and without atomic-scale surface

morphology, are shown in Figure 3.4 as a function of indenter displacement and loading. A representative contour of the von Mises stress showing the peak stress to be within the interior of the crystal is shown in Figure 3.5. The nonlinear evolution of the peak pressure and stresses can be explained by stick slip events for models without atomic-scale surface morphology and changing contact conditions for models with atomic-scale surface morphology.

For example, when atomic-scale surface morphology is present in conjunction with the appropriately oriented grains, the contact pressure increases in a non-monotonic fashion (Figure 3.4 E-H). The indenter makes initial contact with the atomic-scale “bumps” on the (110) that protrudes the highest above the surface (Figure 3.4 E) resulting in an increase in the contact pressure. Additional displacement of the indenter causes it to come into contact with a larger, flat, region of the (110) crystal. This results in the decrease in contact pressure between the points labeled Figure 3.4 F and 3.4 G. Continued motion of the indenter causes it to come into contact with all the atomic-scale “bumps” available on the surface (Figure 3.4 H) and the peak contact pressure continuously increases with increasing load. Without atomic-scale surface morphology, a nonlinear evolution of the peak surface stress is due to the friction induced, lateral-slip locking between the deforming crystal surface and the indenter at the critical indenter displacement of 0.4 nm (Figure 3.4 A-D).

The peak values of pressure and stress occurred at different locations for models with and without atomic-scale surface morphology. Thus, to use FE simulations to accurately predict the location of regions with elevated potential for chemical and electronic bonding,

the inclusion of atomic-scale surface structure is crucial. In addition, these bonding regions may be localized to high stress regions.

From these results the use of finite element simulations at the nano scale has been shown to be quantitatively accurate within limits and to provide excellent qualitative results. Within the short- to long-range transition, quantitative finite element results deviate from MD predictions on average from 20% to 60% over all models and loads, with some models having much less error than others. After the long-range transition, the two modeling techniques produce the same results. Further, finite element simulations can be extended to model sizes that are prohibitive for MD simulations as well as conditions (such as a lack of surface morphology) that are not feasible in MD simulations.

3.1 CONCLUSIONS

In order to compare and validate the FE simulations with the MD simulations of nano-indentation of the MDN system with a spherical indenter, multiple sets of FE simulations were conducted with and without surface morphology that represents atomic-scale structure, with a shallow and deep diamond substrate attached to the films, and using both rigid and deformable indenters.

Materials properties of diamond grains within the FE mesh were calculated from the experimentally determined elastic constants of diamond and an isotropic modulus was used for the amorphous carbon regions. The correspondence between the FE and the MD simulations was explored by simulating multiple sets of conditions using FE.

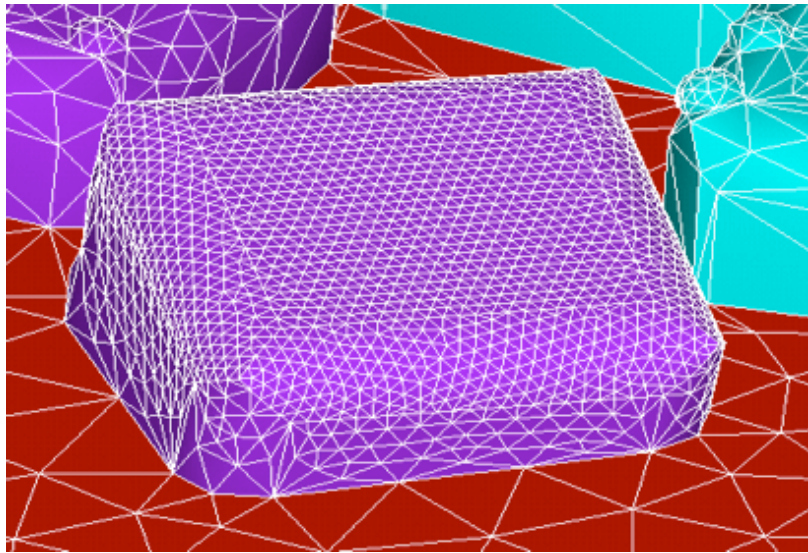
The atomic-surface morphology of individual (111) and (110) grains of a MDN sample along with the grain orientations were incorporated into the FE mesh at the continuum level as surface roughness.

All of the FE simulations at low loads yielded the qualitative trends consistent with the MD predictions. This suggests that FE simulation results could be used in the short range if an appropriate scaling factor can be determined from MD simulations and was then applied to the FE computed magnitudes.

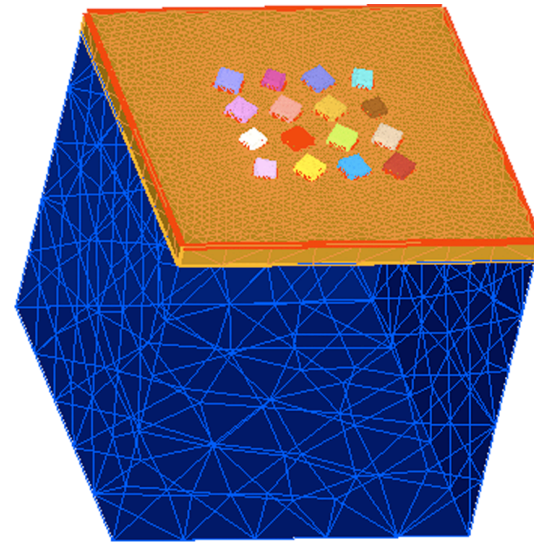
From the results, the use of finite element simulations at the nano scale has been shown to be quantitatively accurate within limits and to provide excellent qualitative results. Within the short- to long-range transition, quantitative finite element results deviate from MD predictions on average from 20% to 60% over all models and loads, with some models

having much less error than others. After the long-range transition, the two modeling techniques produce the same results. Further, finite element simulations can be extended to model sizes that are prohibitive for MD simulations as well as conditions (such as a lack of surface morphology) that are not feasible in MD simulations.

3.2 FIGURES
(CHAPTER 3)



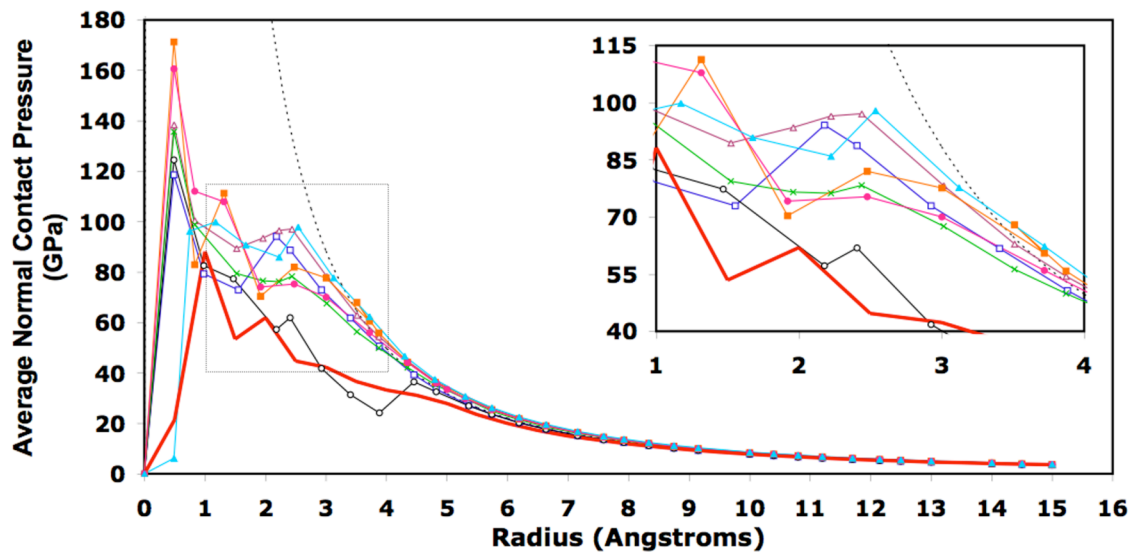
(a)



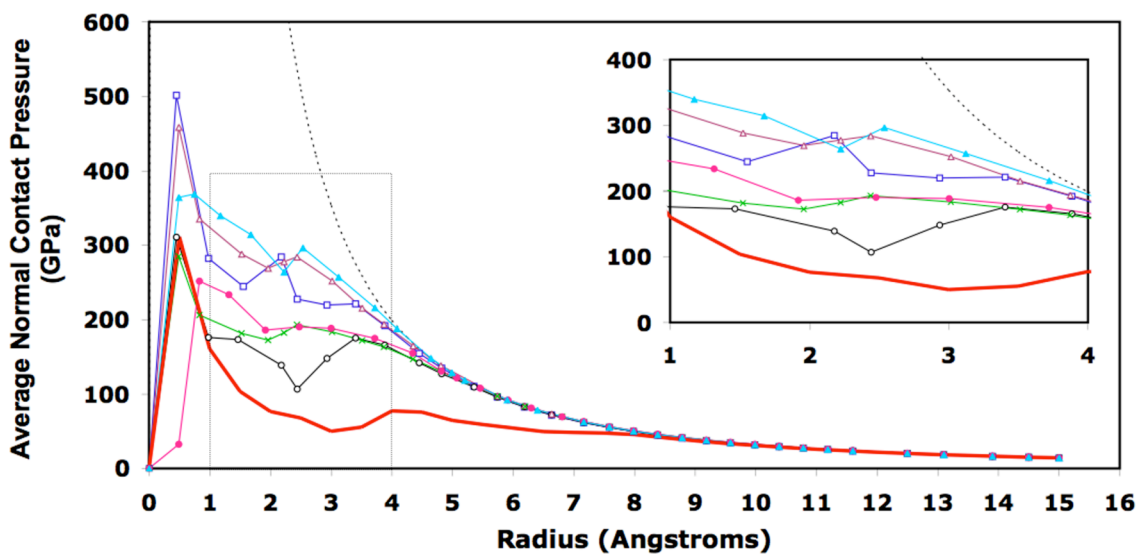
(b)

Figure 3.1: Example of diamond nano-crystal in MDN system with (a) no surface morphology (crystal in purple and substrate in red) and (b) a deeper substrate (in blue). The deeper substrate in (b) is 20 nm deep and does not contain the diamond layer on the bottom.

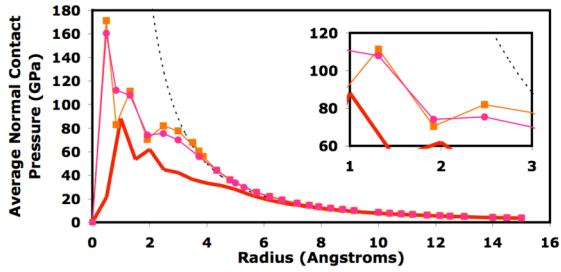
Figure 3.2: Average normal contact pressure, P_{Avg} , versus radius from equation (23) for MD (red, heavy line) and FE simulations. Dotted line in (a)-(e) indicates the maximum bound, P_{Avg}^{MB} . All FE models at (a) 25 nN loading and (b) 100 nN loading. Gray dotted box indicates area of zoom inset. (c) FE models with surface morphology, shallow substrates and both rigid and deformable indenters compared to MD at 25 nN. (d) All FE models with surface morphology compared to MD at 100 nN. All FE models with deep substrates compared to MD at (e) 25 nN and (f) 100 nN.



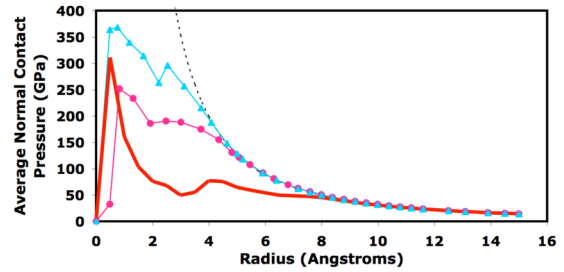
(a)



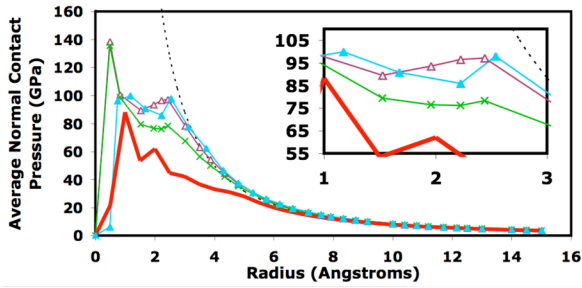
(b)



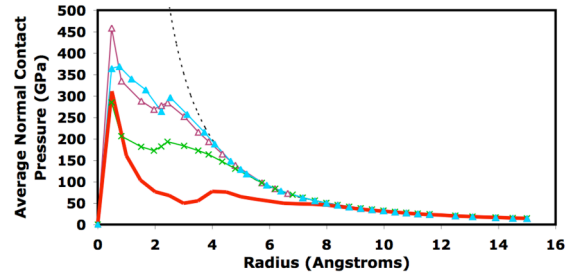
(c)



(d)



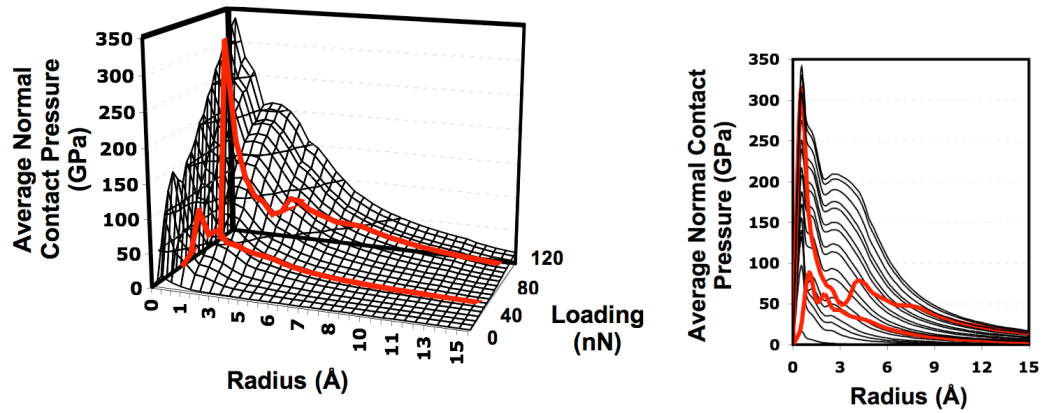
(e)



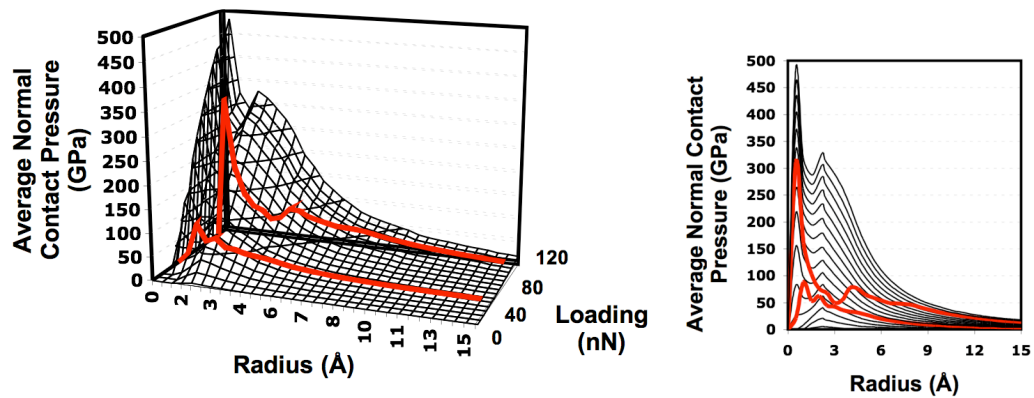
(f)

Legend:

- FEM: No Surface Morphology – Shallow – Rigid
- FEM: Surface Morphology – Shallow – Rigid
- FEM: No Surface Morphology – Shallow – Deformable
- FEM: Surface Morphology – Shallow – Deformable
- △— FEM: No Surface Morphology – Deep – Rigid
- ▲— FEM: Surface Morphology – Deep – Rigid
- ×— FEM: No Surface Morphology – Deep – Deformable
- MD



(a)



(b)

Figure 3.3: Average normal contact pressure, P_{Avg} , distribution for MD (red, thick) and FE (black surface mesh) simulations versus loading. In (a) the FE model data with surface morphology, with a shallow substrate, and using a deformable indenter are shown. In (b) the FE model data without surface morphology, with a shallow substrate, and using a rigid indenter are shown.

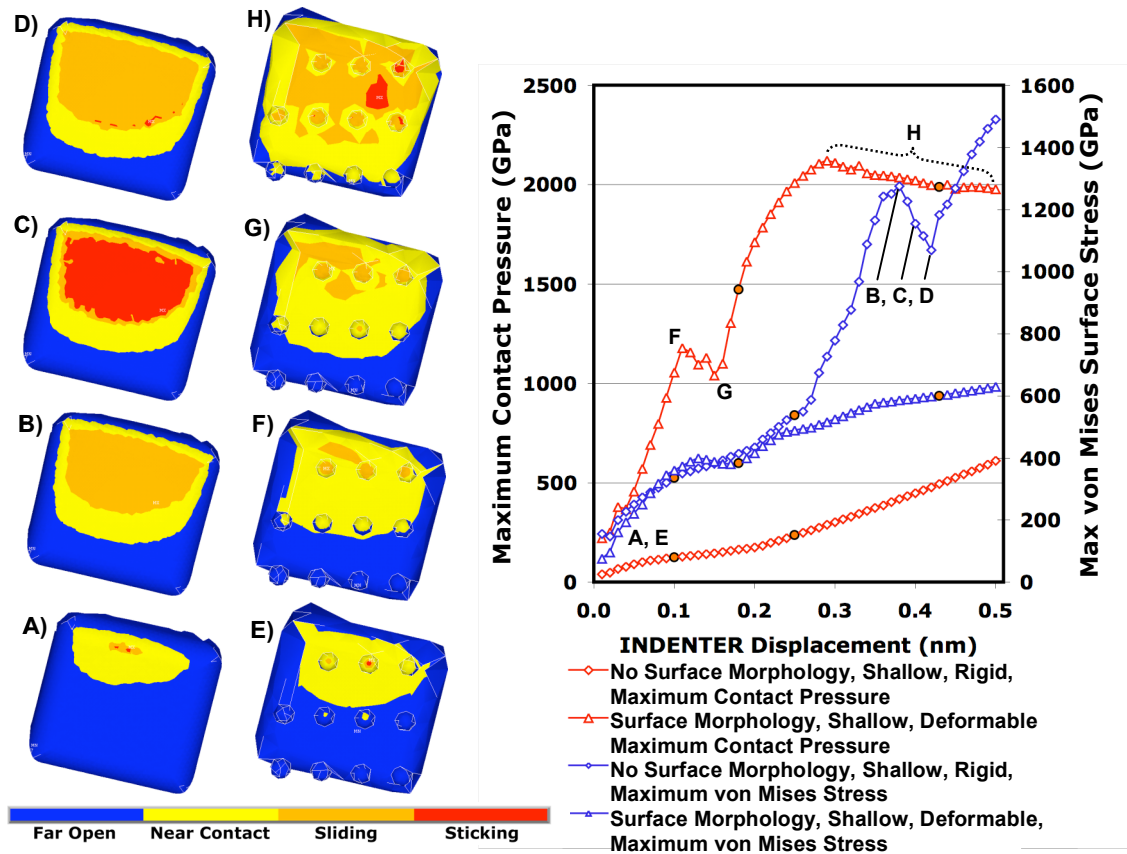


Figure 3.4: (Left panel) MDN grain surface contact status for indicated FE simulations. Only the (110) region of the FE mesh, which is centered under the indenter, is shown. (Right panel) Maximum FE contact pressure, $P_{Contact}$, (red, left ordinate) and von Mises stress (blue, right ordinate) for selected simulations versus indenter displacement. Orange circular data points for each simulation indicate the 25 and 100 nN loadings respectively.

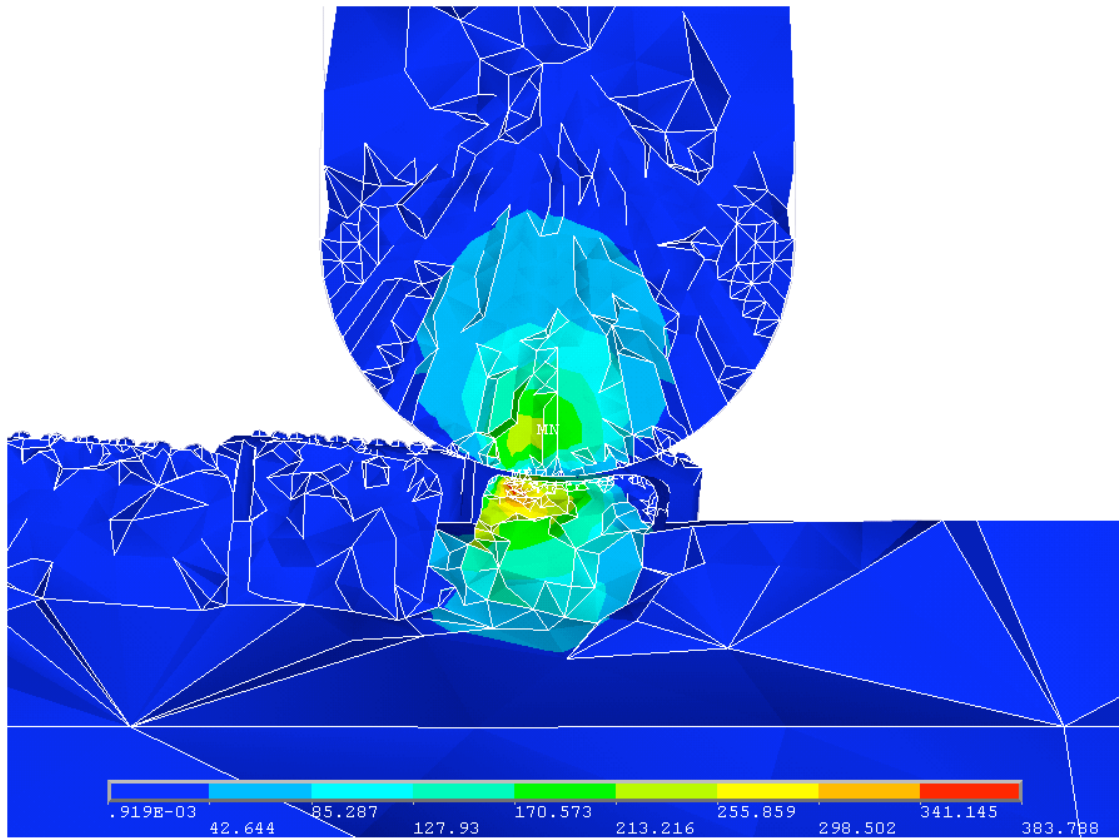


Figure 3.5: Representative contour of the von Mises stress through a cross-section of a diamond crystal (and the indenter) middle showing the peak stress to be within the interior of the crystal. Stress in GPa.

4. NANOCOMPOSITE COATING BEHAVIOR

The nanocomposite coatings were modeled under varying indentation and sliding loads with changing composition, grain size and matrix width to optimize and understand how the coatings respond under load until failure. Critical areas in the coating where failure would begin were identified. Single component coatings of each constituent were modeled and used as the limiting case to determine the effects of grain morphology, interfacial regions between the constituents and mechanical properties for coatings with different compositions. Sliding simulations of a linear reciprocating ball-on-flat configuration were undertaken to demonstrate the influence of tangential forces on plastic deformation and fracture. Indentation simulations were used to computationally determine relative H/E ratios (hardness to elastic modulus) for different grain size coatings in order to rank each coating in terms of wear resistance.

4.1 COMPOSITION VARIATIONS AND INDENTATION RESPONSE

The composite mechanics RVE described in Section 2.1.1 was simulated with numerous varying compositions as described. The resulting homogenized moduli of the coating computed from the composite mechanics RVE as well as the composite mechanics rule of mixtures are shown in Table 4.1. Note in these simulations and calculations the modulus of the DLC was taken as 500 GPa.

As can be seen from the results, both the RVE and ROM techniques differ by generally less than 15% in their prediction of the coatings homogenized elastic modulus. From Chromik *et al.* 2006 nanoindentation measurements of nanocomposite coatings with varying compositions in the same range as in Table 4.1 report coating moduli in the range from 66 to 133 GPa.

The RVE and ROM models predict moduli much higher than those that are measured leading to the conclusion (from the computational results) that the coating is not fully dense and contains voids. By adding in a percentage of voids in the rule of mixtures and the representative volume element, the modeling techniques predict 60% and 40% respectively voids in the coatings.

As can be seen in Figure 4.1 (a) and (b) this prediction is confirmed. The coating is not fully dense, as is typical for coatings fabricated in this manner, i.e. at low temperatures and high partial pressures in the vacuum chamber necessary for creating and maintaining the plasma sheath involved with magnetron sputtering. The low modulus and void content of the coating were factored into reducing the DLC matrix modulus to 250 GPa in all other finite

element simulations. The voids are predominantly expected to occur in the matrix phase of the coatings, thus reducing the modulus of the matrix would imitate the effect of the voids without their presence explicitly modeled.

4.1.1 INDENTATION TO 20% NOMINAL STRAIN

Stresses in an equal composition nanocomposite coating modeled with the refined mesh and 300-600 nm grain size at 20% nominal strain (the indented displacement normalized by the coating thickness) were compared to the limiting cases of single-component coatings for each constituent. This nominal strain and load level are typical of the experimental wear tests typically conducted for these coatings.

For both the nanocomposite mixtures and single component coatings, there was no significant plastic deformation in the steel substrate or titanium interlayer at 20% nominal strain. The stiffest single component coating was the DLC coating with a maximum effective stress at the free surface in contact with the indenter of 510 MPa (Table 4.2). The steel substrate underlying the DLC coating had a maximum effective, or von Mises, stress of approximately 300 MPa at 10-20 μm below the coating interface, which is both consistent with Hertzian theory and comparable to indentation results of the steel substrate without a coating. These results indicate that the coating does not support or resist the applied loads. In essence, the coating is not load bearing and falls into the category of a soft coating on a hard substrate. The maximum stress occurs at the free surface and not at the titanium interlayer. If the coating and the interlayer were to have a dominant role in load bearing, high delamination bending stresses would have occurred at the titanium/substrate interface (Zhang *et al.* 2006).

In contrast to the single component coatings of each material, the multicomponent nanocomposite coating exhibited localized stress gradients that were dependent on both

composition and materials properties. The nanocomposite with equal composition of constituents had maximum effective stresses not at the free surface, but within the DLC-metal interfaces (Figure 4.2 (a)). Large gradients in stress developed across the DLC borders between separate inclusions, and these are the locations where failure and de-cohesion have been also observed experimentally (Voevodin and Zabinski 1998; Voevodin *et al.* 2002; Voevodin and Zabinski 2000). However, this change in the location of maximum stress only increased the effective stress magnitude in the coating by 28% (to 653 MPa) as compared to the single-component DLC coating (Figure 4.2 (a), Table 4.2). Hence, this indicates inclusion of separate materials in a DLC coating can permit expanded tribological performance while producing a significant but manageable (28%) rise in effective stresses.

When the Au content of the nanocomposite was increased to 50% Au (25%DLC, 12.5%YSZ and 12.5% MoS₂), which may occur for coating systems whose predominant loadings occur at high temperature where DLC matrices are tribologically unstable for use in an oxidizing environment (Cartier 2003) and gold has been shown an effective lubricant (Lince 2004), the maximum stresses in the DLC matrix decreased slightly (to 613 MPa) in comparison with the nanocomposite with equal (25% Au) composition of constituents (Figure 4.2 (b), Table 4.2). In contrast, when the equal composition nanocomposite system was changed in composition to 50% MoS₂, (25% DLC, 12.5% YSZ and 12.5%Au), as may occur for coating systems where increased solid lubrication or extraterrestrial operation is desired, the maximum stresses in the DLC matrix significantly increased, in comparison with a 25% MoS₂ composition, to 1.06 GPa (Figure 4.2 (c), Table 4.2).

For both nanocomposite systems with either 50% MoS₂ or 50% Au, the maximum effective stress in the remaining phases YSZ and either Au or MoS₂ remained essentially unchanged from the stresses developed in the nanocomposite coating with equal constituent composition. The largest changes occurred in the 50% MoS₂ system with increased stresses in all phases. This indicates that while increasing the composition of MoS₂ in the composite coating may be expected to reduce friction and wear, the competing effects of large increases in intrinsic coating stresses may induce undesired mechanical weaknesses.

Modifying the nanocomposite compositions resulted in changes in the maximum effective stresses of the ductile phases, Au and MoS₂, relative to the single component coatings of these phases (Table 4.2). For a pure coating of gold versus the nanocomposite coatings, the maximum effective stress in the gold coating was 205 MPa (Table 4.2) which was reduced to 154 MPa for the equal composition nanocomposite (Figure 4.2 (a)) and 137 MPa for the 50% gold composition (Figure 4.2 (b)). This trend was also evident when the nanocomposite composition was changed from 25% gold to 50% MoS₂ where the gold inclusions had a maximum stress of 141 MPa (Figure 4.2 (c)). This further substantiates that increasing the percentage of MoS₂ increases the coating stress. This underscores Au is the most ductile and weak material in the coating, and any compositional changes do not markedly affect the gold phase's stress state.

A coating of pure MoS₂ is similar in its behavior to gold when compared to the equal composition coating. The maximum effective stress in a pure MoS₂ coating was 288 MPa (Table 4.2) and decreased to 238 MPa (Figure 4.2 (a)) for the equal composition coating.

This trend was similar when the composition was changed from 25% to 50% gold where the maximum effective stress in the MoS₂ inclusions was 235 MPa (Figure 4.2 (b)). Furthermore, when the composition was changed again to 50% MoS₂, the maximum effective stress increased to 244 MPa (Figure 4.2 (c)). In general, increasing the percentage of MoS₂ in the nanocomposites correlated with increased maximum effective stress in the coatings.

For the equal composition nanocomposite, both ductile materials have maximum effective stress greater than their yield stress. For the gold and MoS₂ inclusions, the stress was 1.3 times higher than the respective yield stress. For the pure coatings of gold and MoS₂, the stress was 1.6 times higher than the respective yield stress.

For ductile materials under contact, the pressure to cause yielding varies dramatically with yield stress. From a Hertzian analysis of a sphere (body 1) indenting a homogenous body (body 2) with load P , the contact area (circle with radius \bar{a}) and maximum pressure, p_o , in the indented body is given by (Budynas 1999):

$$\begin{aligned} \bar{a} &= \sqrt[3]{\frac{3PR_e}{4E_e}} \\ p_o &= \frac{3P}{2\pi\bar{a}^2} = \frac{1}{\pi} \sqrt[3]{\frac{6PE_e^2}{R_e^2}} \end{aligned} \quad (25)$$

where R_e and E_e are the effective radius and elastic modulus of the bodies given by:

$$\begin{aligned} \frac{1}{R_e} &= \frac{1}{R_1} + \frac{1}{R_2} \\ \frac{1}{E_e} &= \frac{1-\nu_1^2}{E_1} + \frac{1-\nu_2^2}{E_2} \end{aligned} \quad (26)$$

where the subscripts 1 and 2 indicate the respective body.

The maximum Hertzian shear stress in the indented body occurs beneath the surface and can be given as (Mencík 1995):

$$\tau_{Max} \approx 0.31p_o \quad (27)$$

where the Poisson ratio is assumed to be 0.3 for demonstration purposes. The von Mises yield criterion states that yielding occurs when the maximum shear stress is equal to the uniaxial tensile yield stress divided by the square root of three. Thus the yield stress can be expressed in terms of the load using equation (25) as (Mencík 1995):

$$\begin{aligned} \tau_{Max} &\approx 0.31p_o \approx \frac{\sigma_Y}{\sqrt{3}} \\ \sigma_Y &= \frac{\sqrt{3}(0.31)}{\pi} \sqrt[3]{\frac{6PE_e^2}{R_e^2}} \\ \sigma_Y &= \frac{\sqrt{3}(0.31)}{\pi} \sqrt[3]{\frac{6P \left(\frac{1-\nu_1^2}{E_1} + \frac{1-\nu_2^2}{E_2} \right)^2}{\left(\frac{1}{\frac{1}{R_1} + \frac{1}{R_2}} \right)^2}} = \frac{\sqrt{3}(0.31)}{\pi} \sqrt[3]{\frac{6P \left(\frac{1-0.3^2}{E_1} + \frac{1-0.3^2}{2E_1} \right)^2}{\left(\frac{1}{\frac{1}{R_1} + \frac{1}{\infty}} \right)^2}} \\ \sigma_Y &= \frac{\sqrt{3}(0.31)}{\pi} \sqrt[3]{\frac{6P \left(\frac{E_1}{1.365} \right)^2}{(R_1)^2}} = 0.252 \sqrt[3]{\frac{PE_1^2}{R_1^2}} \\ \therefore P_Y &= 62.2 \sigma_Y^3 \left(\frac{R_1}{E_1} \right)^2 \end{aligned} \quad (28)$$

where it is assumed that the substrate modulus is half the modulus of the indenter and they both have equal Poisson ratio's of 0.3.

Thus it can be seen from equation (28) that the allowable load before plastic deformation, P_Y , varies with the third power of the yield stress. Notice also that a more compliant material system will need a higher load before plastic deformation due primarily to the increased contact area. These results imply that small variations in yield stress can cause large changes in maximum allowable loads. Generally, plastic strains are undesirable in coatings due to fatigue and cracking which are associated with plasticity and lead to an increased wear rate. Optimizing the constituents by slight changes in the yield stress can lead to large changes in increased allowable loads without significant changes to the wear rate.

4.1.2 INDENTATION TO 56% NOMINAL STRAIN

For both the equal composition nanocomposite with 300-600 nm grain size and refined mesh and the pure coatings, indentations were undertaken to a depth of 56% nominal strain to further understand the coatings response under increased loadings, which could correspond to high local stresses and strains associated with frictional spiking and transfer film removal.

When an uncoated steel substrate is indented, plastic strains develop quickly and attain a maximum of approximately 0.5% at 56% nominal strain (Table 4.3). When a micron thick coating and a titanium interlayer are also included, the nominal strain to induce plastic deformations in the substrate almost triples and the maximum plastic strains are slightly less than an order of magnitude lower in comparison with a pure steel substrate. It should be noted this trend applies for the hard brittle coatings of pure DLC and the soft ductile coatings of pure gold. This effect is due to the increased uniform diffusion of the load over the contact area when applied through a thin combination of coating and a titanium interlayer, which would not resist the load because they are generally more compliant than the substrate.

The maximum normal stresses, σ_{YY} , and maximum equivalent plastic strains for the equal composition nanocomposite coating and a pure DLC coating are shown in Figure 4.3 for nominal strains ranging from 1 to 56%. For the equal composition coating, the final equivalent plastic strains reached in the ductile phases (gold and MoS₂) at 56% nominal strain are much lower than for a pure coating of either gold or MoS₂ (Table 4.3). However, this tradeoff between the lubrication of the MoS₂ and toughening of the gold occurred with

increases of approximately 77% in the maximum normal stress in the DLC phase for the equal composition nanocomposite in comparison with a pure DLC coating (Figure 4.3). A large increase is seen in the maximum DLC normal stress for the equal composition coating in comparison with a pure DLC coating. Stresses in the titanium interlayer are largely unchanged between the two coatings, as seen in Figure 4.3. In both cases, the rate of stress increase in the DLC phase is largest when plastic deformation develops in the substrate (Figure 4.3).

In comparison with the pure DLC case, the rate of increase in the normal stress for the remaining equal composition coating constituents (gold, MoS₂ and YSZ) remains largely unchanged with the start of substrate plastic deformation (Figure 4.3 (a)). The rate of accumulation of plastic strains in these phases however increases slightly and temporarily before returning to values from before plastic deformation in the substrate (Figure 4.3). Hence, loads for coatings, which introduce plasticity in the substrate, should be avoided in design and result in increases in plastic strain accumulation in the ductile phases. This is likely to increase the probability of coating failure by increasing the interfacial stresses at DLC borders where failure is known to initiate (Voevodin and Zabinski 1998; Voevodin *et al.* 2002; Voevodin and Zabinski 2000).

4.2 SLIDING MODELS

The tangential forces and shear stresses from sliding originate from the friction coefficient, and result in stresses in addition to those induced by the normal load in both the wake and zone preceding the center of contact of the slider. The additional mechanical energy, E^* , introduced into the coatings contact zone by sliding a sapphire indenter can be expressed as a function of the friction coefficient as (Cartier 2003):

$$E^* = \int_0^{t_f} PVf(t)dt \quad (29)$$

where P is the applied load, V the sliding velocity, $f(t)$ the coefficient of friction as a function of time and t_f the final time at the end of sliding. This energy is dissipated in many forms, most notably as wear, heat generation, fracture, and in plastic deformations. Results from the finite element simulations of sliding using an equal composition coating with 300-600 nm grain size and the refined mesh under 20% nominal strain are used to analyze the energy dissipation modes of fracture and plastic work.

Plastic deformations account for a portion of the energy dissipated by the coating, and this is shown in Figure 4.4. Plastic strains develop during the first sliding trip of the indenter, and these strains accumulate rapidly in the MoS₂ phase and slower in the gold (Figure 4.4 (a)). Residual plastic strains remaining in the wake of the slider cause permanent residual stresses up to 100 MPa.

As seen in Figure 4.4 (b), plastic deformations account for up to 15% of the total energy input during the initial pass. Figure 4.4 (a) shows the total energy dissipated by plastic work for both the gold and MoS₂ phases. As seen, the MoS₂ dissipates two orders of

magnitude more work than the gold phase during the first sliding trip of the indenter (160 μm total slid distance). The MoS_2 equilibrates quickly after the first pass, and the second pass dissipates only 3.6% of the energy dissipated during the first pass. The gold behaves similarly, except during the second pass, the rate of energy dissipation is 38.9% that of the first pass. This type of successively decreasing plastic strain accumulation in the ductile phases has been verified experimentally (Jahanmir 1985).

In the wake of the indenter, the shear stresses fall quickly to zero, while underneath the indenter the shear stresses reach a maximum of around 100-200 MPa. The highest stresses are confined to the DLC borders. In the leading edge of the contact, the shear stresses are higher in the coating in comparison with the trailing edge of the contact (Figure 4.5 (a)-(b)). It is not clear whether the shear stress increase is more heavily dominated by sliding velocity or the friction coefficient, although it has been previously shown that friction shifts the location of maximum shear stress toward the edge of the contact, and that sliding velocity has a larger effect on temperature in the contact than on stress distribution (Cartier 2003).

Sliding over the same area, but in an opposite direction, induces different maximum stresses in the DLC matrix borders depending on the orientation of the border with respect to the sliding. The coating could be optimized for sliding direction in some cases. Figure 4.6 (a)-(b) illustrates this effect for DLC borders around MoS_2 inclusions, and Figure 4.6 (c)-(d) illustrate this effect to a lesser extent for the gold inclusions. As can be seen from these

images, borders which are slanted perpendicular to the direction of sliding have higher stresses than borders of opposite orientation for each pass of the slider.

In the wake of the indenter during the sliding simulations, tensile stresses develop in the coating material which can lead to the opening of Mode I surface cracks. Figure 4.7 (a)-(c) shows cross sectional views of the in-plane tensile stress distribution at the trailing edge of the indenter 21 μm and 60 μm after the first sliding pass as well as an idealized surface flaw which can develop with coating wear.

These flaws can be of any shape subjected to an opening mode of stress. In the present analysis, we assume semi-elliptical surface-flaws (Figure 4.7 (c)) to show how increases in the stress-intensity factor can lead to unstable crack growth in the coating. Since the DLC is brittle, has the highest stress and strength, and is the matrix material where cracking is experimentally observed, we only use the stresses in the DLC regions (which is also elastic) to calculate the stress-intensity factor. The mechanics governing crack opening involve a combination of crack geometry, applied stress, and material properties. For an idealized, semi-elliptical surface flaw, the stress-intensity factor, K_I , is given by:

$$K_I = 1.12\sigma^* \sqrt{\frac{\pi a}{Q^*}} \quad (30)$$

where a is the maximum crack depth of penetration into the coating, σ^* is the applied Mode I tensile stress field and Q^* is dependent upon the material's yield stress and an elliptic integral of the second kind as:

$$Q^* = \left(\int_0^{\frac{\pi}{2}} \left[1 - \left(\frac{c^2 - a^2}{c^2} \right) \sin^2 \phi \right]^{\frac{1}{2}} d\phi \right)^2 - 0.212 \left(\frac{\sigma^*}{\sigma_Y} \right)^2 \quad (31)$$

where c is the cracks half-width in the plane of the coating and σ_Y is the material's yield strength.

The maximum tensile stresses in the plane of the coating reach a maximum depth of 10% of the coating's thickness (Figure 4.7 (a)). This corresponds to a maximum stress field of $\sigma^* = 100$ MPa at an assumed maximum crack depth $a = 0.1$ μm . The crack's width in the plane of the coating can be estimated from SEM images taken of a TiC coating system as reported on by Voevodin and Zabinski (Voevodin and Zabinski 1998). In this work, SEM images reveal surface cracks range from <1 μm to ≈ 10 μm in length, giving a range for c from 0.5 μm to 5 μm . With these assumptions, the range for Q^* , assuming cracking in the DLC matrix material at the surface, is 1.10 with $c = 0.5$ μm and 1 for $c = 5$ μm .

Assuming $Q^* = 1$ for the worst case scenario, the calculated fracture toughness for the DLC matrix to avoid a self propagating crack under the tensile stresses in the indenter's wake is shown in Table 4.4. Experimental reports of the fracture toughness of DLC coatings (Nastasi *et al.* 1999; Hou and Gao 2001; Li and Bhushan 1999) (Table 4.4) have shown that the fracture toughness of DLC alone is orders of magnitude below that required to support the tensile stresses in the presence of a pre-existing surface flaw at the free surface without crack growth and failure.

However, the fracture toughness of a material is a function of the surface energy. The difference in surface energy of each of the coating constituents determines the relative interfacial bonding strengths of the nanocrystalline regions. The fracture toughness, K_{IC} , in a homogeneous material is given (Hou and Gao 2001) as:

$$K_{IC} = \sqrt{2\gamma^*E} \quad (32)$$

where E is the materials modulus and γ^* is the surface energy. Table 4.4 lists surface energies (Cartier 2003; Nastasi *et al.* 1999) of the coatings constituents and the calculated theoretical fracture toughness of each material. Note that zirconium oxide is substituted for YSZ and pure molybdenum is substituted for MoS₂ in the table.

As the table indicates, the stress intensity factor is generally greater than the critical fracture toughness. The coating is able to support these cracks because of the toughening provided by the ductile elements and the observation that the tensile stresses decay through the thickness of the coating to approximately 25 MPa at the titanium interlayer junction (Figure 4.7 (a)-(b)). At this depth and stress, the calculated K_{IC} value to prevent crack propagation is approximately 25% of the value determined at the surface.

4.3 MICROSTRUCTURAL OPTIMIZATION

Using the optimized coating as described in Section 2.4, finite element models of an equal composition coating were created and the grain size was computationally varied from ~270 nm to 54 nm and the coatings placed under nominal strains from zero to approximately 50%. The maximum von Mises stress in all the materials of the coating versus the percent nominal strain applied is shown in Figure 4.8 for average grain sizes 270 nm, 135 nm and 54 nm.

From the previous work with 300-600 nm grains and a refined mesh of 125,000 quadrilateral elements, the present work with a reduced mesh and 270 nm grain sizes reports von Mises stresses which are at most 20% higher for the brittle matrix material, which is the most highly stressed constituent in the microstructure. These differences are due to the large stress gradients in between individual grains, the mismatch in material properties, and the nonlinear effects of plasticity and contact intermixed with brittle materials which are treated as elastic without plastic deformations. Quadrilateral elements give a more accurate solution using fewer elements versus an equivalent number of constant strain triangular elements, and thus their use was preferred in the finite element models.

From Figure 4.8 (a)-(c) it is apparent the stress in the coating increases as the grain size decreases. As the grain size decreases, the maximum plastic strains in the ductile phases increase as well. The large stress increase between grain sizes of 270 nm in Figure 4.8 (a) and grain sizes of 135 nm in Figure 4.8 (b) can be explained by analyzing the model in Figure 2.13. From 270 nm to 135 nm, the grain interactions change from predominately

horizontal between grains to both horizontal and vertical interactions. Further, the DLC top layer of the model diminishes greatly in between the two models leading to the effect of the coating microstructure assuming a more dominant role in load bearing. These two effects combined create a stress increase in all phases of the coating.

The coating is more able to withstand higher stresses as the grain size becomes smaller due to the commonly known effect of increasing strength with decreasing grain size (up to a certain minimum grain size). This type of relationship shows that a materials yield stress, σ_Y , is proportional to the inverse square root of the grain diameter, d , as:

$$\sigma_Y \sim \sqrt{\frac{1}{d}} \quad (33)$$

for grain diameters greater than around 10 nm. Examining this form of strength increase versus the stress increase in the matrix phase, where failure and de-cohesion are seen first experimentally (Voevodin and Zabinski 2000; Voevodin and Zabinski 1998; Voevodin *et al.* 2002) and in simulations (Pearson *et al.* 2006; Pearson and Zikry 2009; Pearson *et al.* 2009; Pan *et al.* 2008), shows that the coating strength is increasing at a rate faster than the stress increases as the grain size falls. The normalized effective stress at 50% nominal strain as a function of grain size for the coating and the strength increase given by the relationship in equation (33) are shown in Figure 4.9. The coating normalized effective stress is the average of the four constituents (Au, MoS₂, DLC and YSZ) normalized effective stresses, where the normalized values are the effective stresses divided by the highest stress in the material (found at typically the smallest grain diameter). As can be seen from Figure 4.9, the rate of

strength increase given by the type of relationship in equation (33) is greater than the rate of stress increase in the coating as the grain size decreases. Hence, smaller grain sizes, to the limit of applicability of equation (33) as grain size decreases below 10 nm, will lead to lower wear rates, and this conclusion has been verified experimentally for different material systems (Cho *et al.* 1989; Patscheider *et al.* 2001).

Using the specialized Voronoi tessellation technique reported earlier, the coating microstructure was used to represent matrix reinforcement normal to and parallel with the normal loading direction. Figure 4.10 illustrates the enhanced vertical and horizontal DLC matrix widths. Regions of the matrix, which are within 20° of either horizontal or vertical, are scaled to 1.5 times the original matrix thickness. The original thickness of the matrix material, compared to the original simulations, is reduced slightly to maintain the same composition of DLC in the coating. While the composition remains unchanged, the effective volume fraction of the DLC matrix which is normal to the load, and is load bearing, is changed.

Figure 4.11 illustrates the typical results of these variations in microstructure for the 91 nm grain size models. The maximum effective stress in the brittle coating phases (DLC and YSZ) decreases for matrix widths which are increased in the horizontal direction as in Figure 4.10 (a) and increases for matrix widths which are larger in the vertical direction. Furthermore, the maximum plastic strains in the coating ductile phases (Gold and MoS_2) decrease for increased horizontal width matrices. These results indicate that DLC matrices, which are expanded so as to provide more load support in the normal direction by increasing

the effective volume fraction with respect to the loading would provide a greater wear resistance through decreasing the coating stresses.

Hardness is generally related to wear resistance, and the hardness to modulus of elasticity ratio, H/E , has proven a reliable method of predicting wear susceptibility between material systems (Chromik *et al.* 2006; Holmberg and Matthews 1994; Blau 1997; Leyland and Matthews 2000). Experimental characterization of the nanocomposite films (Baker *et al.* 2007; Chromik *et al.* 2006) has led to a range of H/E ratios from 0.035 to 0.052 (or 494 to 735 based on normalizing H/E by the square root of the grain size where the experimental characterization assumes a 5 nm grain size) as seen in Figure 4.12 (a) based on composition variations. Using the coating simulations, an equivalent H/E ratio can be calculated as follows. The coating modulus can be taken as the average of the coating constituents since the simulations use equal percentages (25%) of each constituent. A J_2 plasticity formulation was used in the simulations, and the hardness is in general for metals equal to three times the yield stress, which is equal to the von Mises stress at yield. Therefore, the hardness of the coating can be approximated by taking three times the average effective stress in the coatings (computed as the volume weighted average of the effective stresses in the individual coating constituents) at 20% nominal strain. Thus, the H/E ratio calculated from the simulations appears as:

$$\frac{H}{E} \approx \frac{3(\sigma_{vm\ DLC} + \sigma_{vm\ MoS_2} + \sigma_{vm\ Au} + \sigma_{vm\ YSZ})/4}{(E_{DLC} + E_{MoS_2} + E_{Au} + E_{YSZ})/4} \quad (34)$$

Figure 4.12 (b) plots the results of the simulated $H/E/d^{1/2}$ calculation for different nanocomposite coating grain sizes. As can be seen, the $H/E/d^{1/2}$ ratio increases as the grain size falls, thus indicating and agreeing with the previous conclusion based on the type of effect in equation (33) that wear resistance of the coating increases with decreasing grain size.

4.4 CONCLUSIONS

Finite element simulations and microstructural models of adaptive nanocomposite coatings were investigated to understand how different ductile and brittle material mechanisms, coating constituents, and toughening and strengthening behavior are affected by indentation and sliding.

Composite mechanics approaches were initially used to compute homogenized modulus predictions for the coatings, and these results indicated a high percentage of voids and a non fully dense coating which was confirmed through microscopy.

In the coating simulations, critical regions, which are associated with an accumulation of stresses and strains, generally occurred at interfaces between the ductile constituents and the DLC matrix. The computational results indicate that increasing the relative percentage of MoS₂ results in higher stresses in the coating compared with increasing the relative percentage of gold. These results underscore a competition between the effects of superior tribological properties associated with MoS₂ and maintaining manageable stress levels that would not exceed the coating strength. The highest rates of stress increase were seen to occur in the coating when plastic deformation began in the substrate.

The grain size was computationally varied from 300 to 54 nm and the results indicated the stress in the coating increases as the grain size decreases. A Hall-Petch analysis shows that the coating strength is increasing at a rate faster than the stress increases as the grain size falls, hence leading to the conclusion that smaller grain size will reduce wear.

The DLC matrix dimensions were expanded in the vertical and horizontal directions to determine the effect of changing the effective volume fraction of DLC in these directions while leaving the net coating composition unchanged. The results indicate that DLC matrices, which are expanded so as to provide more load support in the normal direction by increasing the effective volume fraction with respect to the loading, would provide a greater wear resistance through decreasing the coating stresses.

Computational predictions of H/E were performed, and the results indicated again that the wear resistance of the coating increases with decreasing grain size.

In sliding simulations, the computational analyses indicate that the presence of MoS₂ and Au resulted in approximately 15% of the initial energy dissipation through plastic work. This rate decreased by an order of magnitude as the number of sliding trips increased. For the Au phases, the plastic work was lower in comparison with the MoS₂, but these ductile phases essentially dissipate the applied energy associated with sliding, and also toughen the nanocomposite coating.

Sliding over the same area, but in an opposite direction, induces different maximum stresses in the DLC matrix borders depending on the orientation of the border with respect to the sliding. The coating could be optimized for sliding direction in some cases by orienting the angle of the matrix borders to be predominately in the sliding direction.

The highest stresses are located in the interior of the coating, and do not occur at the surface where the predominant wear occurs. It is believed the subsurface plastic deformations from the high stresses weaken the coating and increase its susceptibility to wear

and fracture at the surface. A fracture analysis revealed that the coatings could withstand the applied Mode I tensile stresses in the wake of a sliding indenter so long as the friction coefficient remains low and steady due to the toughening provided by the ductile materials.

4.5 TABLES AND FIGURES
(CHAPTER 4)

Table 4.1: Coating composition and predicted homogenized coating modulus using the composite mechanics approach and the composite mechanics rule of mixtures. Percent difference between the two methods also indicated. Moduli greater than 200 GPa in red, in between 175 and 200 GPa in orange, in between 150 and 175 GPa in purple and less than 150 GPa in blue.

Composite Mechanics Rule of Mixtures (ROM)	Composite Mechanics Representative Volume Element (RVE)	Percent Difference between RVE and ROM	Volume Fraction Gold	Volume Fraction MoS ₂	Volume Fraction YSZ	Volume Fraction DLC
<i>E</i> (GPa)	<i>E</i> (GPa)	(%)	(%)	(%)	(%)	(%)
222	183	19	25	25	25	25
180	156	14	35	25	25	15
209	163	25	35	25	15	25
220	176	22	35	15	25	25
167	135	21	45	25	15	15
178	152	16	45	15	25	15
207	160	26	45	15	15	25
164	140	16	55	15	15	15
124	126	1	55	25	15	5
175	148	17	55	5	25	15
193	142	31	55	15	5	25
264	212	22	15	25	25	35
262	212	21	25	15	25	35
251	192	27	25	25	15	35
304	249	20	15	15	25	45
293	229	24	15	25	15	45
291	230	23	25	15	15	45
333	267	22	15	15	15	55
320	245	27	25	15	5	55
335	269	22	5	25	15	55
344	288	18	15	5	25	55

Table 4.1 Continued

Composite Mechanics Rule of Mixtures (ROM)	Composite Mechanics Representative Volume Element (RVE)	Percent Difference between RVE and ROM	Volume Fraction Gold	Volume Fraction MoS ₂	Volume Fraction YSZ	Volume Fraction DLC
<i>E</i> (GPa)	<i>E</i> (GPa)	(%)	(%)	(%)	(%)	(%)
224	181	21	15	35	25	25
211	163	26	25	35	15	25
182	157	15	25	35	25	15
213	166	25	15	45	15	25
184	159	15	15	45	25	15
171	142	19	25	45	15	15
173	147	16	15	55	15	15
131	127	3	25	55	15	5
186	160	16	5	55	25	15
202	157	25	15	55	5	25
235	206	13	15	25	35	25
233	195	18	25	15	35	25
193	171	12	25	25	35	15
206	188	9	15	25	45	15
246	209	16	15	15	45	25
204	185	10	25	15	45	15
217	200	8	15	15	55	15
175	172	2	25	15	55	5
219	202	8	5	25	55	15
257	233	10	15	5	55	25

Table 4.2: Locations and magnitudes of maximum effective stress in each nanocomposite coating with the refined mesh and 300-600 nm grain size under 20% nominal strain. Subscripts indicate coating chemical composition by volume.

Coating	Coating $\sigma_{Eff, Max}$ (MPa)	Coating $\sigma_{Eff, Max}$ Location	Maximum effective stress (MPa) within each material		
			Gold	MoS ₂	DLC
(C) _{1.00}	510	<i>surface</i>	--	--	510
(Au) _{1.00}	205	<i>surface</i>	205	--	--
(MoS ₂) _{1.00}	288	<i>surface</i>	--	288	--
(YSZ) _{0.25} Au _{0.25} (MoS ₂) _{0.25} C _{0.25}	653	<i>interior</i>	154	238	653
(YSZ) _{0.25} Au _{0.25} (MoS ₂) _{0.25} C _{0.25} - <i>Elastic</i>	520	<i>interior</i>	119	368	520
(YSZ) _{0.125} Au _{0.50} (MoS ₂) _{0.125} C _{0.25}	613	<i>interior</i>	137	235	613
(YSZ) _{0.125} Au _{0.125} (MoS ₂) _{0.50} C _{0.25}	1060	<i>interior</i>	141	244	1060
Steel substrate (no coating)	~300	<i>interior</i>	--	--	--

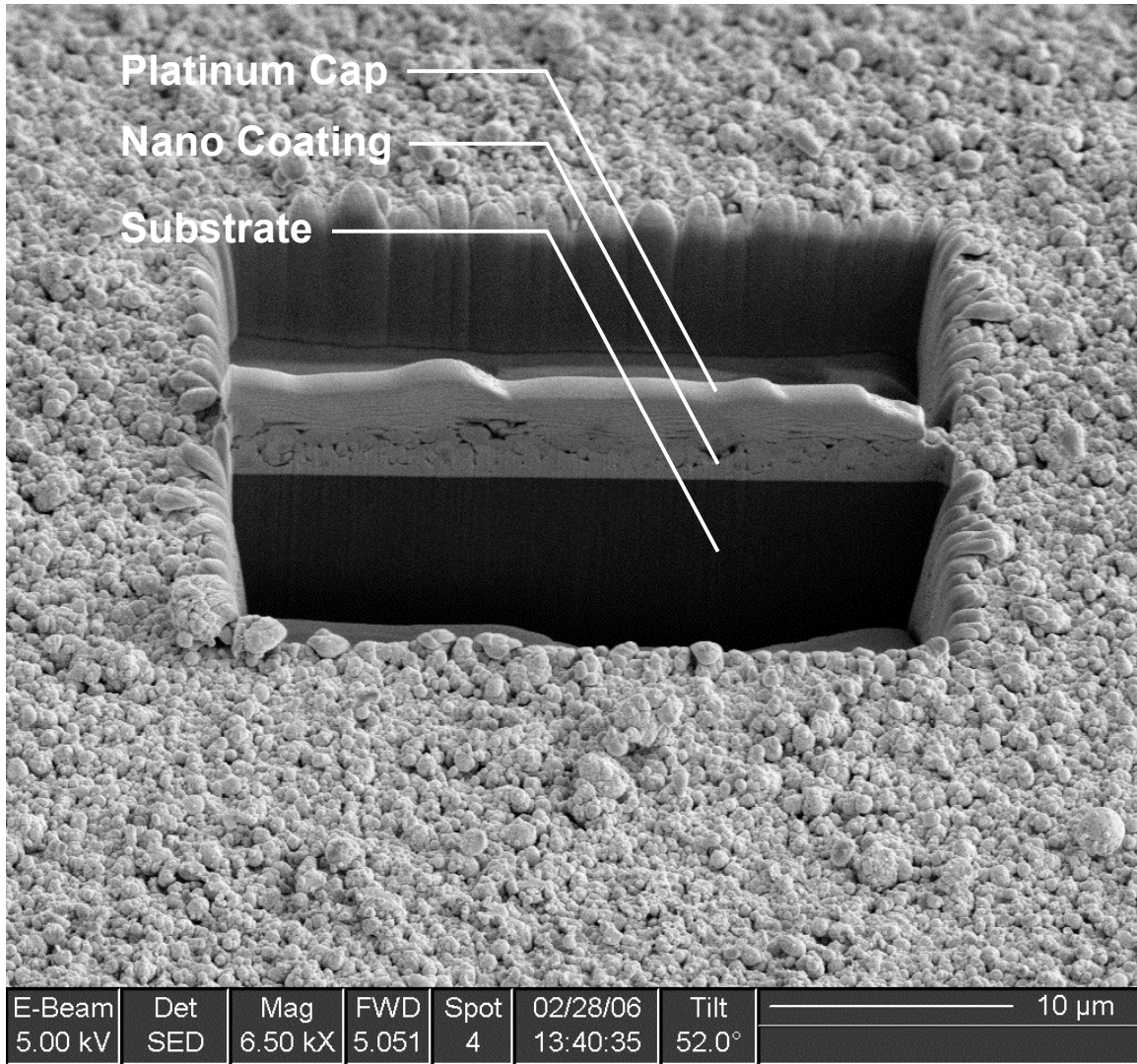
Table 4.3: Nominal strain at the start of plastic deformation in the steel substrate with and without thin film coatings with 300-600 nm grain size and refined mesh. von Mises effective plastic strain in each ductile phase present at 56% nominal strain.

Coating	Nominal Strain (%)	Steel Plastic Strain (%)	Coating Plastic Strains (%)		
			Gold	MoS ₂	Titanium
Steel Substrate (no coating)	12.6	0.580	-N/A-	-N/A-	-N/A-
(YSZ) _{0.25} Au _{0.25} (MoS ₂) _{0.25} C _{0.25}	31.4	0.088	0.129	0.251	0
(C) _{1.00}	31.4	0.088	-N/A-	-N/A-	0
(MoS ₂) _{1.00}	32.6	0.086	-N/A-	1.196	0
(Au) _{1.00}	31.4	0.089	2.100	-N/A-	0
Homogenized Properties	33.7	0.085	Film Plastic Strain: 1.918		0

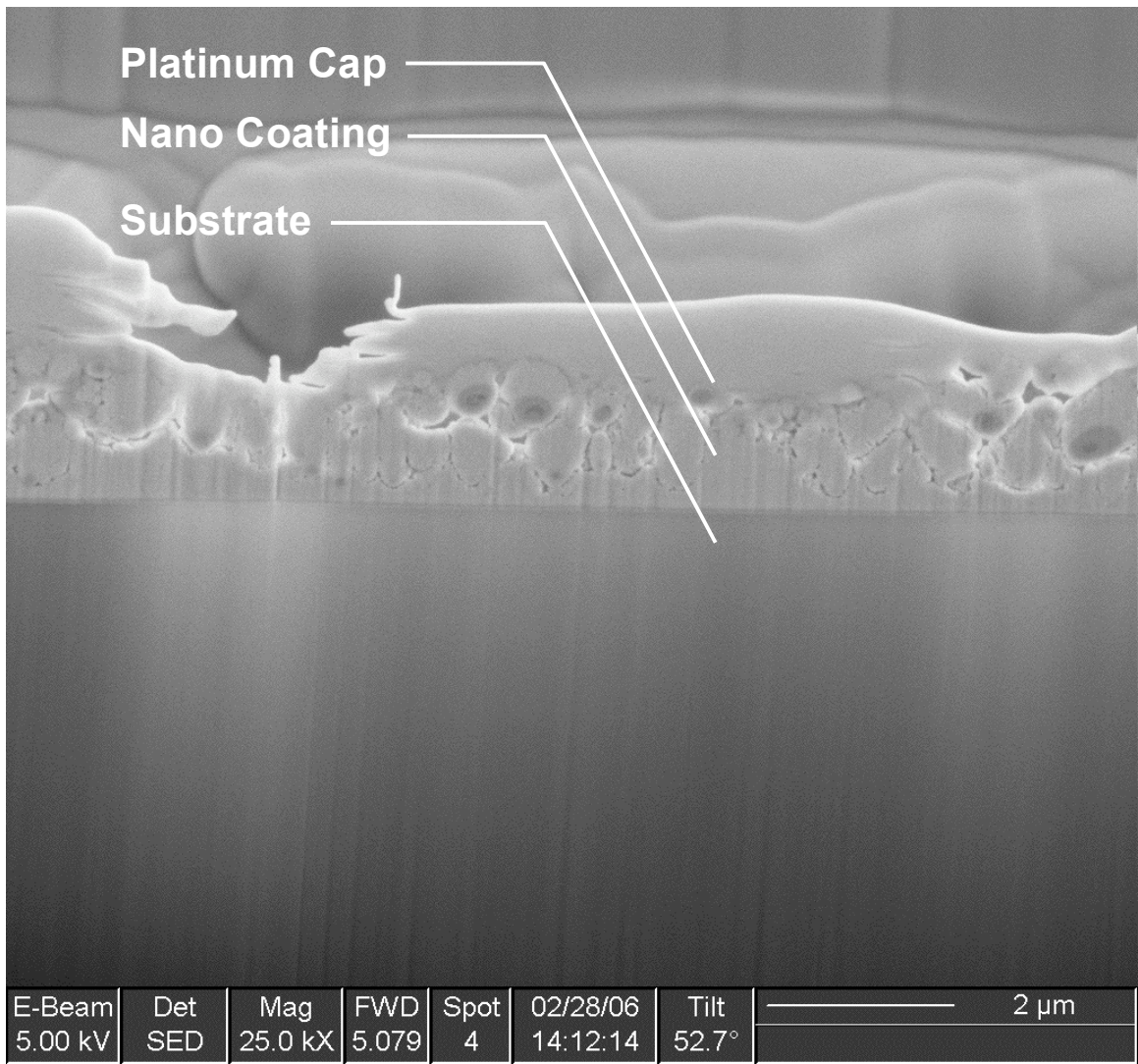
Table 4.4: Fracture toughness, K_{IC} , of DLC matrix material in $\text{MPa}\sqrt{\text{mm}}$. Surface energy, γ^* , of coating constituents in mJ m^{-2} .

Measurement	Fracture Toughness
Surface Flaw, $Q^* = 1$, Equation (31)	1.98
Nastasi <i>et. al.</i> 1999	3.19×10^{-4}
Hou and Gao 2001	$3.1 \times 10^{-5} - 7.1 \times 10^{-5}$
Li and Bhushan 1999	$8.9 \times 10^{-2} - 3.7 \times 10^{-1}$
Irwin Formula:	
Pure • DLC ($\gamma^* = 5400$)	1.64
• Mo ($\gamma^* = 2300$)	8.84×10^{-1}
• Au ($\gamma^* = 1100$)	4.14×10^{-1}
• ZrO ₂ ($\gamma^* = 530$)	4.72×10^{-1}

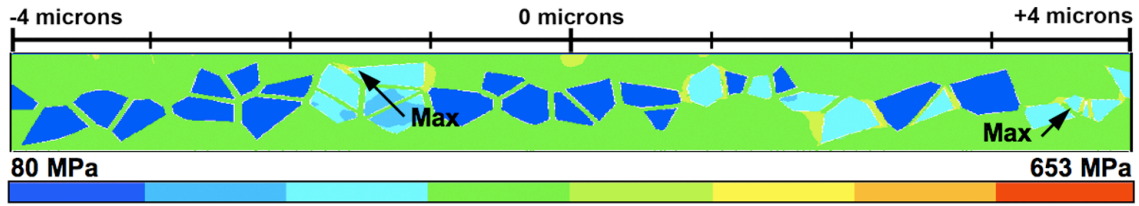
Figure 4.1: SEM images of nanocomposite coating cross-sections taken during FIB cutting of a TEM sample. Magnification in (a) approximately 6.5K times and in (b) 25.0K times.



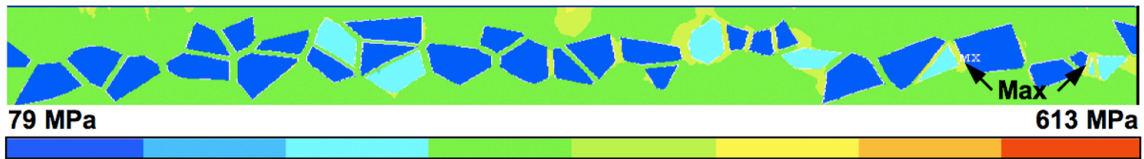
(a)



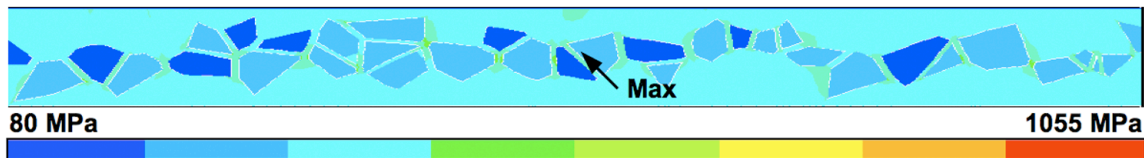
(b)



(a)



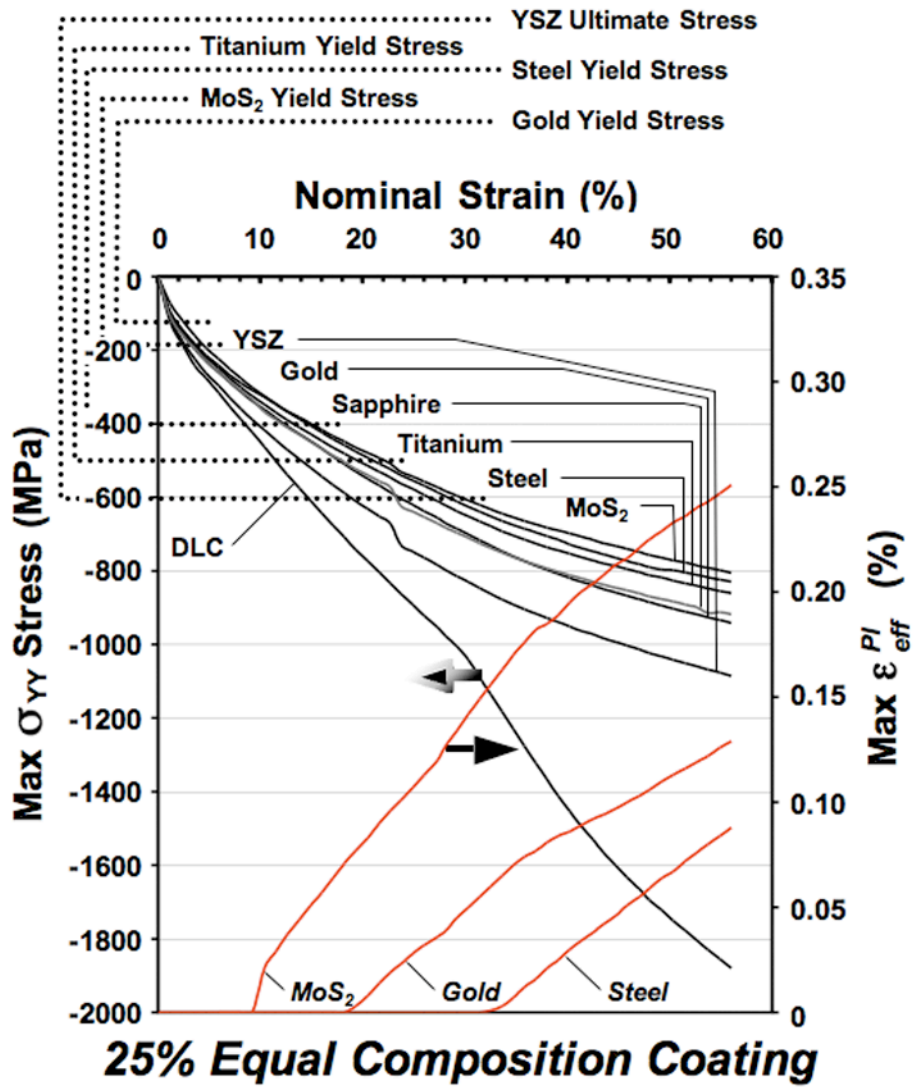
(b)



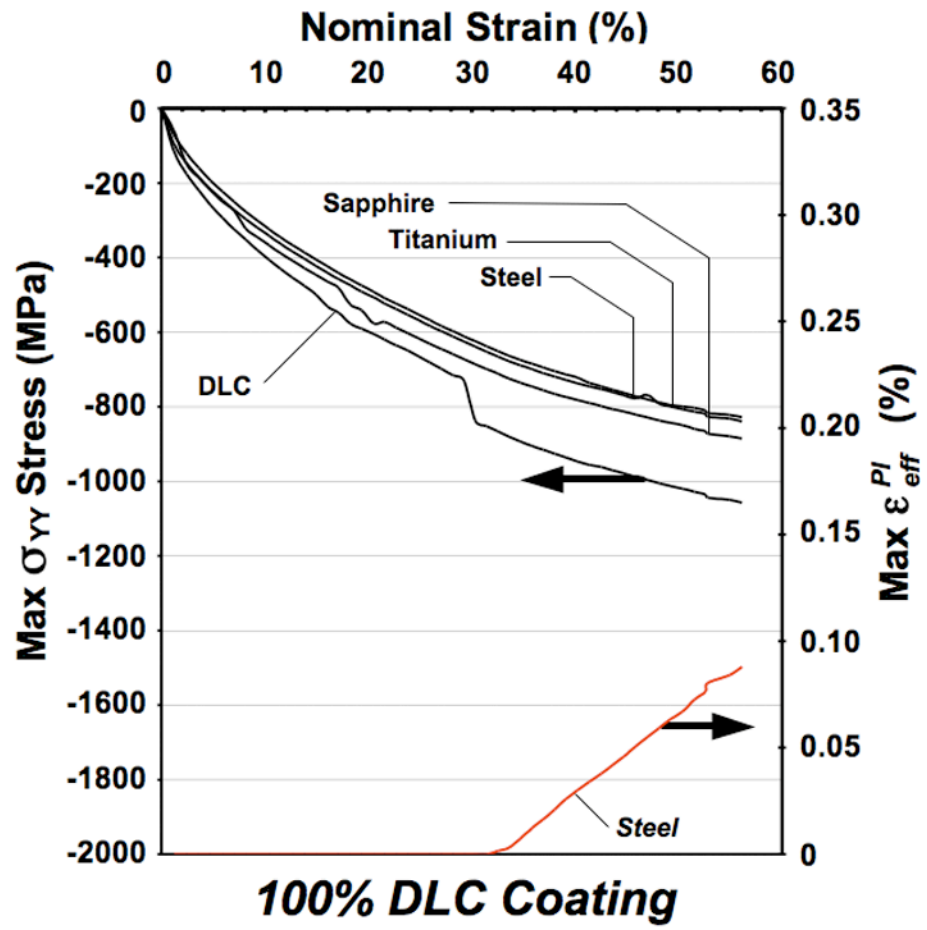
(c)

Figure 4.2: Locations and magnitudes of greatest effective stress for (a) a typical 25% equal composition coating, (b) a 50% gold composition coating, and (c) a 50% MoS₂ composition coating with 300-600 nm grain size and a refined mesh. Distance scale in (a) indicates microns from center of indenter for (a)-(c).

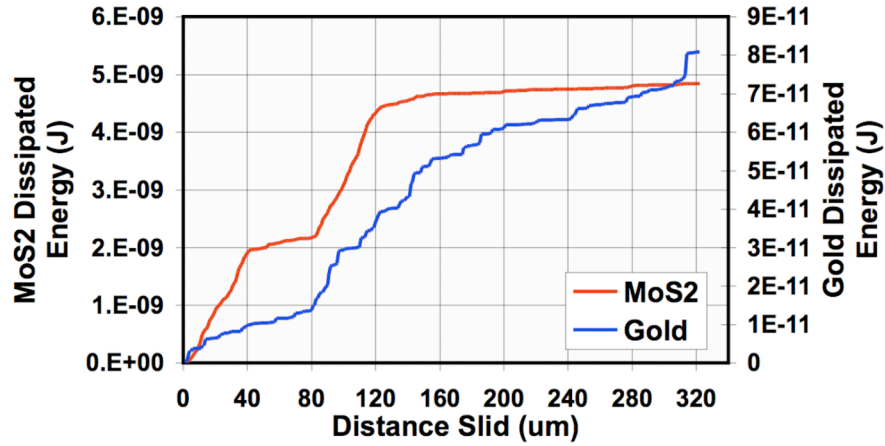
Figure 4.3: (a) Coating maximum normal stress, σ_{YY} , (leftmost ordinate) in each material and effective von Mises plastic strain (rightmost ordinate, materials marked in italics) developed in the MoS₂, gold, and steel phases (no plastic deformation in other remaining materials) for the 25% equal composition nanocomposite. (b) Coating maximum normal stress (leftmost ordinate) in each material and effective von Mises plastic strain (rightmost ordinate, material marked in italics) developed in the steel phase (no plastic deformation in other remaining materials) for a pure DLC coating and titanium interlayer.



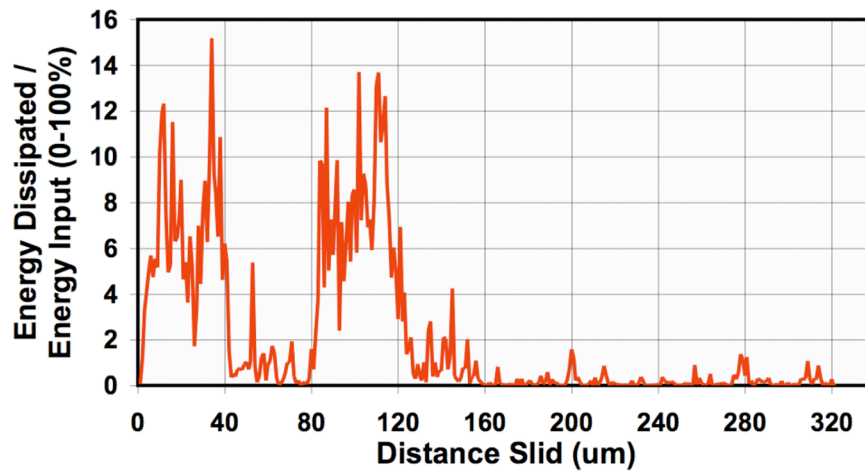
(a)



(b)

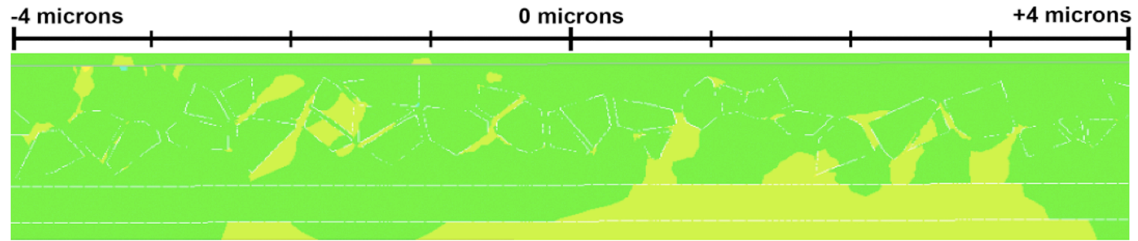


(a)

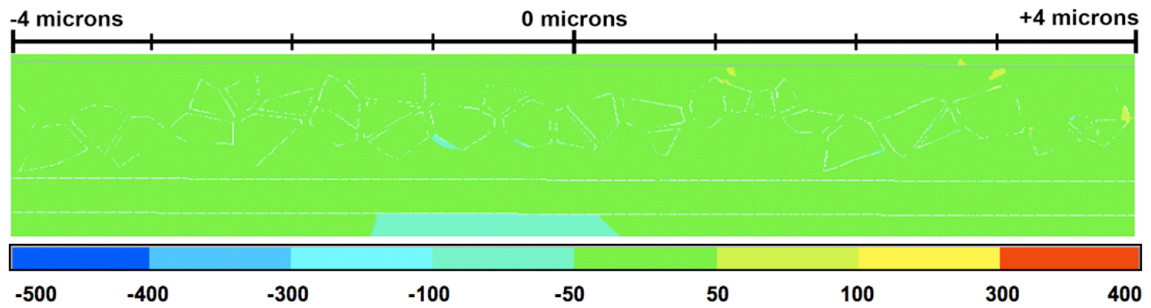


(b)

Figure 4.4: (a) Total energy dissipated (J) through plastic work in the ductile coating phases (Au and MoS₂) versus total slid distance of the indenter for coatings with equal composition and 300-600 nm grain size with refined mesh. Note that gold is measured against the rightmost ordinate and MoS₂ against the leftmost ordinate. (b) Ratio of total energy dissipated via plastic work to the energy input during sliding (in %).



(a)



(b)

Figure 4.5: Shear stress developed under the slider within the same region of coating in (a) the leading edge of the contact and (b) the trailing edge of the contact as the slider passes for the first trip. Stresses are measured in MPa and distances measure distance from center of coating in microns. For equal composition coatings with 300-600 nm grain size and refined mesh.

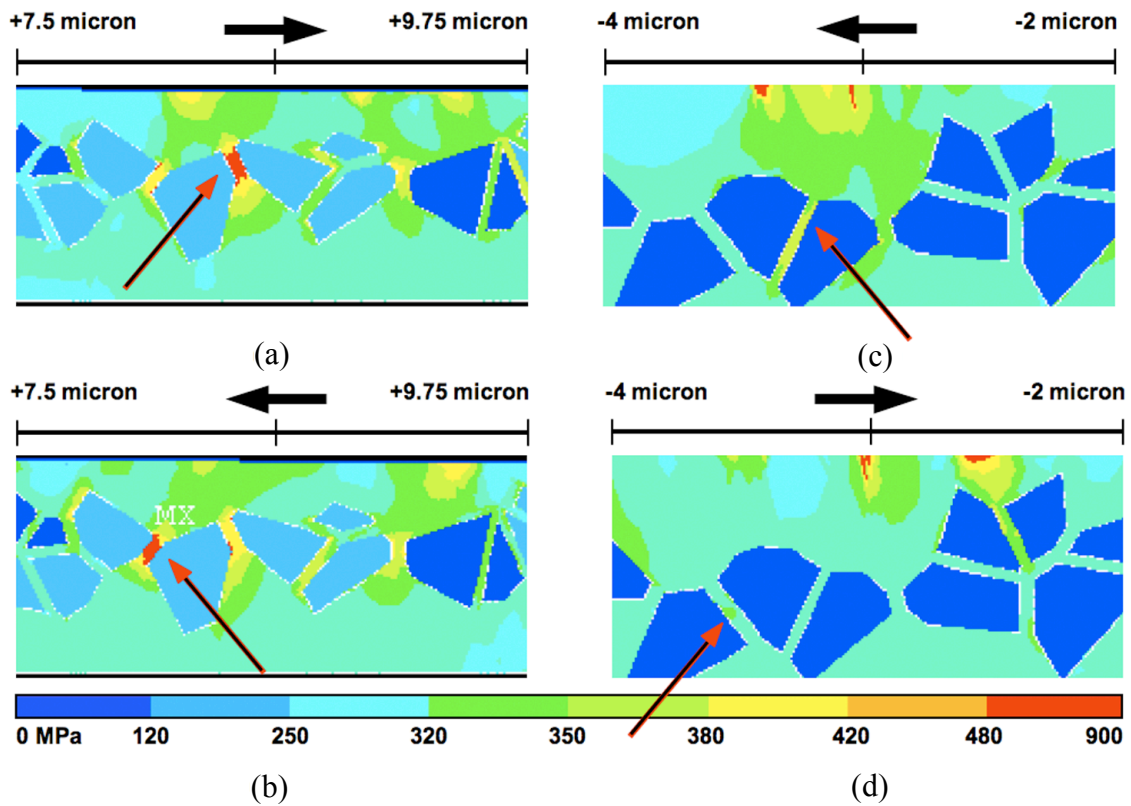


Figure 4.6: Maximum effective stress (MPa) in the DLC matrix material when between (a)-(b) MoS₂ and (c)-(d) Gold inclusions. Slider position in (a) and (b) is at +11 μm from center of coating. Slider position in (c) and (d) is at -5 μm from center of coating. Slider direction of travel is indicated by the arrow in the distance scale for each image. Distance scale indicates position in microns from center of coating. Arrows on figures indicate regions of coating where maximum stresses are dependant upon orientation of border with sliding direction. For equal composition coating with 300-600 nm grain size and refined mesh.

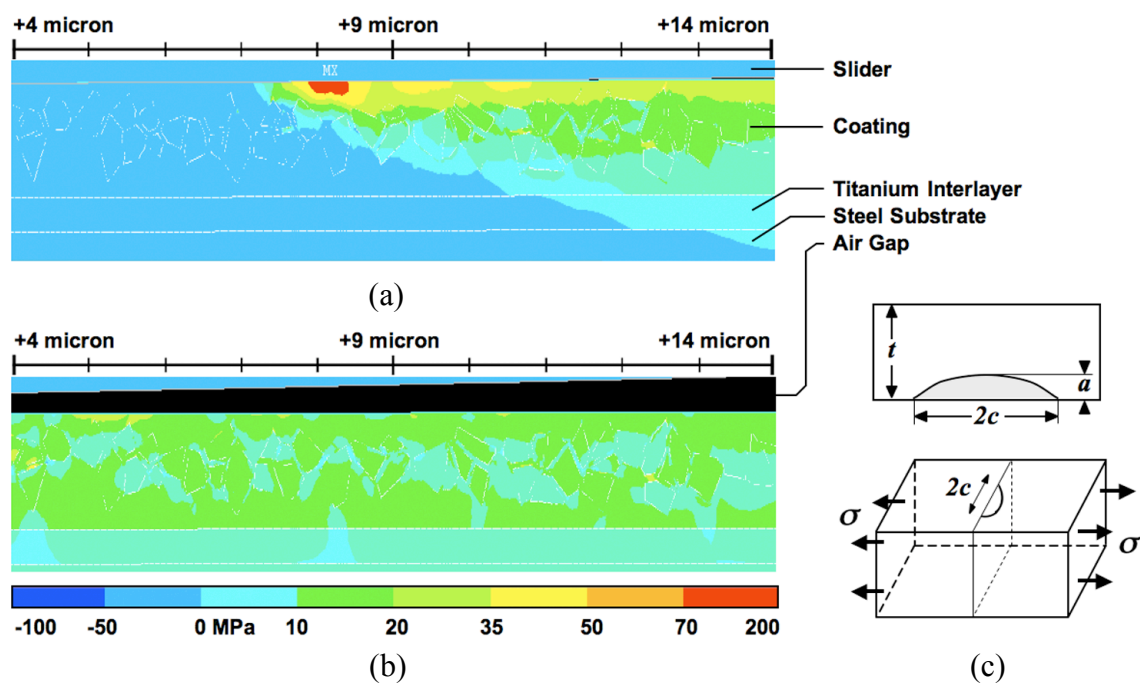
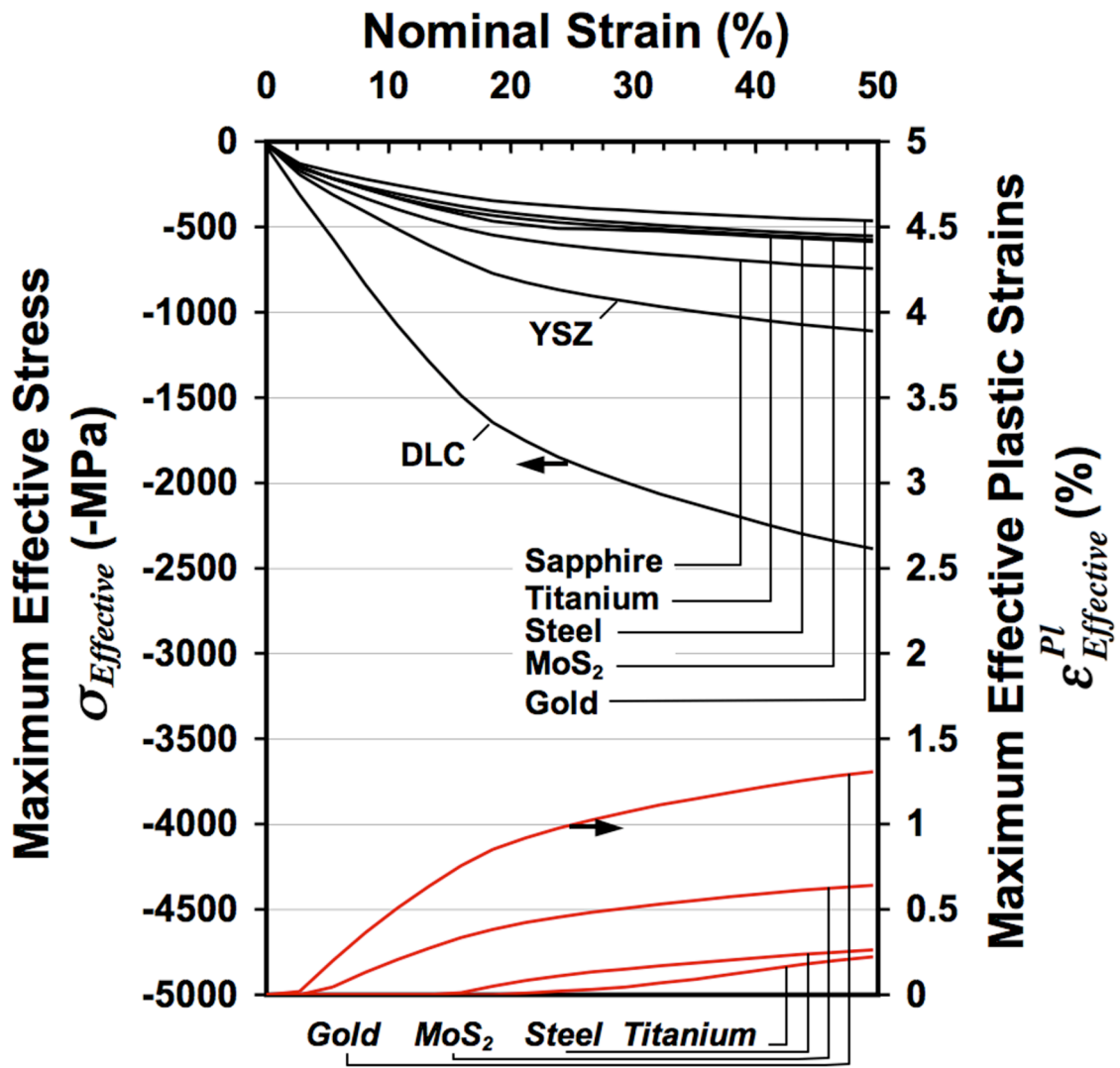
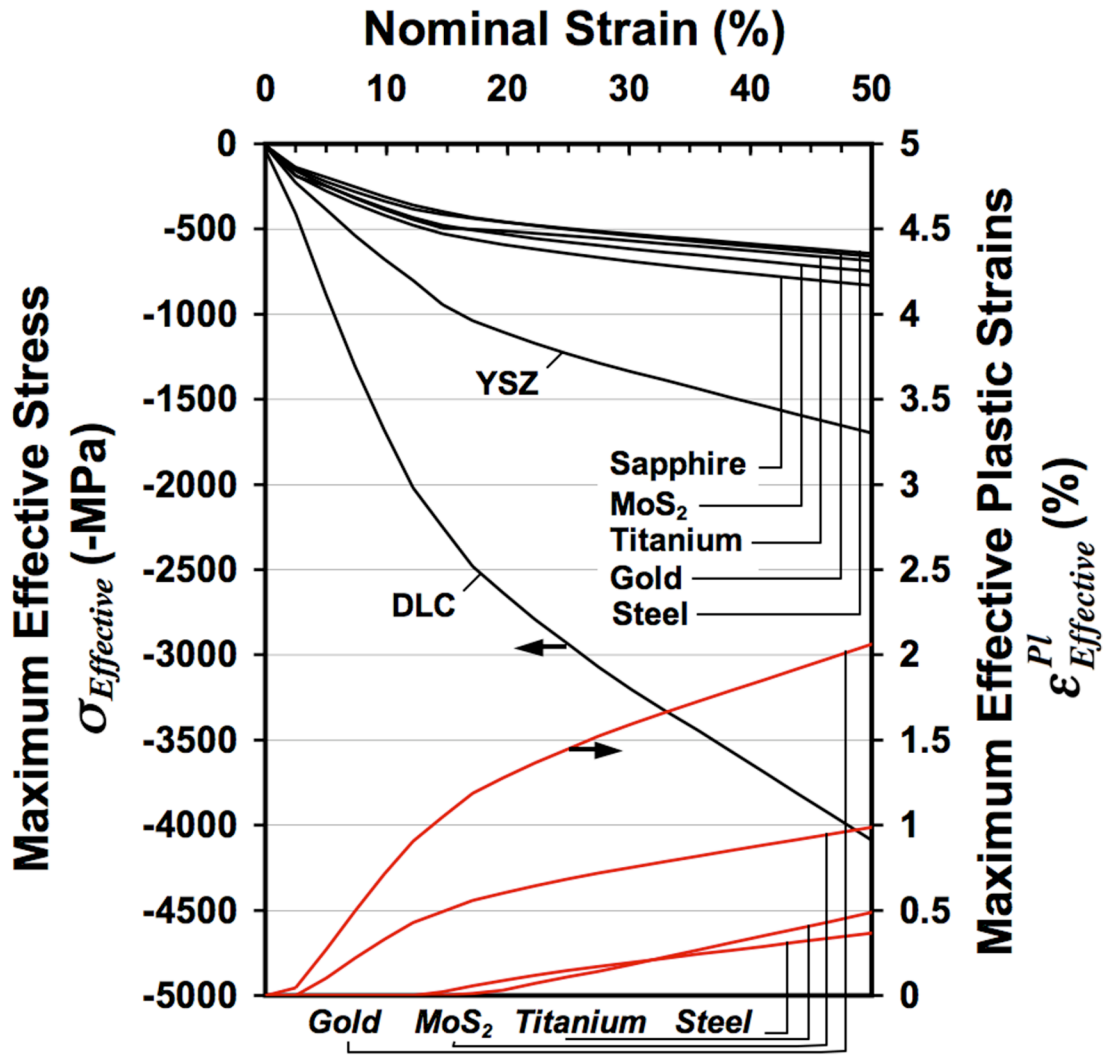


Figure 4.7: In plane tensile stresses (MPa) developed 21 μm behind indenter (a) in the coating material after first sliding pass. In plane tensile stresses developed +60 μm behind indenter (b) after first sliding pass showing the decay and uniformity of the far field tensile stresses. (c) Typical semi-elliptical surface-flaw dimensions. Distance scales in (a) and (b) indicate distance in microns from center of coating. Coating with equal composition and 300-600 nm grain size with refined mesh.

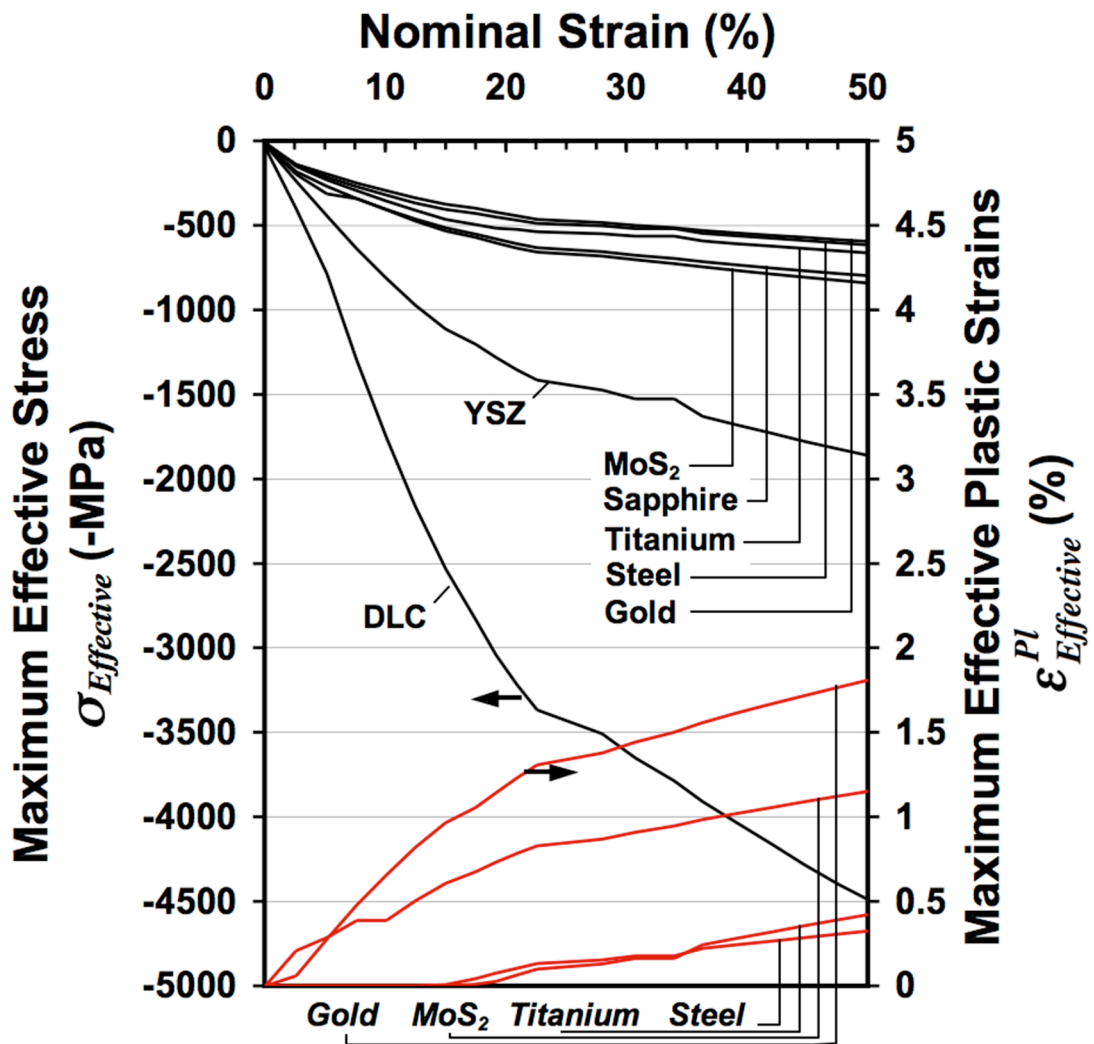
Figure 4.8: Coating maximum effective von Mises stress, (leftmost ordinate, values displayed as opposite sign (negative) of computed positive values) in each material and effective von Mises plastic strain (rightmost ordinate, materials marked in italics) developed in the MoS₂, gold, titanium and steel phases for the 25% equal composition nanocomposite coating using the optimized mesh versus nominal strain for grain sizes (a) 270 nm, (b) 135 nm and (c) 54 nm.



(a)



(b)



(c)

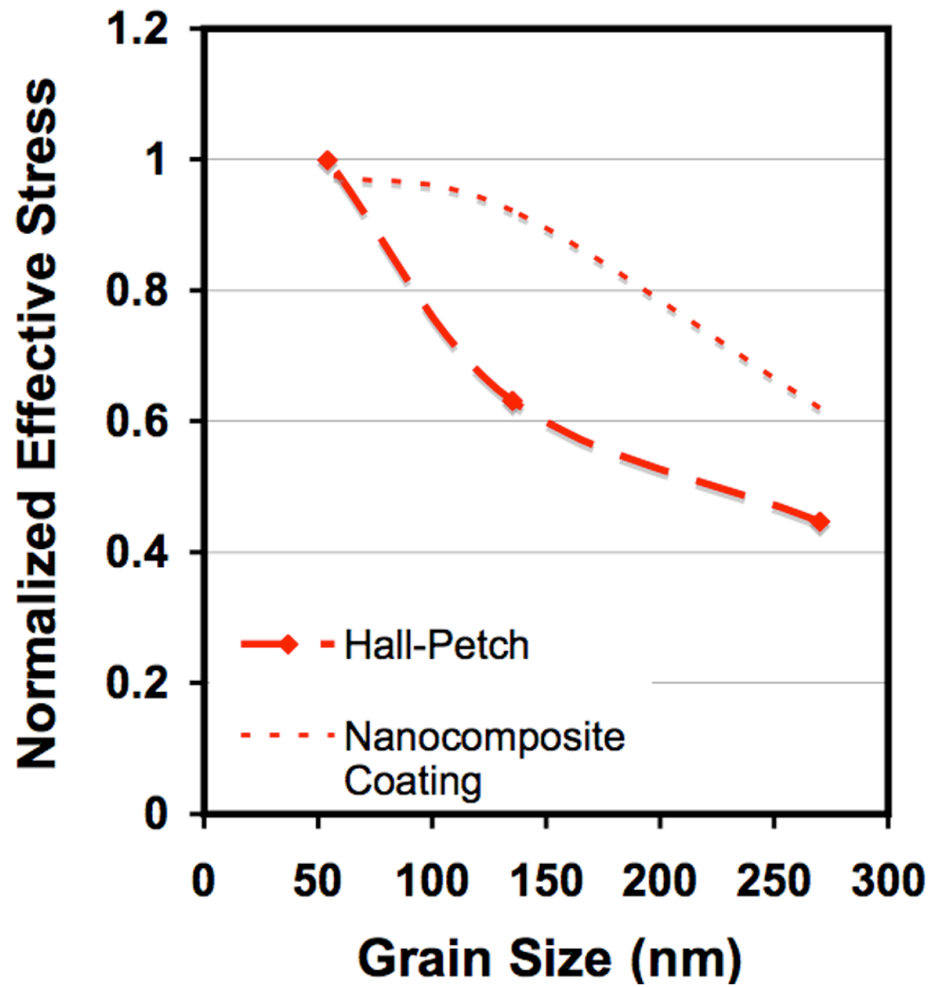
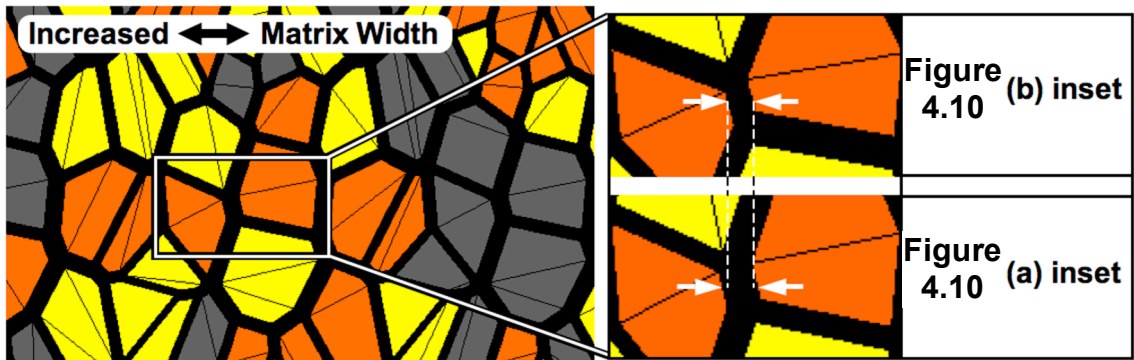
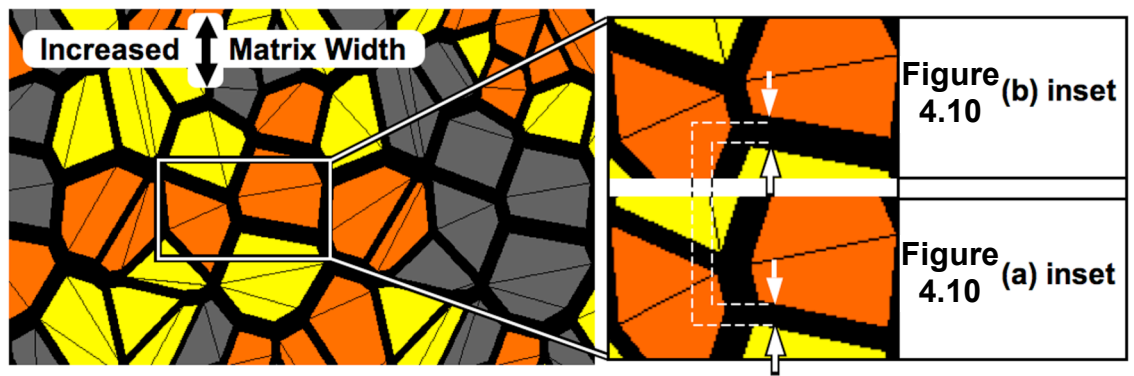


Figure 4.9: Normalized effective stress in the equal composition nanocomposite coating using the optimized mesh from simulations at 50% nominal strain and normalized strength increase based on equation (33) from the Hall-Petch effect as grain size decreases.



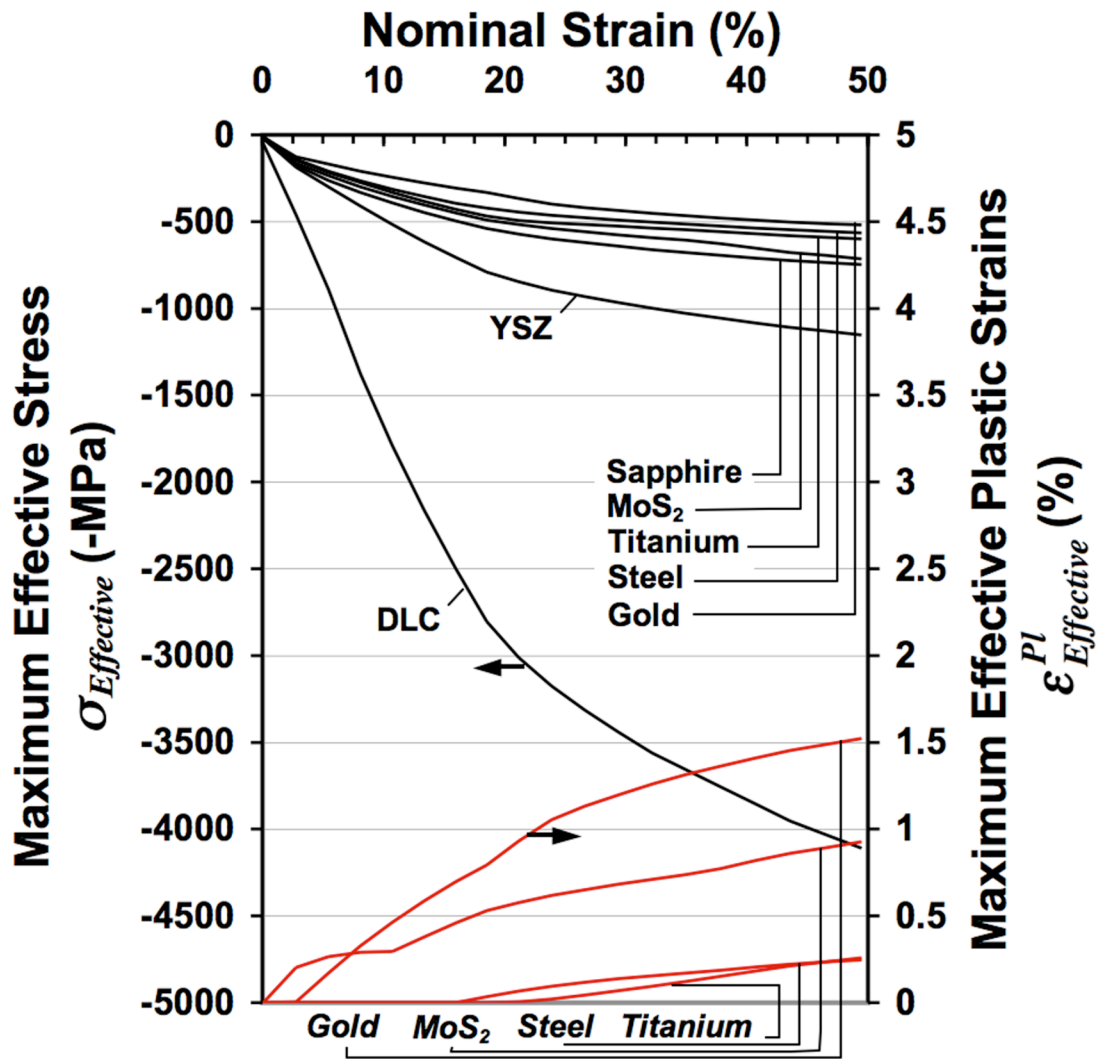
(a)



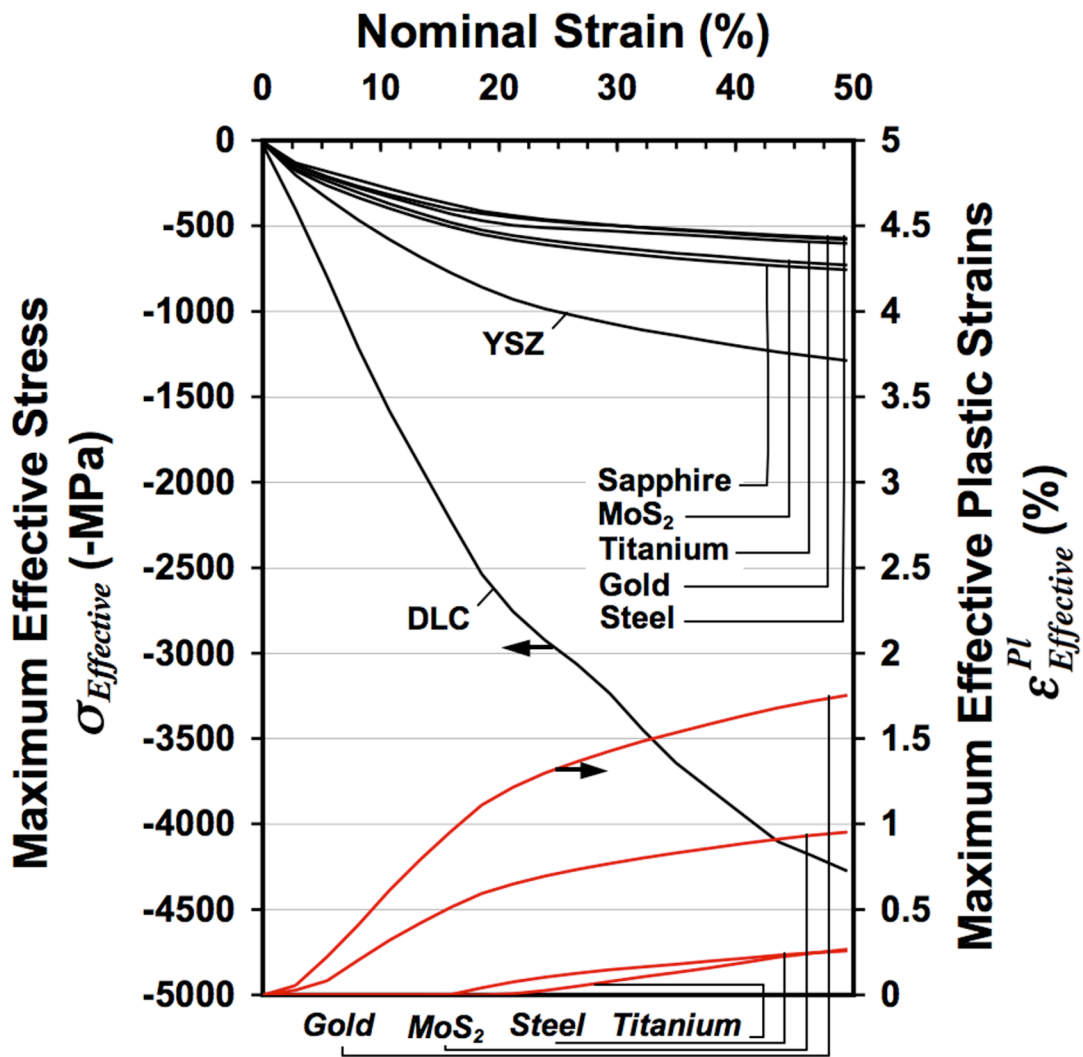
(b)

Figure 4.10: Variation in (a) horizontal and (b) vertical DLC matrix width for a 91 nm grain size nanocomposite coating using the optimized mesh. The loading direction is from the top of the page toward the bottom. Zoom insets in (a) and (b) illustrate matrix thickness variations.

Figure 4.11: Coating maximum effective von Mises stress (leftmost ordinate, values displayed as opposite sign (negative) of computed positive values) in each material and effective von Mises plastic strain (rightmost ordinate, materials marked in italics) developed in the MoS₂, gold, titanium and steel phases for the 25% equal composition nanocomposite using the optimized mesh versus coating nominal strain with grain size 91 nm and expanded DLC matrix in (a) horizontal and (b) vertical directions.

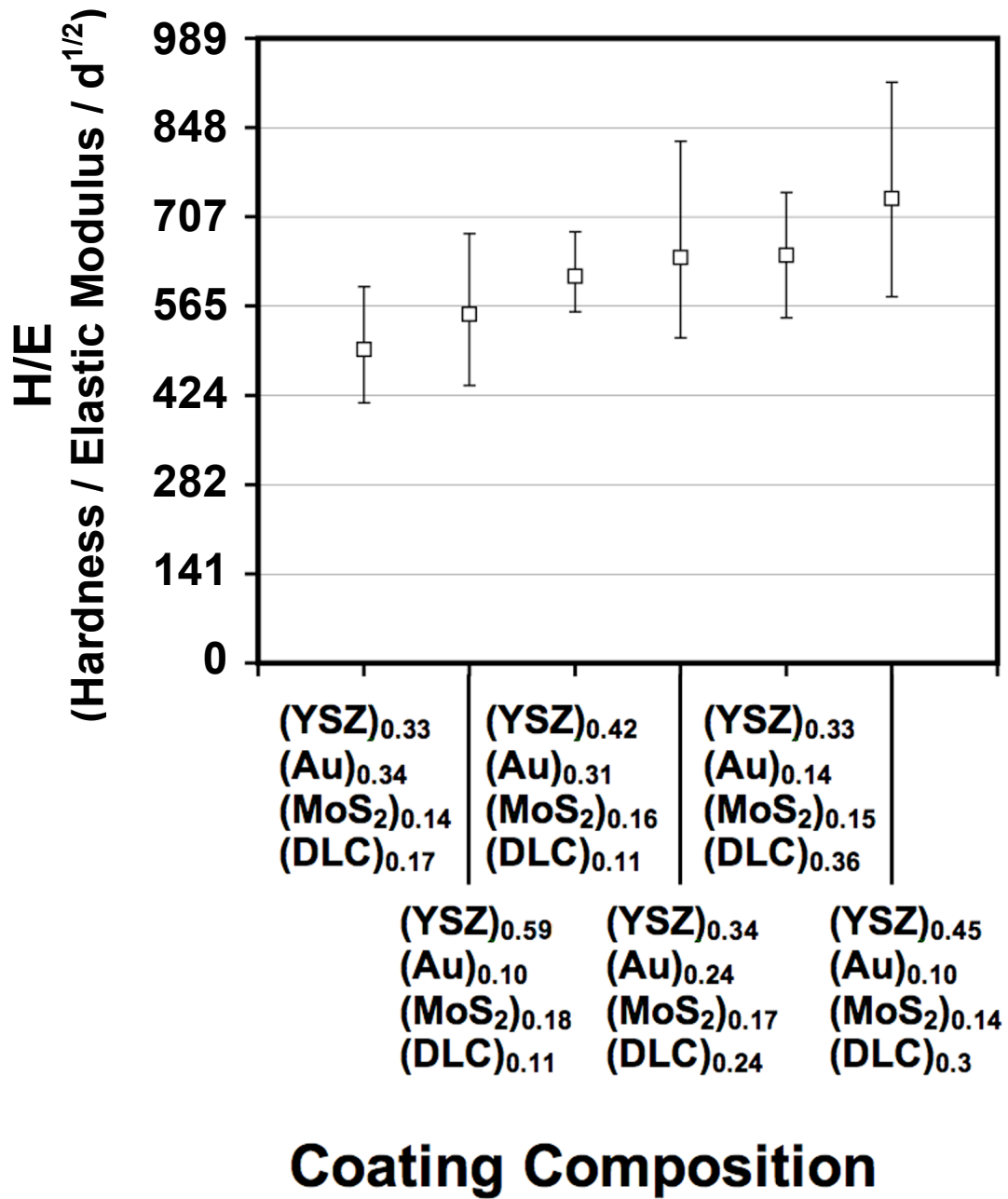


(a)

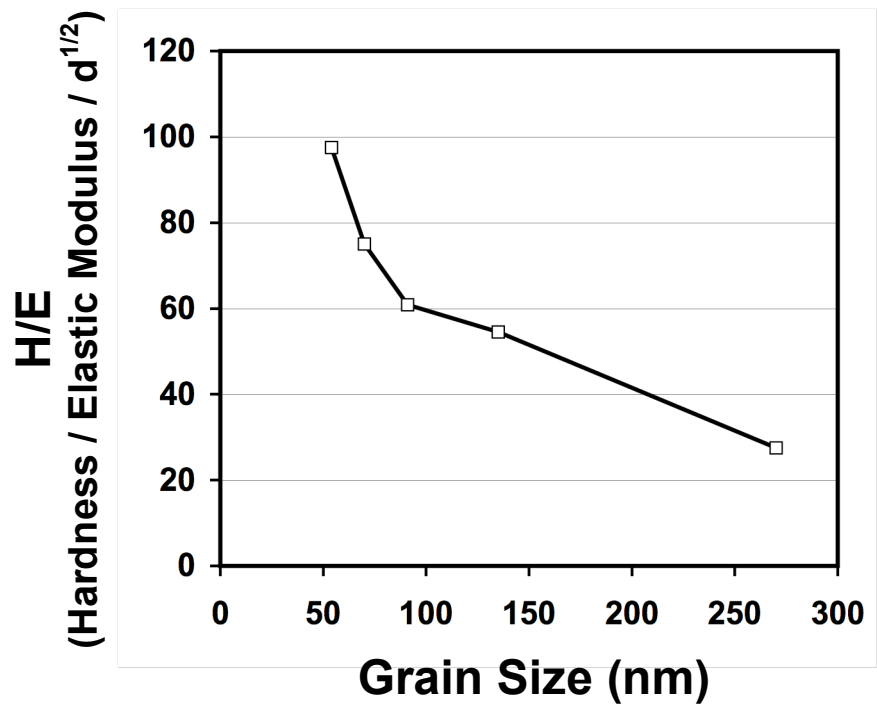


(b)

Figure 4.12: Hardness to elastic modulus ($H/E/d^{1/2}$) for (a) experimental characterization of nanocomposite coatings based on composition (Baker *et al.* 2007; Chromik *et al.* 2006) and (b) computational simulations of nanocomposite coatings based on grain size using the optimized coating mesh. Data in (a) assumes a 5 nm grain size.



(a)



(b)

5. TRANSFER FILM MODELS

Transfer films are third bodies which form in the contact, usually from wear debris, and have been shown to affect the friction coefficient and wear rate for these coatings (Chromik *et al.* 2006; Wahl *et al.* 2008; Dvorak *et al.* 2007). It has been observed that wear increases during friction spikes; this may be due to changes in transfer film adhesion and debris accumulation (Chromik *et al.* 2006). Hence, it is essential to include the effects of these free materials found within the contact. In this analysis, a 200 nm thick homogenized third body was included in the 1 micron thick equal composition nanocomposite coating model with 300-600 nm grains and refined mesh to simulate a uniform transfer film (T.F.) and the coating was then indented to 1.4% nominal strain by the sapphire slider pressing upon the transfer film.

Transfer films are dynamic during wear tests and change in thickness at the transition between low wear and high wear (Chromik *et al.* 2006). The mechanism for adherence of the film to the counterface is also dynamic, and it is not well characterized or understood (Scharf and Singer 2002). For these reasons, the transfer film was modeled as a free third body in the contact in two ways:

- 1) Completely free from adhesion to the indenter (frictional sliding between counterface and T.F. and between the T.F. and the coating) simulating an unstable T.F.; and

- 2) Rigidly bonded to the indenter upon initial contact with frictional sliding between the T.F. and the coating only, simulating a stable, bonded, transfer film.

Both methods represent the interfacial sliding velocity accommodation mode (VAM), which is the most often identified accommodation mode for these coatings (Singer *et al.* 2003). The unstable T.F. model represents the start of the change from interfacial sliding to the interfacial shearing VAM and extrusion of debris. It should be noted that stability here does not refer to the transfer film remaining stable over long sliding distances in the contact region, but rather to the simulated bonding between the T.F. and the counterface.

Both transfer film models were indented to 1.4% nominal coating strain, and the results were compared to determine the effects of bonding on the transfer film and the coating. Results indicate that the stable transfer film has higher stresses for both the coating and the transfer film in comparison with an unstable film (Figure 5.1 (a)). In general, maximum effective stresses in each material are significantly higher in the stable film with the largest increases occurring in the DLC and the transfer film.

For the unstable transfer film, the free third body experiences the highest stress in the model, whereas for the stable film, the highest stress is experienced by the DLC surpassing that of even the transfer film. The stable transfer film has a maximum effective stress 7.6 times greater than the yield stress, and 3.4 times greater than the yield stress for the unstable film. Both films have the highest stresses at the free surface in contact with the coating, but

the stable film has a larger region of high stress on the surface. This region also extends at the periphery upward toward the indenter contact surface (Figure 5.1 (b)-(c)).

Plastic strains are not notable in the steel and MoS₂ at these low loads, and plastic strains accumulate significantly faster in the transfer film than in the coating ductile phases. These results all indicate that stable, or rigidly bonded, transfer films, where the VAM is by definition interfacial sliding, induce stress states that are destructive to both the thin-film coating and the transfer film. These high stresses arising from rigid bonding serve to damage the transfer film and the coating. However, when the transfer film is modeled as a free third body (unstable film) as may happen with a stable transfer film when the stresses grow larger than the adhesion strength of the transfer film to the indenter, the stresses in the film and coating decrease.

Assuming the transfer film constituents (gold, MoS₂, DLC) have higher affinities for adhesion (see Table 4.4 surface energies) to each other than the counterface material (sapphire), these results indicate the following: wear rates are greatest when the transfer film is absent or being removed. In this case, debris from the coating is generated, and from this debris a transfer film begins to form from debris bonding to the indenter. As the current results indicate, this bonding represents the stable T.F., which causes high stresses in the coating and the transfer film. Hence, the T.F. film, which formed on the counterface from debris, is able to increase in size and not be removed due to the rigid bonding, but fails by debonding as a film from the slider due to both high stresses (from bonding) and the greater affinity between T.F. constituents over the sapphire indenter. This transfer film mode now

represents the unstable transfer film model, which results in a reduced state of stress. While this mode reduces the stress and is beneficial to the T.F. and coating, without bonding between the indenter and transfer film, the T.F. will eventually be transported and worn away from the contact zone. Thus, the wear cycle is initiated with the generation of new debris. In summary:

- 1) Tribo-chemical bonding due to energy (mechanical pressure, heat and friction) in the contact forms rigid bonds between wear debris and slider, thus developing a T.F. with *stable* bonding.
- 2) Rigid bonding, however, induces higher stresses in the T.F. and leads to eventual debonding of the T.F. (*unstable*). This leads to a competing period of beneficial low wear balanced with gradual loss of the T.F. due to the coupling between lack of bonding with the slider and the mechanical extruding action of the contact.
- 3) The debonded film is eventually worn away (leading to high wear and friction spiking periods) and replaced by new worn debris material from the contact and coating.

Recognizing that transfer films change in thickness at the moments between high and low wear Chromik *et al.* 2006, the thickness of the unstable transfer film was modified and these results are shown in Figure 5.2.

Transfer films were varied in thickness from 100 to 1000 nm and indented to 5% nominal coating strain using the 270 nm grain size nanocomposite coating models with optimized mesh. While the stress in the coating and individual coating materials did not markedly change with variation of the transfer film thickness, the maximum stress in the transfer film itself decreases by 3 times as the thickness increases from 100 to 1000 nm. This is an important conclusion that illustrates measured ‘wear’ could in fact be occurring from increased and decreased loss of the transfer film due to changes in thickness and, thus, stress and that actual loss of material from the coating may be more steady state and independent of the transfer film thickness.

As the transfer film becomes thicker, the onset of plastic strains in the film is noticeably delayed, especially for transfer films equal to or greater than 800 nm in thickness. Furthermore, there appears to be an equilibrium thickness (approached after 700 nm) greater than 1000 nm where any additional change in thickness of the transfer film does not cause a noticeable reduction in stress suggesting that the most beneficial effects of mitigating wear through the presence of a transfer film are limited to and after this thickness. Experimentally it is known that transfer films are more likely to be debonded and extruded from the contact with increasing thickness (Chromik *et al.* 2006), thus a competing system is illustrated in balancing the reduction of transfer film stress and the probability of extrusion and debonding of the transfer film. Comparison with data from experimental tests of the nanocomposite coating in Chromik *et al.* 2006 reveal that the transfer film fluctuates in thickness between 100 and 400 nm thus correlating with the computational results. Computationally it is

predicted that there is an equilibrium thickness which minimizes the internal stress (by becoming more thick) and likelihood of extrusion (by becoming less thick) between 100 and 700 nm. This result is confirmed by the experimental tests on coatings of varying composition.

5.1 CONCLUSIONS

Transfer films are third bodies which form in the contact, usually from wear debris, and have been shown to affect the friction coefficient and wear rate for these coatings. In this study, the bonding and thickness of transfer films were investigated to delineate effects on coating performance.

Transfer film bonding to the indenter was found to dominate the stress distribution within both the coating and the transfer film. Stable adhered films resulted in higher stresses than those for debonded films. Based on these results, the motion in the contact forms this type of film, and tribo-chemical reactions occur which promote bonding of loose debris associated with wear to each other and the slider. These reactions continue until the stresses are too high and the film must delaminate from the slider. This leads to competing periods of beneficial low wear balanced with gradual loss of the TF due to the coupling between lack of bonding with the slider and the mechanical extruding action of the contact. The debonded film is eventually worn away (leading to high wear and friction spiking periods) and replaced by new worn debris material from the contact and coating.

Models of unstable transfer films indicate that stresses in the coating are largely unchanged with changes in the transfer film thickness, while stresses in the transfer film decrease by a factor of three as the thickness increases from 100 to 1000 nm.

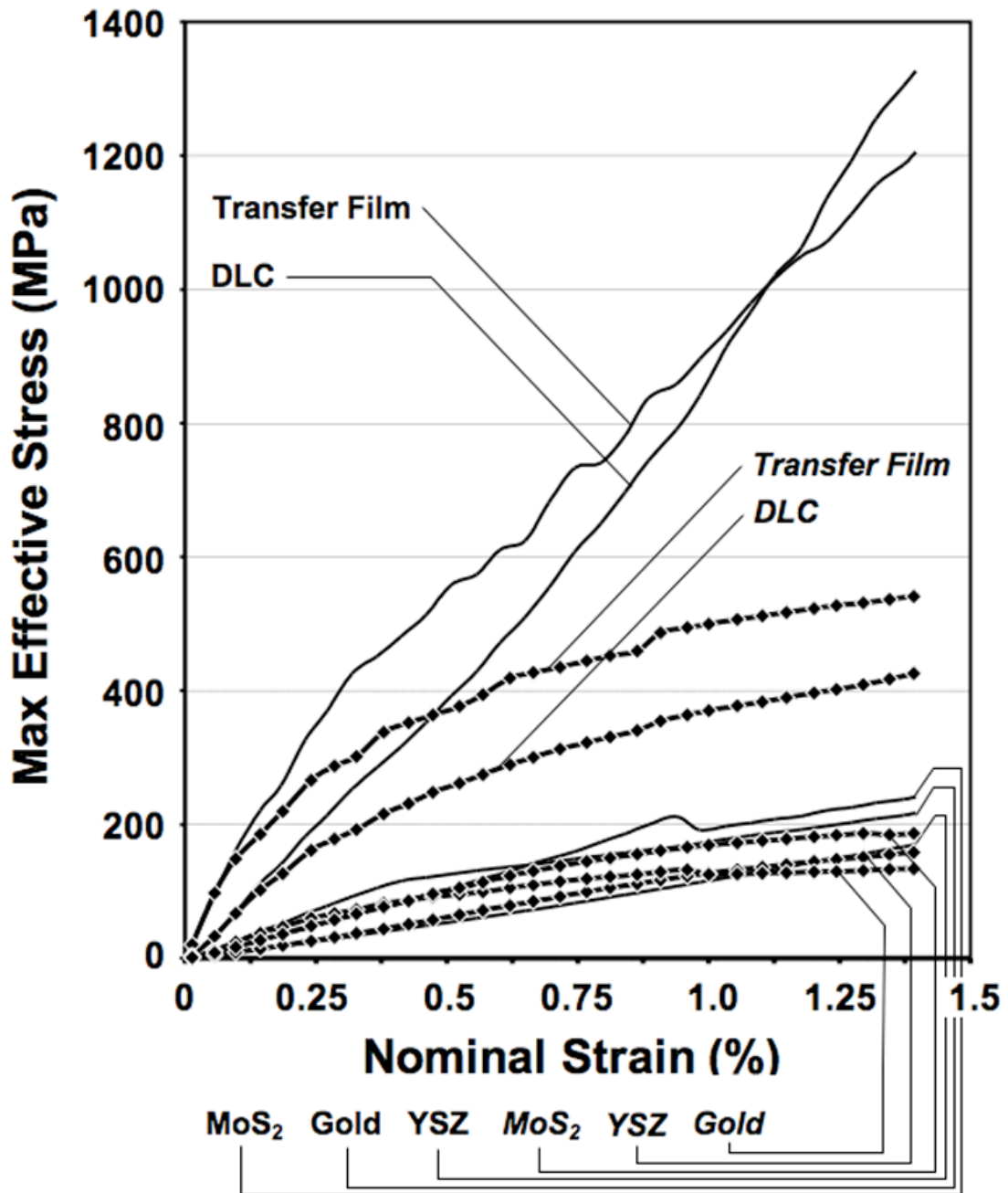
This is an important conclusion that illustrates measured 'wear' could in fact be occurring from increased and decreased loss of the transfer film due to changes in thickness

and, thus, stress and that actual loss of material from the coating may be more steady state and independent of the transfer film thickness.

There appears to be an equilibrium thickness (approached after 700 nm) greater than 1000 nm where any additional change in thickness of the transfer film does not cause a noticeable reduction in stress suggesting that the most beneficial effects of mitigating wear through the presence of a transfer film are limited to and after this thickness. Comparison with data from experimental tests of the nanocomposite coating in Chromik *et al.* 2006 reveal that the transfer film fluctuates in thickness between 100 and 400 nm thus correlating with the computational results. Computationally it is predicted that there is an equilibrium thickness which minimizes the internal stress (by becoming more thick) and likelihood of extrusion (by becoming less thick) between 100 and 700 nm. This result is confirmed by the experimental tests on coatings of varying composition.

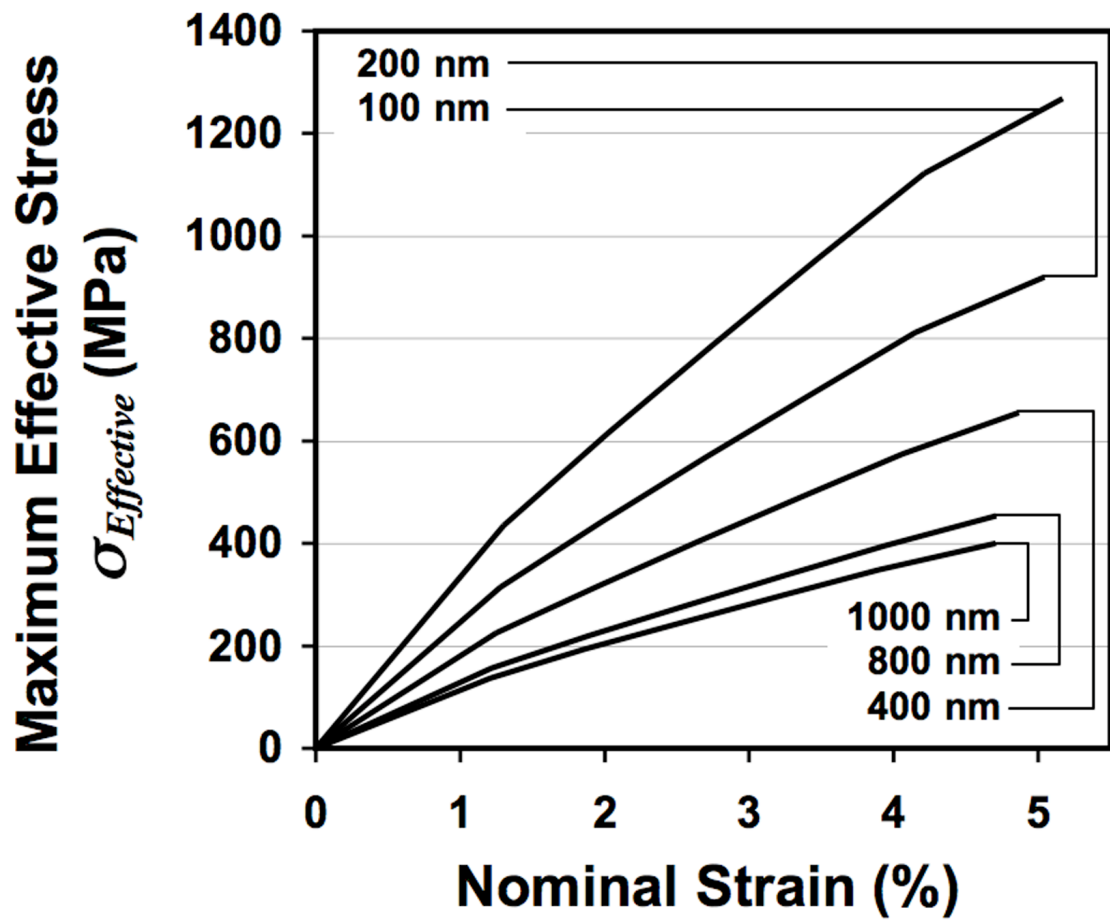
5.2 FIGURES
(CHAPTER 5)

Figure 5.1: (a) Coating and 200 nm thick transfer film maximum effective stress in each material for the 25% equal composition nanocomposite with refined mesh. Stable transfer film results in solid black lines and regular text from highest stress to lowest, Unstable transfer film in bold lines with markers and italicized text from highest stress to lowest. Transfer film effective stress in the central most loaded region under 1.4% nominal coating strain for (b) Stable and (c) Unstable models. Note that above the TF film in (b) and (c) is the indenter and below is the nanocomposite coating.

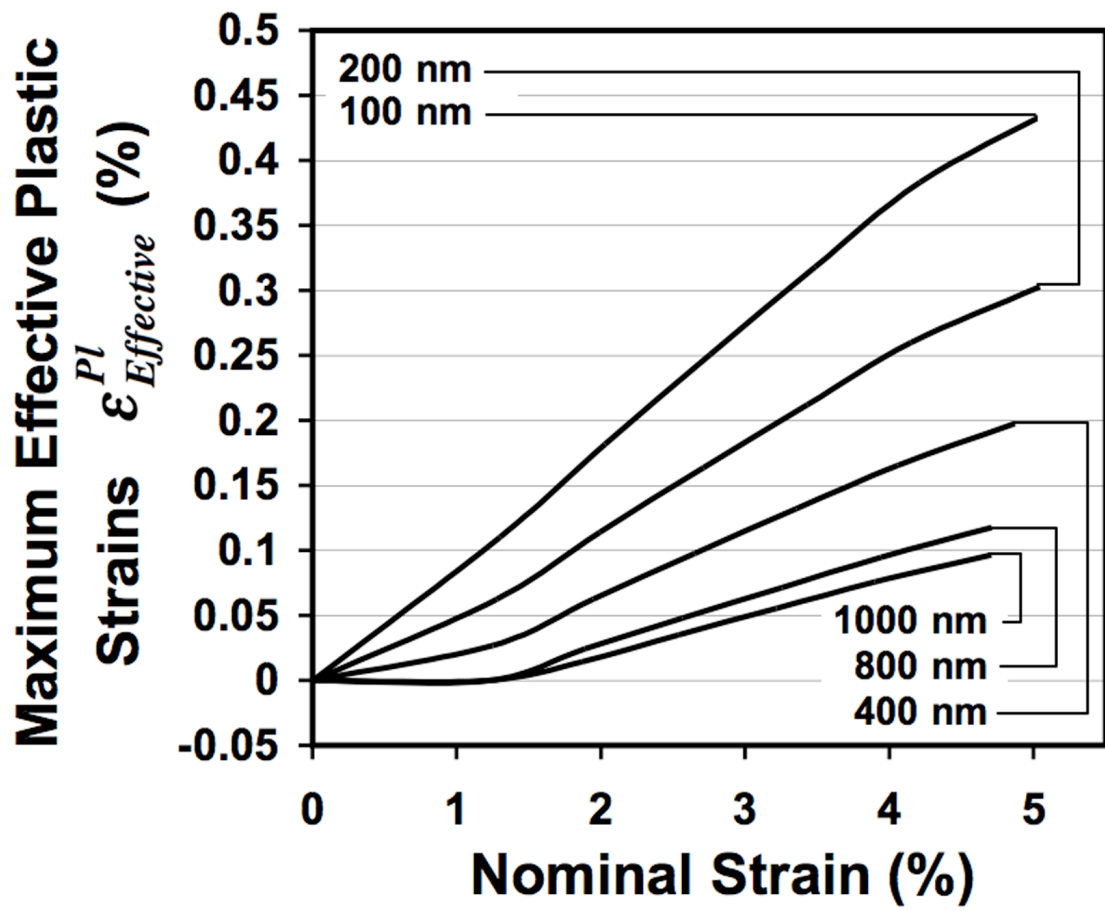


(a)

Figure 5.2: Maximum effective stress (a) and maximum effective plastic strain (b) developed in the unstable transfer film under indentation with change in thickness when indented against the nanocomposite coatings with 300-600 nm grain size and optimized mesh. Transfer film thickness indicated by text in each plot.



(a)



(b)

6. WEAR MODELS

Simulations of wear and failure were conducted using both the 300-600 nm grain size models with refined mesh, as well as the 135 nm grain size models with optimized mesh. The refined mesh models were simulated with explicit contact loads from the indenter at 20% nominal strain loading and the optimized mesh models were used with the RVE approach described in Section 2.1.3 with an applied pressure loading and shear traction at 50% nominal strain. All simulations used an equal constituent composition coating.

These models account for both sliding and indentation. Two different approaches were used to model failure and wear as described in Sections 6.1 and 6.2. The failure of the coating constituents gold, MoS₂, YSZ and DLC were modeled, but the failure of the substrate, titanium interlayer and transfer film were not. In general, both approaches used the same type of criterion for determining whether a material fails or is worn off. For ductile materials (gold and MoS₂) a critical plastic strain criterion was used. When the von Mises plastic strain exceeded a certain value, wear or failure was assumed to occur. For brittle materials (YSZ and DLC), whenever the ratio of the von Mises stress to the elastic modulus of the material exceeded a certain value, wear or failure was assumed to occur.

A more detailed criterion was also investigated for wear. This criterion is based on the material properties of the constituents and is applied individually to each separate material in the coating. It is postulated as:

$$\mathbf{Material\ Wear\ Resistance} = \left(\frac{H}{E}\right)(\epsilon_{Break})(\sigma_{Ult})(K_{IC}) \quad (35)$$

where ϵ_{Break} is the ultimate elongation before rupture, and σ_{Ult} is the ultimate strength before rupture. As can be seen, this criteria depends on the material properties inherent to wear resistance. A higher wear resistance is indicated by a higher value of material wear resistance in equation (35). Using this criterion, we can delineate wear resistance more accurately than the hardness to elastic modulus ratio, H/E , (Zum Gahr 1987). It is particularly useful in instances where materials may have similar H/E ratios, but different wear resistances. The application of this criterion in the computational models was undertaken by applying the first criterion to generate a set of elements which have the potential for failure. The second criterion in equation (35) was then computed for each material type and the inverse taken, thus the materials with the lowest value will have the highest wear resistance. The material with the highest value of the inverse of equation (35) was used to normalize all the materials to the range 0 to 1 with 1 being indicative of the highest wear rate and least wear resistance. The normalized values for each material on the range from 0 to 1 were then treated as a percentage. This percentage was taken as the percentage of elements that experienced failure. The selected set of elements which met the first criterion were multiplied by the percentage (based on material type), and this is the number of elements that were failed in the model. In essence, 100% of the least wear resistant material whose elements can satisfy the first criterion were failed, and a necessarily

lesser percentage of the remaining materials elements, which satisfy the first criterion were failed.

Upon application of the second criterion (after application of the first), it was found that the coatings failure was inhibited in comparison with just using the first criterion. For this reason, in this chapter, only the results of the first criterion are reported on. The second criterion is more useful for vetting individual materials suitability for use in the coating before simulations or experiments are performed.

6.1 ELEMENT FAILURE

Element failure was used for models with 300-600 nm grain size, refined mesh and explicit contact loads for indentations at 20% nominal strain. As the indenter slides across the coating surface, after every one micron of sliding, at a velocity of one micron per second, the first criterion is applied. In the element failure technique, elements, which have exceeded the first criterion are assumed to have failed, where failure is defined as first setting the loads for the elements to zero in the load vector, and then setting the strains to zero for each relevant element. The residual stiffness of the element is reduced to one quarter of the original stiffness, and the simulation continues with the criterion applied again after the next micron of sliding. An element which has failed is not 'failed' again.

The first criterion was applied using a value of 0.55% for the ductile materials critical plastic strain and 0.25% for the brittle materials ratio of the maximum von Mises stress to the constituent elastic modulus. The low value used in this criteria was selected to accelerate the coatings failure computationally without modeling meters of sliding trips which occur in the experimental tests. The results are shown in Figure 6.1 (a)-(g). As can be seen, the failure initiates in the interior of the coating and not at the surface. This result is consistent with previous results reported in Section 4.1 and experimental observations of Ahmed 2002 for tungsten carbide composite coatings. The failure initiates in the DLC matrix material which upon its failure (Figure 6.1 (a)-(c)) and weakening causes the stress and strains in the bordering ductile materials to increase until they also subsequently fail (Figure 6.1 (d)-(g)).

As can be seen in Figure 6.1 (g), the failure in the interior of the coating eventually propagates to the surface after a critical number of elements in the interior of the coating have failed. Thus, internal plasticity and the failure of subsurface elements cause the surface to weaken and become more susceptible to failure as proposed in Section 4.4. Note that these surface elements which fail are predicted to become wear particles and form transfer films.

A separate simulation was run where the first criterion was applied using a value of 1.0% for the ductile materials critical plastic strain and 0.20% for the brittle materials ratio of maximum von Mises stress to elastic modulus. The results are shown in Figure 6.2. As can be seen, the failure also initiates in the interior of the coating and not at the surface. Also, the failure again propagates to the surface (but at a different location in comparison to the results in Figure 6.1) after a critical number of interior elements have failed. The higher plastic strain before failure for the ductile elements leads to a reduced amount of failure of these elements, however the top surface is still made more susceptible to wear due to the failure of the matrix material.

When the reduction of the failed elements moduli is decreased to only seventy five percent of the original modulus instead of one quarter as in the previous simulations, there is little change in the failure patterns as shown in Figure (6.3). In this figure, the failure pattern from the simulation after 4 microns of sliding with a criterion of 1.0% for the ductile materials critical plastic strain and 0.20% for the brittle materials ratio of maximum von Mises stress to elastic modulus was repeated using a reduction of elastic modulus to either

25% (Figure 6.3 (a)) or 75% (Figure 6.3 (b)). As can be clearly seen, the results are very similar. This indicates that any weakening, whether by 25% or 75%, of interior elements leads to large increases in stress and strain in neighboring elements, which accelerates the failure process. The model with higher reduction in elastic modulus of failed elements has slightly more failure locations in comparison with the model with a lesser reduction in failed element moduli. When the elastic modulus reduction is 50%, the results are similar to the results for a reduction to 75% of the elastic modulus.

6.2 MATERIAL TRANSFER TECHNIQUES: CHANGE OF MATERIAL CONSTITUENTS

A scheme to change the material constituents to transfer films for the models with 135 nm grain size, optimized mesh and pressure and shear tractions is proposed to accurately model wear and failure. As pressure loads translate across the coating surface after every increment of translation, the first criterion is applied. With this technique, using the RVE approach allows sliding trips of over 350 microns to be simulated along with 10 passes (or trips) of the loading over the same coating area. In the proposed scheme, elements that have exceeded the first criterion are converted into transfer film material and left in place in the coating. An element, which has been changed to transfer film, is not changed again.

This technique differs from the first in that the load vector and element strain are not set to zero after failure and the material is changed to transfer film. Also, all elements which failed have the same material constituent properties (of the transfer film) after failure.

To implement this scheme, a restart of the model is involved since the material properties are evolving at each load increment. This was achieved by first applying the failure criterion, converting elements to the transfer film, and then restarting the model. On the restart, the previous nodal displacements from the deformed geometry at the end of the last simulation were applied as displacement boundary conditions. The simulation was then solved to regenerate the identical plastic strains and loads as were present before the restart, which in essence accounts for residual strain effects. The next increment of sliding and

translating loads was then applied and the displacement boundary conditions were deleted to allow the system to deform under the new loads.

Using this technique, simulations, where the applied criterion for failure was set at 0.1% for the ductile materials critical plastic strain and 0.05% for the brittle materials ratio of maximum von Mises stress to elastic modulus, resulted in nearly complete conversion of the coating to a transfer film within 2 sliding trips as shown in Figure 6.4. This is to be expected from the results of Section 6.1 given the low magnitude of the failure criteria used. When the criteria is increased to 0.6% for the brittle materials, then elements that converted to a transfer film are only the ductile elements as shown in Figure 6.5. At these levels of the failure criterion, 17% of the gold and MoS₂ converted into the transfer film material. With this lack of brittle material conversion to a transfer film, if the ductile conversion criteria is increased to the range 1.75% to 4% plastic strains, then no conversion of the coating would occur, and the failure criterion would never be exceeded.

A more realistic criterion for the coating failure is approximately 2% for the ductile materials critical plastic strain and 0.4% for the brittle materials ratio of maximum von Mises stress to elastic modulus. This can be seen from the results from simulations using this criterion over ten sliding trips shown in Figure 6.6 (a)-(j). As is evident, ductile materials fail even though the criterion of 2% is slightly higher than 1.75%, where no failure occurred as was reported on earlier. This is due to the weakening of the DLC matrix, which fails first and thus reduces the support for the ductile materials, which then develop higher strains and

stresses leading to failure. This reinforces predictions related to failure occurring at DLC interfaces.

Furthermore, as can be seen in Figure 6.6, the coatings failure continually evolves and does not equilibrate within ten trips. The brittle elements fail first followed by the ductile elements. Using this setting for the criterion, approximately 8% of the coating is converted into transfer film material in ten trips. While elements of gold, MoS₂ and YSZ are converted to the transfer film, the preponderance of the failure occurs in the DLC where 33% of the original DLC is converted into transfer film material.

As shown in Section 6.1, the failure using this technique also initiates at the subsurface, and propagates to neighboring materials before reaching the surface. These elements at the surface, which have converted to the transfer film can subsequently become wear particles. This can be modeled as a free third body transfer film as outlined in Section 5.

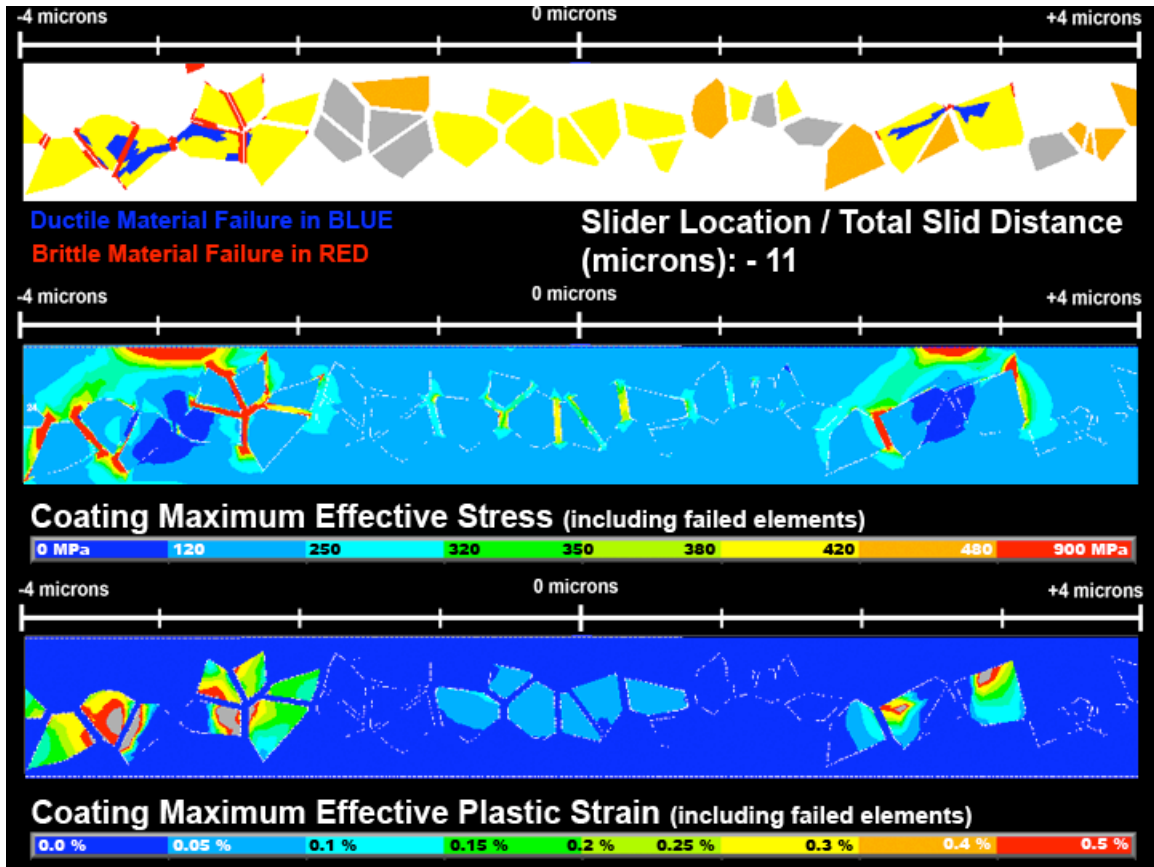
6.3 CONCLUSIONS

Two different criteria and two different techniques to model wear and failure of the coatings constituents were simulated. In general, both techniques underscore that failure initiates at the subsurface, and not at the free surface in contact with the loading traction, and that failure of these interior elements weakens the surface and increases its susceptibility to failure and wear. The simulations also indicate that elements and materials, which were previously resistant to failure can fail if neighboring elements, which support and surround them fail first. This result can be used to investigate the tolerance of thin-film coatings to manufacturing and microstructural defects.

Once a significant percentage of the coating has failed, it is necessary to include the presence of wear particles and a free third body transfer film in order to accurately simulate the experimental conditions experienced by the coating during wear. This will be the focus of future investigations.

6.4 FIGURES
(CHAPTER 6)

Figure 6.1: Progression of coating failure under sliding loads using element failure and criterion of 0.55% plastic strain for ductile elements and 0.25% ratio of maximum von Mises stress to elastic modulus for brittle materials. Failed brittle elements shown in red and ductile elements in blue. First image in every frame shows the coating constituents and DLC matrix in white. Distance scale indicates distance in microns from the start of the sliding trip. Total slid distance is (a) 0 microns, (b) 2 microns, (c) 4 microns, (d) 6 microns, (e) 8 microns, (f) 10 microns and (g) 11 microns.



(g)

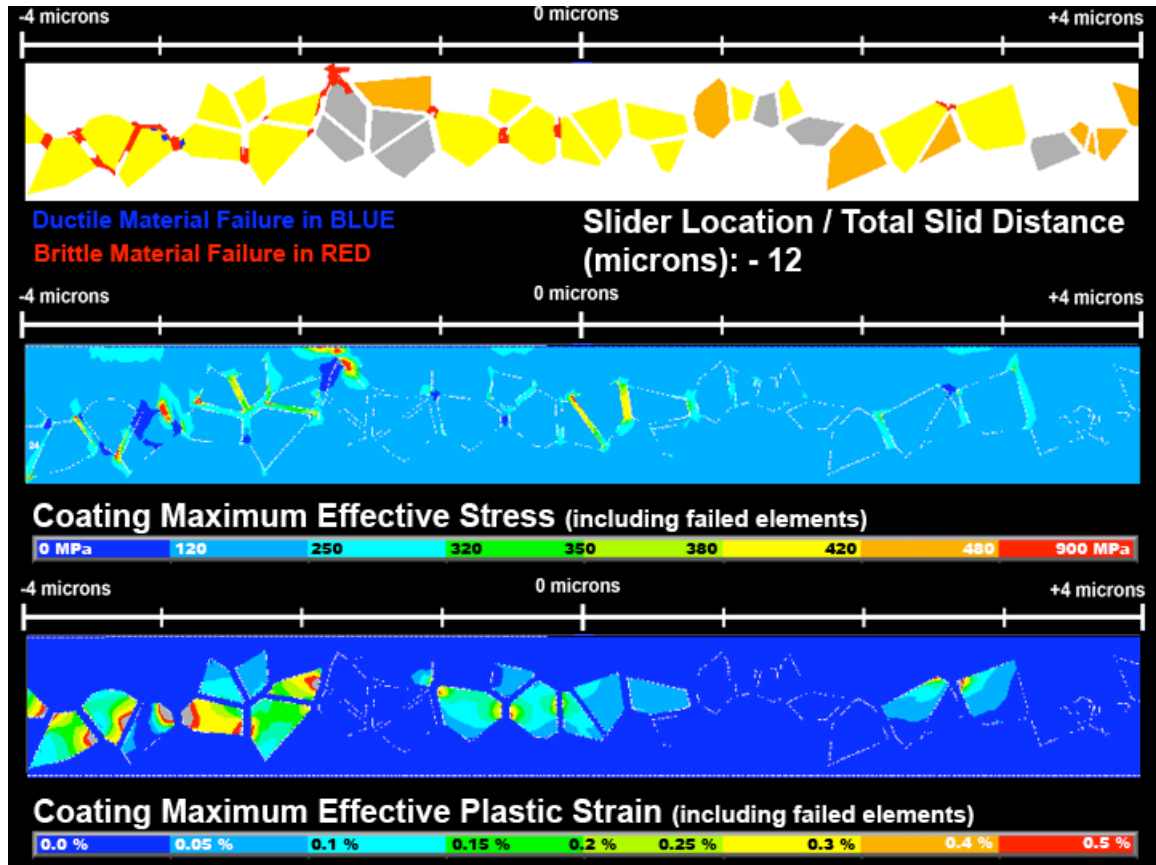
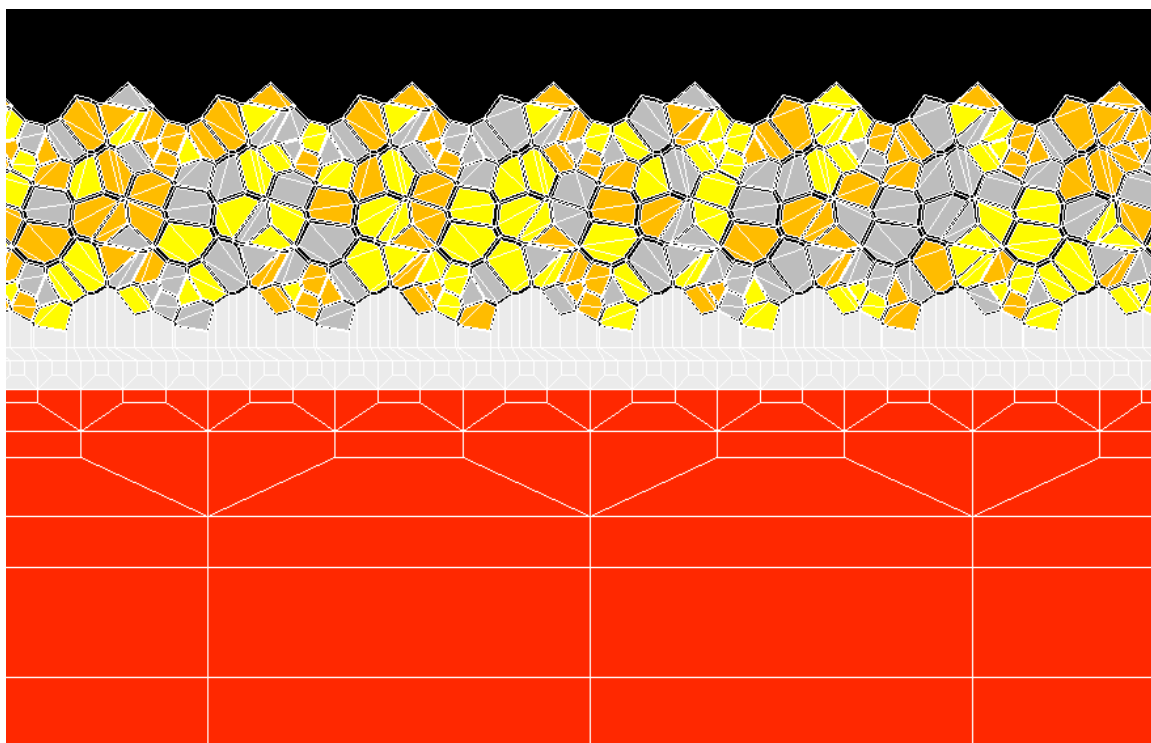


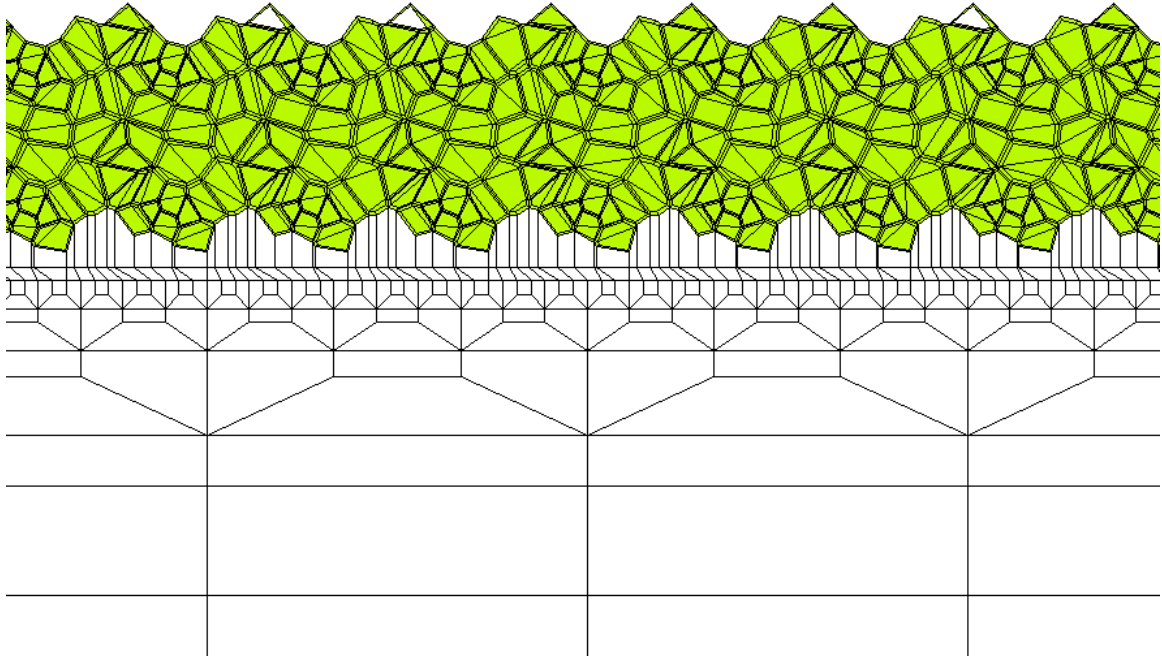
Figure 6.2: Progression of coating failure under sliding loads using element failure and criterion of 1.0% plastic strain for ductile elements and 0.2% ratio of maximum von Mises stress to elastic modulus for brittle materials. Failed brittle elements shown in red and ductile elements in blue. First image in panel shows the coating constituents and DLC matrix in white. Distance scale indicates distance in microns from the start of the sliding trip. Total slid distance is 12 microns.

Figure 6.3: Progression of coating failure under sliding loads using element failure and criterion of 1.0% plastic strain for ductile elements and 0.2% ratio of maximum von Mises stress to elastic modulus for brittle materials and a reduction of the failed elements moduli to (a) 25% and (b) 75% of the original elastic modulus. Failed brittle elements shown in red and ductile elements in blue. First image in every frame shows the coating constituents and DLC matrix in white. Distance scale indicates distance in microns from the start of the sliding trip. Total slid distance is 4 microns.

Figure 6.4: Coating conversion into transfer film material within two sliding trips using failure criteria of 0.1% plastic strain for ductile elements and 0.05% ratio of maximum von Mises stress to elastic modulus for brittle materials. (a) Original coating composition and (b) coating conversion almost entirely into transfer film material indicated in green. Only converted elements are shown in (b).

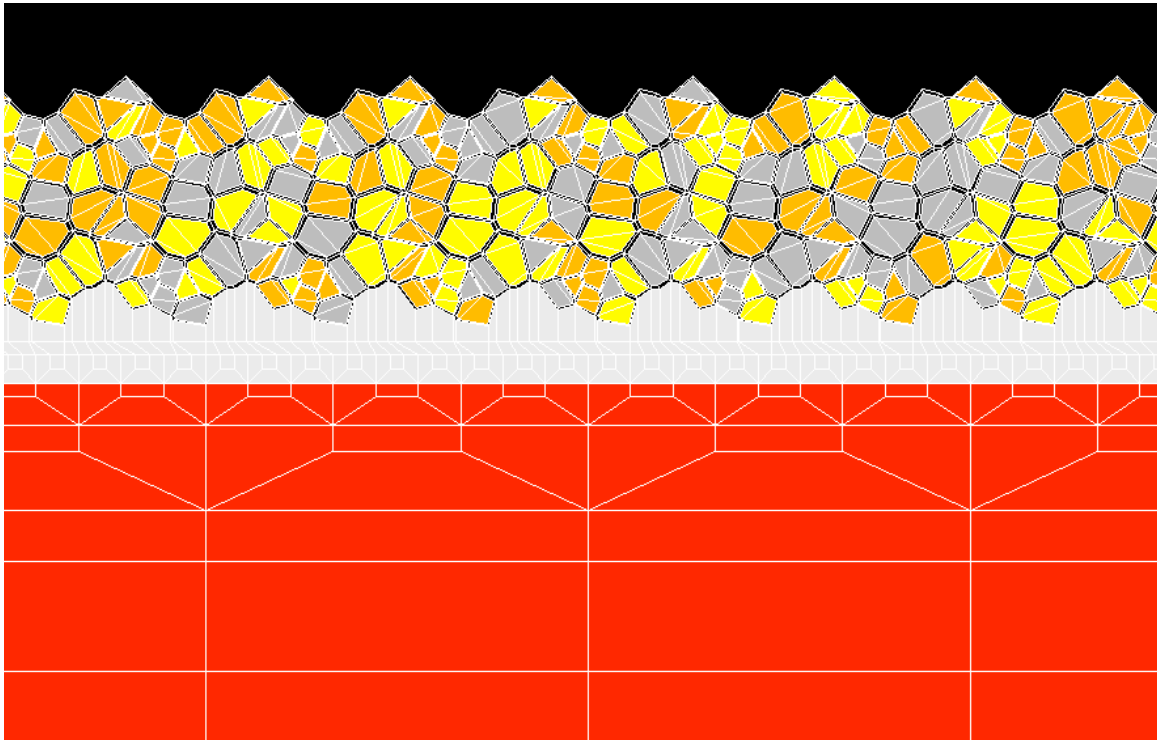


(a)

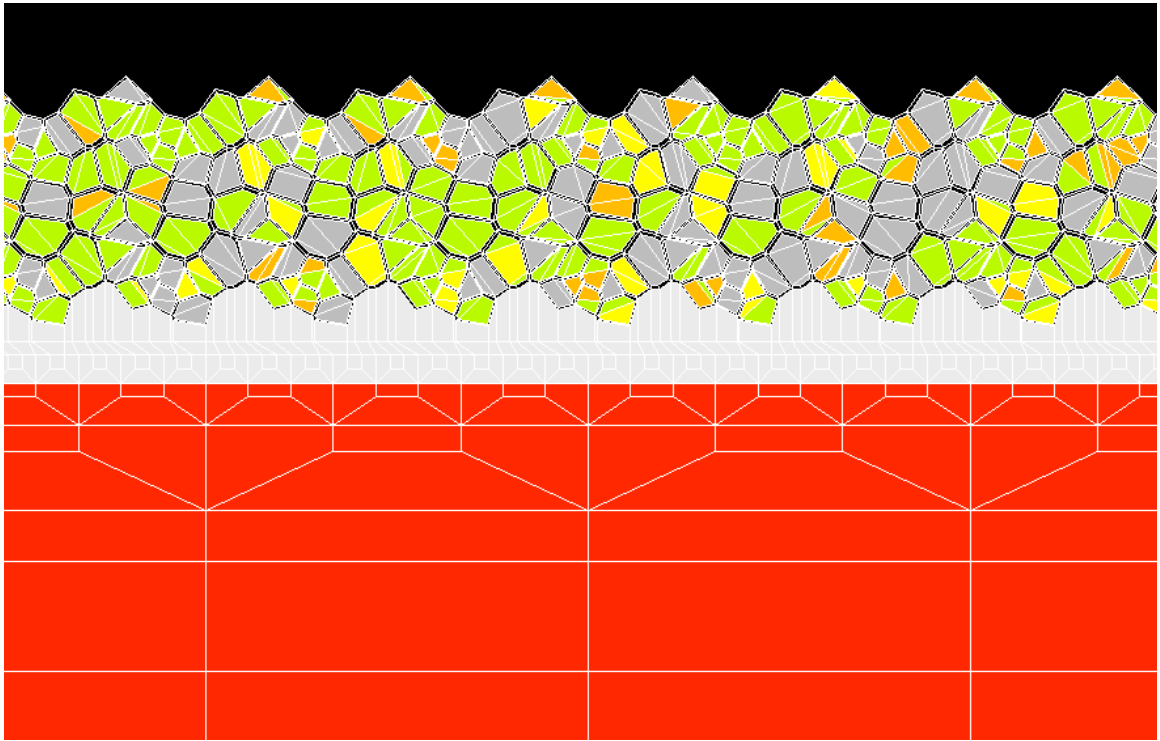


(b)

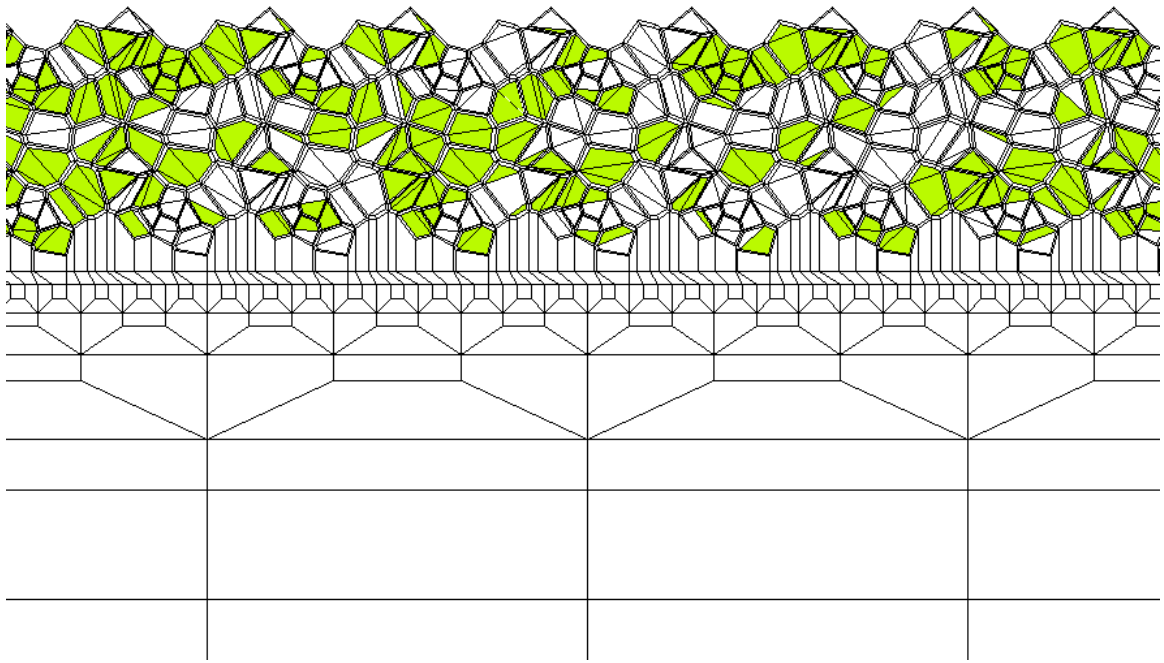
Figure 6.5: Coating conversion of ductile elements into transfer film material using failure criteria of 0.1% plastic strain for ductile elements and 0.6% ratio of maximum von Mises stress to elastic modulus for brittle materials. (a) Original coating composition and (b)-(c) coating conversion almost entirely into transfer film material indicated in green. Image (c) shows only converted elements.



(a)

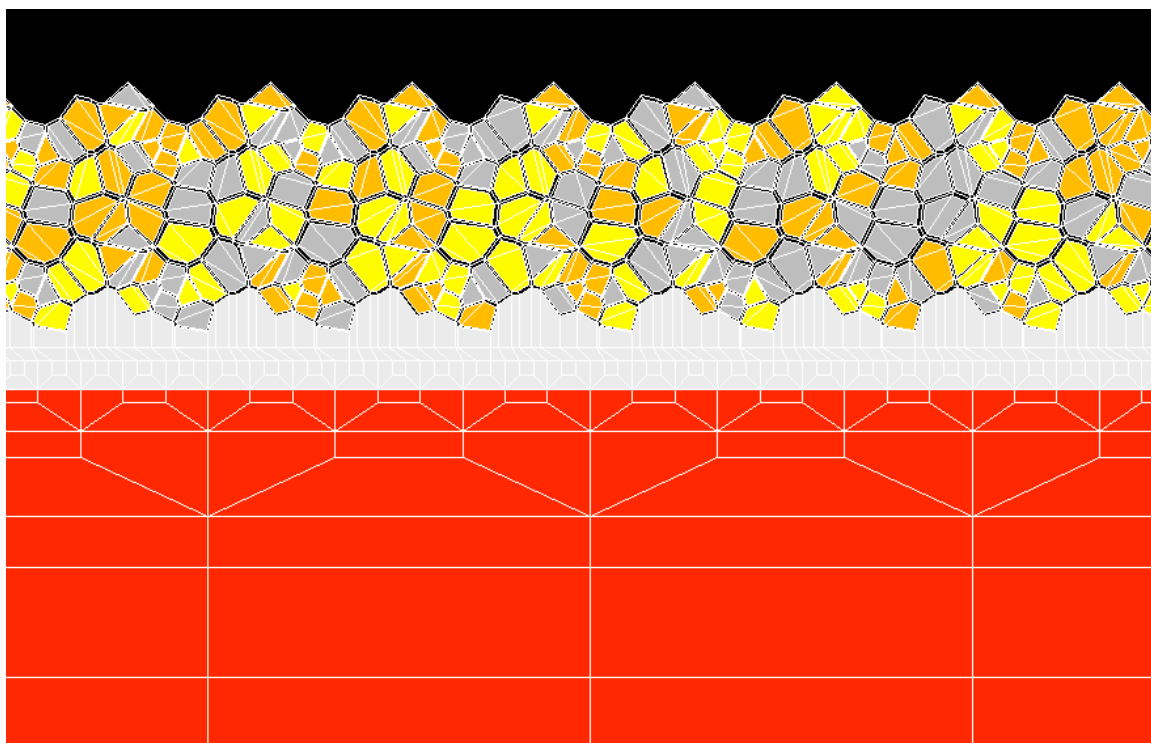


(b)

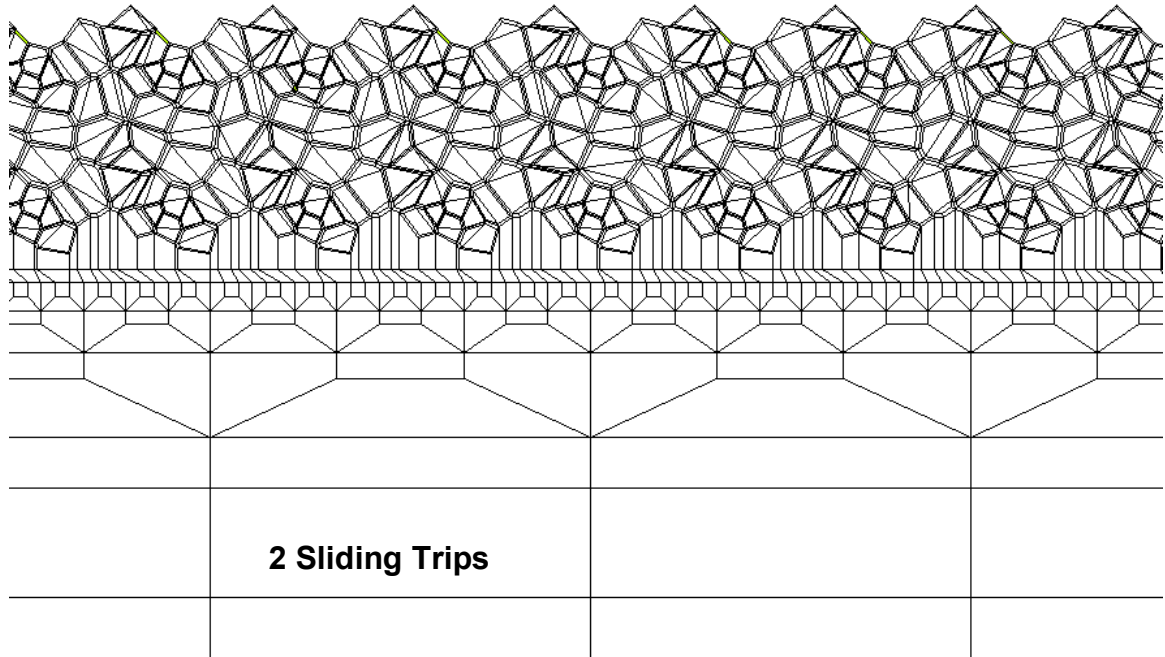


(c)

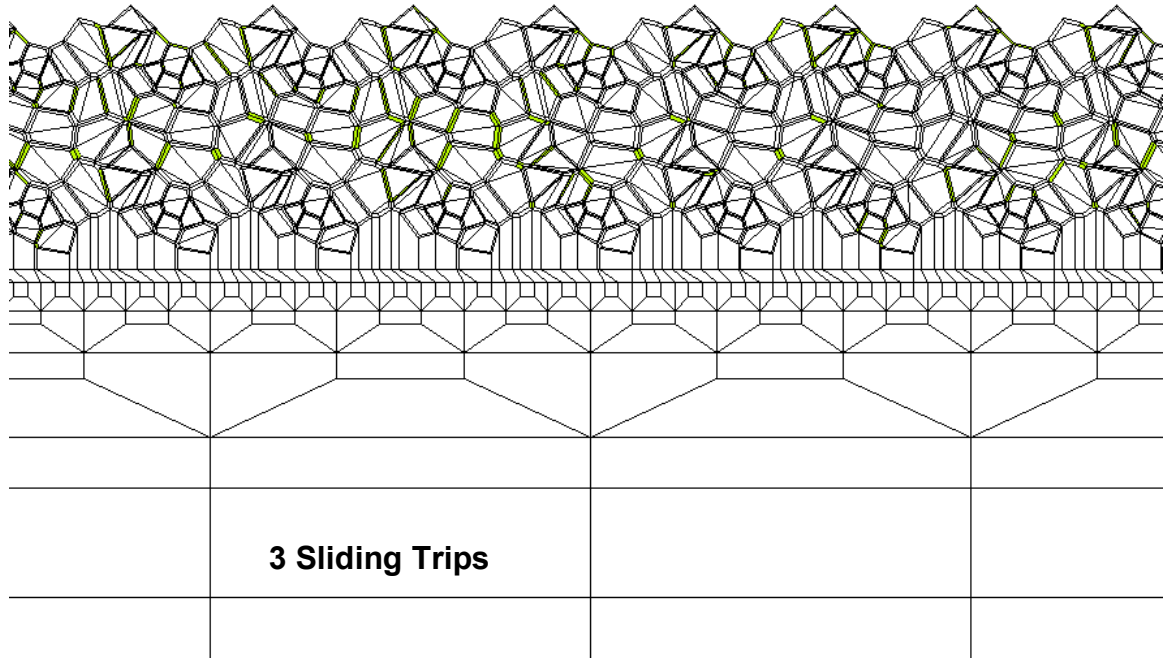
Figure 6.6: Coating transfer of elements into transfer film material over ten sliding trips using failure criteria of 2% plastic strain for ductile elements and 0.4% ratio of maximum von Mises stress to elastic modulus for brittle materials. (a) Original coating composition. Only converted elements shown in (b)-(j). Converted elements shown after (b) 2, (c) 3, (d) 4, (e) 5, (f) 6, (g) 7, (h) 8, (i) 9 and (j) 10 sliding trips.



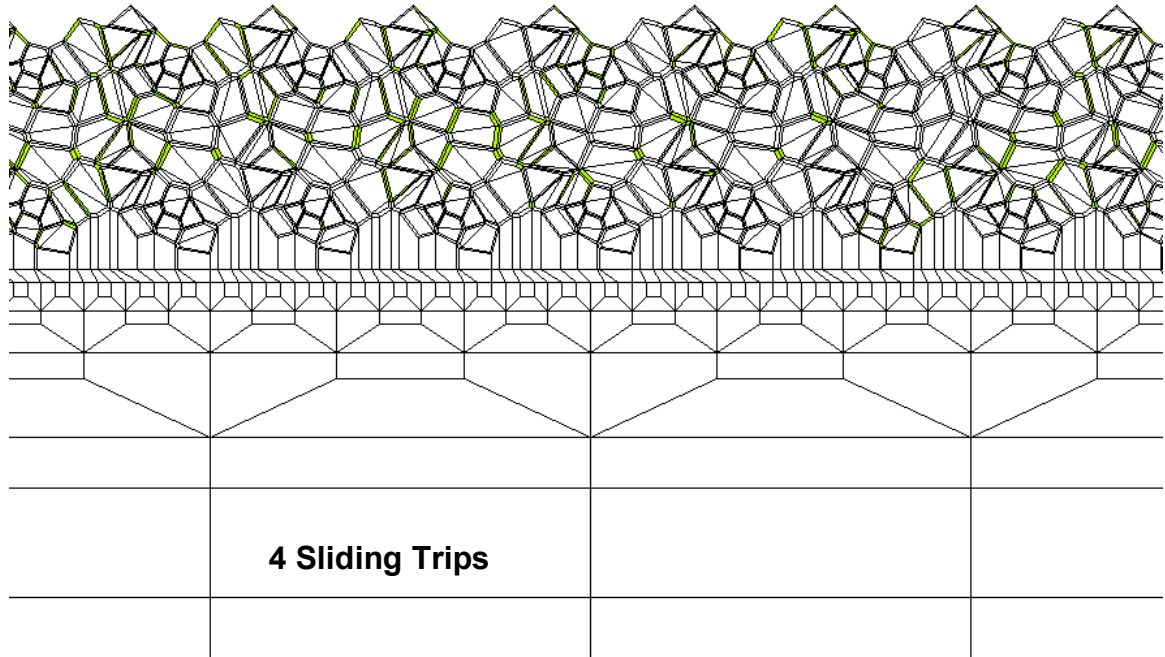
(a)



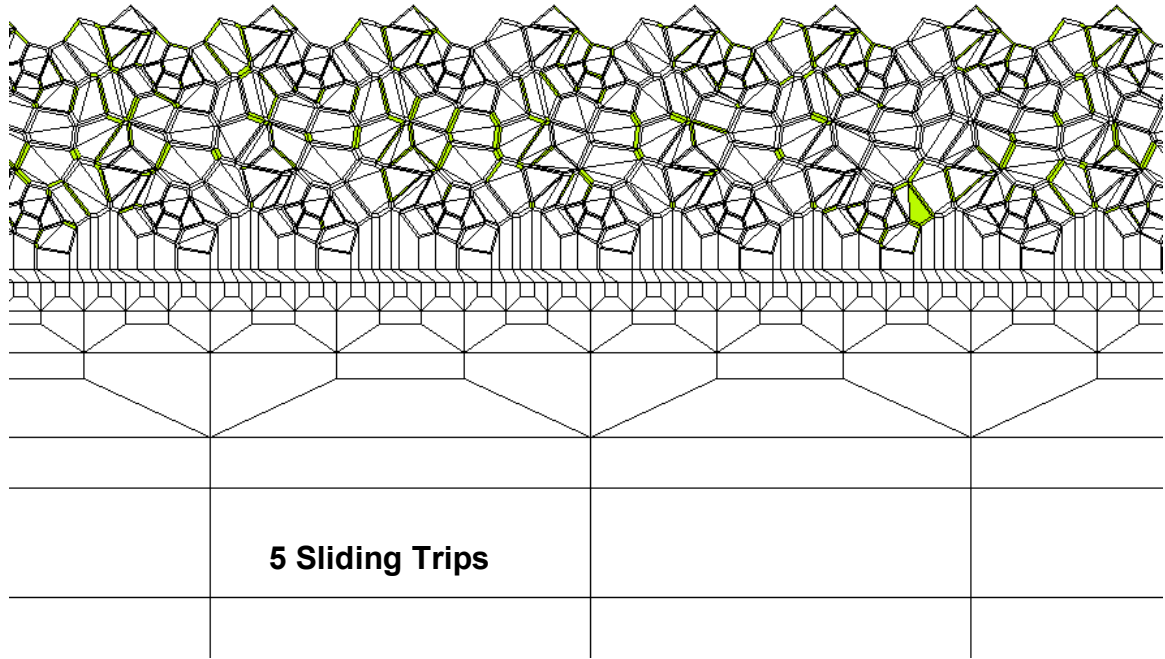
(b)



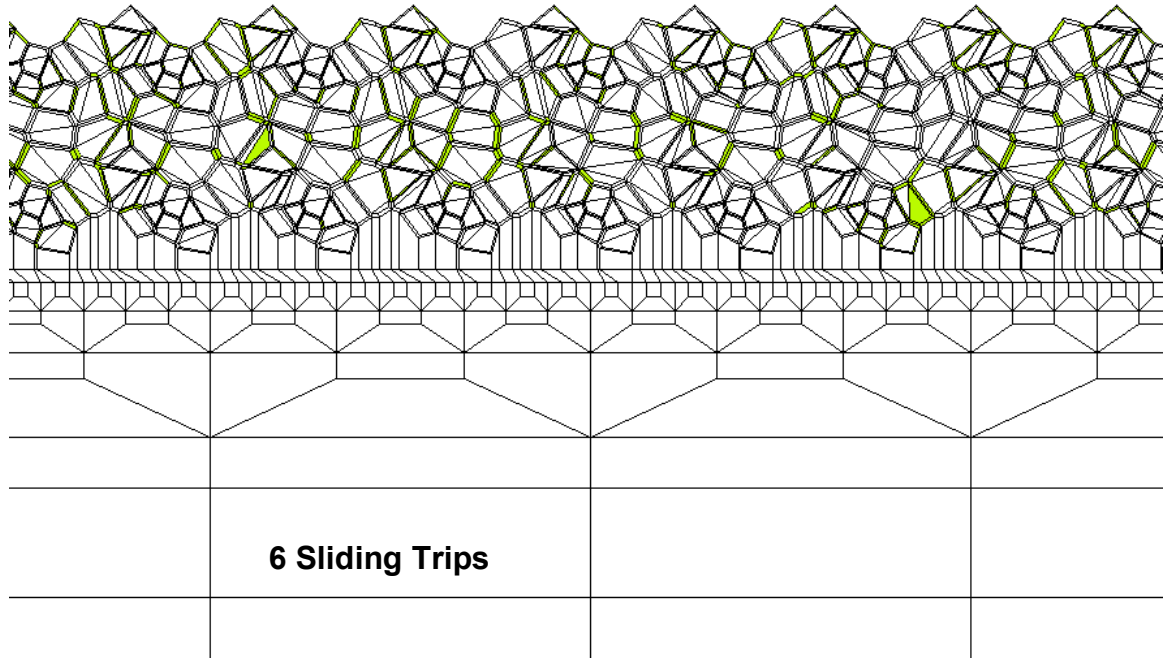
(c)



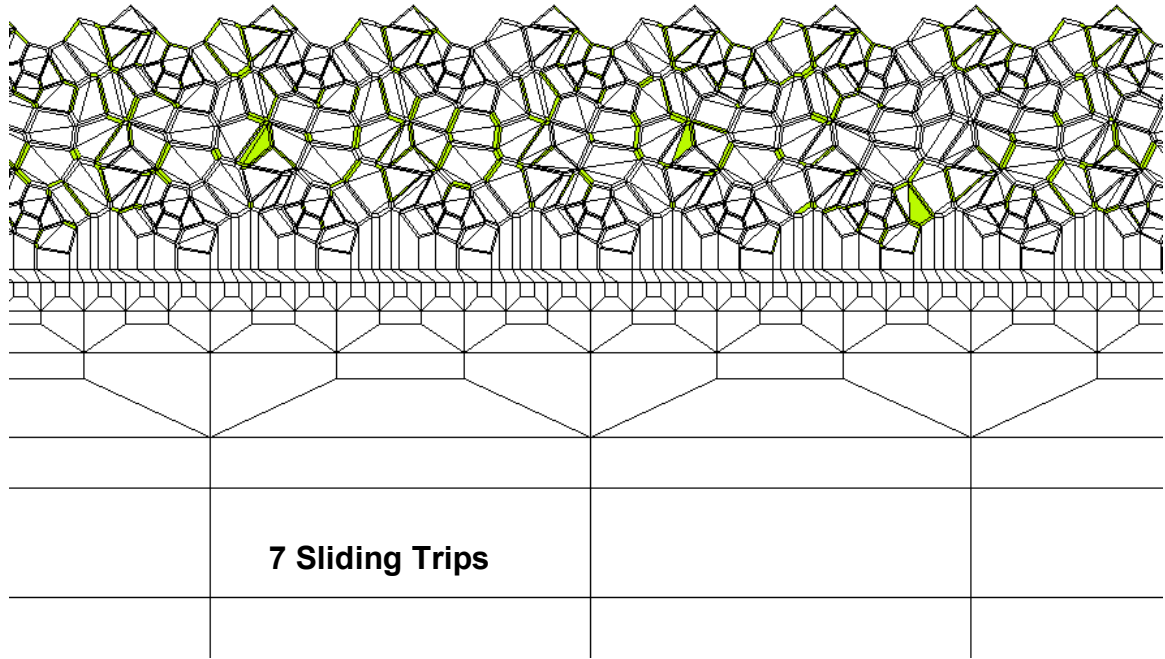
(d)



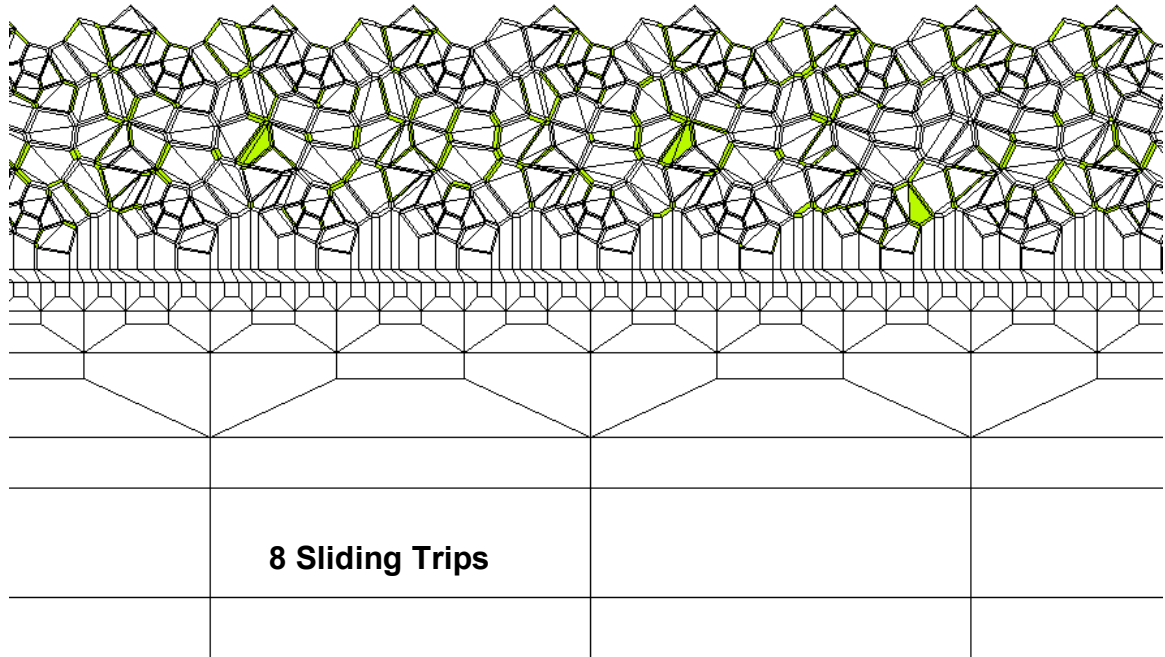
(e)



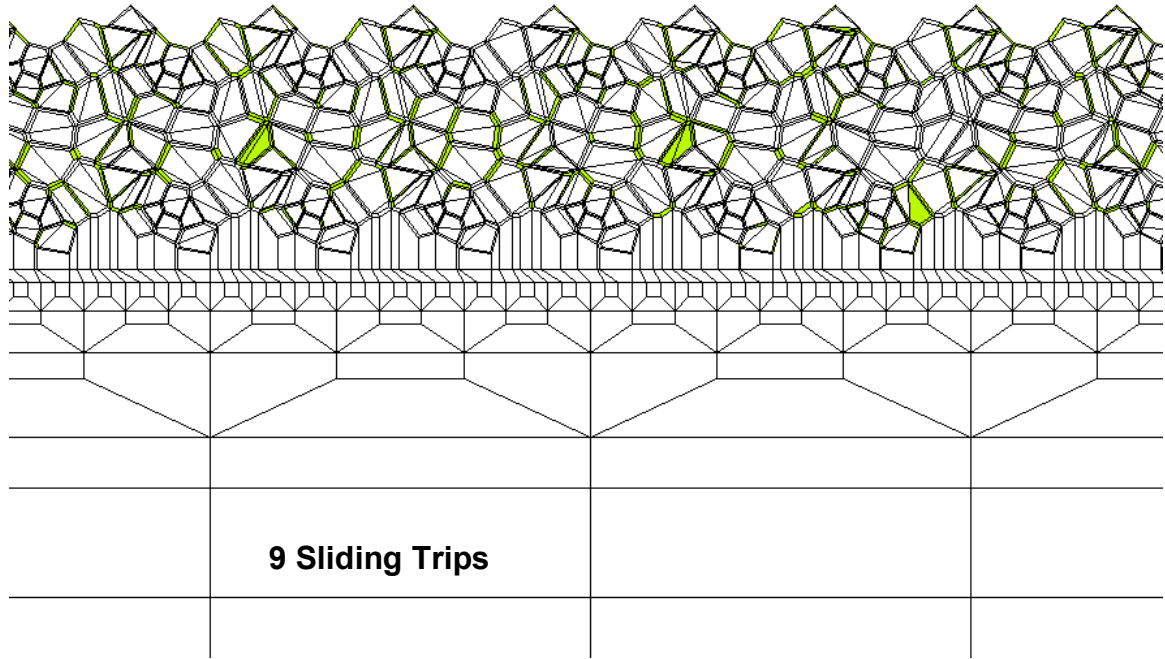
(f)



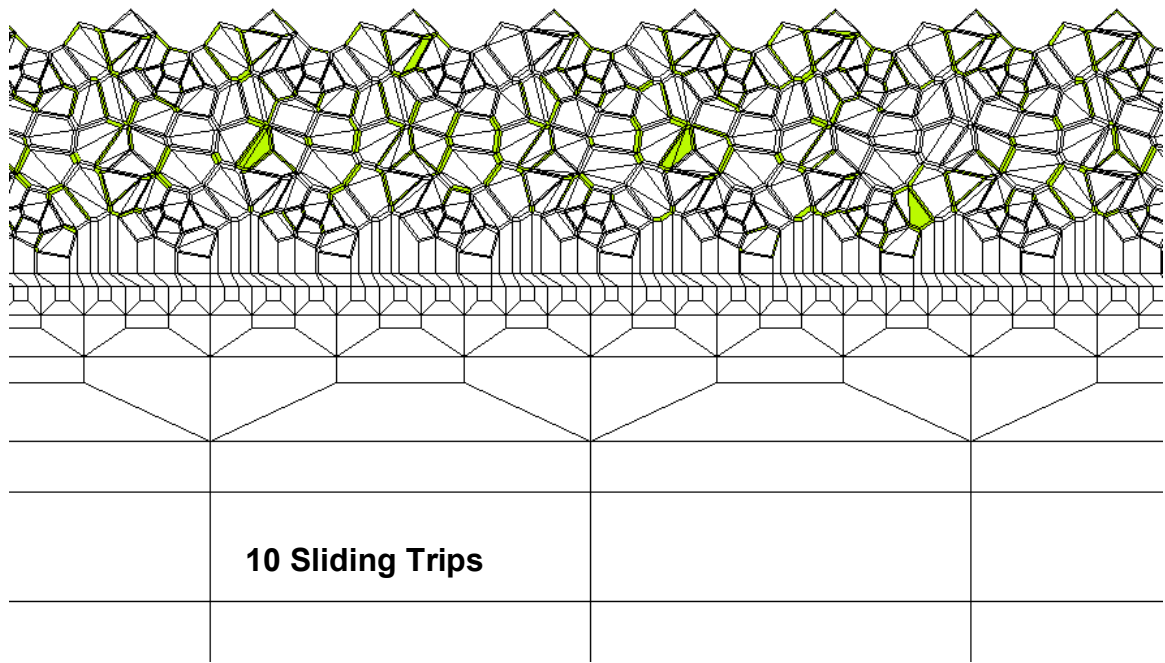
(g)



(h)



(i)



(j)

7. FUTURE RESEARCH RECOMMENDATIONS

Based on the current results using the microstructurally based finite element technique to simulate the dominant microstructural parameters of grain size, material models, composition, presence of voids, presence of matrix material, contact or traction loads, and forms of failure and wear, future research should address the following objectives:

1. Further development of the failure simulations by including node release (decohesion failure) to simulate fracture in the brittle phases and generate wear particles which can be used to predict an accurate wear rate based on the effects of the dominant microstructural parameters.
2. The extensive use of physically based material models more representative of the amorphous and crystalline (Bcc, Fcc, Hcp) forms of the coating constituents complete with scale effects for strength and stiffness as well as inclusion of the effects of voids.
3. The inclusion of additional physics into the model to make it multidisciplinary instead of the current purely mechanistic form.

4. The inclusion of variable surface roughness and adaptive *in situ* friction coefficients in the model and the extension of the model to three-dimensions.

5. The optimal design of thin films by using a thin 200 nm MoS₂ overcoat or buffer layer which is flashed on the surface of the coating after production and serves as a sacrificial layer to initiate, and increase the initial rate of, transfer film formation. Also, a thin 5 to 10 nm layer of antimony trioxide added over the MoS₂ overcoat in terrestrial applications to increase its life and serve as a sacrificial antioxidant layer and bond with free oxygen (Lansdown 1999).

8. REFERENCES

- Ahmed R. (2002). Contact fatigue failure modes of HVOF coatings. *Journal of Wear* Vol. **253** No. 3-4: 473-487
- Aldeman S. A., Doll J. D. (1976). Generalized langevin equation approach for atom-solid-surface scattering – general formulation for classical scattering off harmonic solids. *Journal of Chemical Physics* Vol. **64** No. 6: 2375-2388
- Baker C. C., Chromik R. R., Wahl K. J., Hu J. J., Voevodin A. A. (2007). Preparation of chameleon coatings for space and ambient environments. *Journal of Thin Solid Films* Vol. **515** No. 17: 6737-6743
- Baker C. C., Hu J. J., Voevodin A. A. (2006). Preparation of Al₂O₃/DLC/Au/MoS₂ chameleon coatings for space and ambient environments. *Journal of Surface and Coatings Technology* Vol. **201** No. 7: 4224-4229
- Bellemare S. C., Dao M., Suresh S. (2008). Effects of mechanical properties and surface friction on elasto-plastic sliding contacts. *Journal of Mechanics of Materials* Vol. **40**: 206-219
- Belytschko T., Liu W. K., Moran B. (2000). *Nonlinear Finite Elements for Continua and Structures*. John Wiley & Sons, Inc., New York, New York: 284
- Bhushan B. (1999). Chemical, mechanical and tribological characterization of ultra-thin and hard amorphous carbon coatings as thin as 3.5 nm: Recent developments. *Journal of Diamond and Related Materials* Vol. **8**: 1985-2015
- Blanchet T. A., Sawyer W. G. (2001). Differential application of wear models to fractional thin films. *Journal of Wear* Vol. **251**: 1003-1008
- Blau P. J. (1997). Fifty years of research on the wear of metals. *Tribology International* Vol. **35** No. 5: 321-331
- Brenner D. W., Shenderova O. A., Harrison J. A., Stuart S. J., Ni B., Sinnott S. B. (2002). A second-generation reactive empirical bond order (REBO) potential energy expression for hydrocarbons. *Journal of Physics-Condensed Matter* Vol. **14** No. 4: 783-802

- Budynas R. G. (1999). *Advanced Strength and Applied Stress Analysis: Second Edition*. The McGraw-Hill Companies, Inc., United States of America: 363
- Cantizano A., Carnicero A., Zavarise G. (2002). Numerical simulation of wear-mechanism maps. *Journal of Computational Material Science* Vol. **25**: 54-60
- Cartier M. (2003). *Handbook of Surface Treatments and Coatings*. ASME Press, United States of America: Chapter 4
- Chasiotis I., Bateson C., Timpano K., McCarty A. S., Barker N. S., Stanec J. R. (2007). Strain rate effects on the mechanical behavior of nanocrystalline Au films. *Journal of Thin Solid Films* Vol. **515**: 3183-3189
- Cho S-J., Hockey B. J., Lawn B. R., Bennison S. J. (1989). Grain-size and R-curve effects in the abrasive wear of alumina. *Journal of the American Ceramic Society* Vol. **72** No. 7: 1249-1252
- Chromik R. R., Baker C. C., Voevodin A. A., Wahl K. J. (2006). In situ tribometry of solid lubricant nanocomposite coatings. *Journal of Wear* Vol. **262** No. 9-10: 1239-1252
- Chromik R. R., Winfrey A. L., Luning J., Nemanich R. J., Wahl K. J. (2008). Run in behavior of nanocrystalline diamond coatings studied by in situ tribometry. *Journal of Wear* Vol. **265** No. 3-4: 477-489
- Cook R. D., Malkus D. S., Plesha M. E., Witt R. J. (2002). *Concepts and Applications of Finite Element Analysis: Fourth Edition*. John Wiley & Sons, Inc., New York, New York: 607
- Ding J., Mccoll I. R., Leen S. B., Shipway P. H. (2007). A finite element based approach to simulating the effects of debris on fretting wear. *Journal of Wear* Vol. **263**: 481-491
- Dragon-Louiset M. (2001). On a predictive macroscopic contact-sliding wear model based on micromechanical considerations. *International Journal of Solids and Structures* Vol. **38**: 1625-1639
- Dvorak S. D., Wahl K. J., Singer I. L. (2007). In situ analysis of third body contributions to sliding friction of a Pb-Mo-S coating in dry and humid air. *Tribology Letters* Vol. **28** No. 3: 263-274
- Elalem K., Li D. Y. (1999). Dynamical simulation of an abrasive wear process. *Journal of Computer-Aided Materials Design* Vol. **6**: 185-193

- Erdemir A., Donnet C., in: Bhushan B. (Ed.) (2001). *Modern Tribology Handbook, vol. 2*. CRC Press LLC, Boca Raton, Florida: 871
- Fayeulle S., Ehni P D., Singer I. L. (1990). Analysis of transfer films formed on steel and Co-WC during sliding against MoS₂-coated steel in argon. *Journal of Surface and Coatings Technology* Vol. **41**: 93-101
- Feldman J. L. (1976). Elastic constants of 2H-MoS₂ and 2H-NbSe extracted from measured dispersion curves and linear compressibilities. *Journal of Physics and Chemistry of Solids* Vol. **37**: 1141-1144
- Gao G. T., Cannara R. J., Carpick R. W., Harrison J. A. (2007). Atomic-scale friction on diamond: A comparison of different sliding directions on (001) and (111) surfaces using MD and AFM. *Langmuir* Vol. **23** No. 10: 5394-5405
- Gao G. T., Van Workum K., Schall J. D., Harrison J. A. (2006). Elastic constants of diamond from molecular dynamics simulations. *Journal of Physics-Condensed Matter* Vol. **18** No. 32: S1737-S1750
- Godet M. (1990). Third-bodies in tribology. *Journal of Wear* Vol. **136**: 29-45
- Gonzalez C., Martin A., Llorca J., Garrido M. A., Gomez M. T., Rico A., Rodriguez J. (2005). Numerical analysis of pin on disc tests on Al-Li/SiC composites. *Journal of Wear* Vol. **259**: 609-612
- Hegadekatte V., Huber N., Kraft O. (2005). Finite element based simulation of dry sliding wear. *Journal of Modeling and Simulation in Materials Science and Engineering* Vol. **13**: 57-75
- Hegadekatte V., Huber N., Kraft O. (2006). Modeling and simulation of wear in a pin on disc tribometer. *Tribology Letters* Vol. **24** No. 1: 51-60
- Holmberg K., Matthews A. (1994). *Coatings Tribology: Properties, Techniques and Applications in Surface Engineering*. Elsevier Science Publishers B.V., Netherlands: 257-308
- Hou Q. R., Gao J. (2001). Fracture toughness of diamond-like carbon films. *Journal of Modern Physics Letters B* Vol. **15** No. 4-5: 157-162

- Hsu S. M., Shen M. C., Ruff A. W. (1997). Wear prediction for metals. *Tribology International* Vol. **30** No. 5: 377-383
- Hu J., Li D. Y., Liewellyn R. (2007). Synergistic effects of microstructure and abrasion condition on abrasive wear of composites – a modeling study. *Journal of Wear* Vol. **263**: 218-227
- Jahanmir S. (1985). The relationship of tangential stress to wear particle formation mechanisms. *Journal of Wear* Vol. **103**: 233-252
- Kang J. H., Park I. W., Jae S. S., Kang S. S. (1998). A study on die wear model of warm and hot forgings. *Journal of Metals and Materials-Korea* Vol. **4** No. 3: 477-483
- Kester D. J., Brodbeck C. L., Singer I. L., Kyriakopoulos A. (1999). Sliding wear behavior of diamond-like nanocomposite coatings. *Journal of Surface and Coatings Technology* Vol. **113**: 268-273
- Ko D. C., Iyer S. S., Vaughan H., Gadala M. (2001). Finite element modelling of crack growth and wear particle formation in sliding contact. *Journal of Wear* Vol. **251**: 1265-1278
- Ko D. C., Kim D. H., Kim B. H. (2002). Finite element analysis for the wear of Ti-N coated punch in the piercing process. *Journal of Wear* Vol. **252**: 856-869
- Kreig R. D., Kreig D. B. (1977). Accuracies of numerical solution methods for the elastic-perfectly plastic model. *Journal of Pressure Vessel Technology* Vol. **99** No. 4: 510-515
- Lansdown A. R. (1999). *Molybdenum Disulphide Lubrication: Tribology Series Volume 35*. Elsevier Science Publishers B.V., Netherlands: Chapter 7
- Leyland A., Matthews A. (2000). On the significance of the H/E ratio in wear control: a nanocomposite approach to optimised tribological behaviour. *Journal of Wear* Vol. **246** No. 1-2: 1-11
- Li X., Bhushan B. (1999). Evaluation of fracture toughness of ultra-thin amorphous carbon coatings deposited by different deposition techniques. *Journal of Thin Solid Films* Vol. **355-356**: 330-336
- Lince J. R. (2004). Tribology of co-sputtered nanocomposite Au/MoS₂ solid lubricant films over a wide contact stress range. *Journal of Tribology Letters* Vol. **17** No. 3: 419-428

- Liu F., Wriggers P., Li L. (2004). Wear simulation based on node-to-segment element. *Key Engineering Materials* Vol. **274-276**: 577-582
- Lovell M. R., Khonsari M. M. (1993). On the frictional characteristics of ball bearings coated with solid lubricants. *Journal of Tribology* Vol. **121**: 761-767
- Luan B., Robbins M. O. (2005). The breakdown of continuum models for mechanical contacts. *Nature Letters* Vol. **435**: 929-932
- Lupkowski M., van Swol F. (1990). Computer simulation of fluids interacting with fluctuating walls. *Journal of Chemical Physics* Vol. **93** No. 1: 737-745
- Mary C., Fouvry S. (2007). Numerical prediction of fretting contact durability using energy wear approach: optimization of finite-element model. *Journal of Wear* Vol. **263**: 444-450
- Mencík J., 1995. *Mechanics of Components with Treated or Coated Surfaces*. Kluwer Academic Publishers, United States of America: Chapter 3
- Molinari J. F., Ortiz M., Radovitzky R., Repetto E. A. (2001). Finite-element modeling of dry sliding wear in metals. *Journal of Engineering Computations* Vol. **18** No. 3/4: 592-609
- Nastasi M., Kodali P., Walter K. C., Embury J. D., Nakamura R. Y. (1999). Fracture toughness of diamondlike carbon coatings. *Journal of Materials Research* Vol. **14** No. 5: 2173-2180
- Pan L., Dawson B., Barefoot K., Krim J., Pearson J., Zikry M., Baker C., Voevodin A. (2008). Nanoscale design of adaptive tribological coatings. *Proceedings of the STLE/ASME International Joint Tribology Conference*, Miami, Florida, USA, October 20-22
- Patscheider J. (2003). Nanocomposite hard coatings for wear protection. *MRS Bulletin* Vol. **28** No. 3: 180-183
- Patscheider J., Zehnder T., Diserens M. (2001). Structure-performance relations in nanocomposite coatings. *Journal of Surface and Coatings Technology* Vol. **146-147**: 201-208

- Pearson J. D., Zikry M. A. (2009). Computational design of thin-film nanocomposite coatings for optimized stress and velocity accommodation response. *Journal of Wear, In Press, Manuscript ID: 0121R2*
- Pearson J. D., Zikry M. A., Rezvanian O. (2006). Computational modeling and design of adaptive thin-film composite coatings. *MRS Symposium Proceeding* Vol. **977**: Paper #0977-FF08-10
- Pearson J. D., Zikry M. A., Wahl K. J. (2009). Microstructural modeling of adaptive nanocomposite coatings for durability and wear. *Journal of Wear, In Press, Manuscript ID: IH-4966*
- Podra P., Andersson S. (1999a). Finite element analysis wear simulation of a conical spinning contact considering surface topography. *Journal of Wear* Vol. **224**: 13-21
- Podra P., Andersson S. (1999b). Simulating sliding wear with finite element method. *Tribology International* Vol. **32**: 71-81
- Pramanik A., Zhang L. C., Arsecularatne J. A. (2007). An FEM investigation into the behavior of metal matrix composite: tool-particle interaction during orthogonal cutting. *International Journal of Tools and Manufacture* Vol. **47**: 1497-1506
- Scharf T. W., Singer I. L. (2002). Role of third bodies in friction behavior of diamond-like nanocomposite coatings studied by in situ tribometry. *Tribology Transactions* Vol. **45** No. 3: 363-371
- Seitzman L. E., Bolster R. N., Singer I. L. (1995). Relationship of endurance to microstructure of MoS_2 coatings. *Tribology Transactions* Vol. **38** No. 2: 445-451
- Simo J. C., Taylor R. L. (1985). Consistent tangent operators for rate-independent elastoplasticity. *Journal of Computer Methods in Applied Mechanics and Engineering* Vol. **48**: 101-118
- Singer I. L., Dvorak S. D., Wahl K. J., Scharf T. W. (2003). Role of third bodies in friction and wear of protective coatings. *Journal of Vacuum Science and Technology A* Vol. **21** No. 5: 232-240
- Singer I. L., Fayeulle S., Ehni P. D. (1996). Wear behavior of triode-sputtered MoS_2 coatings in dry sliding contact with steel and ceramics. *Journal of Wear* Vol. **195**: 7-20

- Suh N. P. (1977). An overview of the delamination theory of wear. *Journal of Wear* Vol. **44**: 1-6
- Tilbook M. T., Paton D. J., Xie Z., Hoffman M. (2007). Microstructural effects on indentation failure mechanisms in TiN coatings: finite element simulation. *Acta Materialia* Vol. **55**: 2489-2501
- Tyler J. C., Ku P. M. (1967). Compressive and tensile properties of molybdenum disulfide compacts. *American Society of Lubrication Engineers Transactions* Vol. **10**: 28-37
- Van Workum K., Gao G. T., Schall J. D., Harrison J. A. (2006). Expressions for the stress and elasticity tensors for angle-dependent potentials. *Journal of Chemical Physics* Vol. **125** No. 14: Article 144506: 1-10
- Voevodin A. A., Fitz T. A., Hu J. J., Zabinski J. S. (2002). Nanocomposite tribological coatings with “chameleon” surface adaptation. *Journal of Vacuum Science and Technology A* Vol. **20** No. 4: 1434-1444
- Voevodin A. A., Hu J. J., Fitz T. A., Zabinski J. S. (2001). Tribological properties of adaptive nanocomposite coatings made of yttria stabilized zirconia and gold. *Journal of Surface and Coatings Technology* Vol. **146-147**: 351-356
- Voevodin A. A., Jones J. G., Back T. C., Zabinski J. S., Strel’nitzki V. E., Aksenov I. I. (2005). Comparative study of wear-resistant DLC and fullerene-like CN_x coatings produced by pulsed laser and filtered cathodic arc depositions. *Journal of Surface and Coatings Technology* Vol. **197**: 116-125
- Voevodin A. A., Zabinski J. S. (1998). Load-adaptive crystalline-amorphous nanocomposites. *Journal of Materials Science* Vol. **33**: 319-327
- Voevodin A. A., Zabinski J. S. (2003). Smart nanocomposite coatings with chameleon surface adaptation in tribological applications. *Proceedings of the NATO Advanced Research Workshop on Nanostructured Thin Films and Nanodispersion Strengthened Coatings – NATO Science Series, Series II: Mathematics, Physics and Chemistry* Vol. **155**: 1-8
- Voevodin A. A., Zabinski J. S. (2000). Supertough wear-resistant coatings with ‘chameleon’ surface adaptation. *Journal of Thin Solid Films* Vol. **370**: 223-231

- Wahl K. J., Chromik R. R., Lee G. Y. (2008). Quantitative in situ measurements of transfer film thickness by a Newton's rings method. *Journal of Wear* Vol. **264** No. 7-8: 731-736
- Wahl K. J., Seitzman L. E., Bolster R. N., Singer I. L., Peterson M. B. (1997). Ion-beam deposited Cu-Mo coatings as high temperature solid lubricants. *Journal of Surface and Coatings Technology* Vol. **89**: 245-251
- Wu H., Wang J. M. (1995). Non-hertzian conformal contact at wheel/rail interface. *Proceedings of the 1995 IEEE/ASME Joint Railroad Conference*: 137-144
- Xia S. M., Gao Y. F., Bower A. F., Lev L. C., Cheng Y. -T. (2007). Delamination mechanism maps for a strong elastic coating on an elastic-plastic substrate subjected to contact loading. *International Journal of Solids and Structures* Vol. **44**: 3685-3699
- Yan W., O'Dowd N. P., Busso E. P. (2002). Numerical study of sliding wear caused by a loaded pin on a rotating disc. *Journal of Mechanics and Physics of Solids* Vol. **50**: 449-470
- Zhang Z. X., Dong H., Bell T. (2006). The load bearing capacity of hydrogen-free Cr-DLC coatings on deep-case oxygen hardened Ti6Al4V. *Journal of Surface and Coatings Technology* Vol. **200**: 5237-5244
- Zum Ghar K-H. (1987). *Microstructure and Wear of Materials: Tribology Series Volume 10*. Elsevier Science Publishers B.V., Netherlands: Chapter 5

†

9. APPENDIX

9.1 APPENDIX A

The Matlab (version 7.2.0.283, R2006a) code used to create (in conjunction with the seed points in Table 2.2) and mesh the optimized mesh finite element models appears below:

```
clear;
% set effective grain size
width=100;
height=2;
ratio=0.134;
% first vertical to desired depth and then expand to width
subdepth=-6000;
subdepth=-60;
subextendwidth=4000;
subextendwidth=40;
% relative thickness of the titanium interlayer between the coating and
% the end of the titanium layer
titanend=-8;
disp('Reading in points....');
% read in self-tessellating patch
fid=fopen('/Applications/MATLAB72/bigV/Points2.txt');
    while feof(fid)==0
        L=fscanf(fid,'%e');
    end
fclose(fid);
[c,d]=size(L);
counter=0;
for i=1:2:((c/2/49)*2)-1
    counter=counter+1;
    trial_points(counter,1)=L(i,1);
    trial_points(counter,2)=L(i+1,1);
end
num_points=(((c/2/49)));

disp('Replicating points....');
% Replicate the points to the desired area
ttrial_points=zeros(width*height*num_points,2);
for i=1:height
    for j=1:width
        for k=1:num_points
            ttrial_points((((i-1)*width+j)-
1)*num_points+k,1)=trial_points(k,1)+(j-1);
            ttrial_points((((i-1)*width+j)-
1)*num_points+k,2)=trial_points(k,2)+(i-1);
        end
    end
end
```

```

    trial_points=ttrial_points;
disp('Voronoi points....');
[V,C]=voronoin(trial_points);
disp('Remove infinite points....');

% Remove all cells and vertices that are out of bounds
ii=0; bb=0; aa=0; jj=0;
for ii=1:length(C)
    aa=(C{ii});
    for jj=1:length(C{ii})
        bb(ii,jj)=aa(1,jj);
    end
end
C=bb;
[a,b]=size(V);
[c,d]=size(C);

numvertcell=zeros(c,1);
disp('Remove infinite points....compute num vert cell');
for i=1:c
    f1=0;
    for j=1:d
        if C(i,j)~=0
            f1=f1+1;
        end
    end
    numvertcell(i,1)=f1;
end

disp('Remove infinite points....flag out of bound vertices');
Vgo=zeros(a,1);
for k=1:a
    if (V(k,1)>width | V(k,1)<0.25 | V(k,2)>height | V(k,2)<0)
        Vgo(k,1)=1;
    end
end
disp('Remove infinite points....flag cells linked to out of bound
vertices');
delete_cell_number=zeros(a,1);
[a,b]=size(C);
for k=1:a
    for j=1:numvertcell(k,1)
        if Vgo(C(k,j),1)==1
            delete_cell_number(k,1)=1;
        end
    end
end
disp('Remove infinite points....delete cells');
% Delete cells linked to out of bounds vertices
[a,b]=size(C);
C2=0; row_new=0;
for kk=1:a

```

```

        if delete_cell_number(kk,1)==0
            row_new=row_new+1;
            for kkk=1:b
                C2(row_new,kkk)=C(kk,kkk);
            end
        end
    end
end
C=0;
C=C2;
[c,d]=size(C)
numvertcell=zeros(c,1);
disp('Remove infinite points....compute num vert cell');
for i=1:c
    f1=0;
    for j=1:d
        if C(i,j)~=0
            f1=f1+1;
        end
    end
    numvertcell(i,1)=f1;
end

disp('Remove infinite points....flag disconnected vertices');
% Find vertices that are not connected to any cells
[a,b]=size(C);
[aa,bb]=size(V);
Vgo=zeros(aa,1);
for k=1:a
    for j=1:numvertcell(k,1)
        Vgo(C(k,j),1)=1;
    end
end

% Remove unused vertices, Vgo is the new vertice number and Vrep is the
new vertice list
Vrep=0;
counter6=0;
disp('Remove infinite points....remove unused vertices');
for i=1:aa
    if Vgo(i,1)==1
        counter6=counter6+1;
        Vrep(counter6,1)=V(i,1);Vrep(counter6,2)=V(i,2);
        Vgo(i,1)=counter6;
    end
end
V=0;V=Vrep;
disp('Remove infinite points....re-number the cell list');
% Renumber Cell list
for i=1:a
    for j=1:numvertcell(i,1)
        C(i,j)=Vgo(C(i,j),1);
    end
end

```

```

end

[a,b]=size(C);
[c,d]=size(V);

% Remove the odd sided cells on the very edges of the tessellated region
and generate list of numbers of vertices in each cell
C2=0; counter=0; Vkeep=zeros(c,1);
disp('Flag odd cells on perimeter....');
for i=1:a
    f1=0;
    for j=1:b
        if C(i,j)~=0
            f1=f1+1;
        end
    end
    if ceil(f1/2)~=f1/2 & round (f1/2)~=f1/2
    else
        counter=counter+1;
        for j=1:f1
            C2(counter,j)=C(i,j);
            Vkeep(C(i,j),1)=1;
        end
    end
end
C=0; C=C2; V2=0; counter=0;
disp('Mark Vertices to keep....');
for i=1:c
    if Vkeep(i,1)==1
        counter=counter+1;
        V2(counter,1)=V(i,1);V2(counter,2)=V(i,2);
        Vkeep(i,1)=counter;
    end
end
V=0; V=V2;
[a,b]=size(C); num_vert=zeros(a,1);
disp('Delete perimeter cells....');
for i=1:a
    f1=0;
    for j=1:b
        if C(i,j)~=0
            f1=f1+1;
            C(i,j)=Vkeep(C(i,j),1);
        end
    end
    num_vert(i,1)=f1;
    if ceil(f1/2)~=f1/2 & round (f1/2)~=f1/2
        disp('Problem');
    end
end

% Create flat perimeter around coating edge for mesh transition

```

```

[a,b]=size(C);
[c,d]=size(V);
% FIND THE PERIMETER POINTS
% Form a matrix of lines, with the lowest vertice number listed first and
% then the ending vertice number
gcount=0; Line=0;
for i=1:a
    f1=0;
    for j=1:b
        if C(i,j)~=0
            f1=f1+1;
        end
    end
    for j=1:f1
        gcount=gcount+1;
        if j==f1
            next=1;
        else
            next=j+1;
        end
        if C(i,j)>C(i,next)
            Line(gcount,1)=C(i,next); Line(gcount,2)=C(i,j);
        else
            Line(gcount,1)=C(i,j); Line(gcount,2)=C(i,next);
        end
    end
end
% Count the number of duplicated lines
Line=sortrows(Line);

[a,b]=size(Line);
gcount=0; Linehold=0;
i=1; stop=0;
while stop==0;
    if i==1
        gcount=gcount+1;
        Linehold(gcount,1)=Line(i,1);
        Linehold(gcount,2)=Line(i,2);
        Linehold(gcount,3)=0;
        i=i+1;
    else
        if (Line(i,1)==Line(i-1,1) & Line(i,2)==Line(i-1,2))
            Linehold(gcount,3)=Linehold(gcount,3)+1;
            i=i+1;
        else
            gcount=gcount+1;
            Linehold(gcount,1)=Line(i,1);
            Linehold(gcount,2)=Line(i,2);
            Linehold(gcount,3)=0;
            i=i+1;
        end
    end
end
end

```

```

        if i>a
            stop=1;
        end
    end
end

[a,b]=size(Linehold); gcount=0; Perim=0; pcount=0; numcount=0;
for i=1:a
    if (Linehold(i,3)==0)
        numcount=numcount+1;
        gcount=gcount+1;
        Perim(gcount,1)=Linehold(i,1);
        gcount=gcount+1;
        Perim(gcount,1)=Linehold(i,2);
    end
end
end
[c,d]=size(V);
Perimconnect=zeros(c,2);
for i=1:a
    if (Linehold(i,3)==0)
        if Perimconnect(Linehold(i,1),1)==0
            Perimconnect(Linehold(i,1),1)=Linehold(i,2);
        else
            [c,d]=size(Perimconnect);
            f1=0;
            for j=1:d
                if Perimconnect(Linehold(i,1),j)~=0
                    f1=f1+1;
                end
            end
            Perimconnect(Linehold(i,1),f1+1)=Linehold(i,2);
        end
        if Perimconnect(Linehold(i,2),1)==0
            Perimconnect(Linehold(i,2),1)=Linehold(i,1);
        else
            [c,d]=size(Perimconnect);
            f1=0;
            for j=1:d
                if Perimconnect(Linehold(i,2),j)~=0
                    f1=f1+1;
                end
            end
            Perimconnect(Linehold(i,2),f1+1)=Linehold(i,1);
        end
    end
end
end

Perim=sort(Perim);
gcount=0;
[a,b]=size(Perim); Perim2=0; Perim3=0;

for i=1:a
    if i==1

```

```

        gcount=gcount+1;
        Perim2(gcount,1)=Perim(i,1);
    else
        gcount=gcount+1;
        Perim2(gcount,1)=Perim(i,1);
        if Perim(i,1)==Perim(i-1,1)
            gcount=gcount-1;
            if i==a
                for j=1:gcount
                    Perim3(j,1)=Perim2(j,1);
                end
                Perim2=0; Perim2=Perim3;
            end
        end
    end
end
end
[a,b]=size(Perim2);
gcount=0;
for i=1:a
    X100(i,1)=V(Perim2(i,1),1);
    Y100(i,1)=V(Perim2(i,1),2);
end
% Perim is a matrix where each row is a perimeter vertice, the first
% column is the vertice number in the V list.
% Perimconnect is a matrix where the row number is the vertice number
% whose nearest neighbors are in (vertices numbers) the first and second
% column of the row.
Perim=0; Perim=Perim2;

X103(1,1)=V(Perimconnect(Perim2(3,1),1),1);
X103(2,1)=V(Perimconnect(Perim2(3,1),2),1);
Y103(1,1)=V(Perimconnect(Perim2(3,1),1),2);
Y103(2,1)=V(Perimconnect(Perim2(3,1),2),2);
X103(3,1)=V(Perim2(3,1),1);
Y103(3,1)=V(Perim2(3,1),2);

X103(4,1)=V(Perimconnect(Perim2(23,1),1),1);
X103(5,1)=V(Perimconnect(Perim2(23,1),2),1);
Y103(4,1)=V(Perimconnect(Perim2(23,1),1),2);
Y103(5,1)=V(Perimconnect(Perim2(23,1),2),2);
X103(6,1)=V(Perim2(23,1),1);
Y103(6,1)=V(Perim2(23,1),2);

% FIND THE CORNER POINTS
uplf=0; uprt=0; dnlf=0; dnrt=0;
disuplf=100000; disuprt=100000; disdnlf=100000; disdnrt=10000;
[a,b]=size(Perim2);
for i=1:a
    curdisuplf=sqrt((V(Perim2(i,1),1)-0)^2+(V(Perim2(i,1),2)-height)^2);
    curdisuprt=sqrt((V(Perim2(i,1),1)-width)^2+(V(Perim2(i,1),2)-
height)^2);
    curdisdnlf=sqrt((V(Perim2(i,1),1)-0)^2+(V(Perim2(i,1),2)-0)^2);

```

```

curdisdnrt=sqrt((V(Perim2(i,1),1)-width)^2+(V(Perim2(i,1),2)-0)^2);;
if curdisuplf<disuplf
    disuplf=curdisuplf; uplf=i;
end
if curdisuprt<disuprt
    disuprt=curdisuprt; uprt=i;
end
if curdisdnlf<disdnlf
    disdnlf=curdisdnlf; dnlf=i;
end
if curdisdnrt<disdnrt
    disdnrt=curdisdnrt; dnrt=i;
end
end

X44(1,1)=V(Perim2(uplf,1),1); Y44(1,1)=V(Perim2(uplf,1),2);
X44(2,1)=V(Perim2(uprt,1),1); Y44(2,1)=V(Perim2(uprt,1),2);
X44(3,1)=V(Perim2(dnlf,1),1); Y44(3,1)=V(Perim2(dnlf,1),2);
X44(4,1)=V(Perim2(dnrt,1),1); Y44(4,1)=V(Perim2(dnrt,1),2);

% FORM ORDERED LISTS OF NODES FOR THE LEFT BOTTM AND RIGHT SIDES
% lists are sorted with the first column a x or y coordinate of the
% vertice and the second column is the vertice number
lflst=0; lfcunt=0; rtlst=0; rtcunt=0; cntlst=0; cntcunt=0;
[a,b]=size(Perim);
for i=1:a
    if (V(Perim(i,1),1)<0.7 & V(Perim(i,1),2)>V(Perim(dnlf,1),2) &
V(Perim(i,1),2)<V(Perim(uplf,1),2))
        lfcunt=lfcunt+1;
        lflst(lfcunt,2)=Perim(i,1);
        lflst(lfcunt,1)=V(Perim(i,1),2);
    end
    if (V(Perim(i,1),1)<V(Perim(dnrt,1),1) &
V(Perim(i,1),1)>V(Perim(dnlf,1),1) & V(Perim(i,1),2)<0.7)
        cntcunt=cntcunt+1;
        cntlst(cntcunt,2)=Perim(i,1);
        cntlst(cntcunt,1)=V(Perim(i,1),1);
    end
    if (V(Perim(i,1),1)>(width-0.53125) &
V(Perim(i,1),2)>V(Perim(dnrt,1),2) & V(Perim(i,1),2)<V(Perim(uprt,1),2))
        if V(Perim(i,1),1)<V(Perim(dnrt,1),1)
            if V(Perim(i,1),2)>0.625
                rtcunt=rtcunt+1;
                rtlst(rtcunt,2)=Perim(i,1);
                rtlst(rtcunt,1)=V(Perim(i,1),2);
            else
                end
        else
            rtcunt=rtcunt+1;
            rtlst(rtcunt,2)=Perim(i,1);
            rtlst(rtcunt,1)=V(Perim(i,1),2);
        end
    end
end

```

```

end
if i==a
    lfcoun=lfcount+1;
    lflst(lfcoun,2)=Perim(dnlf,1);
    lflst(lfcoun,1)=V(Perim(dnlf,1),2);
    lfcoun=lfcount+1;
    lflst(lfcoun,2)=Perim(uplf,1);
    lflst(lfcoun,1)=V(Perim(uplf,1),2);
    cntcount=cntcount+1;
    cntlst(cntcount,2)=Perim(dnlf,1);
    cntlst(cntcount,1)=V(Perim(dnlf,1),1);
    cntcount=cntcount+1;
    cntlst(cntcount,2)=Perim(dnrt,1);
    cntlst(cntcount,1)=V(Perim(dnrt,1),1);
    rtcount=rtcount+1;
    rtlst(rtcount,2)=Perim(dnrt,1);
    rtlst(rtcount,1)=V(Perim(dnrt,1),2);
    rtcount=rtcount+1;
    rtlst(rtcount,2)=Perim(uprt,1);
    rtlst(rtcount,1)=V(Perim(uprt,1),2);
end
end

lflst=sortrows(lflst);
rtlst=sortrows(rtlst);
cntlst=sortrows(cntlst);

[myown,myown2]=size(rtlst);
for i=1:myown
    fprintf('%12.12g    %12.12g\n',V(rtlst(i,2),1)*32,V(rtlst(i,2),2)*32);
end

% ADD THE TRANSITION CELLS after the bordering of the inclusions with the
% matrix

[a,b]=size(lflst); lflst2=0;
for i=1:a
end

% Add in the borders to each cell
[a,b]=size(C);
[c,d]=size(V);

Number_incusions=a;
num_inclusions=a;

Orig_area=zeros(a,1); New_area=zeros(a,1); New_border_area=zeros(a,1);
Orig_cell_centroid=zeros(a,2); count=0; CellCounter=0;
disp('Add borders to cells....');
for i=1:a
    % Store original vertice numbers of cell
    e1=zeros(1,num_vert(i,1));

```

```

for j=1:num_vert(i,1)
    e1(1,j)=C(i,j);
end
% Determine original area of cell
AL=0;
for j=1:num_vert(i,1)
    if j==num_vert(i,1)
        N=1;
    else
        N=j+1;
    end
    mm=[V(C(i,j),1) V(C(i,j),2)];
    nn=[V(C(i,N),1) V(C(i,N),2)];
    AL=AL+0.5*((mm(1,1)*(nn(1,2)))-(nn(1,1)*mm(1,2)));
end
Orig_area(i,1)=AL;
% Determine original centroid of cell
SX=0;SY=0;
for j=1:num_vert(i,1)
    if j==num_vert(i,1)
        N=1;
    else
        N=j+1;
    end
    mm=[V(C(i,j),1) V(C(i,j),2)];
    nn=[V(C(i,N),1) V(C(i,N),2)];
    SX=SX+(mm(1,1)+nn(1,1))*(mm(1,1)*nn(1,2)-nn(1,1)*mm(1,2));
    SY=SY+(mm(1,2)+nn(1,2))*(mm(1,1)*nn(1,2)-nn(1,1)*mm(1,2));
end
SX=(1/(6*AL))*SX;
SY=(1/(6*AL))*SY;
Orig_cell_centroid(i,1)=SX; Orig_cell_centroid(i,2)=SY;
% Determine distance from vertice to original center
Distance=zeros(num_vert(i,1),1);
for j=1:num_vert(i,1)
    Distance(1,j)=sqrt((SX-V(C(i,j),1))^2+(SY-V(C(i,j),2))^2);
end
% Determine angle to move vertice along and store in vector
thetaa=zeros(num_vert(i,1),1);
for j=1:num_vert(i,1)
    m=[V(C(i,j),1) V(C(i,j),2)];
    n=[SX SY];
    q=n-m;
    s=[1 0];
thetaa(1,j)=acos(dot(q,s)/(sqrt(q(1,1)^2+q(1,2)^2)*sqrt(s(1,1)^2+s(1,2)^2
));
    if q(1,2)<0
        thetaa(1,j)=(-1)*thetaa(1,j);
    end
end
for j=1:num_vert(i,1)

```

```

xmod=ratio*Distance(1,j)*cos(thetaa(1,j));
ymod=ratio*Distance(1,j)*sin(thetaa(1,j));
% CREATE NEW VERTICE AND UPDATE THE C LIST
New_Vert_x=V(C(i,j),1)+xmod;
New_Vert_y=V(C(i,j),2)+ymod;
count=count+1;
V(c+count,1)=New_Vert_x;
V(c+count,2)=New_Vert_y;
C(i,j)=c+count;
end
for j=1:num_vert(i,1)
if j==num_vert(i,1)
CellCounter=CellCounter+1;
C(a+CellCounter,1)=C(i,num_vert(i,1));
C(a+CellCounter,2)=C(i,1);
C(a+CellCounter,3)=e1(1,1);
C(a+CellCounter,4)=e1(1,num_vert(i,1));
else
CellCounter=CellCounter+1;
C(a+CellCounter,1)=C(i,j);
C(a+CellCounter,2)=C(i,j+1);
C(a+CellCounter,3)=e1(1,j+1);
C(a+CellCounter,4)=e1(1,j);
end
end
% Determine new area of cell
AL=0;
for j=1:num_vert(i,1)
if j==num_vert(i,1)
N=1;
else
N=j+1;
end
mm=[V(C(i,j),1) V(C(i,j),2)];
nn=[V(C(i,N),1) V(C(i,N),2)];
AL=AL+0.5*((mm(1,1)*(nn(1,2)))-(nn(1,1)*mm(1,2)));
end
New_area(i,1)=AL;
% Detmerine the border areas for each cell
ALtotal=0;
for k=1:num_vert(i,1)
AL=0;
for j=1:4
if j==4
N=1;
else
N=j+1;
end
mm=[V(C(a+CellCounter-k+1,j),1) V(C(a+CellCounter-k+1,j),2)];
nn=[V(C(a+CellCounter-k+1,N),1) V(C(a+CellCounter-k+1,N),2)];
AL=AL+0.5*((mm(1,1)*(nn(1,2)))-(nn(1,1)*mm(1,2)));
end
end

```

```

        if AL<0
            ALtotal=ALtotal-AL;
        else
            ALtotal=ALtotal+AL;
        end
    end
    New_border_area(i,1)=ALtotal;
end

num_borders=CellCounter;

% Form a matrix which points to each cell and assign it a material
% The row is the cell,
% THE first column is (1= inclusion, 2= border/matrix,
% 3= region below coating 4=region left of coating 5=region right of
% coating),
% THE second column is the material number (1=gold, 2=MoS2,
% 3=YSZ, 4=DLC, 5=Ti, 6=Substrate, 7=Homog Coating, 8=Transfer Film,
% 9=Sapphire/slider),
% THE third column is the area of the inclusion
% (in square nm) and
% THE fourth column is the line length of the perimeter
% in nm of the inclusion (for border cells - the line length is the length
% of the line abutting the inclusion (not the other three sides - as they
% all border additional matrix material)
% THE fifth, sixth, seventh and eighth columns are the element number(s)
% which make up the incusion or border
percent1=0.25; curpercent1=0;
percent2=0.25; curpercent2=0;
percent3=0.25; curpercent3=0;
percent4=0.25; curpercent4=0;

[a,b]=size(C);
[c,d]=size(V);
Material_Numbers=zeros(a,8); Area_matrix=0;

% find area of matrix
for i=(Number_incusions+1):(Number_incusions+num_borders)
    AL=0;
    f1=0;
    for j=1:b
        if C(i,j)~=0
            f1=f1+1;
        end
    end
    for j=1:f1
        if j==f1
            N=1;
        else
            N=j+1;
        end
    end
end

```

```

mm=[V(C(i,j),1) V(C(i,j),2)]; nn=[V(C(i,N),1) V(C(i,N),2)];
AL=AL+0.5*((mm(1,1)*(nn(1,2)))-(nn(1,1)*mm(1,2)));
end
if AL<0
    Area_matrix=Area_matrix-AL;
    Material_Numbers(i,3)=-AL;
else
    Area_matrix=Area_matrix+AL;
    Material_Numbers(i,3)=AL;
end
Material_Numbers(i,1)=2;
Material_Numbers(i,4)=sqrt((V(C(i,2),1)-
V(C(i,1),1))^2+(V(C(i,2),2)-V(C(i,1),2))^2);
Material_Numbers(i,2)=4;
end

% find total area of coating (borders and inclusions)
Total_coating_area=0;
for i=1:(Number_incusions+num_borders)
    f1=0;
    for j=1:b
        if C(i,j)~=0
            f1=f1+1;
        end
    end
    AL=0;
    for j=1:f1
        if j==f1
            N=1;
        else
            N=j+1;
        end
        mm=[V(C(i,j),1) V(C(i,j),2)]; nn=[V(C(i,N),1) V(C(i,N),2)];
        AL=AL+0.5*((mm(1,1)*(nn(1,2)))-(nn(1,1)*mm(1,2)));
    end
    if AL<0
        Total_coating_area=Total_coating_area-AL;
    else
        Total_coating_area=Total_coating_area+AL;
    end
end
fprintf('Total coating area is: %12.12g\n',Total_coating_area);
fprintf('The percentage of area that is matrix is:
%12.12g\n',Area_matrix/Total_coating_area);
curpercent4=Area_matrix/Total_coating_area;
oldmatnum=0;

for i=1:Number_incusions
    AL=0; SL=0;
    for j=1:num_vert(i,1)
        if j==num_vert(i,1)
            N=1;

```

```

        else
            N=j+1;
        end
        mm=[V(C(i,j),1) V(C(i,j),2)]; nn=[V(C(i,N),1) V(C(i,N),2)];
        AL=AL+0.5*((mm(1,1)*(nn(1,2)))-(nn(1,1)*mm(1,2)));
        SL=SL+sqrt((V(C(i,N),1)-V(C(i,j),1))^2+(V(C(i,N),2)-
V(C(i,j),2))^2);
    end
    Material_Numbers(i,1)=1;
    Material_Numbers(i,4)=SL;
    if AL<0
        Material_Numbers(i,3)=-AL;
    else
        Material_Numbers(i,3)=AL;
    end
    % assign material types
    cc=clock;

rand('state',cc(1,1)+cc(1,2)+cc(1,3)+cc(1,4)+cc(1,5)+(cc(1,6))^2.5*1000);
matnum=0;
matnum=rand(2,1);
if matnum(1,1)==oldmatnum
    oldmatnum=matnum;
    matnum=matnum(2,1);
else
    oldmatnum=matnum;
    matnum=matnum(1,1);
end
if matnum<=0.33
    MATnum=1;
elseif matnum>0.33 & matnum<=0.66
    MATnum=2;
elseif matnum>0.66 & matnum<=1
    MATnum=3;
end
if MATnum==1
    if curpercent1<percent1
        Material_Numbers(i,2)=1;

curpercent1=curpercent1+Material_Numbers(i,3)/Total_coating_area;
    elseif curpercent2<percent2
        Material_Numbers(i,2)=2;

curpercent2=curpercent2+Material_Numbers(i,3)/Total_coating_area;
    elseif curpercent3<percent3
        Material_Numbers(i,2)=3;

curpercent3=curpercent3+Material_Numbers(i,3)/Total_coating_area;
    end
elseif MATnum==2
    if curpercent2<percent2
        Material_Numbers(i,2)=2;

```

```

curpercent2=curpercent2+Material_Numbers(i,3)/Total_coating_area;
    elseif curpercent3<percent3
        Material_Numbers(i,2)=3;

curpercent3=curpercent3+Material_Numbers(i,3)/Total_coating_area;
    elseif curpercent1<percent1
        Material_Numbers(i,2)=1;

curpercent1=curpercent1+Material_Numbers(i,3)/Total_coating_area;
    end
    elseif MATnum==3
        if curpercent3<percent3
            Material_Numbers(i,2)=3;

curpercent3=curpercent3+Material_Numbers(i,3)/Total_coating_area;
    elseif curpercent1<percent1
        Material_Numbers(i,2)=1;

curpercent1=curpercent1+Material_Numbers(i,3)/Total_coating_area;
    elseif curpercent2<percent2
        Material_Numbers(i,2)=2;

curpercent2=curpercent2+Material_Numbers(i,3)/Total_coating_area;
    end
end

end

fprintf('The percentage of area that is gold is: %12.12g\n',curpercent1);
fprintf('The percentage of area that is MOS2 is: %12.12g\n',curpercent2);
fprintf('The percentage of area that is YSZ is: %12.12g\n',curpercent3);

% Form the transition layer and expansion mesh
% We will create duplicate vertices and then remove them later.
% first the transition layers,
[a,b]=size(C); [c,d]=size(V);
counter=a; counter2=c;
[a,b]=size(lflst);
for i=1:a-1
    if i==1
        counter=counter+1;
        C(counter,1)=(lflst(i,2));
        C(counter,2)=(lflst(i+1,2));
        counter2=counter+1;
        V(counter2,2)=V((lflst(i+1,2)),2);
        V(counter2,1)=0;
        C(counter,3)=counter2;
        counter2=counter2+1;
        V(counter2,2)=V((lflst(i,2)),2);
        V(counter2,1)=0;
        lfA=counter2;

```

```

C(counter,4)=counter2;
Material_Numbers(counter,1)=4;
Material_Numbers(counter,2)=5;
Material_Numbers(counter,4)=0;
Material_Numbers(counter,5)=counter;
    AL=0;
    for j=1:4
        if j==4
            N=1;
        else
            N=j+1;
        end
        mm=[V(C(i,j),1) V(C(i,j),2)]; nn=[V(C(i,N),1)
V(C(i,N),2)];
        AL=AL+0.5*((mm(1,1)*(nn(1,2)))-(nn(1,1)*mm(1,2)));
    end
    Material_Numbers(counter,3)=AL;
elseif i==2
    counter=counter+1;
    C(counter,1)=(lflst(i,2));
    C(counter,2)=(lflst(i+1,2));
    counter2=counter2+1;
    V(counter2,2)=V((lflst(i+1,2)),2);
    V(counter2,1)=0;
    C(counter,3)=counter2;
    C(counter,4)=counter2-2;
    Material_Numbers(counter,1)=4;
    Material_Numbers(counter,2)=5;
    Material_Numbers(counter,4)=0;
    Material_Numbers(counter,5)=counter;
    AL=0;
    for j=1:4
        if j==4
            N=1;
        else
            N=j+1;
        end
        mm=[V(C(i,j),1) V(C(i,j),2)]; nn=[V(C(i,N),1)
V(C(i,N),2)];
        AL=AL+0.5*((mm(1,1)*(nn(1,2)))-(nn(1,1)*mm(1,2)));
    end
    Material_Numbers(counter,3)=AL;
else
    counter=counter+1;
    C(counter,1)=(lflst(i,2));
    C(counter,2)=(lflst(i+1,2));
    counter2=counter2+1;
    V(counter2,2)=V((lflst(i+1,2)),2);
    V(counter2,1)=0;
    C(counter,3)=counter2;
    C(counter,4)=counter2-1;
    Material_Numbers(counter,1)=4;

```

```

Material_Numbers(counter,2)=5;
Material_Numbers(counter,4)=0;
Material_Numbers(counter,5)=counter;
    AL=0;
    for j=1:4
        if j==4
            N=1;
        else
            N=j+1;
        end
        mm=[V(C(i,j),1) V(C(i,j),2)]; nn=[V(C(i,N),1)
V(C(i,N),2)];
        AL=AL+0.5*((mm(1,1)*(nn(1,2)))-(nn(1,1)*mm(1,2)));
    end
    Material_Numbers(counter,3)=AL;
end
end
[a,b]=size(rtlst);
for i=1:a-1
    if i==1
        counter=counter+1;
        C(counter,1)=(rtlst(i,2));
        C(counter,2)=(rtlst(i+1,2));
        counter2=counter2+1;
        V(counter2,2)=V((rtlst(i+1,2)),2);
        V(counter2,1)=width;
        C(counter,3)=counter2;
        counter2=counter2+1;
        V(counter2,2)=V((rtlst(i,2)),2);
        V(counter2,1)=width;
        rtA=counter2;
        C(counter,4)=counter2;
        Material_Numbers(counter,1)=5;
        Material_Numbers(counter,2)=5;
        Material_Numbers(counter,4)=0;
        Material_Numbers(counter,5)=counter;
        AL=0;
        for j=1:4
            if j==4
                N=1;
            else
                N=j+1;
            end
            mm=[V(C(i,j),1) V(C(i,j),2)]; nn=[V(C(i,N),1)
V(C(i,N),2)];
            AL=AL+0.5*((mm(1,1)*(nn(1,2)))-(nn(1,1)*mm(1,2)));
        end
        Material_Numbers(counter,3)=AL;
    elseif i==2
        counter=counter+1;
        C(counter,1)=(rtlst(i,2));
        C(counter,2)=(rtlst(i+1,2));

```

```

counter2=counter2+1;
V(counter2,2)=V((rtlst(i+1,2)),2);
V(counter2,1)=width;
C(counter,3)=counter2;
C(counter,4)=counter2-2;
Material_Numbers(counter,1)=5;
Material_Numbers(counter,2)=5;
Material_Numbers(counter,4)=0;
Material_Numbers(counter,5)=counter;
    AL=0;
    for j=1:4
        if j==4
            N=1;
        else
            N=j+1;
        end
        mm=[V(C(i,j),1) V(C(i,j),2)]; nn=[V(C(i,N),1)
V(C(i,N),2)];
        AL=AL+0.5*((mm(1,1)*(nn(1,2)))-(nn(1,1)*mm(1,2)));
    end
    Material_Numbers(counter,3)=AL;
else
counter=counter+1;
C(counter,1)=(rtlst(i,2));
C(counter,2)=(rtlst(i+1,2));
counter2=counter2+1;
V(counter2,2)=V((rtlst(i+1,2)),2);
V(counter2,1)=width;
C(counter,3)=counter2;
C(counter,4)=counter2-1;
Material_Numbers(counter,1)=5;
Material_Numbers(counter,2)=5;
Material_Numbers(counter,4)=0;
Material_Numbers(counter,5)=counter;
    AL=0;
    for j=1:4
        if j==4
            N=1;
        else
            N=j+1;
        end
        mm=[V(C(i,j),1) V(C(i,j),2)]; nn=[V(C(i,N),1)
V(C(i,N),2)];
        AL=AL+0.5*((mm(1,1)*(nn(1,2)))-(nn(1,1)*mm(1,2)));
    end
    Material_Numbers(counter,3)=AL;
end
end
[a,b]=size(cntlst);
for i=1:a-1
    if i==1
        counter=counter+1;

```

```

C(counter,1)=(cntlst(i,2));
C(counter,2)=(cntlst(i+1,2));
counter2=counter2+1;
V(counter2,1)=V((cntlst(i+1,2)),1);
V(counter2,2)=0;
C(counter,3)=counter2;
counter2=counter2+1;
V(counter2,1)=V((cntlst(i,2)),1);
V(counter2,2)=0;
cntA=counter2;
C(counter,4)=counter2;
Material_Numbers(counter,1)=3;
Material_Numbers(counter,2)=5;
Material_Numbers(counter,4)=0;
Material_Numbers(counter,5)=counter;
    AL=0;
    for j=1:4
        if j==4
            N=1;
        else
            N=j+1;
        end
        mm=[V(C(i,j),1) V(C(i,j),2)]; nn=[V(C(i,N),1)
V(C(i,N),2)];
        AL=AL+0.5*((mm(1,1)*(nn(1,2)))-(nn(1,1)*mm(1,2)));
    end
    Material_Numbers(counter,3)=AL;
elseif i==2
    counter=counter+1;
    C(counter,1)=(cntlst(i,2));
    C(counter,2)=(cntlst(i+1,2));
    counter2=counter2+1;
    V(counter2,1)=V((cntlst(i+1,2)),1);
    V(counter2,2)=0;
    C(counter,3)=counter2;
    C(counter,4)=counter2-2;
    Material_Numbers(counter,1)=3;
    Material_Numbers(counter,2)=5;
    Material_Numbers(counter,4)=0;
    Material_Numbers(counter,5)=counter;
        AL=0;
        for j=1:4
            if j==4
                N=1;
            else
                N=j+1;
            end
            mm=[V(C(i,j),1) V(C(i,j),2)]; nn=[V(C(i,N),1)
V(C(i,N),2)];
            AL=AL+0.5*((mm(1,1)*(nn(1,2)))-(nn(1,1)*mm(1,2)));
        end
        Material_Numbers(counter,3)=AL;

```

```

else
    counter=counter+1;
    C(counter,1)=(cntlst(i,2));
    C(counter,2)=(cntlst(i+1,2));
    counter2=counter2+1;
    V(counter2,1)=V((cntlst(i+1,2)),1);
    V(counter2,2)=0;
    if i==(a-1)
        cntB=counter2;
    end
    C(counter,3)=counter2;
    C(counter,4)=counter2-1;
    Material_Numbers(counter,1)=3;
    Material_Numbers(counter,2)=5;
    Material_Numbers(counter,4)=0;
    Material_Numbers(counter,5)=counter;
    AL=0;
    for j=1:4
        if j==4
            N=1;
        else
            N=j+1;
        end
        mm=[V(C(i,j),1) V(C(i,j),2)]; nn=[V(C(i,N),1)
V(C(i,N),2)];
        AL=AL+0.5*((mm(1,1)*(nn(1,2)))-(nn(1,1)*mm(1,2)));
    end
    Material_Numbers(counter,3)=AL;
end
end
% ADD IN THE TWO CORNER CELLS
counter=counter+1;
C(counter,1)=(lflst(1,2));
C(counter,2)=lfA;
counter2=counter2+1;
V(counter2,1)=0;
V(counter2,2)=0;
C(counter,3)=counter2;
C(counter,4)=cntA;
Material_Numbers(counter,1)=4;
Material_Numbers(counter,2)=5;
Material_Numbers(counter,4)=0;
Material_Numbers(counter,5)=counter;
AL=0;
for j=1:4
    if j==4
        N=1;
    else
        N=j+1;
    end
    mm=[V(C(i,j),1) V(C(i,j),2)]; nn=[V(C(i,N),1)
V(C(i,N),2)];

```

```

        AL=AL+0.5*((mm(1,1)*(nn(1,2)))-(nn(1,1)*mm(1,2)));
    end
Material_Numbers(counter,3)=AL;

counter=counter+1;
C(counter,1)=(rtlst(1,2));
C(counter,2)=rtA;
counter2=counter2+1;
V(counter2,1)=width;
V(counter2,2)=0;
C(counter,3)=counter2;
C(counter,4)=cntB;
Material_Numbers(counter,1)=5;
Material_Numbers(counter,2)=5;
Material_Numbers(counter,4)=0;
Material_Numbers(counter,5)=counter;
    AL=0;
    for j=1:4
        if j==4
            N=1;
        else
            N=j+1;
        end
        mm=[V(C(i,j),1) V(C(i,j),2)]; nn=[V(C(i,N),1)
V(C(i,N),2)];
        AL=AL+0.5*((mm(1,1)*(nn(1,2)))-(nn(1,1)*mm(1,2)));
    end
Material_Numbers(counter,3)=AL;

[a,b]=size(lflst); lflst2=0;
lflst2(1,2)=counter2-1; lflst2(1,1)=V(counter2-1,1);
for i=1:a
    lflst2(i+1,1)=lflst(i,1);lflst2(i+1,2)=lflst(i,2);
end
lflst=0;lflst=lflst2;

[a,b]=size(rtlst); rtlst2=0;
rtlst2(1,2)=counter2; rtlst2(1,1)=V(counter2,2);
for i=1:a
    rtlst2(i+1,1)=rtlst(i,1);rtlst2(i+1,2)=rtlst(i,2);
end
rtlst=0;rtlst=rtlst2;

[a,b]=size(cntlst); cntlst2=0;
cntlst2(1,2)=counter2-1; cntlst2(1,1)=V(counter2-1,1);
for i=1:a
    cntlst2(i+1,1)=cntlst(i,1);cntlst2(i+1,2)=cntlst(i,2);
end
cntlst2(a+2,2)=counter2; cntlst2(a+2,1)=V(counter2,1);
cntlst=0;cntlst=cntlst2;

num_perim=counter-num_inclusions-num_borders;

```

```

% now create expansion layers first left and then right and then downward
% until fully expanded and then fill in sides areas and then remove
% duplicates

Scaleall=1/32;
%Scaleall=1;

[a,b]=size(cntlst);
stop=0; layer=0; near=0; intermed=-1*Scaleall; far=-2*Scaleall;
counter2=0; counter=0; xLoc=0; xLoccounter=1;
num_vert_on_side=a; C1=0; V1=0;
[a,b]=size(cntlst);
for i=1:a
    xLoc(i,1)=cntlst(i,1);
end
while stop==0
    if num_vert_on_side<4
        stop=1;
    else
        layer=layer+1;
        if ((num_vert_on_side-1)/3)==fix((num_vert_on_side-1)/3)
            remainder1=0;
            big4sets=(num_vert_on_side-1)/3;
        else
            remainder1=3*((num_vert_on_side-1)/3-fix((num_vert_on_side-1)/3));
            big4sets=fix((num_vert_on_side-1)/3);
        end
        xLoc2=0;
        for i=1:big4sets
            counter2=counter2+1; V1(counter2,1)=xLoc(i*3-2,1);
V1(counter2,2)=near;
            counter2=counter2+1; V1(counter2,1)=xLoc(i*3-1,1);
V1(counter2,2)=near;
            counter2=counter2+1; V1(counter2,1)=xLoc(i*3-0,1);
V1(counter2,2)=near;
            counter2=counter2+1; V1(counter2,1)=xLoc(i*3+1,1);
V1(counter2,2)=near;
            counter2=counter2+1; V1(counter2,1)=xLoc(i*3-2,1);
V1(counter2,2)=far;
            if i==1
                xLoc2(1,1)=xLoc(1,1);
            end
            counter2=counter2+1; V1(counter2,1)=xLoc(i*3-1,1);
V1(counter2,2)=intermed;
            counter2=counter2+1; V1(counter2,1)=xLoc(i*3,1);
V1(counter2,2)=intermed;
            counter2=counter2+1; V1(counter2,1)=xLoc(i*3+1,1);
V1(counter2,2)=far; xLoccounter=xLoccounter+1;
xLoc2(xLoccounter,1)=xLoc(i*3+1,1);
            counter=counter+1; C1(counter,1)=counter2-

```

```

7;C1(counter,2)=counter2-6;C1(counter,3)=counter2-
2;C1(counter,4)=counter2-3;
    counter=counter+1;    C1(counter,1)=counter2-
6;C1(counter,2)=counter2-5;C1(counter,3)=counter2-
1;C1(counter,4)=counter2-2;
    counter=counter+1;    C1(counter,1)=counter2-
5;C1(counter,2)=counter2-4;C1(counter,3)=counter2;C1(counter,4)=counter2-
1;
    counter=counter+1;    C1(counter,1)=counter2-
3;C1(counter,2)=counter2-2;C1(counter,3)=counter2-
1;C1(counter,4)=counter2;
    end
    for i=1:round(remainder1)
        counter2=counter2+1;
        V1(counter2,1)=xLoc(fix((num_vert_on_side-1)/3)*3+i,1);
V1(counter2,2)=near;
        counter2=counter2+1;
        V1(counter2,1)=xLoc(fix((num_vert_on_side-1)/3)*3+i+1,1);
V1(counter2,2)=near;
        counter2=counter2+1;
        V1(counter2,1)=xLoc(fix((num_vert_on_side-1)/3)*3+i+1,1);
V1(counter2,2)=far;    xLoccounter=xLoccounter+1;
xLoc2(xLoccounter,1)=V1(counter2,1);
        counter2=counter2+1;
        V1(counter2,1)=xLoc(fix((num_vert_on_side-1)/3)*3+i,1);
V1(counter2,2)=far;
        counter=counter+1;
        C1(counter,1)=counter2-3;C1(counter,2)=counter2-
2;C1(counter,3)=counter2-1;C1(counter,4)=counter2;
    end
    xLoc=0; xLoc=xLoc2;
    [aaa,bbb]=size(xLoc);
    num_vert_on_side=aaa;
    xLoccounter=1;
    near=far;
    intermed=far-1*Scaleall;
    far=far-2*Scaleall;
    end
end
subLoc=0; subLoc=xLoc;
centlayer=layer;
num_cent_transition=counter;

% Add in created points to the side lists
[a,b]=size(lflst);
lflst2=0;
for i=1:centlayer
    lflst2(i,1)=-2*(centlayer-i+1)*Scaleall;
end
for i=centlayer+1:(centlayer+a)
    lflst2(i,1)=lflst(i-centlayer,1);
end
end

```

```

lflst=0; lflst=lflst2;

[a,b]=size(rtlst);
rtlst2=0;
for i=1:centlayer
    rtlst2(i,1)=-2*(centlayer-i+1)*Scaleall;
end
for i=centlayer+1:(centlayer+a)
    rtlst2(i,1)=rtlst(i-centlayer,1);
end
rtlst=0; rtlst=rtlst2;

[a,b]=size(rtlst);
stop=0; layer=0; nearr=width; intermedr=width+1*Scaleall;
farr=width+2*Scaleall; xLoc=0; xLoccounter=1;
num_vert_on_side=a;
[a,b]=size(rtlst);
for i=1:a
    xLoc(i,1)=rtlst(i,1);
end
while stop==0
    if num_vert_on_side<4
        stop=1;
    else
        layer=layer+1;
        if ((num_vert_on_side-1)/3)==fix((num_vert_on_side-1)/3)
            remainder1=0;
            big4sets=(num_vert_on_side-1)/3;
        else
            remainder1=3*((num_vert_on_side-1)/3-fix((num_vert_on_side-1)/3));
            big4sets=fix((num_vert_on_side-1)/3);
        end
        xLoc2=0;
        for i=1:big4sets
            counter2=counter2+1; V1(counter2,2)=xLoc(i*3-2,1);
V1(counter2,1)=nearr;
            counter2=counter2+1; V1(counter2,2)=xLoc(i*3-1,1);
V1(counter2,1)=nearr;
            counter2=counter2+1; V1(counter2,2)=xLoc(i*3-0,1);
V1(counter2,1)=nearr;
            counter2=counter2+1; V1(counter2,2)=xLoc(i*3+1,1);
V1(counter2,1)=nearr;
            counter2=counter2+1; V1(counter2,2)=xLoc(i*3-2,1);
V1(counter2,1)=farr;
            if i==1
                xLoc2(1,1)=xLoc(1,1);
            end
            counter2=counter2+1; V1(counter2,2)=xLoc(i*3-1,1);
V1(counter2,1)=intermedr;
            counter2=counter2+1; V1(counter2,2)=xLoc(i*3,1);
V1(counter2,1)=intermedr;
            counter2=counter2+1; V1(counter2,2)=xLoc(i*3+1,1);

```

```

V1(counter2,1)=farr; xLoccounter=xLoccounter+1;
xLoc2(xLoccounter,1)=xLoc(i*3+1,1);
    counter=counter+1; C1(counter,1)=counter2-
7;C1(counter,2)=counter2-6;C1(counter,3)=counter2-
2;C1(counter,4)=counter2-3;
    counter=counter+1; C1(counter,1)=counter2-
6;C1(counter,2)=counter2-5;C1(counter,3)=counter2-
1;C1(counter,4)=counter2-2;
    counter=counter+1; C1(counter,1)=counter2-
5;C1(counter,2)=counter2-4;C1(counter,3)=counter2;C1(counter,4)=counter2-
1;
    counter=counter+1; C1(counter,1)=counter2-
3;C1(counter,2)=counter2-2;C1(counter,3)=counter2-
1;C1(counter,4)=counter2;
end
for i=1:round(remainder1)
    counter2=counter2+1;
    V1(counter2,2)=xLoc(fix((num_vert_on_side-1)/3)*3+i,1);
V1(counter2,1)=nearr;
    counter2=counter2+1;
    V1(counter2,2)=xLoc(fix((num_vert_on_side-1)/3)*3+i+1,1);
V1(counter2,1)=nearr;
    counter2=counter2+1;
    V1(counter2,2)=xLoc(fix((num_vert_on_side-1)/3)*3+i+1,1);
V1(counter2,1)=farr;
    xLoccounter=xLoccounter+1;
    xLoc2(xLoccounter,1)=V1(counter2,2);
    counter2=counter2+1;
    V1(counter2,2)=xLoc(fix((num_vert_on_side-1)/3)*3+i,1);
V1(counter2,1)=farr;
    counter=counter+1;
    C1(counter,1)=counter2-3;C1(counter,2)=counter2-
2;C1(counter,3)=counter2-1;C1(counter,4)=counter2;
end
xLoc=0; xLoc=xLoc2;
[aaa,bbb]=size(xLoc);
num_vert_on_side=aaa;
xLoccounter=1;
nearr=farr;
intermedr=farr+1*Scaleall;
farr=farr+2*Scaleall;
end
end
subrtLoc=xLoc;
rtlayers=layer;
num_right_transition=counter-num_cent_transition;

stop=0; layer=0; nearl=0; intermedl=-1*Scaleall; farl=-2*Scaleall; xLoc=0;
xLoccounter=1;
[a,b]=size(lflst);
num_vert_on_side=a;
for i=1:a

```

```

        xLoc(i,1)=lflst(i,1);
end
remainder1=0; remainder=0;
while stop==0
    if num_vert_on_side<4
        stop=1;
    else
        layer=layer+1;
    if ((num_vert_on_side-1)/3)==fix((num_vert_on_side-1)/3)
        remainder1=0;
        big4sets=(num_vert_on_side-1)/3;
    else
        remainder1=3*((num_vert_on_side-1)/3-fix((num_vert_on_side-1)/3));
        big4sets=fix((num_vert_on_side-1)/3);
    end
    xLoc2=0;
    for i=1:big4sets
        counter2=counter2+1; V1(counter2,2)=xLoc(i*3-2,1);
V1(counter2,1)=nearl;
        counter2=counter2+1; V1(counter2,2)=xLoc(i*3-1,1);
V1(counter2,1)=nearl;
        counter2=counter2+1; V1(counter2,2)=xLoc(i*3-0,1);
V1(counter2,1)=nearl;
        counter2=counter2+1; V1(counter2,2)=xLoc(i*3+1,1);
V1(counter2,1)=nearl;
        counter2=counter2+1; V1(counter2,2)=xLoc(i*3-2,1);
V1(counter2,1)=farl;
        if i==1
            xLoc2(1,1)=xLoc(1,1);
        end
        counter2=counter2+1; V1(counter2,2)=xLoc(i*3-1,1);
V1(counter2,1)=intermedl;
        counter2=counter2+1; V1(counter2,2)=xLoc(i*3,1);
V1(counter2,1)=intermedl;
        counter2=counter2+1; V1(counter2,2)=xLoc(i*3+1,1);
V1(counter2,1)=farl; xLoccounter=xLoccounter+1;
xLoc2(xLoccounter,1)=xLoc(i*3+1,1);
        counter=counter+1; C1(counter,1)=counter2-
7;C1(counter,2)=counter2-6;C1(counter,3)=counter2-
2;C1(counter,4)=counter2-3;
        counter=counter+1; C1(counter,1)=counter2-
6;C1(counter,2)=counter2-5;C1(counter,3)=counter2-
1;C1(counter,4)=counter2-2;
        counter=counter+1; C1(counter,1)=counter2-
5;C1(counter,2)=counter2-4;C1(counter,3)=counter2;C1(counter,4)=counter2-
1;
        counter=counter+1; C1(counter,1)=counter2-
3;C1(counter,2)=counter2-2;C1(counter,3)=counter2-
1;C1(counter,4)=counter2;
    end
    for i=1:round(remainder1)
        counter2=counter2+1;

```

```

        V1(counter2,2)=xLoc(fix((num_vert_on_side-1)/3)*3+i,1);
V1(counter2,1)=nearl;
        counter2=counter2+1;
        V1(counter2,2)=xLoc(fix((num_vert_on_side-1)/3)*3+i+1,1);
V1(counter2,1)=nearl;
        counter2=counter2+1;
        V1(counter2,2)=xLoc(fix((num_vert_on_side-1)/3)*3+i+1,1);
V1(counter2,1)=farl;
        xLoccounter=xLoccounter+1;
        xLoc2(xLoccounter,1)=V1(counter2,2);
        counter2=counter2+1;
        V1(counter2,2)=xLoc(fix((num_vert_on_side-1)/3)*3+i,1);
V1(counter2,1)=farl;
        counter=counter+1;
        C1(counter,1)=counter2-3;C1(counter,2)=counter2-
2;C1(counter,3)=counter2-1;C1(counter,4)=counter2;
        end
        xLoc=0; xLoc=xLoc2;
        [aaa,bbb]=size(xLoc);
        num_vert_on_side=aaa;
        xLoccounter=1;
        nearl=farl;
        intermedl=farl-1*Scaleall;
        farl=farl-2*Scaleall;
        end
end
sublfLoc=xLoc;
lflayer=layer;
num_left_transition=counter-(num_cent_transition+num_right_transition);

% NOW create the filling in areas and expand the sides to
% first go down vertical to desired depth and then expand to width

[a,b]=size(subLoc);
subLoc2=0; subLoccount=0;
for i=1:lflayer
    subLoc2(i,1)=-2*(lflayer-i+1)*Scaleall;
end
for i=lflayer+1:lflayer+a
    subLoc2(i,1)=subLoc(i-lflayer,1);
end
for i=lflayer+a+1:lflayer+a+rflayer
    subLoc2(i,1)=width+2*(i-lflayer-a)*Scaleall;
end
subLoc=0;subLoc=subLoc2;

% add in the elements which make the bottom of the substrate under the
% coating
Scaleall2=32;

[a,b]=size(subLoc);

```

```

stop=0; layer=0; xLoc=0; xLoccounter=1; near=centlayer*(-2)*Scaleall;
intermed=near-1*Scaleall; far=near-2*Scaleall;
num_vert_on_side=a;
[a,b]=size(subLoc);
for i=1:a
    xLoc(i,1)=subLoc(i,1);
end
while stop==0
    if num_vert_on_side<4
        stop=1;
        if far>subdepth
            stop2=0; countsub=0;
            [ax,bx]=size(xLoc);
            while stop2==0
                countsub=countsub+1;
                for j=1:ax
                    counter2=counter2+1; V1(counter2,1)=xLoc(j,1);
V1(counter2,2)=near;
                end
                for j=1:ax
                    counter2=counter2+1; V1(counter2,1)=xLoc(j,1);
V1(counter2,2)=far;
                end
                for j=1:(ax-1)
                    counter=counter+1; C1(counter,1)=counter2-ax-
ax+j;C1(counter,2)=counter2-ax-ax+j+1;C1(counter,3)=counter2-
ax+j+1;C1(counter,4)=counter2-ax+j;
                end
                near=far;
                far=far-2*Scaleall*Scaleall2;
                if far<subdepth
                    stop2=1;
                end
            end
        end
    else
        layer=layer+1;
        if ((num_vert_on_side-1)/3)==fix((num_vert_on_side-1)/3)
            remainder1=0;
            big4sets=(num_vert_on_side-1)/3;
        else
            remainder1=3*((num_vert_on_side-1)/3-fix((num_vert_on_side-1)/3));
            big4sets=fix((num_vert_on_side-1)/3);
        end
        xLoc2=0;
        for i=1:big4sets
            counter2=counter2+1; V1(counter2,1)=xLoc(i*3-2,1);
V1(counter2,2)=near;
            counter2=counter2+1; V1(counter2,1)=xLoc(i*3-1,1);
V1(counter2,2)=near;
            counter2=counter2+1; V1(counter2,1)=xLoc(i*3-0,1);
V1(counter2,2)=near;
        end
    end
end

```

```

        counter2=counter2+1; V1(counter2,1)=xLoc(i*3+1,1);
V1(counter2,2)=near;
        counter2=counter2+1; V1(counter2,1)=xLoc(i*3-2,1);
V1(counter2,2)=far;
        if i==1
            xLoc2(1,1)=xLoc(1,1);
        end
        counter2=counter2+1; V1(counter2,1)=xLoc(i*3-1,1);
V1(counter2,2)=intermed;
        counter2=counter2+1; V1(counter2,1)=xLoc(i*3,1);
V1(counter2,2)=intermed;
        counter2=counter2+1; V1(counter2,1)=xLoc(i*3+1,1);
V1(counter2,2)=far; xLoccounter=xLoccounter+1;
xLoc2(xLoccounter,1)=xLoc(i*3+1,1);
        counter=counter+1; C1(counter,1)=counter2-
7;C1(counter,2)=counter2-6;C1(counter,3)=counter2-
2;C1(counter,4)=counter2-3;
        counter=counter+1; C1(counter,1)=counter2-
6;C1(counter,2)=counter2-5;C1(counter,3)=counter2-
1;C1(counter,4)=counter2-2;
        counter=counter+1; C1(counter,1)=counter2-
5;C1(counter,2)=counter2-4;C1(counter,3)=counter2;C1(counter,4)=counter2-
1;
        counter=counter+1; C1(counter,1)=counter2-
3;C1(counter,2)=counter2-2;C1(counter,3)=counter2-
1;C1(counter,4)=counter2;
        end
        for i=1:round(remainder1)
            counter2=counter2+1;
            V1(counter2,1)=xLoc(fix((num_vert_on_side-1)/3)*3+i,1);
V1(counter2,2)=near;
            counter2=counter2+1;
            V1(counter2,1)=xLoc(fix((num_vert_on_side-1)/3)*3+i+1,1);
V1(counter2,2)=near;
            counter2=counter2+1;
            V1(counter2,1)=xLoc(fix((num_vert_on_side-1)/3)*3+i+1,1);
V1(counter2,2)=far; xLoccounter=xLoccounter+1;
xLoc2(xLoccounter,1)=V1(counter2,1);
            counter2=counter2+1;
            V1(counter2,1)=xLoc(fix((num_vert_on_side-1)/3)*3+i,1);
V1(counter2,2)=far;
            counter=counter+1;
            C1(counter,1)=counter2-3;C1(counter,2)=counter2-
2;C1(counter,3)=counter2-1;C1(counter,4)=counter2;
        end
        xLoc=0; xLoc=xLoc2;
        [aaa,bbb]=size(xLoc);
        num_vert_on_side=aaa;
        xLoccounter=1;
        near=far;
        intermed=far-1*Scaleall*Scaleall2;
        far=far-2*Scaleall*Scaleall2;

```

```

        if far<subdepth
            stop=1;
        end
    end
end
centsublayer=layer;
num_cent_sub_transition=counter-
(num_left_transition+num_cent_transition+num_right_transition);

% Add in the left part of the substrate
[a,b]=size(sublfLoc);
sublfLoc2=0;
for i=1:centsublayer+countsub
    sublfLoc2(i,1)=-2*(centsublayer+countsub-
i+1)*Scaleall*Scaleall2+sublfLoc(1,1);
end
for i=(centsublayer+countsub+1):(centsublayer+countsub+a);
    sublfLoc2(i,1)=sublfLoc(i-centsublayer-countsub,1);
end
sublfLoc=0; sublfLoc=sublfLoc2;

stop=0; layer=0; nearl=lflayer*(-2)*Scaleall; intermedl=nearl-1*Scaleall;
farl=nearl-2*Scaleall; xLoc=0; xLoccounter=1;
[a,b]=size(sublfLoc);
num_vert_on_side=a;
for i=1:a
    xLoc(i,1)=sublfLoc(i,1);
end
remainder1=0; remainder=0;
while stop==0
    if num_vert_on_side<4
        stop=1;
        if farl>-subextendwidth
            stop2=0; countlfsub=0;
            [ax,bx]=size(xLoc);
            while stop2==0
                countlfsub=countlfsub+1;
                for j=1:ax
                    counter2=counter2+1; V1(counter2,2)=xLoc(j,1);
V1(counter2,1)=nearl;
                end
                for j=1:ax
                    counter2=counter2+1; V1(counter2,2)=xLoc(j,1);
V1(counter2,1)=farl;
                end
                for j=1:(ax-1)
                    counter=counter+1; C1(counter,1)=counter2-ax-
ax+j;C1(counter,2)=counter2-ax-ax+j+1;C1(counter,3)=counter2-
ax+j+1;C1(counter,4)=counter2-ax+j;
                end
                nearl=farl;
                farl=farl-2*Scaleall*Scaleall2;
            end
        end
    end
end

```

```

        if far1<-subextendwidth
            stop2=1;
        end
    end
end
else
    layer=layer+1;
if ((num_vert_on_side-1)/3)==fix((num_vert_on_side-1)/3)
    remainder1=0;
    big4sets=(num_vert_on_side-1)/3;
else
    remainder1=3*((num_vert_on_side-1)/3-fix((num_vert_on_side-1)/3));
    big4sets=fix((num_vert_on_side-1)/3);
end
xLoc2=0;
for i=1:big4sets
    counter2=counter2+1; V1(counter2,2)=xLoc(i*3-2,1);
V1(counter2,1)=near1;
    counter2=counter2+1; V1(counter2,2)=xLoc(i*3-1,1);
V1(counter2,1)=near1;
    counter2=counter2+1; V1(counter2,2)=xLoc(i*3-0,1);
V1(counter2,1)=near1;
    counter2=counter2+1; V1(counter2,2)=xLoc(i*3+1,1);
V1(counter2,1)=near1;
    counter2=counter2+1; V1(counter2,2)=xLoc(i*3-2,1);
V1(counter2,1)=far1;
    if i==1
        xLoc2(1,1)=xLoc(1,1);
    end
    counter2=counter2+1; V1(counter2,2)=xLoc(i*3-1,1);
V1(counter2,1)=intermed1;
    counter2=counter2+1; V1(counter2,2)=xLoc(i*3,1);
V1(counter2,1)=intermed1;
    counter2=counter2+1; V1(counter2,2)=xLoc(i*3+1,1);
V1(counter2,1)=far1; xLoccounter=xLoccounter+1;
xLoc2(xLoccounter,1)=xLoc(i*3+1,1);
    counter=counter+1; C1(counter,1)=counter2-
7;C1(counter,2)=counter2-6;C1(counter,3)=counter2-
2;C1(counter,4)=counter2-3;
    counter=counter+1; C1(counter,1)=counter2-
6;C1(counter,2)=counter2-5;C1(counter,3)=counter2-
1;C1(counter,4)=counter2-2;
    counter=counter+1; C1(counter,1)=counter2-
5;C1(counter,2)=counter2-4;C1(counter,3)=counter2;C1(counter,4)=counter2-
1;
    counter=counter+1; C1(counter,1)=counter2-
3;C1(counter,2)=counter2-2;C1(counter,3)=counter2-
1;C1(counter,4)=counter2;
end
for i=1:round(remainder1)
    counter2=counter2+1;
    V1(counter2,2)=xLoc(fix((num_vert_on_side-1)/3)*3+i,1);

```

```

V1(counter2,1)=near1;
    counter2=counter2+1;
    V1(counter2,2)=xLoc(fix((num_vert_on_side-1)/3)*3+i+1,1);
V1(counter2,1)=near1;
    counter2=counter2+1;
    V1(counter2,2)=xLoc(fix((num_vert_on_side-1)/3)*3+i+1,1);
V1(counter2,1)=far1;
    xLoccounter=xLoccounter+1;
    xLoc2(xLoccounter,1)=V1(counter2,2);
    counter2=counter2+1;
    V1(counter2,2)=xLoc(fix((num_vert_on_side-1)/3)*3+i,1);
V1(counter2,1)=far1;
    counter=counter+1;
    C1(counter,1)=counter2-3;C1(counter,2)=counter2-
2;C1(counter,3)=counter2-1;C1(counter,4)=counter2;
    end
    xLoc=0; xLoc=xLoc2;
    [aaa,bbb]=size(xLoc);
    num_vert_on_side=aaa;
    xLoccounter=1;
    near1=far1;
    intermed1=far1-1*Scaleall*Scaleall2;
    far1=far1-2*Scaleall*Scaleall2;
    if far1<-subextendwidth
        stop=1;
    end
end
end
sublfLoc=xLoc;
lfsublayer=layer;
num_left_sub_transition=counter-
(num_cent_sub_transition+num_left_transition+num_cent_transition+num_right
_transition);

% add in the right part of the substrate
[a,b]=size(subrtLoc);
subrtLoc2=0;
for i=1:centsublayer+countsub
    subrtLoc2(i,1)=-2*(centsublayer+countsub-
i+1)*Scaleall*Scaleall2+subrtLoc(1,1);
end
for i=(centsublayer+countsub+1):(centsublayer+countsub+a);
    subrtLoc2(i,1)=subrtLoc(i-centsublayer-countsub,1);
end
subrtLoc=0; subrtLoc=subrtLoc2;

stop=0; layer=0; nearr=rtlayer*(2)*Scaleall+width;
intermedr=nearr+1*Scaleall; farr=nearr+2*Scaleall; xLoc=0; xLoccounter=1;
[a,b]=size(subrtLoc);
num_vert_on_side=a;
for i=1:a
    xLoc(i,1)=subrtLoc(i,1);

```

```

end
remainder1=0; remainder=0;
while stop==0
    if num_vert_on_side<4
        stop=1;
        if farr<(subextendwidth+width)
            stop2=0; countlfsub=0;
            [ax,bx]=size(xLoc);
            while stop2==0
                countlfsub=countlfsub+1;
                for j=1:ax
                    counter2=counter2+1; V1(counter2,2)=xLoc(j,1);
V1(counter2,1)=nearr;
                end
                for j=1:ax
                    counter2=counter2+1; V1(counter2,2)=xLoc(j,1);
V1(counter2,1)=farr;
                end
                for j=1:(ax-1)
                    counter=counter+1; C1(counter,1)=counter2-ax-
ax+j;C1(counter,2)=counter2-ax-ax+j+1;C1(counter,3)=counter2-
ax+j+1;C1(counter,4)=counter2-ax+j;
                end
                nearr=farr;
                farr=farr+2*Scaleall*Scaleall2;
                if farr>(subextendwidth+width)
                    stop2=1;
                end
            end
        end
    else
        layer=layer+1;
        if ((num_vert_on_side-1)/3)==fix((num_vert_on_side-1)/3)
            remainder1=0;
            big4sets=(num_vert_on_side-1)/3;
        else
            remainder1=3*((num_vert_on_side-1)/3-fix((num_vert_on_side-1)/3));
            big4sets=fix((num_vert_on_side-1)/3);
        end
        xLoc2=0;
        for i=1:big4sets
            counter2=counter2+1; V1(counter2,2)=xLoc(i*3-2,1);
V1(counter2,1)=nearr;
            counter2=counter2+1; V1(counter2,2)=xLoc(i*3-1,1);
V1(counter2,1)=nearr;
            counter2=counter2+1; V1(counter2,2)=xLoc(i*3-0,1);
V1(counter2,1)=nearr;
            counter2=counter2+1; V1(counter2,2)=xLoc(i*3+1,1);
V1(counter2,1)=nearr;
            counter2=counter2+1; V1(counter2,2)=xLoc(i*3-2,1);
V1(counter2,1)=farr;
            if i==1

```

```

        xLoc2(1,1)=xLoc(1,1);
    end
        counter2=counter2+1; V1(counter2,2)=xLoc(i*3-1,1);
V1(counter2,1)=intermedr;
        counter2=counter2+1; V1(counter2,2)=xLoc(i*3,1);
V1(counter2,1)=intermedr;
        counter2=counter2+1; V1(counter2,2)=xLoc(i*3+1,1);
V1(counter2,1)=farr; xLoccounter=xLoccounter+1;
xLoc2(xLoccounter,1)=xLoc(i*3+1,1);
        counter=counter+1; C1(counter,1)=counter2-
7;C1(counter,2)=counter2-6;C1(counter,3)=counter2-
2;C1(counter,4)=counter2-3;
        counter=counter+1; C1(counter,1)=counter2-
6;C1(counter,2)=counter2-5;C1(counter,3)=counter2-
1;C1(counter,4)=counter2-2;
        counter=counter+1; C1(counter,1)=counter2-
5;C1(counter,2)=counter2-4;C1(counter,3)=counter2;C1(counter,4)=counter2-
1;
        counter=counter+1; C1(counter,1)=counter2-
3;C1(counter,2)=counter2-2;C1(counter,3)=counter2-
1;C1(counter,4)=counter2;
    end
    for i=1:round(remainder1)
        counter2=counter2+1;
        V1(counter2,2)=xLoc(fix((num_vert_on_side-1)/3)*3+i,1);
V1(counter2,1)=narr;
        counter2=counter2+1;
        V1(counter2,2)=xLoc(fix((num_vert_on_side-1)/3)*3+i+1,1);
V1(counter2,1)=narr;
        counter2=counter2+1;
        V1(counter2,2)=xLoc(fix((num_vert_on_side-1)/3)*3+i+1,1);
V1(counter2,1)=farr;
        xLoccounter=xLoccounter+1;
        xLoc2(xLoccounter,1)=V1(counter2,2);
        counter2=counter2+1;
        V1(counter2,2)=xLoc(fix((num_vert_on_side-1)/3)*3+i,1);
V1(counter2,1)=farr;
        counter=counter+1;
        C1(counter,1)=counter2-3;C1(counter,2)=counter2-
2;C1(counter,3)=counter2-1;C1(counter,4)=counter2;
    end
    xLoc=0; xLoc=xLoc2;
    [aaa,bbb]=size(xLoc);
    num_vert_on_side=aaa;
    xLoccounter=1;
    narr=farr;
    intermedr=farr+1*Scaleall*Scaleall2;
    farr=farr+2*Scaleall*Scaleall2;
    if farr>(subextendwidth+width)
        stop=1;
    end
end
end

```

```

end
subrtLoc=xLoc;
rtsublayer=layer;
num_right_sub_transition=counter-
(num_left_sub_transition+num_cent_sub_transition+num_left_transition+num_c
ent_transition+num_right_transition);

% Remove duplicates

[aa,bb]=size(V1);
[cc,dd]=size(C1);
for i=1:aa
    V1(i,3)=i;
end
V1=sortrows(V1); V2=0;
gcount=0; lcount=0;
    gcount=gcount+1;
    V2(gcount,1)=V1(1,1); V2(gcount,2)=V1(1,2); V2(gcount,3)=V1(1,3);
for i=2:aa
    if (V1(i,1)==V1(i-1,1) & V1(i,2)==V1(i-1,2))
        lcount=lcount+1;
        V2(gcount,3+lcount)=V1(i,3);
    else
        gcount=gcount+1;
        V2(gcount,1)=V1(i,1); V2(gcount,2)=V1(i,2);
V2(gcount,3)=V1(i,3);
        lcount=0;
    end
end
[aa,bb]=size(V2); V1=0; gcount=0; Vrep=0;
for i=1:aa
    V1(i,1)=V2(i,1);V1(i,2)=V2(i,2);
    f1=2;
    for j=3:bb
        if V2(i,j)~=0
            f1=f1+1;
        end
    end
    for j=3:f1
        Vrep(V2(i,j),1)=i;
    end
end

[cc,dd]=size(C1);
for i=1:cc
    for j=1:dd
        if C1(i,j)~=0
            C1(i,j)=Vrep(C1(i,j),1);
        end
    end
end
end

```

```

% define the y location where (when scaled at the end) the cutoff is
% between the coating and the end of the titanium layer
disp('Combine coating and transition layers');
% Combine coating and transition layers
[a,b]=size(V);
[c,d]=size(C);
[e,f]=size(V1);
[g,h]=size(C1);
for i=a+1:e+a
    V(i,1)=V1(i-a,1);V(i,2)=V1(i-a,2);
end
for i=c+1:c+g
    for j=1:h
        C(i,j)=C1(i-c,j)+a;
    end
    avgx=(V1(C1(i-c,1),1)+V1(C1(i-c,2),1)+V1(C1(i-c,3),1)+V1(C1(i-
c,4),1))/4;
    avgy=(V1(C1(i-c,1),2)+V1(C1(i-c,2),2)+V1(C1(i-c,3),2)+V1(C1(i-
c,4),2))/4;
    if (avgx<0 & avgy>0)
        Material_Numbers(i,1)=4;    Material_Numbers(i,2)=7;
    elseif (avgx<0 & avgy<0 & avgy>=titanend)
        Material_Numbers(i,1)=4;    Material_Numbers(i,2)=5;
    elseif (avgx<0 & avgy<titanend)
        Material_Numbers(i,1)=4;    Material_Numbers(i,2)=6;
    elseif (avgx>0 & avgx<width & avgy>titanend)
        Material_Numbers(i,1)=3;    Material_Numbers(i,2)=5;
    elseif (avgx>0 & avgx<width & avgy<titanend)
        Material_Numbers(i,1)=3;    Material_Numbers(i,2)=6;
    elseif (avgx>=width & avgy>0)
        Material_Numbers(i,1)=5;    Material_Numbers(i,2)=7;
    elseif (avgx>=width & avgy<0 & avgy>=titanend)
        Material_Numbers(i,1)=5;    Material_Numbers(i,2)=5;
    elseif (avgx>=width & avgy<titanend)
        Material_Numbers(i,1)=5;    Material_Numbers(i,2)=6;
    end
    Material_Numbers(i,4)=0;
    Material_Numbers(i,5)=i;
    AL=0;
    for j=1:4
        if j==4
            N=1;
        else
            N=j+1;
        end
        mm=[V(C(i,j),1) V(C(i,j),2)]; nn=[V(C(i,N),1)
V(C(i,N),2)];
        AL=AL+0.5*((mm(1,1)*(nn(1,2)))-(nn(1,1)*mm(1,2)));
    end
    Material_Numbers(i,3)=AL;
end
end

```

```

% Remove duplicates at the interface

V1=V;
C1=C;

[aa,bb]=size(V1);
[cc,dd]=size(C1);
for i=1:aa
    V1(i,3)=i;
end
V1=sortrows(V1); V2=0;
gcount=0; lcount=0;
    gcount=gcount+1;
    V2(gcount,1)=V1(1,1); V2(gcount,2)=V1(1,2); V2(gcount,3)=V1(1,3);
for i=2:aa
    if (V1(i,1)==V1(i-1,1) & V1(i,2)==V1(i-1,2))
        lcount=lcount+1;
        V2(gcount,3+lcount)=V1(i,3);
    else
        gcount=gcount+1;
        V2(gcount,1)=V1(i,1); V2(gcount,2)=V1(i,2);
    V2(gcount,3)=V1(i,3);
        lcount=0;
    end
end
[aa,bb]=size(V2); V1=0; gcount=0; Vrep=0;
for i=1:aa
    V1(i,1)=V2(i,1);V1(i,2)=V2(i,2);
    f1=2;
    for j=3:bb
        if V2(i,j)~=0
            f1=f1+1;
        end
    end
    for j=3:f1
        Vrep(V2(i,j),1)=i;
    end
end

[cc,dd]=size(C1);
for i=1:cc
    for j=1:dd
        if C1(i,j)~=0
            C1(i,j)=Vrep(C1(i,j),1);
        end
    end
end

V=V1;
C=C1;

```

```

disp('Meshing routine');
% Split up the cells with six sides into 2 four sided cells based on
% jacobian and internal angles
% Form the element list, with the element vertices in the first four
% columns and the fifth column is the association (i.e. the number of the
% parent cell it came from or 0 for the border regions
[a,b]=size(C);
num_vert=0;
for i=1:a
    f1=0;
    for j=1:b
        if C(i,j)~=0
            f1=f1+1;
        end
    end
    num_vert(i,1)=f1;
end

elements=0; counter=0; ctoelements=zeros(Number_inculsions,4);
disp('Form border element list....');
for
i=(num_inclusions)+1:(num_inclusions+num_borders+num_perim+num_cent_transi
tion+num_left_transition+num_right_transition+num_cent_sub_transition+num_
left_sub_transition+num_right_sub_transition)
    counter=counter+1;
    elements(counter,1)=C(i,1);
    elements(counter,2)=C(i,2);
    elements(counter,3)=C(i,3);
    elements(counter,4)=C(i,4);
    elements(counter,5)=0;
    ctoelements(i,1)=counter;
    Material_Numbers(i,5)=counter;
end
disp('Form inclusion element list (mesh)....');
for i=1:Number_inculsions
    if num_vert(i,1)==4
        counter=counter+1;
        elements(counter,1)=C(i,1);
        elements(counter,2)=C(i,2);
        elements(counter,3)=C(i,3);
        elements(counter,4)=C(i,4);
        elements(counter,5)=i;
        ctoelements(i,1)=counter;
        Material_Numbers(i,5)=counter;
    elseif num_vert(i,1)==6
        % Three different possible ways to mesh - investigate all three
        % pick the best one - greatest jacobian + best aspect ratio +
        % minimum ratio of shortest to longest side
        ele_list=zeros(2,4,3); % The rows are the elements, the columns
% are the vertices, and the third dimension is the possible element
% variation

```

```

        ele_list(1,1,1)=C(i,1); ele_list(1,2,1)=C(i,2);
ele_list(1,3,1)=C(i,3); ele_list(1,4,1)=C(i,4);
        ele_list(2,1,1)=C(i,4); ele_list(2,2,1)=C(i,5);
ele_list(2,3,1)=C(i,6); ele_list(2,4,1)=C(i,1);
        ele_list(1,1,2)=C(i,2); ele_list(1,2,2)=C(i,3);
ele_list(1,3,2)=C(i,4); ele_list(1,4,2)=C(i,5);
        ele_list(2,1,2)=C(i,5); ele_list(2,2,2)=C(i,6);
ele_list(2,3,2)=C(i,1); ele_list(2,4,2)=C(i,2);
        ele_list(1,1,3)=C(i,3); ele_list(1,2,3)=C(i,4);
ele_list(1,3,3)=C(i,5); ele_list(1,4,3)=C(i,6);
        ele_list(2,1,3)=C(i,6); ele_list(2,2,3)=C(i,1);
ele_list(2,3,3)=C(i,2); ele_list(2,4,3)=C(i,3);

    % Compute the internal angles
    internalangle=zeros(2,4,3);
    for T=1:3
        for j=1:2
            for k=1:4
                if k==1
                    m=[V(ele_list(j,1,T),1) V(ele_list(j,1,T),2)];
n=[V(ele_list(j,2,T),1) V(ele_list(j,2,T),2)]; r=[V(ele_list(j,4,T),1)
V(ele_list(j,4,T),2)];
                    elseif k==2
                        m=[V(ele_list(j,2,T),1) V(ele_list(j,2,T),2)];
n=[V(ele_list(j,3,T),1) V(ele_list(j,3,T),2)]; r=[V(ele_list(j,1,T),1)
V(ele_list(j,1,T),2)];
                    elseif k==3
                        m=[V(ele_list(j,3,T),1) V(ele_list(j,3,T),2)];
n=[V(ele_list(j,4,T),1) V(ele_list(j,4,T),2)]; r=[V(ele_list(j,2,T),1)
V(ele_list(j,2,T),2)];
                    elseif k==4
                        m=[V(ele_list(j,4,T),1) V(ele_list(j,4,T),2)];
n=[V(ele_list(j,1,T),1) V(ele_list(j,1,T),2)]; r=[V(ele_list(j,3,T),1)
V(ele_list(j,3,T),2)];
                    end
                    q=n-m;
                    s=r-m;

                internalangle(j,k,T)=acos(dot(q,s)/(sqrt(q(1,1)^2+q(1,2)^2)*sqrt(s(1,1)^2+
s(1,2)^2)));
            end
        end
    end
    % Find the maximum and minimum internal angles
    maxmininternalangles=zeros(2,2,3);
    for T=1:3
        for j=1:2
            maxv=0; minv=10000;
            for k=1:4
                if internalangle(j,k,T)>maxv
                    maxv=internalangle(j,k,T);
                end
            end
        end
    end

```

```

        if internalangle(j,k,T)<minv
            minv=internalangle(j,k,T);
        end
    end
    maxmininternalangles(j,1,T)=maxv;
    maxmininternalangles(j,2,T)=minv;
end
end
% Isoparamteric Coordinates
S(1,1)=0;S(2,1)=1;S(3,1)=1;S(4,1)=0;
S(1,2)=0;S(2,2)=0;S(3,2)=1;S(4,2)=1;

% Compute the Jacobian for each Mesh
for T=1:3
    J=zeros(1,3);
    for jjj=1:4
        H1=(0.25*(1+S(j,1))*V(ele_list(1,1,T),1)-
0.25*(1+S(j,1))*V(ele_list(1,2,T),1)-0.25*(1-
S(j,1))*V(ele_list(1,3,T),1)+0.25*(1-S(j,1))*V(ele_list(1,4,T),1));
        H2=(0.25*(1+S(j,2))*V(ele_list(1,1,T),1)-
0.25*(1+S(j,2))*V(ele_list(1,2,T),1)-0.25*(1-
S(j,2))*V(ele_list(1,3,T),1)+0.25*(1-S(j,2))*V(ele_list(1,4,T),1));
        H3=(0.25*(1+S(j,1))*V(ele_list(1,1,T),2)-
0.25*(1+S(j,1))*V(ele_list(1,2,T),2)-0.25*(1-
S(j,1))*V(ele_list(1,3,T),2)+0.25*(1-S(j,1))*V(ele_list(1,4,T),2));
        H4=(0.25*(1+S(j,2))*V(ele_list(1,1,T),2)-
0.25*(1+S(j,2))*V(ele_list(1,2,T),2)-0.25*(1-
S(j,2))*V(ele_list(1,3,T),2)+0.25*(1-S(j,2))*V(ele_list(1,4,T),2));
        J(1,T)=det([H1 H3;H2 H4]);
    end
end
MaxJ=-100;
BestMesh=0;
for T=1:3
    if J(1,T)>MaxJ
        BestMesh=T;
    end
end
% Pick the meshing option which gives the greatest minimum
% internal
% angle and the smallest maximum internal angle
max=zeros(3,1);
for T=1:3
    if maxmininternalangles(1,1,T)>maxmininternalangles(2,1,T)
& BestMesh==T
        max(T,1)=maxmininternalangles(1,1,T);
    elseif
maxmininternalangles(1,1,T)<maxmininternalangles(2,1,T) & BestMesh==T
        max(T,1)=maxmininternalangles(2,1,T);
    elseif
maxmininternalangles(2,2,T)==maxmininternalangles(2,1,T) & BestMesh==T
        max(T,1)=maxmininternalangles(1,2,T);
    end
end

```

```

        elseif
maxmininternalangles(2,1,T)==maxmininternalangles(2,2,T) & BestMesh==T
            max(T,1)=maxmininternalangles(2,2,T);
        end
    end
    meshopt=0;
    if (max(1,1)<max(2,1) & max(1,1)<max(3,1))
        meshopt=1;
    elseif (max(2,1)<max(1,1) & max(2,1)<max(3,1))
        meshopt=2;
    elseif (max(3,1)<max(1,1) & max(3,1)<max(2,1))
        meshopt=3;

    elseif (max(1,1)==max(2,1) & max(1,1)<max(3,1))
        meshopt=1;
    elseif (max(1,1)==max(2,1) & max(1,1)>max(3,1))
        meshopt=3;

    elseif (max(2,1)==max(3,1) & max(2,1)<max(1,1))
        meshopt=2;
    elseif (max(2,1)==max(3,1) & max(2,1)>max(1,1))
        meshopt=1;

    elseif (max(3,1)==max(1,1) & max(1,1)<max(2,1))
        meshopt=1;
    elseif (max(3,1)==max(1,1) & max(1,1)>max(2,1))
        meshopt=2;
    else
        disp('No mesh max was found here, so default was used (1)');
        disp([max(1,1) max(2,1) max(3,1)]);
        meshopt=1;
    end

    % Perform the meshing now
    for j=1:2
        counter=counter+1;
        elements(counter,1)=ele_list(j,1,meshopt);
        elements(counter,2)=ele_list(j,2,meshopt);
        elements(counter,3)=ele_list(j,3,meshopt);
        elements(counter,4)=ele_list(j,4,meshopt);
        elements(counter,5)=i;
        ctoelements(i,j)=counter;
        Material_Numbers(i,4+j)=counter;
    end

elseif num_vert(i,1)==8

    % Four different possible ways to mesh - investigate all three and
    % pick the best one - greatest jacobian + best aspect ratio +
    % minimum ratio of shortest to longest side
    ele_list=zeros(3,4,4); % The rows are the elements, the columns
% are the vertices, and the third dimension is the possible element

```

```

% variation
    ele_list(1,1,1)=C(i,1); ele_list(1,2,1)=C(i,2);
ele_list(1,3,1)=C(i,3); ele_list(1,4,1)=C(i,4);
    ele_list(2,1,1)=C(i,4); ele_list(2,2,1)=C(i,5);
ele_list(2,3,1)=C(i,8); ele_list(2,4,1)=C(i,1);
    ele_list(3,1,1)=C(i,5); ele_list(3,2,1)=C(i,6);
ele_list(3,3,1)=C(i,7); ele_list(3,4,1)=C(i,8);

    ele_list(1,1,2)=C(i,2); ele_list(1,2,2)=C(i,3);
ele_list(1,3,2)=C(i,4); ele_list(1,4,2)=C(i,5);
    ele_list(2,1,2)=C(i,5); ele_list(2,2,2)=C(i,6);
ele_list(2,3,2)=C(i,1); ele_list(2,4,2)=C(i,2);
    ele_list(3,1,2)=C(i,6); ele_list(3,2,2)=C(i,7);
ele_list(3,3,2)=C(i,8); ele_list(3,4,2)=C(i,1);

    ele_list(1,1,3)=C(i,3); ele_list(1,2,3)=C(i,4);
ele_list(1,3,3)=C(i,5); ele_list(1,4,3)=C(i,6);
    ele_list(2,1,3)=C(i,6); ele_list(2,2,3)=C(i,7);
ele_list(2,3,3)=C(i,2); ele_list(2,4,3)=C(i,3);
    ele_list(3,1,3)=C(i,7); ele_list(3,2,3)=C(i,8);
ele_list(3,3,3)=C(i,1); ele_list(3,4,3)=C(i,2);

    ele_list(1,1,4)=C(i,4); ele_list(1,2,4)=C(i,5);
ele_list(1,3,4)=C(i,6); ele_list(1,4,4)=C(i,7);
    ele_list(2,1,4)=C(i,7); ele_list(2,2,4)=C(i,8);
ele_list(2,3,4)=C(i,3); ele_list(2,4,4)=C(i,4);
    ele_list(3,1,4)=C(i,8); ele_list(3,2,4)=C(i,1);
ele_list(3,3,4)=C(i,2); ele_list(3,4,4)=C(i,3);
    % Compute the internal angles
    internalangle=zeros(3,4,4);
    for T=1:4
        for j=1:3
            for k=1:4
                if k==1
                    m=[V(ele_list(j,1,T),1) V(ele_list(j,1,T),2)];
n=[V(ele_list(j,2,T),1) V(ele_list(j,2,T),2)]; r=[V(ele_list(j,4,T),1)
V(ele_list(j,4,T),2)];
                    elseif k==2
                        m=[V(ele_list(j,2,T),1) V(ele_list(j,2,T),2)];
n=[V(ele_list(j,3,T),1) V(ele_list(j,3,T),2)]; r=[V(ele_list(j,1,T),1)
V(ele_list(j,1,T),2)];
                    elseif k==3
                        m=[V(ele_list(j,3,T),1) V(ele_list(j,3,T),2)];
n=[V(ele_list(j,4,T),1) V(ele_list(j,4,T),2)]; r=[V(ele_list(j,2,T),1)
V(ele_list(j,2,T),2)];
                    elseif k==4
                        m=[V(ele_list(j,4,T),1) V(ele_list(j,4,T),2)];
n=[V(ele_list(j,1,T),1) V(ele_list(j,1,T),2)]; r=[V(ele_list(j,3,T),1)
V(ele_list(j,3,T),2)];
                    end
                    q=n-m;
                    s=r-m;
                end
            end
        end
    end

```

```

internalangle(j,k,T)=acos(dot(q,s)/(sqrt(q(1,1)^2+q(1,2)^2)*sqrt(s(1,1)^2+
s(1,2)^2)));
    end
end
end
% Find the maximum and minimum internal angles
maxmininternalangles=zeros(3,2,4);
for T=1:4
    for j=1:3
        maxv=0; minv=10000;
        for k=1:4
            if internalangle(j,k,T)>maxv
                maxv=internalangle(j,k,T);
            end
            if internalangle(j,k,T)<minv
                minv=internalangle(j,k,T);
            end
        end
        maxmininternalangles(j,1,T)=maxv;
        maxmininternalangles(j,2,T)=minv;
    end
end

% Isoparametric Coordinates
S(1,1)=0;S(2,1)=1;S(3,1)=1;S(4,1)=0;
S(1,2)=0;S(2,2)=0;S(3,2)=1;S(4,2)=1;

% Compute the Jaconian for each mesh
for T=1:4
    J=zeros(1,4);
    for jjj=1:4
        H1=(0.25*(1+S(j,1))*V(ele_list(1,1,T),1)-
0.25*(1+S(j,1))*V(ele_list(1,2,T),1)-0.25*(1-
S(j,1))*V(ele_list(1,3,T),1)+0.25*(1-S(j,1))*V(ele_list(1,4,T),1));
        H2=(0.25*(1+S(j,2))*V(ele_list(1,1,T),1)-
0.25*(1+S(j,2))*V(ele_list(1,2,T),1)-0.25*(1-
S(j,2))*V(ele_list(1,3,T),1)+0.25*(1-S(j,2))*V(ele_list(1,4,T),1));
        H3=(0.25*(1+S(j,1))*V(ele_list(1,1,T),2)-
0.25*(1+S(j,1))*V(ele_list(1,2,T),2)-0.25*(1-
S(j,1))*V(ele_list(1,3,T),2)+0.25*(1-S(j,1))*V(ele_list(1,4,T),2));
        H4=(0.25*(1+S(j,2))*V(ele_list(1,1,T),2)-
0.25*(1+S(j,2))*V(ele_list(1,2,T),2)-0.25*(1-
S(j,2))*V(ele_list(1,3,T),2)+0.25*(1-S(j,2))*V(ele_list(1,4,T),2));
        J(1,T)=det([H1 H3;H2 H4]);
    end
end
MaxJ=-100;
BestMesh=0;
for T=1:4
    if J(1,T)>MaxJ
        BestMesh=T;
    end
end

```

```

        end
    end

    % Pick the meshing option which gives the greatest minimum
    % internal
    % angle and the smallest maximum internal angle
max=zeros(4,1);
    for T=1:4
        if maxmininternalangles(1,1,T)>maxmininternalangles(2,1,T)
& BestMesh==T
            if
maxmininternalangles(1,1,T)>maxmininternalangles(3,1,T) & BestMesh==T
                max(T,1)=maxmininternalangles(1,1,T);
            else
                max(T,1)=maxmininternalangles(3,1,T);
            end
            elseif
maxmininternalangles(2,1,T)>maxmininternalangles(1,1,T) & BestMesh==T
                if
maxmininternalangles(2,1,T)>maxmininternalangles(3,1,T) & BestMesh==T
                    max(T,1)=maxmininternalangles(2,1,T);
                else
                    max(T,1)=maxmininternalangles(3,1,T);
                end
            end
        end
    end
    meshopt=0;
    if max(1,1)<max(2,1)
        if max(1,1)<max(3,1)
            if max(1,1)<max(4,1)
                meshopt=1;
            else
                meshopt=4;
            end
        else
            if max(3,1)<max(4,1)
                meshopt=3;
            else
                meshopt=4;
            end
        end
    else
        if max(2,1)<max(3,1)
            if max(2,1)<max(4,1)
                meshopt=2;
            else
                meshopt=4;
            end
        else
            if max(3,1)<max(4,1)
                meshopt=3;
            end
        end
    end
end

```

```

        else
            meshopt=4;
        end
    end
end
% Perform the meshing now
for j=1:3
    counter=counter+1;
    elements(counter,1)=ele_list(j,1,meshopt);
    elements(counter,2)=ele_list(j,2,meshopt);
    elements(counter,3)=ele_list(j,3,meshopt);
    elements(counter,4)=ele_list(j,4,meshopt);
    elements(counter,5)=i;
    ctoelements(i,j)=counter;
    Material_Numbers(i,4+j)=counter;
end

elseif num_vert(i,1)>8
    disp('Problem, greater than 8 vertices');
end
end

[a,b]=size(elements);
C=0;
for i=1:a
    for k=1:4
        C(i,k)=elements(i,k);
    end
end

disp('The number of elements is');
disp([a]);
disp('that is all.....');

% Point material assignments to the elements number (no longer the
% inclusion number in the original Voronoi C list)
[a,b]=size(C);
[c,d]=size(Material_Numbers);
Material_Numbers_elements=0;
for
i=1:(num_inclusions+num_borders+num_perim+num_cent_transition+num_left_tra
nsition+num_right_transition+num_cent_sub_transition+num_left_sub_transiti
on+num_right_sub_transition)
    f1=0;
    for j=5:d
        if Material_Numbers(i,j)~=0
            f1=f1+1;
        end
    end
    for j=5:4+f1
Material_Numbers_elements(Material_Numbers(i,j),1)=Material_Numbers(i,1);

```

```

Material_Numbers_elements(Material_Numbers(i,j),2)=Material_Numbers(i,2);
    end
end

disp('Reassigned material numbers to elements numbers');

disp('The number of elements is:');
[a,b]=size(C)

fid1=fopen('/Applications/MATLAB72/bigV/meshbigv_Nodes_8-20-07.txt','w');
[a,b]=size(V);
    fprintf(fid1,'%12.12g %12.12g\n',height,width);
for i=1:a
    fprintf(fid1,'%12.12g %12.12g\n',V(i,1),V(i,2));
end
fclose(fid1);

fid1=fopen('/Applications/MATLAB72/bigV/meshbigv_Elements_8-20-
07.txt','w');
[a,b]=size(C);
for i=1:a
    fprintf(fid1,'%12.12g %12.12g %12.12g
%12.12g\n',C(i,1),C(i,2),C(i,3),C(i,4));
end
fclose(fid1);

fid1=fopen('/Applications/MATLAB72/bigV/meshbigv_Materials_8-20-
07.txt','w');

for i=1:(a)
    fprintf(fid1,'%12.12g\n',Material_Numbers_elements(i,2));
end
fclose(fid1);

```

THE END